Dissertation

# The interplay between supermassive black holes and their host galaxies

von

**Sabine Thater**

Leibniz-Institut für Astrophysik Potsdam (AIP)

zur Erlangung des akademischen Grades

doctor rerum naturalium (Dr. rer. nat.)

in der Wissenschaftsdisziplin Astrophysik


eingereicht an der

Universität Potsdam
Mathematisch-Naturwissenschaftliche Fakultät
Institut für Physik und Astronomie

19.Juni 2019

Betreuer: Dr. Davor Krajnović, Prof. Dr. Lutz Wisotzki

1. Gutachter: Prof. Dr. Lutz Wisotzki
Leibniz-Institute for Astrophysics Potsdam

2. Gutachter: Prof. Dr. Philipp Richter
University of Potsdam

3. Gutachter: Prof. Dr. Karl Gebhardt
University of Texas

Published online at the
Institutional Repository of the University of Potsdam:
https://doi.org/10.25932/publishup-43757
https://nbn-resolving.org/urn:nbn:de:kobv:517-opus4-437570

*We keep moving forward, opening new doors, and doing new things, because we're curious and curiosity keeps leading us down new paths.*

Walt Disney

# Zusammenfassung

Supermassereiche schwarze Löcher befinden sich in den Herzen von fast allen massiven Galaxien. Ihr evolutionärer Werdegang scheint stark mit dem Wachstum ihrer Muttergalaxien in Verbindung zu stehen, wie mehrere empirische Beziehungen zwischen der Masse der schwarzen Löcher ($M_{\rm BH}$) und verschiedenen Eigenschaften der Muttergalaxien andeuten. Der physikalische Ursprung dieser Koevolution ist jedoch immer noch nicht verstanden. Weitere Massenmessungen über homogene Galaxienproben und ein detailliertes Verständnis der systematischen Unsicherheiten sind erforderlich, um den Ursprung dieser Skalierungsbeziehungen zu ergründen.

In dieser Arbeit präsentiere ich die Massenabschätzungen von Supermassereichen Schwarzen Löchern der Zentren einer Spiral- und dreizehn elliptischer und linsenförmiger Galaxien. Meine SMASHING-Probe erstreckt sich vom mittleren bis zum hohen Galaxienmassenbereich und wurde ausgewählt, um Lücken entlang der Skalierungsbeziehungen zu schließen. Alle Galaxien wurden mit hoher räumlicher Auflösung beobachtet, wobei der adaptiv-optische Modus von Integralfeldspektrographen (IFU) modernster Teleskope (SINFONI, NIFS, MUSE) verwendet wurde. Aus diesen Beobachtungen habe ich die Sternenkinematik extrahiert und dynamische Jeans- und Schwarzschildmodelle konstruiert, um die Masse der zentralen Schwarzen Löcher robust zu bestimmen. Meine neuen Massenschätzungen erhöhen die Anzahl elliptischer Galaxien mit vermessenen Schwarzen Löchern um 15%. Die sieben vermessenen Galaxien mit inneren Lichtdefiziten ("Cores") ergänzen die Probe der *Core*-Galaxien mit gemessenen schwarzen Löchern um 40%. Neben der Bestimmung ist die Beurteilung der Genauigkeit von Schwarzlochmassen entscheidend für das Verständnis der intrinsischen Streuung der Beziehungen zwischen schwarzem Loch und Muttergalaxie. Ich habe meine abgeleiteten Massenabschätzungen auf verschiedene systematische Fehlerquellen getestet.

Für das Schwarzen Loch der einzigen Spiralgalaxie der SMASHING-Probe war es mir nur möglich eine obere Grenzmasse zu bestimmen, die ich aber sehr robust eingrenzen konnte. Ich testete die Auswirkungen von Staub, Variation des Masse-Licht-Verhältnisses (M/L) und Dunkler Materie auf meine gemessenen $M_{\rm BH}$ . Auf Grundlage dieser Tests kann das typischerweise angenommene konstante M/L-Verhältnis eine angemessene Annahme sein, um den geringen Anteil dunkler Materie im Zentrum dieser Galaxie zu berücksichtigen. Ich habe auch den Effekt einer variablen M/L-Variation auf die $M_{\rm BH}$ -Messung an einer zweiten Galaxie getestet. Unter Berücksichtigung der stellaren M/L-Variationen in der dynamischen Modellierung reduzierte sich die gemessene $M_{\rm BH}$ um 30%. In Zukunft sollte dieser Test auf weitere Galaxien angewandt werden, um zu erfahren, wie ein als konstant angenommenes M/L die geschätzten Schwarzlochmassen verfälscht.
Meine genaue Massenmessung der Obergrenze der Schwarzlochmasse der Spiralgalaxie bestätigt frühere Vorschläge, dass die räumliche Auflösung des Einflussbereichs Schwarzer Löcher keine notwendige Bedingung für die Messung von Schwarzlochmassen ist. Stattdessen ist es nur eine grobe Orientierung für das Auffinden Schwarzer Löcher, wenn für die Messung hochwertige und mit geringem Bildrauschen versehene IFU-Daten verwendet werden.
Etwa die Hälfte meiner Probe besteht aus massiven elliptischen Galaxien, die Kernober-

flächenhelligkeitsdefizite und Anzeichen von Triaxialität aufweisen. Während diese Arten von Galaxien typischerweise mit achsensymmetrischen Modellierungsmethoden vermessen werden, sind die Auswirkungen auf $M_{\mathrm{BH}}$ noch nicht gut untersucht. Die massiven Galaxien meiner vorgestellten Galaxienprobe eignen sich gut, um die Wirkung verschiedener dynamischer Modelle auf die gemessene Schwarzlochmasse in offensichtlich triaxialen Galaxien zu testen. Ich habe sphärische Jeans- und achsensymmetrische Schwarzschildmodelle verglichen und werde in Zukunft triaxiale Schwarzschildmodelle zu diesem Vergleich hinzufügen. Die konstruierten Jeans- und Schwarzschildmodelle sind weitgehend inkonsistent und können viele der triaxialen Merkmale der Galaxien (z.B. nukleare Subkomponenten, Prolatenrotation) nicht nachbilden. Die Konsequenz der achsensymmetrisch-triaxialen Annahme auf die Genauigkeit von $M_{\mathrm{BH}}$ und ihre Auswirkungen auf die Beziehung zwischen Schwarzem Loch und Muttergalaxie muss in Zukunft sorgfältig untersucht werden.
In der Stichprobe von Galaxien mit veröffentlichtem $M_{\mathrm{BH}}$ befinden sich Messungen, die auf verschiedenen dynamischen Tracern basieren und unterschiedliche Beobachtungen, Annahmen und Methoden erfordern. Entscheidend ist, dass verschiedene Tracer nicht immer konsistente Ergebnisse liefern. Ich habe zwei unabhängige Tracer (kaltes molekulares Gas und Sterne) verwendet, um $M_{\mathrm{BH}}$ in einer normalen Galaxie unserer Galaxienprobe zu schätzen. Während die beiden Schätzungen innerhalb ihrer Fehler konsistent sind, ist die stellarbasierte Massenmessung doppelt so hoch wie die gasbasierte. ähnliche Trends wurden auch in der Forschungsliteratur gefunden. Daher ist in Zukunft ein rigoroser Test der Systematik der verschiedenen Modellierungsmethoden erforderlich. Daher ist es von entscheidender Bedeutung, die Auswirkungen verschiedener Tracer (und Methoden) bei der Diskussion der Skalierungsbeziehungen nicht zu berücksichtigen.

Ich schließe diese Arbeit, indem ich meine Galaxienprobe mit der den in der Forschungsliteratur zusammengestellten Galaxien mit bereits vermessenen Schwarzen Löchern vergleiche und auch sechs SMASHING-Galaxien hinzufüge, die außerhalb dieser Arbeit veröffentlicht wurden. Keine der SMASHING-Galaxien weicht signifikant von den veröffentlichten Messungen ab. Eine gemeinsame Analyse meiner Messungen und der veröffentlichten elliptischen Galaxien ergibt eine Abflachung der Steigung für die $M_{\mathrm{BH}}$ - effektive Geschwindigkeitsdispersionsbeziehung, die hauptsächlich von den massiven Galaxien meiner Probe bewirkt wird. In Zukunft sind unvoreingenommene und homogenere Messungen erforderlich, um die Form der Skalierungsbeziehung zu bestimmen und ihren physikalischen Ursprung zu verstehen.

# Abstract

Supermassive black holes reside in the hearts of almost all massive galaxies. Their evolutionary path seems to be strongly linked to the evolution of their host galaxies, as implied by several empirical relations between the black hole mass ($M_{\rm BH}$) and different host galaxy properties. The physical driver of this co-evolution is, however, still not understood. More mass measurements over homogeneous samples and a detailed understanding of systematic uncertainties are required to fathom the origin of the scaling relations.

In this thesis, I present the mass estimations of supermassive black holes in the nuclei of one late-type and thirteen early-type galaxies. Our SMASHING sample extends from the intermediate to the massive galaxy mass regime and was selected to fill in gaps in number of galaxies along the scaling relations. All galaxies were observed at high spatial resolution, making use of the adaptive-optics mode of integral field unit (IFU) instruments on state-of-the-art telescopes (SINFONI, NIFS, MUSE). I extracted the stellar kinematics from these observations and constructed dynamical Jeans and Schwarzschild models to estimate the mass of the central black holes robustly. My new mass estimates increase the number of early-type galaxies with measured black hole masses by 15%. The seven measured galaxies with nuclear light deficits ('cores') augment the sample of cored galaxies with measured black holes by 40%. Next to determining massive black hole masses, evaluating the accuracy of black hole masses is crucial for understanding the intrinsic scatter of the black hole- host galaxy scaling relations. I tested various sources of systematic uncertainty on my derived mass estimates.

The $M_{\rm BH}$ estimate of the single late-type galaxy of the sample yielded an upper limit, which I could constrain very robustly. I tested the effects of dust, mass-to-light ratio ($M/L$) variation, and dark matter on my measured $M_{\rm BH}$. Based on these tests, the typically assumed constant $M/L$ ratio can be an adequate assumption to account for the small amounts of dark matter in the center of that galaxy. I also tested the effect of a variable $M/L$ variation on the $M_{\rm BH}$ measurement on a second galaxy. By considering stellar $M/L$ variations in the dynamical modeling, the measured $M_{\rm BH}$ decreased by 30%. In the future, this test should be performed on additional galaxies to learn how an as constant assumed $M/L$ flaws the estimated black hole masses.
Based on our upper limit mass measurement, I confirm previous suggestions that resolving the predicted BH sphere-of-influence is not a strict condition to measure black hole masses. Instead, it is only a rough guide for the detection of the black hole if high-quality, and high signal-to-noise IFU data are used for the measurement.
About half of our sample consists of massive early-type galaxies which show nuclear surface brightness cores and signs of triaxiality. While these types of galaxies are typically modeled with axisymmetric modeling methods, the effects on $M_{\rm BH}$ are not well studied yet. The massive galaxies of our presented galaxy sample are well suited to test the effect of different stellar dynamical models on the measured black hole mass in evidently triaxial galaxies. I have compared spherical Jeans and axisymmetric Schwarzschild models and will add triaxial Schwarzschild models to this comparison in the future. The constructed Jeans and Schwarzschild models mostly disagree with each other and cannot reproduce many of the triaxial features of the galaxies (e.g., nuclear sub-components, prolate rotation). The

consequence of the axisymmetric-triaxial assumption on the accuracy of $M_{\rm BH}$ and its impact on the black hole - host galaxy relation needs to be carefully examined in the future.
In the sample of galaxies with published $M_{\rm BH}$, we find measurements based on different dynamical tracers, requiring different observations, assumptions, and methods. Crucially, different tracers do not always give consistent results. I have used two independent tracers (cold molecular gas and stars) to estimate $M_{\rm BH}$ in a regular galaxy of our sample. While the two estimates are consistent within their errors, the stellar-based measurement is twice as high as the gas-based. Similar trends have also been found in the literature. Therefore, a rigorous test of the systematics associated with the different modeling methods is required in the future. I caution to take the effects of different tracers (and methods) into account when discussing the scaling relations.

I conclude this thesis by comparing my galaxy sample with the compilation of galaxies with measured black holes from the literature, also adding six SMASHING galaxies, which were published outside of this thesis. None of the SMASHING galaxies deviates significantly from the literature measurements. Their inclusion to the published early-type galaxies causes a change towards a shallower slope for the $M_{\rm BH}$ - effective velocity dispersion relation, which is mainly driven by the massive galaxies of our sample. More unbiased and homogenous measurements are needed in the future to determine the shape of the relation and understand its physical origin.

# Contents

# 1 Introduction

## 1 Supermassive black holes

Supermassive black holes (SMBH) belong to, if not are, the most extreme objects in the Universe. They are so mysterious that it took decades for people to stop doubting their existence. While first theoretical thoughts were already set in 1783 when geologist and astronomer John Mitchell postulated his theory about massive dark stars, the advent of integral field spectroscopy and high-spatial resolution radio interferometry has improved our understanding of SMBHs rapidly over the last decade. The discovery of gravitational waves from the merger of stellar black holes (e.g., Abbott et al. 2016; LIGO Scientific Collaboration et al. 2018) and finally the recent publication of an "image" of the event horizon of the supermassive black hole in Sgr A* and M 87 (Event Horizon Telescope Collaboration et al. 2019a,b) has finally convinced most sceptics.

While not simple to grasp, black holes have a relatively simple concept. They are objects which are so massive that even light cannot escape their gravitational pull. Expressed in Newton mechanics, a black hole is a compact collapsed object which fits inside its Schwarzschild radius

$$R_{\mathrm{S}} = 2\frac{GM_{\mathrm{BH}}}{c^2} \tag{1.1}$$

that is defined by inserting the speed of light for the escape velocity. This definition immediately holds the for the observer very depressing implication that black holes are not directly observable. Nevertheless, it was possible to find strong observational evidence for the existence of black holes. A first strong (but not decisive) evidence was the realization that Active Galactic Nuclei (AGN) were not stars, but incredibly energetic phenomena at high redshift (e.g. Baade & Minkowski 1954). Following studies noted more and more of these phenomena in radio-loud and radio-quiet galaxies, suggesting them to be ubiquitous in the Universe. AGN being supermassive black holes residing in the centers of galaxies was shortly thereafter suggested by Lynden-Bell (1969) and Lynden-Bell & Rees (1971). Since then, the search for an unambiguous proof of the existence of supermassive black holes was carried out observationally and progressed more and more over the years. The strongest evidence for a black hole came from the center of the Milky Way which was monitored over many years, and the orbital motion of individual stars in the Galactic center revealed such a high mass-density which could almost only be explained by a supermassive black hole (Eckart & Genzel 1996; Ghez et al. 2005, 2008; Gillessen et al. 2009). Finally, it was possible to utilize the incredibly high angular resolution of the Event Horizon telescope to obtain an image of the event horizon of Sgr A* and M 87, the closest high-mass supermassive black

hole, and provide the final decisive evidence that black holes do indeed exist!

## 2 Black hole - host galaxy co-evolution

Remarkable tight correlations have been found between the mass of central black holes and different properties of their host galaxies. Connecting two galaxy components of vastly different scales, the physical origin of these relations is very puzzling. While correlation does not always mean causality, many people attribute these correlations to some kind of co-evolution between the different galaxy components. In order to discuss this apparent co-evolution, I will start this section with a summary about the black hole and galaxy formation and evolution and then move to a throughout evaluation of the scaling relations.

### 2.1 Formation and growth of supermassive black holes

The formation and growth of supermassive black holes is still an open field of research which is mainly driven by high-redshift observations and simulations. Quasars at high redshift are so luminous and compact that they can only be explained by harboring an accreting supermassive black hole in their center. Observations show that luminous quasars with massive black holes already existed when the Universe was still very young, only 0.8 Gyrs old (z$\sim$ 7; Willott et al. 2007, 2010; Mortlock et al. 2011; Momjian et al. 2014; Venemans et al. 2017; Bañados et al. 2018; Tenneti et al. 2019; Matsuoka et al. 2019), suggesting that the first black holes already formed before the first galaxies started to exist. Having a luminosity of more than $10^{47}$erg s$^{-1}$, these high-redshift quasars were powered by supermassive black holes with masses reaching up to $10^9$ $M_\odot$. In order to reach such masses in such a short time, SMBHs need to have evolved from massive initial seeds of more than 100 $M_\odot$ and grown very rapidly via accretion and mergers (e.g., Pacucci et al. 2015, 2017). Following

$$t_{\rm growth} = 0.45 \frac{\epsilon}{1-\epsilon} \ln\left(\frac{M_{\rm BH}}{M_0}\right) {\rm Gyr} \tag{1.2}$$

a seed BH of 100 $M_\odot < M_0 < 10^5$ $M_\odot$ would need more than 0.5 Gyrs to reach a mass of $10^9 M_\odot$ when accreting at Eddington rate with a typical efficiency $\epsilon$ of 10% (e.g., Volonteri 2010; Melia & McClintock 2015). Therefore, the existence of massive supermassive black holes at such high redshifts in combination with current accretion models imply that the first black hole seeds need to have formed at redshifts z > 10, which is the time, called the epoch of reionization, when dark matter halos started to grow out of small primodial density fluctuations by gravitational instablities (see Section 2.2). Several hypotheses for the formation of the progenitors of SMBH seeds have been proposed (see Figure 1.1 and reviews by Volonteri 2010, 2012; Natarajan 2014; Mezcua 2017; Woods et al. 2018), from which I will describe the three most prominent scenarios here. All three scenarios start with a dark matter halo, that is filled with pristine (metal-free) gas which will eventually contribute to the formation of the first stars and massive black holes.

The first scenario describes SMBHs as remnants of the first generation of *massive Population III* (PopIII) stars (Madau & Rees 2001; Haiman & Loeb 2001; Schneider et al.2002, Volonteri, Haardt & Madau 2003) which have however not been observed yet. Pop III stars were metal-poor and according to cosmological hydrodynamical simulations possibly able to reach masses of a few hundred and up to 1000 $M_\odot$ (Bromm & Larson 2004; Susa et al. 2014; Hirano et al. 2014,

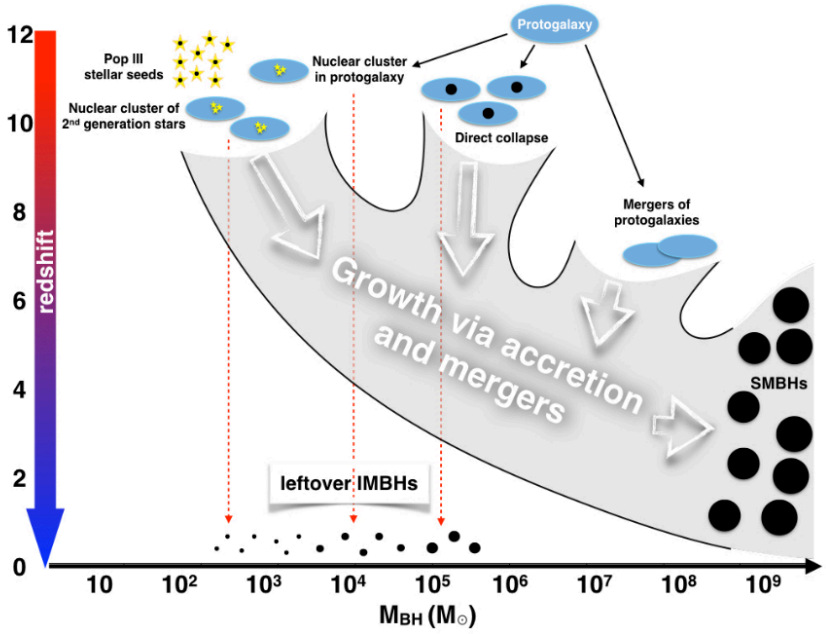


**Figure 1.1 —** Formation scenarios of massive black holes. Seed black holes in the early Universe could have formed from Population III stars, mergers in dense stellar clusters or from direct collapse of dense gas in protogalaxies. They grow via accretion and merging to masses of $10^9\ M_\odot$ at around a redshift of 7. They continue to grow via accretion and merging until they reach today's masses of up to $10^{10}\ M_\odot$. Seed black holes which did not grow into SMBHs can be found in the local Universe as leftover IMBHs. Image credit: Mezcua (2017).

2015). If the first stars remained this massive, they would have collapsed after a very short ($\approx$ Myrs) lifetime, the remnant being dependent on the mass of the star. While metal-poor stars with masses between 140 and 260 $M_\odot$ are completely destroyed in pair-instability supernovae, more massive stars, instead of exploding due to thermonuclear reactions, continue to collapse more rapidly due to photodisintegration and eventually evolve into black holes, which contain about half of the initial stellar mass (Bond et al. 1984; Fryer et al. 2001; Heger & Woosley 2002; Zhang et al. 2008). The formed BH seeds then grow via accretion of matter until they reach contemporary masses of about $10^6\ M_\odot$ or more.
Although this explanation of MBH formation seems very natural, it is not clear if PopIII stars were indeed massive enough to form massive black holes. Early studies of the formation of first stars predicted that the initial mass function at high redshift was rather top-heavy compared to today (Bromm et al. 2002) which would make sufficiently massive stars possible. However, more recent state-of-the-art simulations indicate that most of the first stars formed in multiples and were much less massive than 250 $M_\odot$ (Turk et al. 2009; Clark et al. 2011; Hosokawa et al. 2011; Greif et al. 2012; Latif et al. 2013; Stacy et al. 2016). Growing from less than 100 $M_\odot$ to $10^9\ M_\odot$ within 0.5 Gyrs would thus require BH seeds to grow via supra-exponential accretion (Alexander & Natarajan 2014) or undergo phases of accretion at super-Eddington rates (Volonteri & Rees 2005; Madau et al. 2014; Smole et al. 2015; Pezzulli et al. 2016; Takeo et al. 2019). Hence, the first scenario is very unlikely to explain the observed SMBH population.

An alternative model associates the formation of SMBHs with dynamical instabilities that occur either in the gaseous or stellar component of metal-poor protogalaxies. Gas that resides in protogalaxies typically cools down and contracts until rotation equilibrates the contraction and a rotationally-supported disk forms. However, gravitational instabilities of low-angular

momentum gas can omit the rotational support and transport gas into the center of the halos instead. A possible driver for the gravitational instabilities are bars in bars (Begelman et al. 2006). Depending on the size of the instabilities, two possible paths of SMBH formation are debated.
If the gas instabilities are global, the gas flows rapidly to the center of the halo, where it gradually cools down to T$\sim 10^4$ K and *directly collapses* into a supermassive star (Loeb & Rasio 1994; Eisenstein & Loeb 1995; Bromm & Loeb 2003; Lodato & Natarajan 2006) of about $10^5\ M_\odot$ (Begelman et al. 2006; Johnson et al. 2012). In order to not explode in a large supernova but collapse instead, the gas must have accumulated in less than around 2 million years , which is the thermonuclear time scale. When the core of the supermassive star collapses, a BH of around $10^4 - 10^5\ M\odot$ forms (Ferrara et al. 2014). Still being enveloped from the shell of the dying star the formed BH can accrete matter very rapidly. It quickly turns into an intermediate-mass BH and potentially into an SMBH provided that the accretion-rate is not quenched at higher masses. While super-critical accretion is not required in this model (e.g., Valiante et al. 2016), fragmentation and star formation in the cooling gas might hinder the formation of a massive black hole (Inayoshi & Haiman 2014; Latif & Ferrara 2016). As the cosmic UV background may not be powerful enough to suppress $H_2$ formation and gas fragmentation (Johnson et al. 2008), direct collapse can only occur in halos close to luminous star-forming galaxies which produce sufficient Lyman-Werner radiation to photo-dissociate the $H_2$ molecules (e.g., Dijkstra et al. 2008, 2014; Agarwal et al. 2012, 2014; Habouzit et al. 2016). Therefore, direct collapse is likely a less common mechanism for forming massive black holes.

Alternatively, the first massive black holes might have formed in *dense stellar clusters* (e.g., Rees 1978; Portegies Zwart et al. 1999, 2004; Devecchi & Volonteri 2009; Yajima & Khochfar 2016; Stone et al. 2017; Schleicher et al. 2018). Local instabilities drive gas flow towards the center of the halo, where the gas fragments and a stellar cluster forms (Ebisuzaki et al. 2001; Devecchi et al. 2010, 2012; Omukai et al. 2008). Stellar clusters are so dense, that *runaway stellar collisions* and merging can create a massive star of a few thousand $M_\odot$ (Devecchi et al. 2010, 2012; Sakurai et al. 2017; Schleicher et al. 2018). Even before heavy elements accrue, the massive star collapses into a BH having a similar mass to its progenitor. The IMBH can then grow via gas accretion and tidal disruption events of stars (Sakurai et al. 2019). When the abundance of heavy elements increases, though, powerful stellar winds occur and carry a large fraction of the stellar mass away, before the heavy star evolves into a stellar BH. This scenario, therefore, required a very metal-poor environment and occurred most likely only in the early Universe.

The different scenarios are not mutually exclusive. However, currently, no direct observation gives preference for a specific formation scenario (Barrow et al. 2018). The biggest mystery remains: how is it possible that massive supermassive black holes existed already so early in the history of the Universe? Each of the current explanations are well justified, but also lack a solution to their main weaknesses. A possible path to constrain the mass of black hole seeds is to search for the smallest nuclear black holes in present-day dwarf galaxies (e.g., reviews by Reines & Comastri 2016 and Mezcua 2017). Alternatively, catching the gravitational wave signals from merging black holes at large redshifts (z$\approx$ 5-20) could uniquely illuminate details about SMBH infancy to us (Colpi 2018; Barack et al. 2018; Dayal et al. 2019; Huang et al. 2019). In conclusion, the search for supermassive black hole seeds promises to remain exciting for the next decade, until we will finally find decisive observational evidence (see White Papers by Pacucci et al. 2019; Haiman et al. 2019; Natarajan et al. 2019).

The last topic, that I want to discuss a bit further in this section is the growth of supermassive black holes, which is strongly debated in the literature. Current explanations suggest that black holes grow via two main channels: accretion of gas onto the black hole, facilitated by galaxy merging or accretion of intergalactic gas (Silk & Rees 1998; Fabian 1999; Di Matteo et al. 2008; Volonteri 2010) and by mergers of black holes, following dry major mergers.
Details of the accretion process and accretion rates are not well understood yet. A widely adopted formula for the estimation of the mass accretion rates onto black holes in simulations is given by the Bondi rate, which is determined by the boundary conditions of the accretion flow (e.g., Springel et al. 2005; Vogelsberger et al. 2014; Schaye et al. 2015; Pillepich et al. 2018). Recent studies, however, show that the Bondi rate does not describe the actual black hole accretion very well and needs more refinement (Gaspari et al. 2013; Yang & Bu 2018; Bu & Yang 2019). The accretion onto the black hole is theoretically limited by the Eddington accretion rate which is dictated by the Eddington luminosity $L_{\mathrm{Edd}} = 3.4 \times 10^4 L_{\odot}(M_*/M_{\odot})$. If the luminosity would exceed the Eddington luminosity, the gas, surrounding the black hole, would just be blown away by the radiation pressure. Nevertheless, several works (Volonteri & Rees 2005; Alexander & Natarajan 2014; Madau et al. 2014; Volonteri et al. 2015; Begelman & Volonteri 2017) have predicted the occurrence of a series of super-Eddington accretion episodes at high redshift, if the central gas density was sufficiently high (Li 2012; Pacucci et al. 2015, 2017), to explain the existence of massive black holes at large redshifts. Unfortunately, our closest massive black hole Sgr A* does not provide additional insights into black hole feeding processes. Although our observing facilities have substantially improved over the last two decades, transportation of gas towards the central SMBH was not observed yet (e.g., recent work by Morsony et al. 2017; Eckart et al. 2018).
While accretion is probably the main channel of black hole growth, galaxy mergers become relevant for more massive galaxies with a merger history (Yoo et al. 2007; Kulier et al. 2015; Krajnović et al. 2018a).

## 2.2 Dynamical evolution of galaxies

In most cosmological scenarios, galaxies have formed early and rapidly out of density perturbations in the early Universe (Frenk & White 2012, for review), but continued to evolve in luminosity, morphology and dynamics over the entire cosmic lifespan. In the current standard picture (ΛCDM; White & Rees 1978; Blumenthal et al. 1984; Planck Collaboration et al. 2018), the Universe is dominated by dark energy, followed by dark matter and then by only a small percentage baryonic matter. Dark matter is assumed to be cold, which means that it is composed of non-relativistic, collisionless particles which obey only gravitational forces. It is thought that the baryonic components of galaxies are embedded in dark matter halos, which play a key role in cosmic structure formation. In the following, I will give a short summary of our current understanding of the formation and evolution of galaxies[1].
Shortly after the big bang, small primordial quantum fluctuations in the primordial dark matter distribution expanded into small density perturbations, which evolved into more and more over-dense regions during the expansion of the Universe. At some point, small dark matter halos formed out of these cosmological density fluctuations and hierarchically grew into larger dark matter halos via accretion of surrounding material and halo merging (Kauffmann & White 1993; Lacey & Cole 1994; Navarro et al. 1997). Once, the pristine gas, located in the dark matter

[1] As it is possible to fill complete books with physical details about galaxy evolution, I would like to refer the curious reader to the reviews by Somerville & Davé (2015), Cappellari (2016) and Naab & Ostriker (2017) as well as the textbook "Galaxy formation and evolution" by Houjun Mo, Frank van den Bosch and Simon White.

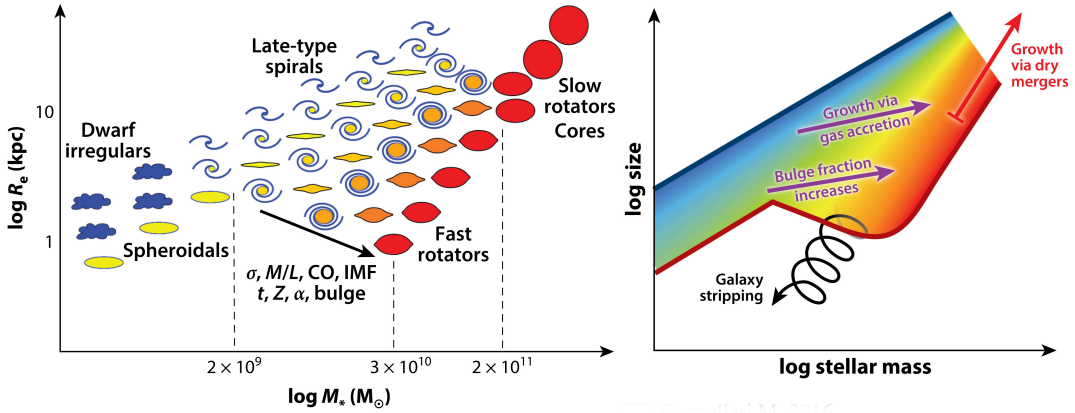


**Figure 1.2 —** Galaxy evolution on the mass-size diagram. The *left panel* shows the different galaxy morphologies. Dwarf irregulars and spheroidals in the low-mass region, late-type galaxies with intermediate masses and early-type galaxies divided into fast and slow rotators. The sequence of late-type galaxies aligns smoothly with the sequence of early-type galaxies. Massive galaxies are dominated by round or weakly triaxial slow rotators. The *right panel* shows the expected average evolution of an ensemble of galaxies. Fast-rotators have likely formed from star-forming disks which mostly grew via gas accretion. At some point, the star formation was quenched, leaving behind the bulge-dominated passive fast-rotators that we see in the present Universe. Slow rotators have probably evolved via gas-poor (dry) mergers, letting them grow very big and massive, to the top of the mass-size diagram. Galaxy stripping is a third evolutionary process, which could be the cause for ultra-compact dwarfs (UCDs). It is believed that UCDs are the cores of normal galaxies, which had their envelopes stripped by the gravitational influence of larger galaxies. Image credit: Cappellari et al. 2013a and Cappellari 2016.

halo, was able to efficiently cool down, it lost its pressure support, sank to the center of the halo potential well and accumulated there. As soon as the gas became denser than the dark matter halo, it became self-gravitating and collapsed under its own gravity into small clumps (thermal Jeans mass). Eventually, this cooling process leads to dense, cold gas clouds within which star formation could occur. The formation of stars likely happened in two phases. In the first phase, PopIII stars formed in a gas cooling with molecular hydrogen. In a second phase, the gas continued to cool due to atomic hydrogen and first proto-galaxies formed at around z=10. This is also likely the time when the first black hole seeds were forming (see Section 2.1).
A variety of processes contributed to the subsequent galaxy evolution. If the protostellar cloud had a non-zero angular momentum (Bodenheimer 1995), the pristine gas must have settled into a disk when falling into the center of the dark matter halo (Fall & Efstathiou 1980). Galaxy bulges might have assembled from these gas disks, albeit details of the bulge formation depend on the bulge-type and are still intensively debated[2]. Within the time of a few rotation periods, gravitational instabilities in the gas disk could have generated gravitational torques which then continuously transported gas to the center of the disk (De Lucia et al. 2011; Forbes et al. 2014; Goldbaum et al. 2015, 2016; Tonini et al. 2016). In this usually slowly acting process pseudo-bulges are believed to have formed via secular evolution (e.g., Kormendy & Kennicutt 2004; Kormendy & Fisher 2008; Kormendy & Ho 2013). Classical bulges, on the other hand, have likely assembled in hierarchical gas-rich mergers (e.g., Aguerri et al. 2001; Naab & Trujillo 2006; Hopkins et al. 2010; Izquierdo-Villalba et al. 2019).

While the described scenario is able to explain the existence of disk galaxies, the population of elliptical galaxies needs to be added to the picture. Compared to late-type/disk galaxies,

[2]For more details about the different bulge types, I want to refer to Section 2.4.

early-type/elliptical galaxies are classified by their uniformly old stellar populations, negligible amounts of gas, little star formation, and large stellar mass (see Figure 1.2). About 20% of the present galaxy population belong to early-type galaxies, and they are usually more abundant in dense enviroments. These observational facts led to the idea of two possible formation proccesses for early-type galaxies. In the monolithic scenario (Eggen et al. 1962), early-type galaxies have formed from the pristine gas cloud in rapid dissipationless collapse, leading to a random motion of stars. According to this model, early-type galaxies must have formed at redshifts z>5 and undergone a passive evolution of their stellar populations until the present day. This classical view has however, often been challenged by a large number of observational disagreements. Alternatively, (Toomre & Toomre 1972; Toomre 1977, but see also White & Rees 1978; White 1979) proposed hierarchical merging of disk galaxies and subsequent morphological transformation as possible origin of early-type galaxies. Already a decade later, the usage of different numerical simulations showed that equal-mass disk galaxy mergers were indeed able to reproduce spheroids which shared many of the characteristics of massive ellipticals of the present Universe (Barnes 1988, 1992; Kauffmann & White 1993; Kauffmann & Charlot 1998; Baugh et al. 1999; De Lucia et al. 2006). Observationally, it later turned out that early-type galaxies can be classified into two main classes: bright, boxy slow-rotators and fainter, disky fast-rotators (e.g., Kormendy & Bender 1996; Emsellem et al. 2007; Cappellari et al. 2007; Cappellari 2016; Veale et al. 2017; Schulze et al. 2018; Smethurst et al. 2018). Massive slow-rotators are believed to indeed have assembled in dissipationless "dry" mergers and accretion of satellite systems (Bois et al. 2010; Duc et al. 2011; Khochfar et al. 2011; Naab et al. 2014; Penoyre et al. 2017), while fast-rotators have likely evolved by gas accretion (Cappellari et al. 2013a; Johnston et al. 2014) or in dissipational mergers (Duc et al. 2011; Khochfar et al. 2011; Penoyre et al. 2017; Tacchella et al. 2019). During these processes, the galaxy's bulge slowly grew up over time, eventually overwhelming the disk and thus forming the fast-rotator. Figure 1.2 gives an overview of the processes and how they move the galaxies in the mass-size diagram.

After all, the relative contributions of dissipational and dissipationless mergers, secular evolution, violent disk instabilities, accretion of gas with low angular momentum, and other mechanisms to the observed structural diversity remain elusive and need further investigation in both simulations and observations. Furthermore, the exact role of supermassive black holes in galaxy formation and evolution is not yet fully understood, but AGN feedback is believed to be one of the drivers for galaxy transformation from star-forming spirals to quenched ellipticals (e.g., Somerville & Davé 2015; Terrazas et al. 2017).

## 2.3 Connecting Supermassive black holes and their host galaxies

Not only pure simulations, but also scaling laws of galaxies can provide important clues about the processes of the formation of first black holes and their cosmic evolution. Several empirical relationships between the mass of massive black holes and some physical properties of their host galaxies have been reported in the last two decades. The relation between black hole mass and bulge velocity dispersion $\sigma_e$ (Ferrarese & Merritt 2000; Gebhardt et al. 2000; Tremaine et al. 2002; Häring & Rix 2004) has been shown to be the tighest relation with the least scatter for both passive (McConnell & Ma 2013; Kormendy & Ho 2013; Saglia et al. 2016) and active black holes (Onken et al. 2004; Greene & Ho 2006; Woo et al. 2010, 2015; Bennert et al. 2015; Sexton et al. 2019). Additional host galaxy properties include the bulge stellar mass (Magorrian et al. 1998; Davis et al. 2018a), the bulge optical or near-infrared luminosity (Kormendy & Richstone 1995; Marconi & Hunt 2003; Läsker et al. 2014), total luminosity (Kormendy & Gebhardt 2001; Kormendy et al. 2011; Läsker et al. 2014), Sersic index (Graham et al. 2001; Graham & Driver

2007; Savorgnan et al. 2013) or pitch-angle for spiral galaxies (Seigar et al. 2008; Berrier et al. 2013; Davis et al. 2017a).
The correlations seem to hold for galaxies of different Hubble types and even highly disturbed morphologies like NGC 5128. Also, different environments (from rich clusters to isolated field galaxies) appear to have no effect on the existence of the scaling relations (Zubovas & King 2012), albeit the exact shape of the relation may vary with different galaxy type, environment and even black hole mass. van den Bosch (2016) show that not only massive black holes, but even the smallest black holes follow the fundamental plane between black hole mass, size of the host stellar spheroid, and its luminosity. A throughout discussion of the scaling relations and the degree of their uniform validity can be found in the recent reviews by Kormendy & Ho (2013),Graham (2016) and Zubovas & King (2019). The $M_{\rm BH} - \sigma_{\rm e}$ relation is simply described as

$$M_{\rm BH} = {\rm k}\sigma_{\rm e}^{\rm p} \tag{1.3}$$

whereas the slope p was revised several times depending on the used sample size and selection. Observational values are typically in the range 3.6 to 5.3 (see Bhattacharyya & Mangalam 2018, for a recent overview).

The tight relations between black hole and host galaxy are rather surprising as many of the stars of the bulge are too far away from the SMBH to be affected by its gravitational field. If the relations have a causal origin, there must have been some kind of physical coupling between the evolution of SMBHs and their host galaxy bulges. Despite galaxy mergers and gas accretion processes, which are expected to increase the scatter over time, massive black holes are believed to regulate the growth and evolution of their host galaxies due to feedback mechanisms associated with the AGN phase (see, e.g., Croton et al. 2006; Lagos et al. 2008; Fabian 2012; McNamara & Nulsen 2012; Ishibashi & Fabian 2014; Baron et al. 2018). Both simulations and observations suggest that these feedback processes can occur as positive and negative feedback. AGN activity can over-pressurize dense star-formation regions of galaxies and thus enhance star formation, leading to a positive feedback effect (Ishibashi & Fabian 2012; Silk 2013; Zubovas 2017). In negative feedback processes star formation in the host galaxy is suppressed, either by heating or removing the ambient gas, whereas the latter plays a subdominant role (Fabian 1999; Cresci & Maiolino 2018). The details of the feedback mechanisms are complex and not fully understood, but they should reflect in the slope of the scaling relations. Silk & Rees (1998) discuss a self-regulating model in which black holes radiate an energy driven wind which can - if the black hole is massive enough - expel the gas content from the host galaxy and thus suppress its own fuel delivery. Their model predicts a slope for the $M_{\rm BH} - \sigma_{\rm e}$ relation of p=5 based on a protogalaxy assumed as isothermal sphere. King (2003) revisited the concepts of Silk & Rees (1998) and proposed a momentum- rather than energy-driven feedback as response to super-Eddington accretion. In their model, most of the energy released by the black hole is lost to radiation and only a small leftover-fraction can mechanically push the gas away, which leads to a predicted slope of p= 4 and a correct normalization for the scaling relation. After all, both models are in agreement with observations and the details of the feedback processes, albeit extensively studied in numerical simulations (e.g., Di Matteo et al. 2005; Sijacki et al. 2007; Hirschmann et al. 2014; Anglés-Alcázar et al. 2013; Volonteri et al. 2016; Weinberger et al. 2018; Thomas et al. 2019; Zubovas & King 2019), remain a mystery.
An alternative non-causal approach to explain the scaling relations is to associate them with the central limit theorem. Instead of a physical coupling between massive black holes and their host galaxies, the scaling relations could be the result of statistical convergence in the hierarchical assembly history of black holes and their host galaxies (Peng 2007; Jahnke & Macciò 2011). Peng (2007) claims that every arbitrary $M_{\rm BH}/M_{\rm bulge}$ ratio of the early Universe would converge

towards a linear trend due to major merging, such that the scaling relations might be the mere consequence of the ensemble average. The link between major mergers and black hole growth has been extensively tested in the last decade, with the consequence that major interactions likely only play a sub-dominant role in the growth of black holes and the triggering of AGN (Mechtley et al. 2016; Ginat et al. 2016; Simmons et al. 2017; Marian et al. 2019; Villforth et al. 2019). Furthermore, major mergers have likely not happened frequent enough in the lifetime of the Universe, such that the explanation via the "central limit theorem" is rather unlikely (Graham 2016).
On the other hand, it has been suggested that measurements of the black hole scaling relations may be severely biased which could lead to an apparently tight relationship (Bernardi et al. 2007; Gültekin et al. 2009; Batcheldor 2010; Schulze & Wisotzki 2011; Gultekin et al. 2011; Morabito & Dai 2012; Shankar et al. 2016, 2017; Barausse et al. 2017; Shankar et al. 2019, but also see Section 2.4). Improving the scaling relations with complete and unbiased samples in observations and understanding the underlying feedback processes in theoretical studies and simulations are crucially and immediately connected with each other to understand the role of massive black holes in galaxy evolution.

## 2.4 Detailed black hole demographics

With the increasing number of $M_{\rm BH}$ measurements in a range of different galaxy types, it is now possible to have a detailed analysis of the black hole scaling relations. While the exact knowledge of the slope of the scaling relations is crucial for constraining the co-evolution between SMBH and their host galaxy, the discussion about the shape and the magnitude of the slope of the scaling relations is still on-going. Different slopes are found in different galaxy samples which raise the following questions: Are the scaling relations valid for all galaxies? Do different galaxy types follow different scaling relations? Or are we still biased by the remaining methodological measurement uncertainties? In order to assess these questions, Figure 1.3 shows various galaxy subsamples on the $M_{\rm BH} - \sigma_{\rm e}$ relation. The black hole sample are taken from van den Bosch (2016) and expanded with additional recent dynamical mass measurements from the literature.

### Early-type galaxies versus late-type galaxies

Figure 1.3 b) illustrates the location of the different host galaxy types on the $M_{\rm BH} - \sigma_{\rm e}$ relation. While the measurements of the different types are generally consistent with each other, there seems to be a trend of early-type galaxies (ellipticals and lenticulars) being more massive than late type galaxies (spirals) at similar velocity dispersions. Gültekin et al. (2009) noted that the scatter of the scaling relation decreased by excluding late-type galaxies from the fit, giving a first clue of different scaling relations for the different morphologies. McConnell & Ma (2013) fitted the early- and late-type galaxy samples independently, and recovered different coefficients for the two sub-samples. While McConnell & Ma (2013) only found an offset between the two subsamples, the addition of about 20 maser-based measurements for late-type galaxies revealed two very different relations for the two morphologies. The latest fit bei Greene et al. (2016) gives $\log_{10}(M_{\rm BH}/M_{\odot}) = 8.45 + 4.9\ \log_{10}(\sigma_{\rm e}/200\,{\rm km\,s^1})$ for early-tpye galaxies (orange line in Figure 1.3), and a shallower $\log_{10}(M_{\rm BH}/M_{\odot}) = 7.80 + 3.4\ \log_{10}(\sigma_{\rm e}/200\,{\rm km\,s^1})$ for late-type galaxies (purple line in Figure 1.3). A similar trend was found by Savorgnan et al. (2016) for the relation between black hole mass and bulge stellar mass (their Figure 5) where late-type galaxies follow a steeper relation than early-type galaxies (see also Davis et al. 2019; Sahu et al. 2019). The difference in the different relations could be driven by dry-merging scenario for early-type galaxies versus gas-rich accretion processes for late-types.

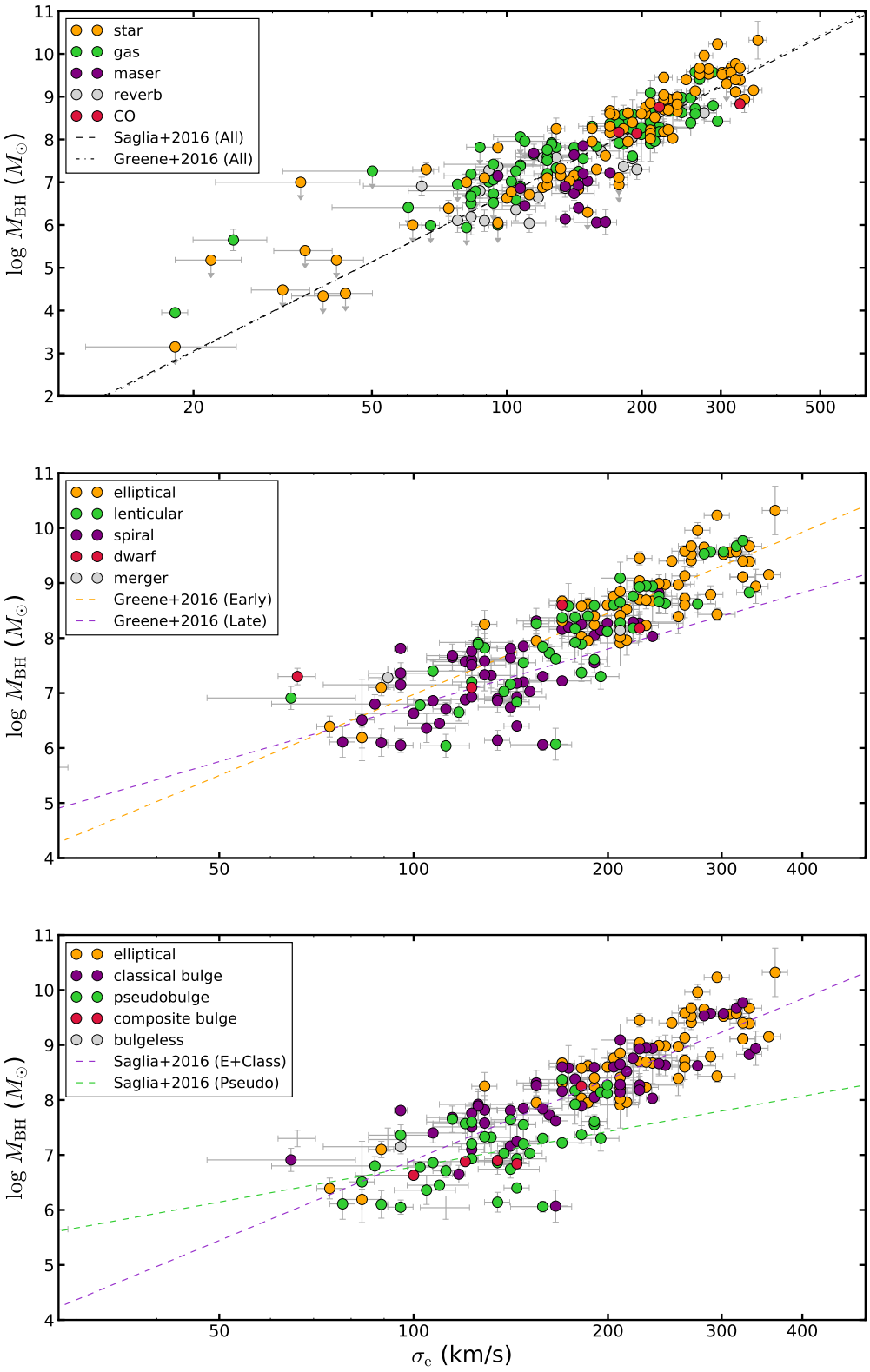


**Figure 1.3 —** $M_{BH} - \sigma_e$ relation for different sub-samples of the appended $M_{BH}$ compendium of van den Bosch (2016). (a) $M_{BH}$ measured with different methods. (b) Different host galaxy types. (c) Different bulge classifications.

However, distinguishing between late- and early-type galaxies is just the tip of the iceberg. Late-type galaxies often contain bars and pseudobulges, and early-type galaxies can be separated into fast and slow rotators, which are connected with different evolution scenarios. The scaling relations in light of these components are discussed in the following sections. For a more throughout conclusion about the shape of the scaling relations for late-type galaxies, more $M_{\rm BH}$ measurements of massive late-type galaxies are needed in the future.

**Pseudobulges versus classical bulges**

Not only galaxies can be classified into different morphologies, but also their central components, the bulges, follow a dichotomy of morphologies (see, e.g., Kormendy & Illingworth 1982; Kormendy 1993; Kormendy & Kennicutt 2004; Fisher & Drory 2016, for review). Classical bulges exhibit a spheroidal shape and show many similarities to elliptical galaxies. Contrarily, pseudobulges, sometimes also called disk-like bulges, have a more disky shape and show nuclear morphological features, such as nuclear bars, spirals or rings (Carollo et al. 1998). They are also composed of younger stellar populations and have flat radial velocity dispersion profiles (Gadotti 2009; Fabricius et al. 2012; Falcón-Barroso 2016). While galaxies usually only contain one type of bulge, a handful of galaxies show evidence for hosting a composite bulge, a mix of classical and a pseudobulge (Erwin et al. 2003; Athanassoula 2005; Erwin 2008; Erwin et al. 2015). The different morphological features could represent a snapshot of different galaxy evolution scenarios. It is believed that classical bulges have formed in galaxy encounters with small satellites (Aguerri et al. 2001), whereas pseudobulges might have formed via secular evolution (for details see Section 2.2).
The fundamental difference in the formation of both bulge types leads to question the uniform validity of the black hole scaling relations for both, galaxies with classical and galaxies with pseudobulges. Following early work by Hu (2008) and Greene et al. (2008), pseudobulges in late-type galaxies have often been proposed not to follow the black hole mass scaling relations. In fact, Sani et al. (2011) and Beifiori et al. (2012) confirmed that pseudobulges tend to contain lower-mass black holes which are significantly displaced from black hole mass - bulge relations. Since these early studies, several additional robust black hole masses were measured in small early-type galaxies.
Figure 1.3 c) is an updated representation of the location of classical and pseudobulges in the $M_{\rm BH} - \sigma_{\rm e}$ relation. The identification of pseudobulges is often not clear and unambiguously. Different combinations of photometric and spectroscopic diagnostics are required to distinguish the different bulge types. A combination of the presence of nuclear sub-components, low Sersic indices (or large concentration index), rotation-dominated kinematics, low velocity dispersions, and intrinsic three-dimensional bulge shape are reliable diagnostics to separate pseudobulges from classical bulges (Gadotti & Kauffmann 2009; Graham 2015; Neumann et al. 2017; Costantin et al. 2018). For the classification of the bulge component of our sample, we have carefully searched in the literature and taken the information from Fisher & Drory (2010), Kormendy & Ho (2013) for mostly inactive galaxies and from Ho & Kim (2014) for active galaxies. The literature classifications are based on a detailed decomposition of high-resolution ground-based and space-based images. Our compilation confirms that black holes in pseudobulges are systematically lower than black holes in classical bulges and ellipticals. The figure also shows the most recent fittings by Saglia et al. (2016), which are fundamentally different for the two bulge types: Classical bulges and elliptical galaxies follow $\log_{10}(M_{\rm BH}/M_{\odot}) = -2.83 + 4.87\ \log_{10}(\sigma_{\rm e})$ (purple line in Figure 1.3 c)). Pseudobulges, on the other hand, follow the much shallower relation $\log_{10}(M_{\rm BH}/M_{\odot}) = 2.53 + 2.13\ \log_{10}(\sigma_{\rm e})$ (green line).

Davis et al. (2017a) recently compiled a base sample of only late-type galaxies and distinguished classical and pseudobulges in their fit. While their classical bulge sample is very limited (their Figure 5), they find that these late-type galaxies have systematically larger black hole masses than late-types hosting a pseudobulge. While their fit to the pseudobulge sample is steeper than from Saglia et al. (2016), their sample shows a large scatter which implies that pseudobulges show only little correlation with their black holes (see also Kormendy & Ho 2013). Bennert et al. (2015) proposed a slightly different result. They compiled a sample of 66 local Seyfert-1 galaxies and distinguished classical and pseudobulges via their flattening in comparison with the outer disk, a Sersic index n<2. In their analysis, pseudobulges do not deviate from the $M_{\rm BH} - \sigma_{\rm e}$ relation, which is in strong contrast to other works. However, the Bennert et al. (2015) sample is relatively limited and their bulge identification might not be reliable. In conclusion, it is well established now, that galaxies with classical and galaxies with pseudobulge follow different scaling relations which originate from the different galaxy evolution histories. A large fraction of the barred galaxies in our compilation also hosts a pseudobulge. Therefore, it is not yet clear if the reason for the larger scatter and the systematic offset in the scaling relations is caused by bars (see the following section) or by pseudobulges.

**Bulgeless galaxies**

Quite a number of galaxies contain neither a classical nor a pseudobulge. They appear to be *bulgeless*. Bulgeless galaxies are expected to not have experienced any major mergers nor significant secular evolution processes, such that no noteworthy bulge component could grow yet. However, the definition is still ambiguous, because the "bulges" of bulgeless galaxies could just appear to be very small. For example, the Milky Way is a galaxy case which, by first glance, looks like a pure disk galaxy not harboring any bulge. However, Dékány et al. (2013) noticed based on an analysis of the stellar populations that the Milky Way likely contains both a small classical bulge and a pseudobulge.
Black hole mass measurements were performed in a few bulgeless galaxies. While most of the measurements are upper-limits and imply no presence of black holes (Gebhardt et al. 2001; Merritt et al. 2001; Kormendy et al. 2007; Kormendy et al. 2010), some galaxies harbor much more massive (but still low-mass) black holes than expected (Filippenko & Ho 2003; Araya Salvo et al. 2012; den Brok et al. 2015). The black holes have observationally been confirmed for some cases by visible nuclear activity (Ghosh et al. 2008). Furthermore, Simmons et al. (2012), followed-up by Simmons et al. (2017) and Martin et al. (2018), showed that normal-mass BHs commonly exist in bulgeless SDSS galaxies, suggesting that the majority of SMBH growth via gas accretion happened due to secular processes (such as bar driven inflows of gas or disk instabilities) instead of galaxy merging.
Figure 1.3 c) also shows bulgeless galaxies. As their number is still small and dominated by upper limits, it is impossible to make a statement on their general trends in the scaling relations yet. Nevertheless, bulgeless galaxies are great testbeds to learn about the link between black hole growth and galaxy evolution, seed black holes in early evolutionary processes and intermediate black holes, as the galaxies likely did not experience any violent growth processes.

**Barred versus unbarred galaxies**

Galactic bars are thought to contribute to the dynamical evolution of their host galaxies significantly. In addition to large stellar bars, many galaxies host an additional short inner bar of radius$\leq$ 1 kpc. According to numerical studies, these bars can drive the transport of gas from the outskirts to the central regions of galaxies, where they can trigger star formation and possibly AGN activity (Shlosman et al. 1989; Hopkins et al. 2010; Alonso et al. 2013). Vice

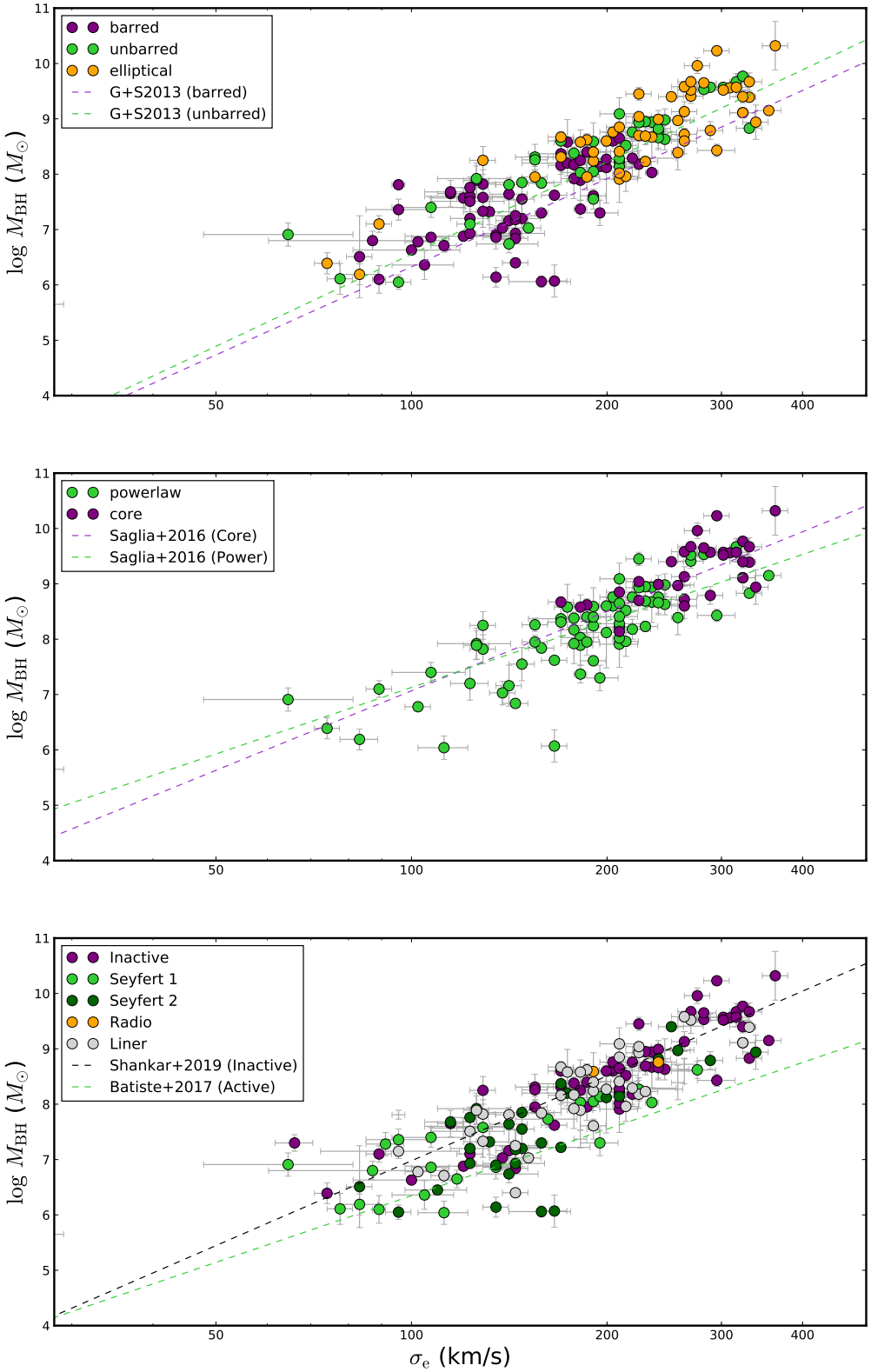


**Figure 1.4 —** $M_{\rm BH} - \sigma_{\rm e}$ relation for different sub-samples of the appended $M_{\rm BH}$ compendium of van den Bosch (2016). (a) Barred versus unbarred galaxies. (b) Core galaxies versus core-less galaxies. (c) Nuclear activity.

versa, massive black holes might be able to destroy galactic bars which would stall the feeding (Shen & Sellwood 2004; Athanassoula et al. 2005; Du et al. 2017). Graham (2008), Hu (2008) and Graham & Li (2009) noticed that barred galaxies are offset towards higher $\sigma_e$ in the $M_{BH}-\sigma_e$ diagram. Graham (2008) attributed this offset to an increased stellar velocity dispersion in the presence of bars. This effect was systematically studied in numerical simulations by Debattista et al. (2013) and Hartmann et al. (2014), and they showed that the evolution of bars results in elevated bulge stellar velocity dispersions to a degree that fully explained the observations.
An illustration of barred and unbarred galaxies of our SMBH compilation in the $M_{BH} - \sigma_e$ diagram can be found in Figure 1.4a. Information about the presence of strong bars in galaxies can be easily obtained by visual inspection and was already compiled in the "Third reference catalog of bright galaxies" by de Vaucouleurs et al. (1991). The presence of smaller bars needs to be extracted from a detailed photometric decomposition. Consequently, in some cases the de Vaucouleurs et al. (1991) classification needed a minor revision. We obtained the revised morphological information from Slavcheva-Mihova & Mihov (2011), Buta et al. (2015), Saglia et al. (2016) and Li et al. (2017b). The discussed offset between barred and unbarred galaxies is also visible in our black hole compilation. We have added the best-fit relations by Graham & Scott (2013), which predict that barred galaxies follow $\log_{10}(M_{BH}/M_\odot) = 7.92 + 5.29\ \log_{10}(\sigma_e/200\,\mathrm{km\,s^1})$ (purple line in Figure 1.4 a), while unbarred galaxies follow with a slight offset $\log_{10}(M_{BH}/M_\odot) = 8.22 + 5.53\ \log_{10}(\sigma_e/200\,\mathrm{km\,s^1})$ (green line). In spite of the fact that newer estimates of the relation are not available, the expressions still describe the about doubled sample very well. Davis et al. (2017a) and Sahu et al. (2019) analyzed the relation between black hole mass and mass of the spherical component of the host galaxy with a barred/unbarred sample and noticed a change in slope for the different populations. It is important to remark that more than 50% of barred galaxies also host a pseudobulge. In the $M_{BH} - M_{*,sph}$ diagram defined by Davis et al. (2018b), the authors do not find pseudobulges to follow a different relation to classical bulges. They conclude that the pseudobulge discrepancy in $M_{BH} - \sigma_e$ could be traced back to the hosted bars and increased velocities. In spite of these works, it is not clear if the reason for the larger scatter in $M_{BH} - \sigma_e$ is caused by bars or by pseudobulges. A test, carefully distinguishing classical and pseudobulges in both barred and unbarred galaxies could provide great insights in the future. It also needs to be mentioned that barred galaxies are strongly biased to certain dynamical measurement methods. In fact, most of the measurement are maser- and gas-based. Barred galaxies are not in dynamical equilibrium, so stellar dynamical measurements would suffer from strong systematic uncertainties which drive the stellar velocity dispersion and black hole mass to larger values (Brown et al. 2013; Dittenber & Valluri 2017). Attempts to dynamically model galaxies including the influence of bars are currently under development (see proceedings by Valluri et al. 2016, 2018; Roberts et al. 2019).

### Cores

While elliptical galaxies can kinematically be distinguished in fast- and slow-rotator galaxies, photometrically they also come in two different flavors: power-law and core (surface-brightness) ellipticals which dominate the high-mass end (Faber et al. 1997). Among other explanations, (Goerdt et al. 2010; Martizzi et al. 2012; Petts et al. 2015), the different types are believed to have formed in different types of mergers. Power-law profiles have likely formed in dissipative mergers with central starbursts, while *depleted* core profiles are the result of dissipationless mergers, where binary SMBHs fling stars away and thus produce a flattening in the central surface brightness profile (Merritt et al. 2007; Kormendy & Bender 2009; Kormendy et al. 2009). The core region has typically a size of about 50-500 pc (e.g., Milosavljević et al. 2002; Ravindranath et al. 2002; Lauer et al. 2007; Rusli et al. 2013a; Dullo & Graham 2014) and

is believed to be growing with time after merging (Bonfini et al. 2018; Rantala et al. 2018). Extreme cases can extend beyond the kpc-scale (e.g., Hyde et al. 2008; Postman et al. 2012; López-Cruz et al. 2014; Bonfini & Graham 2016; Dullo et al. 2017) and might harbour most massive black holes, but are difficult to explain by current formation models (Rantala et al. 2018, 2019). The "core scouring" scenario is motivated by a tight relation between the central black hole mass and the amount of "missing" starlight in the center of the core (Graham 2004; Lauer et al. 2007; Kormendy & Bender 2009; Graham 2012; Dullo & Graham 2014; Thomas et al. 2016).
Core ellipticals also follow their own $M_{\rm BH} - \sigma_{\rm e}$ relation (Hu 2008; Kormendy & Bender 2009; Thomas et al. 2016) which slightly deviates from the relation for power-law ellipticals. Figure 1.4 shows the updated full sample of power-law and core ellipticals in the $M_{\rm BH} - \sigma_{\rm e}$ relation and the careful best-fitting relations by Saglia et al. (2016). Power-law ellipticals can be described by $\log_{10}(M_{\rm BH}/M_{\odot}) = 2.01 + 3.99\ \log_{10}(\sigma_{\rm e})$ (green line in Figure 1.4 c), while core ellipticals follow a very tight relation $\log_{10}(M_{\rm BH}/M_{\odot}) = -2.48 + 4.77\ \log_{10}(\sigma_{\rm e})$ (purple line). The tightness of the latter might be induced by the averaging effect of a series of major mergers as was proposed by Peng (2007). The remaining intrinsic scatter of the relation for core ellipticals might be generated by systematic uncertainties in the role of dark matter in the dynamical modeling (Thomas et al. 2011; Schulze & Wisotzki 2011; Rusli et al. 2013b). It is also clearly visible that in the high-mass end, core ellipticals tend to have more massive black holes than other galaxies. These more massive black holes might be caused by a change of principal growth mechanism from gas accretion toward black hole mergers as gas is absent in dissipationless mergers of massive galaxies (Krajnović et al. 2018a).

#### Active galactic nuclei versus dormant black holes

The last observational property that I want to address is AGN activity. Compared to the previous subsamples, this time I discuss a characteristic which does not belong to the host galaxy but is directly connected to the massive black hole. AGN activity can occur in several forms, whereas the connection between them is still extensively debated and revised. Based on a number of observational features (emission lines, jets, variability, radio), a number of different classes were proposed. The theory of unification proposes that the classes are just a single type which is observed under different conditions (e.g., Antonucci 1993; Urry & Padovani 1995; Gaskell 2014; Netzer 2015; Padovani et al. 2017). The distinction into different types is often not clear as transitions are often smooth and classifications are driven historically. Nevertheless, active galaxies are generally distinguished in radio-quiet and radio-loud galaxies. Among radio-quiet galaxies, one can differentiate between Seyfert galaxies, radio-quiet quasars, and low-ionization nuclear emission-line regions (LINERs). In LINERs either stars or low-luminosity AGN could be a potential source of the activity (Maoz 2007; Cid Fernandes et al. 2011), but a clear distinction is very difficult. Seyfert galaxies and LINERs can be divided into "type 1" and "type 2" which are characterized by broad and narrow central emission lines respectively, and are generated in the vicinity of the massive black hole (see Figure 1.7.) Based on the unification scheme, type 1 and 2 AGNs might just be a single type of galaxy viewed from different angles. Some recent work (e.g., Chen & Hwang 2017; Villarroel et al. 2017), however, suggests that Seyfert 1 are typically located in bulge-dominant, while Seyfert 2 galaxies are located in disk-dominant galaxies and are thus fundamentally different. Ricci et al. (2017) also show that type 1 and type 2 AGN follow different $M_{\rm BH} - \sigma_{\rm e}$ relations, whereas type 2 AGN host lower mass black holes than type 1 AGN. This finding is regardless of the (early/late) AGN host galaxy morphology.
On the other hand, radio-loud galaxies differ significantly from the previous class as they contain highly collimated relativistic jets and broad radio lobes. Radio galaxies are typically found to be

hosted in giant, gas-poor elliptical or lenticular galaxies and host the most massive black holes (Urry & Padovani 1995; McLure et al. 2004; Best et al. 2005). In very rare cases spiral-host radio galaxies also exist (Singh et al. 2015; Kotilainen et al. 2016; Martínez & Andernach 2016). Sheinis & López-Sánchez (2017) analyze a small set of radio-loud and radio-quiet quasars and note a large scatter in the scaling relations of their limited sample. Their radio-loud quasars have larger velocity dispersions and seem to fall below the scaling relation for AGN and quiescent galaxies by Woo et al. (2013). Not so, for their radio-quiet quasars, which follow the relation by Woo et al. (2013). While the uncertainty in their velocity dispersions is very large and their sample is limited, the result could indicate the different formation scenarios, i.e., major mergers in radio-loud quasars and minor mergers in radio-quiet again. Further investigations are urgently needed for a proper conclusion.
In the following, we want to compare the black hole scaling relations of inactive and active with each other. This is an important diagnostic as AGN activity is a sign of on-going active black hole growth. Due to a large number of on-going reverberation mapping campaigns, the field of active galaxies in connection with the scaling relations is currently very actively studied. The degree of consistency between active and dormant black holes is strongly debated. Early studies (e.g., Grier et al. 2013) did not find a significant difference between active and inactive black hole hosting galaxies. However, Woo et al. (2013) updated the observational data for both black hole populations and derived a steeper relation for inactive black holes. They also noted that the two different relations are nevertheless consistent with each other as selection effects drive the differences. In Figure 1.4c) we show again our black hole compilation and this time color-coded are the different types of black hole activity or inactivity. Additionally included are the recent relations for inactive galaxies by Batiste et al. (2017) and for active galaxies by Shankar et al. (2019). Inactive galaxies can be fitted by $\log_{10}(M_{\rm BH}/M_{\odot}) = 8.51 + 5.09\ \log_{10}(\sigma_{\rm e}/200\,{\rm km\,s^1})$ (black line in Figure 1.4 a), while active galaxies (without distinguishing the different types of activity) follow the shallower $\log_{10}(M_{\rm BH}/M_{\odot}) = 7.55 + 4.00\ \log_{10}(\sigma_{\rm e}/200\,{\rm km\,s^1})$ (green line). It is immediately clear that active black holes have systematically lower black hole masses than their inactive counterparts. As the same trends are found for the $M_{\rm BH} - L_{\rm bulge}$ and $M_{\rm BH} - M_{\rm stellar}$ relation (Reines & Volonteri 2015), it is believed that after a merger bulges grow first and black hole growth is delayed by a few 100 Myrs (e.g., Davies 2007; Wild et al. 2010; Busch 2016). However, it can not be excluded that these differences are caused by the nature of the host galaxy instead of the AGN activity. When discussing this work, it also needs to be strongly cautioned that the virial BH masses measured in AGN are very indirect and suffer from various systematic uncertainties. The broad-line region geometry and orientation are very difficult to determine and likely vary between different objects (Kollatschny 2003; Bentz et al. 2009; Denney et al. 2010; Barth et al. 2011). Usually, when the scaling relations between active and inactive galaxies are compared, only a single geometric scaling factor is applied, which is furthermore derived from comparison with the inactive dataset. However, uncertainties in the virial MBH mass estimate is likely in the order of about 0.5 dex (e.g., Vestergaard & Peterson 2006; Shen 2013) and as such considerably smaller than the offset in BH mass between the two relations.

#### Measurement limitations and selection biases

A number of recent investigations suggested that the measurements of the black hole scaling relations are severely biased. Bernardi et al. (2007) and Tundo et al. (2007) showed that the quiescent galaxy sample with dynamically measured black holes differs significantly from the average sample of Sloan Digital Sky Survey (York et al. 2000) galaxies in a way that low-mass black holes and bulges are not properly covered. This finding was confirmed by van den Bosch et al. (2015) and Shankar et al. (2016) who noted that the current samples are biased towards

dense galaxies. As a result, it has been suggested multiple times that measurements of the black hole scaling relations in these samples may be significantly biased (e.g., Bernardi et al. 2007; Gültekin et al. 2009; Batcheldor 2010; Gultekin et al. 2011; Morabito & Dai 2012; Shankar et al. 2016, 2017; Barausse et al. 2017; Shankar et al. 2019).
Additional bias is set by the fact that different methods favor different types of galaxies. This would not be a problem if the black hole mass measurement methods would be less discrepant or less numerous. In fact, six different dynamical measurement methods span the black hole scaling relations, which have different assumptions, systematic uncertainties, and often give inconsistent results (for a detailed discussion see Section 1.8).
Also, the velocity dispersion, effective radius, and other necessary parameters suffer from large systematic uncertainties, such as inconsistent definitions and ambiguous measurement techniques. Common in all mass measurement methods, also the distance and inclination are two properties which are very difficult to determine and can have a not insignificant effect on the shape of the scaling relations (e.g., Bellovary et al. 2014). A lot of work needs to be done in the future to identify and address the different biases in order to improve our understanding of the origin of the scaling relations. As such it was one goal of this thesis to create a black hole sample of significant size which is based on a consistent measurement method (stellar dynamics), having only early-type galaxies as host galaxies, and in a black hole range spanning from the low-mass to the high-mass end to overcome some of the mentioned biases.

## 3 Direct dynamical mass measurement methods

| Method | Telescope | Scale ($R_S$) | $M_{BH}$ Range ($M_\odot$) | # of SMBH Detections |
|---|---|---|---|---|
| Stellar Dynamics | HST, SINFONI, NIFS | $10^6$ | $10^7 - 2\times10^{10}$ | 93 |
| Stellar Proper Motion | Keck, NTT, VLT | 1000 | $4\times10^6$ | 1 |
| Ionized Gas Dynamics | HST, SINFONI, NIFS | $10^6$ | $7\times10^7 - 4\times10^9$ | 106 |
| Molecular Gas Dynamics | ALMA | $10^7$ | $10^5 - 1\times10^9$ | 12 |
| $H_2O$ Megamasers | VLBI, GBT | $10^4$ | $4\times10^7$ | 27 |
| Reverberation Mapping | Ground based Optical | 600 | $10^6 - 4\times10^8$ | 75 |

**Table 1.1 —** An overview of the methods used to determine SMBH masses dynamically. The table shows the given method, telescopes that are typically used for the observations, the typical distance between the probed material and the center of the SMBH, the range of SMBH masses covered and the number of published mass measurements based on the respective method. (Table adapted from Ferrarese & Ford (2005)

Most supermassive black holes cannot be observed directly as they are photometrically invisible[3]. Accreted matter falls into the black hole and disappears behind the event horizon that equals the Schwarzschild radius for non-rotating black holes. Nevertheless, their gravitational influence can expose black holes to us. Albeit not being able to trace back emitted light from black holes, scientists can detect them based on i) their gravitational effect on the surrounding matter such as nuclear gas and stars or ii) the radiation of accreted matter. Table 3 gives an overview of the different methods to measure black hole masses as well as the number of published measurements with the respective method.
A general misconception is that supermassive black holes have such a large gravitational affect that it can influence the entire galaxy. In fact, only a small fraction of the galaxy is dominated by the gravitational potential of the black hole. The gravitational radius of influence is given by

$$R_{SoI} = \frac{GM_{BH}}{\sigma_e} \approx 10.8\,\mathrm{pc}\left(\frac{M_{BH}}{10^8\,M_\odot}\right)\left(\frac{\sigma_e}{200\,\mathrm{km\,s^{-1}}}\right)^{-1} \tag{1.4}$$

where G is the gravitational constant, $M_{BH}$ is the mass of the SMBH and $\sigma_e$ is the velocity dispersion of the stars in the hosting bulge (Peebles 1972). Outside of a few thousand Schwarzschild radii, but still within the sphere of influence, the motion of stars and gas is prevalently driven by Keplerian force reacting on the combined gravitational potential of stars, gas and all the components contributing mass to those regions. The gravitational hold of the SMBH vanishes quickly beyond the sphere of influence (Ferrarese & Ford 2005). A crucial condition for the dynamical detection of the central supermassive black hole was for a long time that the sphere of influence must be adequately resolved. This condition set the minimally required resolution for the telescopes of observational campaigns. Kormendy & Ho (2013) show how important it was to resolve the sphere of influence in early studies changing the accuracy of mass measurements by a factor of two. This discrepancy has been mainly resolved by expanding the kinematic information from two-dimensional long-slit spectra to three-dimensional IFU observations. Krajnović et al. (2009) and Thater et al. (2017) have shown that it is possible to derive black hole masses well below the resolution limit. This might be due to the case that stars on non-circular orbits can be influenced by the black hole's gravitationally, even if they spend

[3]Currently all supermassive black holes, except for the black hole in M87 and Sgr A* whose black hole shadows were successfully observed with the Event Horizon Telescope.

most of their time outside of the SoI.

## 3.1 The general concept

While per se not visible, supermassive black holes leave a dynamical imprint at their surrounding material. Within its sphere of influence, the black hole dominates the gravitational potential of the galaxy and imposes its spherical symmetry on the region. Within the sphere of influence, but still far enough from the black hole to ignore relativistic effects, Keplerian kinematics reign the motion of the orbiting material. Consequently, the orbital velocity is solely a function of black hole mass and distance from the black hole $M_{\rm BH} = V^2 r/G$ . Stars and gas in the vicinity of the black hole are thus accelerated and can reach velocities of up to a few percents of the speed of light. Both stars and illuminated gas can now be observationally traced and restore the information of the gravitational potential in the vicinity of the black hole via

$$\Phi_{\rm grav} = \underbrace{\Phi_{\rm stellar}}_{L_{\rm stellar} \times M/L} + \Phi_{\rm BH} + \Phi_{\rm DM} \tag{1.5}$$

After subtracting the stellar potential, the mass of the invisible black hole is obtained. In the following chapters, I will discuss several dynamical mass measurement methods which make use of this concept to measure supermassive black hole masses.

## 3.2 The case of Sgr A*

In order to find the closest SMBH, it is not necessary to search in distant galaxies: In fact, the closest supermassive black hole resides in the heart of our very own galaxy. Already in 1931, Jansky (1933) discovered a radio signal coming roughly from the Galactic center (with an uncertainty of 30°), which is in the direction of the constellation of Sagitarrius. It took another 40 years and the then-novel 35-km baseline interferometer of the National Radio Astronomy Observatory until Balick & Brown (1974) were able to discover a strong radio emitting compact structure in the Galactic center: Sgr A*. Nowadays, monitoring observations of the vicinity of Sgr A* provide the strongest dynamical evidence for the existence of supermassive black holes. The Galactic center is so close ($\approx 8.0 \pm 0.4$ kpc[4]), that we can resolve individual stars around Sgr A* and monitor their motions over time. Starting in 1992, high-resolution astrometric observations were carried out in the near-infrared[5] to measure the proper motions and radial velocities of these stars with speckle imaging methods and adaptive optics (e.g. Eckart & Genzel 1996; Ghez et al. 2005, 2008; Gillessen et al. 2009, 2017). Several of the stars approach Sgr A* to within a few light hours ($\approx 1000\ r_{\rm S}$) and move there, accelerated by the massive central object, with a speed of several thousand km s$^{-1}$. The groundbreaking success of monitoring more than one complete orbit of the stars S102 and S2 ($T_{\rm orbit} \approx 11.5$ and 15.8 years) confined the position of the compact massive object in Sgr A* within 100 AU and enabled us to obtain very robust mass estimates of Sgr A*. Most recent estimates of the SMBH mass, inferred from tracing the almost perfect Keplerian orbit of the star S2, yield $M_{\rm SgrA*} \approx 4.1 \pm 0.1\,({\rm stat}) \pm 0.2\,({\rm sys}) \times 10^6\ M_\odot$[6]

[4]Most recent distance measurements from stellar orbits around Sgr A* yield distances between $7.86 \pm 0.15$ kpc and $8.32 \pm 0.16$ kpc (Boehle et al. 2016; Gillessen et al. 2017; Abuter et al. 2019). On the other hand, Very Long Baseline Interferometric (VLBI) measurements of the trigonometric parallax of $H_2O$ masers in the star-forming region Sgr B2 provide a value of $7.9 \pm 0.8$ kpc (Reid et al. 2009b), an indirect recent distance measurement based on RR Lyrae stars gives $8.1 \pm 0.2$ kpc (Griv et al. 2019). For more details about the different methods, I refer to the review by Gillessen et al. (2013).

[5]The optical view onto the Galactic center is blocked due to extinction by interstellar dust

[6]For the comparison of the different black hole mass measurements of Sgr A*, I rescaled the SMBH masses and uncertainties to an average distance of 8.0 kpc.

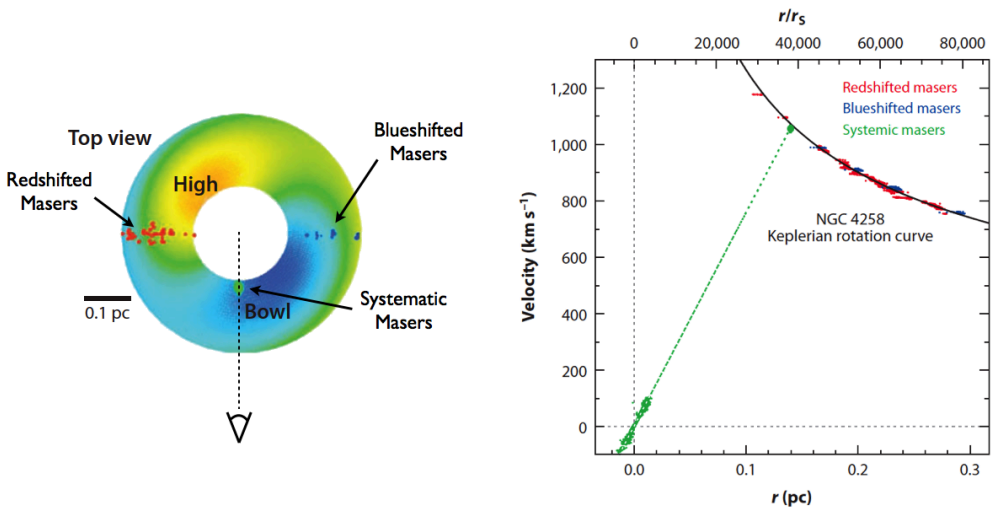


**Figure 1.5 —** Visualisation of the maser dynamics method to estimate $M_{\rm BH}$. The left panel illustrates the gas torus surrounding the central SMBH of NGC 4258. The relative positions of non-systemic and near-systemic masers are shown as red, blue and green spots. The right panel shows the masers overplotted in the rotation versus radius diagram. Red and blue masers follow a Keplerian rotation curve, while green masers follow a linear relationship through the diagram origin. (Images taken from Kormendy & Ho 2013).

(Boehle et al. 2016; Gillessen et al. 2017, but see also Ghez et al. 2005, 2008 and Gillessen et al. 2009) whereas the estimated error is dominated by uncertainties in the distance. As most of the mass of the invisible central object must be contained within the pericenter radius of less than 100 AU, this implies a mass density of this massive central object of $\rho > 8 \times 10^{15}$ $M_\odot$ pc$^{-3}$ [7] which eliminates most reasonable astrophysical alternatives to a black hole (see e.g. Kormendy & Ho 2013).

Next to the mass measurement via stellar orbits, the mass of Sgr A* has been estimated by dynamical modeling of the kinematics of discrete stellar systems in the nuclear star cluster which is also located in the Galactic center. Therefore, individual stellar velocities were spatially binned to construct an estimate of the cluster's velocity distribution and then modeled in a similar manner to nearby galaxies. Compared to the method of monitoring individual orbits, strong assumptions on the dynamical equilibrium of the cluster and its geometry come into play when constructing dynamical models. Recent dynamical measurements include $M_{\rm SgrA*,Jeans} = (3.73 \pm 0.14\,(\rm stat) \pm 0.4\,(\rm sys)) \times 10^6\ M_\odot$[6] (Chatzopoulos et al. 2015), $M_{\rm SgrA*,SS} = (3.0^{+1.1}_{-1.3}) \times 10^6 M_\odot$ (Feldmeier-Krause et al. 2016) and $M_{\rm SgrA*,SS} = (3.62 \pm 0.22) \times 10^6 M_\odot$[6] (Magorrian 2019) and tend to be systematically lower than the measurements based on proper motions. Magorrian (2019) notice that this discrepancy becomes smaller when the population of young stars ($R < 8''$) is ignored in the fitting procedure. The study of the Galactic center continues by improving the astrometric precision (e.g. Jia et al. 2019), continuing mapping the stellar orbits close to Sgr A* over time and exciting tests of fundamental physics paradigms (e.g. Gravity Collaboration et al. 2018, 2019).

## 3.3 $H_2O$ megamasers

The most precise and accurate black hole masses outside of our galaxy can be inferred from $H_2O$ megamasers. Masers ("microwave amplification by stimulated emission of radiation")

[7] In fact, Doeleman et al. (2008) convey an upper limit of the diameter of Sgr A* of about 50 $\mu$as from VLBI measurements, which increases the mass density to $\rho > 10^{24}$ $M_\odot$ pc$^{-3}$.

produce coherent electromagnetic waves based on the principle of stimulated emission and can be envisioned similar to an ordinary laboratory laser, just working in the microwave. The observed galactic water maser emission at 22 GHz originates from a molecular gas disk, which can surround supermassive black holes within a few milliarcsec. By tracing the masing material, the gravitational potential of the black hole can be determined. Figure 1.5 gives a schematic overview of the method based on observations from the well-studied showcase NGC 4258 (Greenhill et al. 1995; Miyoshi et al. 1995). The bulk of masers in the molecular gas torus of NGC 4258 follow a Keplerian rotation curve very closely. With a velocity of 1200 km $s^{-1}$ the innermost edge of the annulus (at around 0.1 pc) constrains the enclosed mass within 0.1 pc to $M_{NGC4258} = (3.81 \pm 0.04) \times 10^7 M_\odot$ whereas uncertainties in the geometry of the gas torus (such as warps) play an important role in the accuracy of this method.
Unfortunately, water masers are not very common in the universe (Ferrarese & Ford 2005). In several surveys targetting different AGN types, only a handful $H_2O$ megamasers could be found: 13 among 354 galaxies within 10 Mpc by Braatz, Wilson and Henkel, one among 26 AGN by Greenhill 1997, one among 131 observed with the Parkes Observatory, 0 among 87 by van den Bosch et al. (2016). The most promising survey was conducted by the MegamaserCosmology Project (Reid et al. 2009a) who are aiming to use the maser disks to determine the Hubble constant to better than 3% accuracy. Scanning many thousand galaxies in the universe, they found 180 megamaser galaxies,[8] from which at least 34 contain an edge-on orientated megamaser disks (Pesce 2015). The search is very challenging as masers are preferentially detected in Seyfert 2 and Liner galaxies with approximately edge-on orientated accretion disks[9](e.g., Braatz et al. 1996, 1997; Henkel et al. 2018; Hagiwara et al. 2018), which are typically not well aligned with circumnuclear disks as traced by stars (Greene et al. 2013). Warped disks are of advantage as they provide numerous sightlines and new methods for inclined maser disks are being developed Darling (2017). Except for the difficulty of finding appropriate $H_2O$ megamaser galaxies, several new maser-based $M_{BH}$ measurements have been added to the black hole compilation in the last years (Pastorini et al. 2007; Greene et al. 2010; Kuo et al. 2011; Greene et al. 2016; Gao et al. 2016, 2017; Pesce et al. 2018; Zhao et al. 2018). The galaxy population of $H_2O$ megamaser galaxies shows quite a few similarities: Hubble types S0-Sbc, often barred and rather low-mass galaxies (Greene et al. 2016), which are seldom probed by other $M_{BH}$ measurement methods. Maser-based measurements are therefore, a great tool to disentangle different formation scenarios from measurement selection biases in the black hole scaling relations (see Section 2.4).

To summarize the advantages and disadvantages of this method: Maser Dynamics are a powerful tool as masing material can be probed within milliarcsec distance to the massive black hole making it the most precise measurement method (except for Sgr A* and M87 with the EHT). However, this method requires the host galaxy to have a masing disk, which can only be found in some specific types of galaxies and are very rare in the universe. While this method can therefore not be applied uniformly for all galaxies, it can be used used to measure black hole masses in galaxies which cannot be studied well with other methods: gas-rich, optically obscured, barred, star-forming and often AGN emitting galaxies. Maser measurements seem to have lower mass black holes than black holes by other measurements. It needs to be seen whether this is a selection effect or points towards systematic inaccuracies in other methods.

[8] https://safe.nrao.edu/wiki/bin/view/Main/PublicWaterMaserList

[9] The reason for this is relatively easy to understand. Maser emission occurs naturally in the interstellar medium. Close to an excitation source, where non-thermal equilibrium conditions reign, the incident photons act via stimulated emission with the excited molecules of the environment to produce a cascade of identical photons which are in phase with the incident photons. The radiation is amplified as it propagates through the medium. In order to achieve a strong signal an adequate long path-length through the disk needs to be traversed by the radiation.

## 3.4 Integrated stellar kinematics

While all other methods require the presence of certain galaxy components (e.g., gas disks, masers or AGN), dynamical modeling of stellar kinematics can theoretically be applied to every relaxed galaxy. Stars reside in every galaxy and their motion is due to the collisionless nature of stellar systems always gravitational (except for dense cores of stellar clusters). Further complexity can arise when having to deal with dust, spiral structures or more complex galaxy potentials, such as a triaxial shape. Therefore, the method of stellar kinematics is the method of choice when determining black holes in regular early-type galaxies (like in this thesis), but it is also a powerful tool for intercomparisons between the different methods.
As this method is used to determine the black hole masses of most of the galaxies discussed in this thesis, I will elaborate this method a bit more thoroughly[10]. In the ideal case, one would like to follow the trajectory of each individual star and describe their individual equations of motion. In a multiple particle system like a galaxy with non-resolved stars, one needs to rely on a statistical description of the entire system. The stellar system can then be described by the distribution function $f(\vec{x}, \vec{v}, t)$ which can be observationally evaluated only along the line-of-sight as line-of-sight velocity distribution (LOSVD)

$$\text{LOSVD}\,(v_z, x, y) = \frac{1}{\mu} \int\int\int f(\vec{x}, \vec{v})\, dv_x\, dv_y\, dz \tag{1.6}$$

In dynamical equilibrium, the distribution function is linked to the velocity field $\vec{v}$ and the gravitational potential $\Phi(\vec{x}, t)$ of the stellar system via the Collisionless Boltzmann equation (CBE)

$$\frac{\partial f(\vec{x}, \vec{v}, t)}{\partial t} + \vec{v} \cdot \vec{\nabla} f(\vec{x}, \vec{v}, t) - \vec{\nabla}\Phi(\vec{x}, t) \cdot \frac{\partial f(\vec{x}, \vec{v}, t)}{\partial \vec{v}} = 0 \tag{1.7}$$

which is like an equation of continuity, but also considers external forces acting on the individual stars, such as the forces associated with the gravitational potential. The gravitational potential, on the other hand, is connected to the total mass distribution $\rho(\vec{x}, t)$ via the Poisson equation

$$\nabla^2 \Phi(\vec{x}, t) = 4\pi G \rho(\vec{x}, t) \tag{1.8}$$

The stellar mass density and the six components of the distribution function are directly connected to observational data. The stellar mass density can be obtained from the observed galaxy luminosity. Assuming, that the distribution function could be fully determined observationally, the gravitational potential would directly follow from equation 1.6. From the derived gravitational potential, one can calculate the total mass density distribution via the Poisson equation. The total mass density is composed of the stellar, black hole and dark matter mass densities (see also equation 1.4). Dark matter is often ignored in dynamical models, such that the mass of the black hole can be directly determined when knowing the stellar mass density.
Unfortunately, not all components of the distribution function can be extracted from spectroscopic observations. Hence, to solve the CBE and Poisson equations analytically, additional assumptions are required to simplify this problem. In the simplest case of a spherical and non-rotating isotropic model the distribution function can be described by only one integral of motion, i.e. the total energy of the system E. In fact, early work by Young et al. (1978) and Sargent et al. (1978) inferred the existence of the black hole in M87 from stellar kinematic observations assuming such a spherically symmetric system. An alternative approach is to break the assumption of isotropy and assume anisotropy in the velocities. In that case, the distribution function depends

[10]For a more detailed discussion and derivation, I refer to the reviews by Ferrarese & Ford (2005) and Kormendy & Ho (2013). Furthermore, the textbooks by Sparke & Gallagher (2007) and Binney & Tremaine (1987) provide a great derivation of the Jeans equations.

on two integrals of motion: the total energy of the system E and the vertical component of the angular momentum $L_z$. Two-integral models are handled through the Jeans equations (Jeans 1922) which follow directly from the CBE and are typically modeled using the Jeans-Anisotropic Modelling method by Cappellari (2008).
Two-integral methods can be further refined by three-integral methods, in which the distribution function also depends on a third integral of motion. Although this third integral cannot be described analytically, the three-integral approach provides a great independent tool to derive black hole masses. In the so-called Schwarzschild (1979) method, an orbit library is created from an assumed gravitational potential of the galaxy which includes the entire system of stars and the black hole. The weighted superposition of the orbits is then optimized to match the kinematics and recover the light distribution of the stars. This approach is applied for several different potentials along a grid. The potential, which best fits the observables, finally provides the best-fitting black hole mass. The Schwarzschild models allow both, axisymmetric (e.g., the models in this thesis) and more computational expensive triaxial potentials (van den Bosch et al. 2008; van den Bosch & de Zeeuw 2010). During the last decade, a number of refinements have been applied to the Schwarzschild models. Gebhardt & Thomas (2009), Schulze & Gebhardt (2011) and Rusli et al. (2013b) considered a dark matter profile in addition to SMBH and stars, McConnell et al. (2013) also take into account a spatial variation of the stellar M/L by using observations at different bands.
Both, JAM and Schwarzschild models have been extensively applied to derive massive black hole masses from stellar kinematics independently, where they usually give consistent results (e.g., Cappellari et al. 2010; Seth et al. 2014; Drehmer et al. 2015; Feldmeier-Krause et al. 2016; Krajnović et al. 2018b; Ahn et al. 2018, but see also chapters 2, 3 and 4 of this thesis). Their capabilities have also been tested on a number of simulations. The derived galaxy properties are typically representative of the simulated galaxies (Li et al. 2016; Leung et al. 2018; Jin et al. 2019), which strengthens the confidence in these methods. By now, about 60% of the whole black hole sample are stellar-kinematics-based. Unfortunately, the complexity of this method restricts it to mainly early-type galaxies with simple light distribution. Due to the assumption of dynamical equilibrium, stellar kinematics methods cannot be applied to barred and merging galaxies.

## 3.5 Ionized gas kinematics

Many galaxies[11] contain regular ionized gas disks in their nuclear regions, which can be studied dynamically to infer black hole masses. Ionized gas is easily traced via nebular emission lines which can be observed in the optical regime of the spectrum and relatively easily analyzed by fitting their line profiles. Figure 5.4 of Chapter 5 shows an example of an optical spectrum that contains several gas emission lines. Prominent nebular emission lines are the Balmer lines of hydrogen and the forbidden [OIII] and [NII] lines. A two-dimensional velocity field can then be re-construted from the measured emission lines and fitted with a projected model circular velocity field with inclination $i$

$$V(r)_{\rm circ} = \sqrt{V(r)^2_{\rm gal} + \frac{GM_{\rm BH}}{r}}\,\sin(i) \tag{1.9}$$

which is an alternative expression of equation 1.4. The model circular velocity field is calculated from the combined gravitational potential of the stellar density, the central SMBH and the gas

[11] In fact, almost all spiral galaxies and more than 50% of lenticular and elliptical galaxies show detectable nebular line emission in their nuclear region (Ho et al. 1997). If the ionized gas is arranged in regular gas disks, it is a great tracer for $M_{\rm BH}$ measurements.

disk itself, assuming that the gas is rotating onto circular orbits in a thin disk. Compared to the computational expensive modeling in stellar kinematics, ionized gas is therefore relatively easy to model.
Using ionized gas as kinematic tracer also suffers from a number of caveats. The gas has to be ordered and mainly influenced by the SMBH's gravitational potential. However, gas is a collisional fluid and there exist many processes that can affect the motion of the gas like magnetic fields, turbulence, radiation pressure or shocks. When these effects occur, the measured gas disk deviates from a Keplerian rotation leading to inaccurate $M_{\rm BH}$ estimates (Neumayer et al. 2007; Mazzalay et al. 2014; Jeter et al. 2018; Slater et al. 2019). The uncertainty of the measured mass can also increase significantly, if the disk inclination is not well constrained, or if the galaxy contains considerable amounts of dust. Crucially, to estimate the black hole mass the SoI needs to be resolved in gas dynamical methods. Regions outside of the SoI can be neglected, whereas those regions still need to be probed in stellar-based methods to account for excentric stellar orbits.

BH mass measurements from ionized gas dynamics have been studied for several galaxies, late-types (Sarzi et al. 2001; Devereux et al. 2003; Coccato et al. 2006; Neumayer et al. 2007; Beifiori et al. 2009; Walsh et al. 2010, 2013), early-types (Ferrarese et al. 1996; Barth et al. 2001; Capetti et al. 2005; Shapiro et al. 2006; de Francesco et al. 2006, 2008; Dalla Bontà et al. 2009) and even for galaxy pairs (Hekatelyne et al. 2018), but the above mentioned modeling complications hinder the confidence of $M_{\rm BH}$ measurements from such dynamically warm tracers (Kormendy & Ho 2013). Therefore, gas dynamical black hole measurements have been shifting towards cold molecular gas, which will be discussed in the next section. (Bellocchi et al. 2019)

## 3.6 Molecular gas kinematics

The mass measurement based on gas kinematics has made an exciting upturn with the advent of the Atacama Large Millimeter/Submillimeter Array (ALMA) telescope and its unprecedented spatial resolution and sensitivity. The key of this method is to trace molecular gas disks that can be found in the center of many galaxies and are dynamically cold (Young et al. 2011; Alatalo et al. 2013). The technique is similar to the measurement via ionized gas dynamics as in the approximately Keplerian motion of the molecular gas disk is used to estimate the enclosed gravitational potential. For that purpose, a model circular velocity field is fitted to the velocity field which is inferred from emission lines in the radio regime. Usually, different transitions from CO are used to derive the velocity field.
Given that molecular gas disks can be found in almost all late-type galaxies (e.g., Young et al. 1995) and about 20% of early-type galaxies (Young et al. 2011; Davis et al. 2012), the method based on molecular gas dynamics is a powerful tool as it is the only technique which can be well applied to measure black holes for all galaxies along the Hubble sequence, for both active and dormant black holes, low-mass black holes in nearby galaxies and sufficiently massive black holes up to large redshifts, and thus resolve current selection biases (see Figure 1.6). In their figure of merit, Davis (2014) show that this method is theoretically feasible to measure SMBHs in about 35.000 local galaxies, providing a complete mass limited census of SMBH. The number of measured black hole masses from molecular gas increases unceasingly (Davis et al. 2013; Onishi et al. 2015; Onishi et al. 2017; Barth et al. 2016; Scharwächter et al. 2016; Davis et al. 2017b, 2018b; Combes et al. 2018; Nguyen et al. 2019; Smith et al. 2019; Nagai et al. 2019; Boizelle et al. 2019, and also Thater et al. (see Chapter 5)), first based on CARMA, now with high-resolution ALMA observations. The method, however, is still in development and possible caveats (such as the effect of non-circular motions and disk warps) still require further analysis

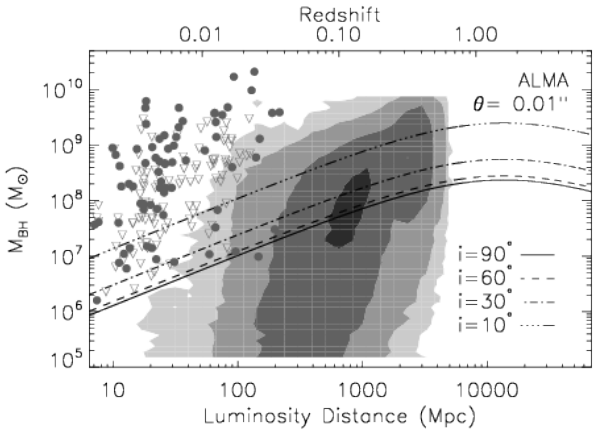


**Figure 1.6 —** Possible limits reachable by applying molecular gas dynamics on ALMA CO(3-2) observations at highest angular resolution of 11 mas at 345 GHz. Taken from Davis (2014).

(e.g., Yoon 2017).

## 3.7 Reverberation mapping

Complimentary to the methods described above, an additional secondary dynamical method was developed to determine BH masses in distant galaxies, where the small angular diameter of the galaxies renders kinematics methods impossible. This method is based on reverberation mapping (RM; Blandford & McKee 1982; Netzer & Peterson 1997) which was originally developed to measure the size of the broad-line region (BLR) around the supermassive black hole in Seyfert galaxies and quasars at a redshift $z \leq 0.5$. The key idea behind RM is to measure the extent of the BLR by observing the response of the BLR to flux variation of the continuum emission arising from the accretion disk[12]. The time-delay $\Delta\tau$ is effectively the mean light travel time in the BLR and can be directly related to the size of the BLR via $r_{\rm BLR} \approx \Delta\tau \cdot c$, assuming that the accretion disk is much smaller than the BLR. As such RM provides a great measurement of the vicinity of the central black hole at spatially-unresolvable scales (~0.01 pc in nearby Seyfert galaxies). Assuming that the BLR is virialized, a virial central BH mass can then be computed via the Virial theorem (e.g., Peterson & Wandel 1999, 2000; Onken & Peterson 2002)

$$GM_{\rm BH} = f r_{\rm BLR} (\sigma_{\rm BLR})^2 \tag{1.10}$$

where the velocity dispersion of the gas in the BLR $\sigma_{\rm BLR}$ is determined from the Doppler broadening of the broad emission lines, and the virial factor $f$ is a scaling factor that encapsulates the unknown geometry, kinematics and inclination angle of the BLR (Wandel et al. 1999). In fact, the virial factor is the main contributor to the uncertainty of this method as it can vary with

[12] In order to understand the RM method it is useful to have a look at the central composition of AGN (see Figure 1.7). The central massive black hole is surrounded by an accretion disk of accreted matter (gas and dust) which emits broad thermal continuum emission (due to the accretion disk's radially changing temperature). Outside of the accretion disk, one can observe the broad-line region which is composed of strongly ionized gas clouds emitting characteristic broad emission lines in the optical and ultraviolet. The characteristic width of the emission lines originates from the fast motion of these ionized clouds around the SMBH, which smear the spectral lines due to Doppler shift. BLR clouds can reach velocities around 1000 to 10000 km/s. At a distance of a few parsecs, the nucleus of the AGN is surrounded by a dust torus. Corresponding to the orientation of the AGN towards us, this torus can hide the BLR from our view.

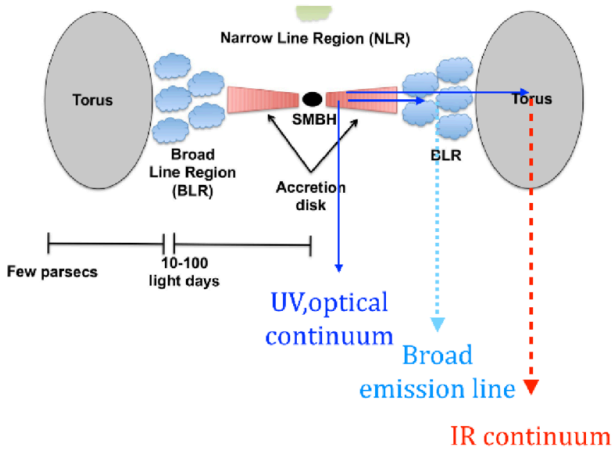


**Figure 1.7 —** Schematic view of the central composition of AGN. The SMBH and its thin accretion disk are surrounded by a thick and dusty torus. Using the time lags among the light in different wavelength, it is possible to estimate the physical size of each component. The figure was taken from Doré et al. 2016. The image credit goes to Claudio Ricci.)

different galaxies but is usually assumed to be a single factor for the complete AGN sample (Park et al. 2012; Yong et al. 2016). The time delay is dependent on the intrinsic luminosity of the AGN (Bentz et al. 2013) and the distance from us: this means that luminous quasars have very long time delays which increase even further due to the time dilations as the photons traverse the expanding universe. The observed time delay may finally reach up to several years. Therefore, it is necessary to monitor AGN over long observing campaigns for many years to characterize the response properly. A great improvement could be achieved with the discovery of a remarkably tight correlation between the size of the BLR and the monochromatic luminosity of the AGN at 5100 Å (Kaspi et al. 2000; Bentz et al. 2013). This new relation could be extensively adopted as single-epoch virial BH mass estimator that allowed the estimation of BH masses based on a single spectrum only (Vestergaard & Peterson 2006; Shen 2013; Ho & Kim 2015). Recently, a number of outliers from this relation have been found (Grier et al. 2017; Du et al. 2018), which imply a more complex nature of the BLR and higher inaccuracies in the black hole masses.

By now, more than 100 $M_{\rm BH}$ from AGN are known due to a large number of successful reverberation campaigns (see the catalog of RM-based black hole mass measurements[13] by Bentz & Katz 2015 and the recent overview by Du et al. 2018). Most of these AGNs are located in the nearby universe (z<0.3), but a handful of these measurements were obtained at higher redshift. In the local universe, the gas velocity $\sigma_{\rm BLR}$ can be obtained from the H$\beta$ line width. After consideration of all the systematic uncertainties of the measurement (BLR size and geometry, variable source luminosity and line width), the derived viral black hole masses have typical uncertainties of a factor 2 (Netzer et al. 2007). For AGNs at higher redshift, to the optical regime shifted rest-frame UV lines are used to measure the gas velocity. Typical lines are CIV $\lambda$1549 (Vestergaard 2002; Park et al. 2013; Hoormann et al. 2019) , MgII $\lambda$2798 (Clavel et al. 1991; Metzroth et al. 2006; Onken & Kollmeier 2008; Shen et al. 2016) and H$\alpha$ (Greene & Ho 2005; Grier et al. 2017). The uncertainties for these high-redshift measurements are still thoroughly debated. While MgII-based measurements tend to be mostly consistent with lower-redshift sources, CIV can be severely affected by non-virial motions, such as outflows and winds, which make this line being a bad surrogate for H$\beta$ (Mejía-Restrepo et al. 2016). The most distant

[13]http://www.astro.gsu.edu/AGNmass/

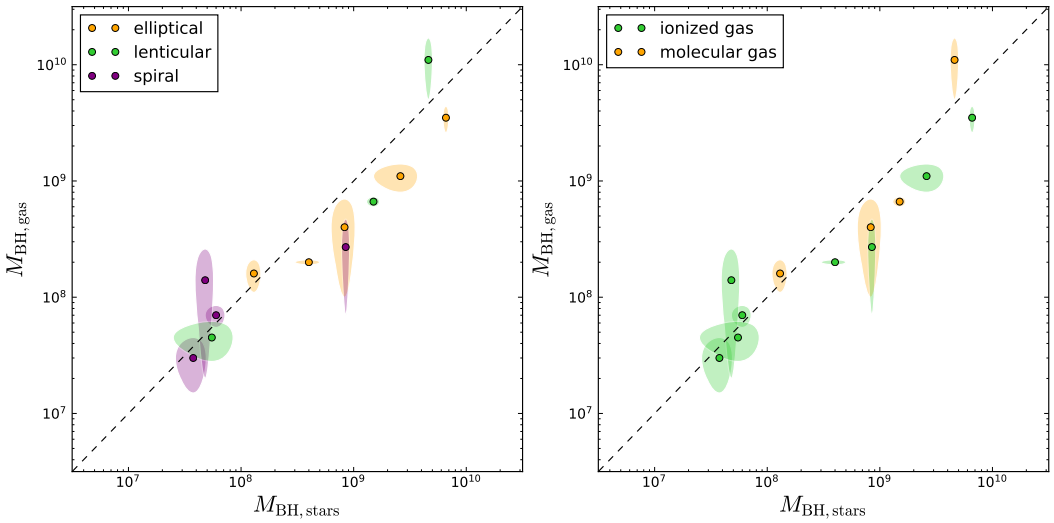


**Figure 1.8 —** Cross comparisons between different $M_{\rm BH}$ measurement methods. Shown are all objects which have both a stellar kinematics and a gas kinematics mass measurement. Colour coded are either different galaxy types (left panel) or different methods (right panel). Despite the low number statistics, gas kinematics provide significantly lower black hole masses than stellar kinematics. Adapted and extended from Kormendy & Ho (2013).

RM-based black hole measurement was obtained from a black hole at z=3.373 (Kaspi2007, Kaspi2017, Lira2018). As such, RM provides a useful tool which has the power to expand the measured black hole masses towards larger redshifts, but also from inactive supermassive black holes, which are mainly probed by other methods, towards active supermassive black holes (Onken et al. 2004). The next very exciting step will be to expand the RM method towards X-ray in order to measure the black hole mass and spin (Zoghbi et al. 2019).

## 3.8 Comparison of different measurement methods

Inconveniently, it is not possible to measure $M_{\rm BH}$ with a single measurement method. Stellar dynamics are well suited for early-type galaxies which usually do not have strongly varying stellar populations nor sub-components like bars or spiral arms. On the other hand, gas dynamics is mostly used in late-type galaxies. Other methods require the presence of nuclear maser emission or an AGN in the galaxy nucleus. Checks for consistencies between the different mass determination methods are important for identifying systematic uncertainties associated within the techniques and deriving robust masses. While SMBH masses have been determined for almost 200 objects, there exists only a handful of galaxies whose black hole masses could be determined through multiple methods. While these are generally consistent in a number of cases (Davies et al. 2006; Pastorini et al. 2007; Neumayer et al. 2007; Cappellari et al. 2009), in more than half of the measurements there is a systematic difference between the stellar-dynamical and gas-dynamical mass estimates (Verdoes Kleijn et al. 2002; de Francesco et al. 2006; Gebhardt et al. 2011; Walsh et al. 2012, 2013, ), with the latter typically being significantly smaller (see Figure 1.8). While the number statistics for the comparisons is still small, Figure 1.8 suggests that the discrepancy tends to occur for elliptical galaxies, for black hole masses above $\approx 10^8\,M_\odot$ and independent of the usage of ionized or gaseous kinematics as tracer. Two galaxies in the sample (NGC 1277, NGC 4258) seem to have more massive black hole masses measured from the gas kinematics measurements, but their gas-based measurements are hardly constrained owing to little information on the inclination and complex gas distributions. We, therefore, urge

to treat these mass-intercomparisons with caution. A particularly interesting case is M87, having an ionized gas-based BH mass of $3.45^{+0.85}_{-0.26} \times 10^9\ M_\odot$ (Walsh et al. 2013) disagreeing with the star-based BH mass of $6.14^{+1.07}_{-0.62} \times 10^9\ M_\odot$ (Gebhardt et al. 2011)[14] by a factor of two. Very recently, the BH mass of M87 was also determined from the size of its black hole shadow yielding $M_{\rm BH,M87} = 6.5 \pm 0.2\,(\rm stat) \pm 0.7\,(\rm sys) \times 10^9\ M_\odot$ (Event Horizon Telescope Collaboration et al. 2019c), which is very consistent with the star-based, but not with the ionized-gas-based measurement. It is likely that the discrepancy between the methods is caused by inaccurate modeling assumptions in the gas dynamics method. This could be of particular concern for massive elliptical galaxies as their gas motion often suggest the presence of substantial random motions (Noel-Storr et al. 2003, 2007) presumably agitated by nongravitational forces associated with radio jets (Verdoes Kleijn et al. 2006). Jeter et al. (2018) analyze the effect of including non-Keplerian motions when modeling ionized gas kinematics and conclude that the derived masses could increase by a factor 2. Therefore, improving the models of ionized gas kinematics could resolve the discrepancy between the ionized gas dynamics and stellar kinematics (see their Figure 4).
Maser measurements also seem to give systematically lower black hole masses than other methods. It needs to be seen whether this is a selection effect or owing to the different evolutionary scenarios, as was discussed in Section 2.4. In conclusion, more objects with more than one $M_{\rm BH}$ measurement are urgently needed to understand this discrepancy in some of the methods. The molecular gas method will greatly contribute in this comparison as it will not only increase the sample but also will provide a valuable cross-check for all other methods (such as reverberation mapping versus molecular gas dynamics). It needs, however, to be cautioned that those samples will also be biased toward galaxies with large amounts of gas in the center (which therefore often have no stellar dynamical $M_{\rm BH}$ measurement).

# 4 The scope of this thesis

The search for massive black holes has recently come to a new level. While we certainly believe in the existence of massive black holes by now, details about the formation and evolution of black holes, in particular connected to the host galaxies, are still not understood. This thesis is motivated to provide new insights into the understanding of the black hole scaling relations.

## 4.1 The SMASHING sample

This thesis is based on a large observing campaign to measure black hole masses from the low- to the high-mass end of the scaling relations. The main observations were conducted with the SINFONI and NIFS near-infrared spectrographs between 2005 and 2013 and were complimented with large-scale data from the SAURON, VIMOS and MUSE spectrographs. In total, our sample, which is called SMASHING sample, consists of 20 galaxies, from which 14 galaxies are examined with great detail in this thesis. The remaining six galaxies were published in Krajnović et al. (2018b) and added in the discussion of Chapter 6.

The SMASHING sample was created to exploit the capabilities of natural guide star (NGS) and laser guide star (LGS) adaptive optics (AO) systems at 8 m ground-based telescopes. By the time of the creation of this project in 2009, $M_{\rm BH}$ measurements were almost exclusively performed by Hubble Space Telescope (HST) measurements with the exception of Nowak et al. (2008) and Krajnović et al. (2009) who pioneered a new method to measure black hole masses

[14] Both measurements scaled to a distance of 16.8 ± 0.8 Mpc.

using ground-based spectroscopy in combination with AO systems, LGS and NGS, respectively. The SMASHING survey was planned to expand the AO method to a wide range of early-type galaxies with different velocity dispersions, from the low ($\approx$ 100 km s$^{-1}$) to the high ($\approx$ 300 km s$^{-1}$) end.

The SMASHING galaxies were selected based on the following criteria:

- *resolvable sphere of influence (SoI)*: The SoI was calculated using black hole masses based on the scaling relation by Tremaine et al. (2002) and the velocity dispersions from the ATLAS$^{3D}$ survey reported in Cappellari et al. (2013b). If velocity dispersions were not available, the central velocity dispersions from Hyperleda were used and extrapolated to the effective radius. This criterium set a limit in distance of about 60 Mpc for our massive galaxies with expected black hole masses of about $10^8$ $M_\odot$.
- *availability of high-resolution imaging (HST):* A robust black hole mass measurement requires detailed knowledge of the light distribution in the galaxy center. The best possible spatial resolution can be obtained with HST imaging. As HST is a very competitive telescope, it was decided to build the sample based on archival data. When selecting the sample galaxies, galaxies with obvious bars or merger features were excluded.
- *observability with SINFONI or NIFS:* SINFONI and NIFS in combination with adaptive optics are the perfect instrument to measure supermassive black hole masses. They combine high spatial resolution close to that of HST with the capability to take spectra in dust-obscured galaxies.
- *availablity of an NGS or TTS for LGS:* In order to achieve optimal spatial resolution, we made use of the adaptive optics system which supports the SINFONI instrument. In that case, we required the presence of a natural guide star close to the galaxy (d<60″) unless we used the laser guide star mode. When using the laser guide star AO, a tip-tilt star, a bright star (< 18mag) close to the galaxy, is usually needed to apply zero-order tip-tilt corrections. We often did not have a suitable tip-tilt star close to the galaxy and tip-tilt on the nucleus was not always possible, such that we applied the SINFONI Seeing Enhancer mode, which provided a slight improvement to the natural seeing.

Based on these criteria, we build a sample of 18 early-type and one late-type galaxy. In a later project, we also added another early-type galaxy (NGC 6958) to this sample, which was observed with the novel AO-mode of the MUSE instrument. 12 galaxies were observed with the SINFONI telescope mounted on the VLT and are discussed in this thesis. Six additional galaxies were observed with the GEMINI NIFS instrument and are discussed in Krajnović et al. (2018a). The late-type galaxy was also observed with NIFS. All observations were performed in the AO mode to obtain the best possible spatial resolution.

## 4.2 Summary of this thesis:

The outline of this Ph.D. thesis is as follows:

- In Chapter 2, we present our $M_{\rm BH}$ estimate in the isolated late-type galaxy NGC 4414, the only late-type galaxy of our sample[15]. Based on large-scale and high-resolution IFU

[15]Chapter 2 is a continuation of my diploma thesis and first results based on only the NIFS data were already presented in that work. During my Ph.D., I improved the stellar kinematics derived from NIFS and added the information from GMOS. I also extended the dynamical models with the Schwarzschild models and performed a detailed study of systematic uncertainties.

data, we derive two-dimensional stellar kinematic maps which show the regular rotation and a velocity dispersion dip in this galaxy. As for other galaxies with a central velocity dip, we are unable to constrain the lower mass limit with our dynamical models and only measure an upper limit of $M_{\rm BH} = 1.56 \times 10^6 M_\odot$ at $3\sigma$ confidence level. Remarkably, we can clearly constrain the upper limit of the black hole mass, which is five times lower than the mass limit anticipated from the resolution limit of the sphere of influence. We show here that via high-quality integral field data in combination with state-of-the-art dynamical models, it is possible to push black hole measurements significantly below the nominal resolution limit.

- In Chapter 3, we present the $M_{\rm BH}$ estimates of six nearby fast-rotating early-type galaxies, namely NGC 584, NGC 2784, NGC 3640, NGC 4281, NGC 4570 and NGC 7049. Our derived masses lie in the intermediate mass range and follow the scaling relations closely. NGC 3640 has a velocity dispersion dip and NGC 7049 a constant velocity dispersion in the center, but we can clearly constrain their lower black hole mass limit.

- In Chapter 4, we re-evaluate black hole masses of six massive galaxies, namely NGC 3706, NGC 3923, NGC 4261, NGC 4636, IC 4296, and IC 4329. Being evidently triaxial, these galaxies are perfectly suited to compare different types of stellar dynamical models with each other, namely spherical Jeans, axisymmetric and triaxial Schwarzschild models. We present the masses measurements from spherical Jeans and axisymmetric Schwarzschild models by fitting the extracted kinematics from SINFONI, VIMOS, SAURON and MUSE IFUs. Half of our galaxies can be constrained, in the other half, we measure upper mass limits. However, our models cannot reproduce the triaxial features.

- In Chapter 5, we compare $M_{\rm BH}$ measurements from two independent methods with each other. NGC 6958 is an ideal test case being a regular elliptical galaxy with regular kinematic features. We first determine the SMBH mass with dynamical models from stellar kinematics extracted from MUSE+AO IFU spectroscopy. We then determine the mass using molecular gas dynamics from ALMA interferometry. Being generally consistent within their uncertainty, both measurements differ by a factor of two, the molecular gas dynamics measurement being lower. Similar trends have also been found in the literature. Therefore, a rigorous test of the systematics associated with the different modeling methods is required in the future.

- In Chapter 6, we conclude this work by comparing the results of our SMASHING sample with the compilation of galaxies with measured black holes from the literature, also adding six SMASHING galaxies, which were published outside of this thesis. None of the SMASHING galaxies deviates significantly from the public measurements. Their inclusion to the published early-type galaxies causes a change towards a shallower slope for the $M_{\rm BH}$ - effective velocity dispersion relation, which is mainly driven by the massive galaxies of our sample. More unbiased and homogenous measurements are needed in the future to determine the shape of the relation and understand its physical origin.

# 2 A low upper-mass limit for the central black hole in the late-type galaxy NGC 4414

**Sabine Thater, Davor Krajnović, Martin A. Bourne, Michele Cappellari, Tim de Zeeuw, Eric Emsellem, John Magorrian, Richard M. McDermid, Marc Sarzi, Glenn van de Ven**

— A version of this chapter is published as S. Thater et al., 2017, A&A 597, A18 —

Abstract

We present our mass estimate of the central black hole in the isolated spiral galaxy NGC 4414. Using natural guide star adaptive optics assisted observations with the Gemini Near-Infrared Integral Field Spectrometer (NIFS) and the natural seeing Gemini Multi-Object Spectrographs-North (GMOS), we derived two-dimensional stellar kinematic maps of NGC 4414 covering the central 1.5 arcsec and 10 arcsec, respectively, at a NIFS spatial resolution of 0.13 arcsec. The kinematic maps reveal a regular rotation pattern and a central velocity dispersion dip down to around 105 km/s. We constructed dynamical models using two different methods: Jeans anisotropic dynamical modeling and axisymmetric Schwarzschild modeling. Both modeling methods give consistent results, but we cannot constrain the lower mass limit and only measure an upper limit for the black hole mass of $M_{\rm BH} = 1.56 \times 10^6\, M_\odot$ (at $3\,\sigma$ level) which is at least $1\sigma$ below the recent $M_{\rm BH} - \sigma_{\rm e}$ relations. Further tests with dark matter, mass-to-light ratio variation and different light models confirm that our results are not dominated by uncertainties. The derived upper mass limit is not only below the $M_{\rm BH} - \sigma_{\rm e}$ relation, but is also five times lower than the lower limit black hole mass anticipated from the resolution limit of the sphere of influence. This proves that via high quality integral field data we are now able to push black hole measurements down to at least five times less than the resolution limit.

# 1 Introduction

In the last decades it has become apparent that supermassive black holes (SMBH) are embedded in the cores of most galaxies irregardless of their morphological types. By now several dozen SMBH masses ($M_{\rm BH}$) have been determined using different measurement methods; stellar kinematics being the most commonly applied method (Kormendy & Ho 2013; Saglia et al. 2016). The majority of SMBH mass measurements were conducted for massive black holes in elliptical and S0 galaxies (e.g., recent compilations by McConnell & Ma 2013; Kormendy & Ho 2013; Graham 2016; Saglia et al. 2016; Greene et al. 2016; van den Bosch 2016). Therefore, by analyzing SMBH statistics, an intrinsic bias arises as not many low-mass late-type galaxy $M_{\rm BH}$ have yet been measured. Recent studies of late-type galaxies include, for example, Greene et al. (2010); De Lorenzi et al. (2013); den Brok et al. (2015); Greene et al. (2016); Bentz et al. (2016). Low-mass galaxies ($M_* < 10^{9.5} M_\odot$) were analyzed by Reines et al. (2011, 2013); Seth et al. (2014); Baldassare et al. (2015), for example.

In this study we present the black hole mass measurement of the isolated, unbarred SA(rc)c late-type galaxy NGC 4414 based on stellar kinematics. NGC 4414 is a flocculent spiral galaxy which shows patchy spiral arms and star formation. Except for a minor interaction with a dwarf galaxy indicated by its low surface brightness stellar shell (de Blok et al. 2014), NGC 4414 does not show any signs of major interactions with other galaxies (Braine et al. 1997). Therefore, its undisturbed dynamical features make NGC 4414 an excellent candidate for dynamical measurements. The inner disk of NGC 4414 is dominated by a stellar component having only a small dark matter contribution (Vallejo et al. 2003; de Blok et al. 2014). Based on different galaxy decomposition studies, it appears that NGC 4414 contains only a small and faint bulge component in its center, while having a large and massive disk.
Over 40 different distance measurements for NGC 4414 are available in the literature ranging from 5 to 25 Mpc. This range includes less accurate measurements from the Tully-Fisher relation. NGC 4414 also belongs to the galaxy sample of the Hubble Space Telescope (HST) Key project (Freedman et al. 2001) measuring distances based on Cepheid brightness. However, the distance measurements are still discordant and tend towards smaller distances. The measurements with the lowest errors give distances of between 16.6 and 21.1 Mpc (Kanbur et al. 2003; Paturel et al. 2002). Therefore, throughout this chapter, we adopt the distance of $D = 18.0 \pm 3.0$ Mpc, which is the mean distance in the NASA/IPAC Extragalactic Database (NED) at the time of writing. At this distance, 1 arcsec corresponds to approximately 86.8 pc. The influence of the distance uncertainty on the black hole measurement is further discussed at the end of this chapter.
Based on its observed effective stellar velocity dispersions of $\sigma_{\rm e} \approx 110$ km/s, the $M_{\rm BH} - \sigma_{\rm e}$ relation (e.g., Ferrarese & Merritt 2000; Gebhardt et al. 2000; Gültekin et al. 2009; Graham et al. 2011) predicts a central black hole mass of $8.7 \times 10^6\, M_\odot$ (all-types; Saglia et al. 2016). While the $M_{\rm BH} - \sigma_{\rm e}$ relation shows a very tight correlation, it is still not fully understood. A number of galaxies have been reported, which show strong deviations from the $M_{\rm BH} - \sigma_{\rm e}$ correlation leading to the question of whether or not all different types of galaxies follow the scaling relations or show different scaling behaviors. The estimate of $M_{\rm BH}$ within NGC 4414 provides a new measurement in the lower mass regime where, due to observational constraints, not many SMBHs have yet been observed. In addition, in the past, only a small number of black hole masses have been recorded for late-type Sc spiral galaxies (Atkinson et al. 2005; Pastorini et al. 2007; Greene et al. 2010, 2016) reinforcing the need for more measurements.

In this chapter, we present optical and adaptive optics-assisted near-infrared integral-field spectroscopic data for NGC 4414, in order to study the stellar kinematics in the vicinity of

**Table 2.1 —** Basic properties of NGC 4414 taken from the literature.

| Property | | Reference |
|---|---|---|
| Morphological type | SA(rc)c | 1 |
| Distance [Mpc] | 18 ± 3.0 | 2 |
| Inclination [ °] | 55 | 3 |
| Bulge effective radius [arcsec] | 3.9 ± 1.4 | 4 |
| $\sigma_e$ [km/s] | 115.5 ± 3 | 5 |

its central black hole. In Section 2, we describe our observational data and in Section 3 the extraction of the stellar kinematics from the GMOS and NIFS integral-field spectroscopic data. In addition to the kinematics, we combine high-resolution HST and Sloan Digital Sky Survey (SDSS) data to model the stellar surface brightness and thus examine the stellar brightness density of NGC 4414. In Section 4, we present the dynamical models which we constructed using two different methods: 1) Jeans Axisymmetric Modeling (Cappellari 2008) and 2) Schwarzschild's orbit superposition method (Schwarzschild 1979). We analyze our assumptions for the dynamical modeling and discuss our results in the context of the $M_{BH}$-host galaxy relationships in Section 5, and finally conclude in Section 6.

## 2 Object selection, observations & data reduction

We used the NIFS and GMOS ground-based integral-field units (IFU) to obtain stellar kinematics in two spatial dimensions allowing better constraints on the black hole mass estimate. High-resolution NIFS data is essential for a precise measurement of the stellar motions in the vicinity of the central black hole, while the large-scale GMOS data constrains the global stellar mass-to-light ratio ($M/L$) and the stellar orbital distribution.

### 2.1 Object selection

In order to achieve the best possible resolution to probe the vicinity of the central black hole, we wanted to utilize adaptive optics in combination with a natural guide star (NGS). Therefore, we undertook a careful study to identify possible targets with bright nearby reference stars by cross-correlating the all-sky 2MASS point and extended source catalogues (Skrutskie et al. 2006). We searched for feasible NGSs close to all galaxies which fulfilled certain criteria: 1) being a northern object since we conducted our observations at the GEMINI observatory; 2) having an available stellar velocity dispersion measurement allowing prediction of the black hole mass based on the $M_{BH} - \sigma_e$ relation (Ferrarese & Ford 2005), that was relevant at that time; 3) from the stellar velocity dispersion and the predicted black hole mass we calculated the sphere of influence (SoI) of the central black hole given by $r_{SoI} = G\,M_{BH}/\sigma_e^2$ where G is the gravitational constant and $\sigma_e$ the stellar velocity dispersion of the host bulge and only considered objects with $r_{SoI} > 0.06''$ reaching the diffraction limit of Gemini at 2.3 micron (Krajnović et al. 2009; Cappellari et al. 2010); 4) the existence of high-resolution HST imaging data. These NGS specifications yielded a sample of six galaxies which were observable at the time of the data acquisition from which NGC 4414 was the only unbarred spiral.

### 2.2 GEMINI NIFS data

Using the NIFS instrument (McGregor et al. 2003), NGC 4414 was observed in May and June 2007 at the 8.1m Gemini North telescope under the science program GN-2007A-Q-45. In order

to improve the natural seeing correction, NIFS operated by using adaptive optics with natural guide star assisted mode. Integral-field spectroscopy in combination with adaptive optics reduces wavefront distortions of the Earth's atmosphere and thus increases the resolving power of the telescope. Figure 2.1 shows the star, which served as the natural guide star for our observations. Projected on the sky it is around 10″ away from the center of our target. The observation was conducted in the K-band to reduce dust contamination and covers a field of view (FoV) of approximately $3'' \times 3''$ centered on the core of NGC 4414 and covering its bulge (Fig. 2.1). In total, NGC 4414 was observed for $34 \times 600$ seconds ($\sim$ 5.5 hours) with NIFS.

The NIFS observations were reduced using the Gemini NIFS reduction routines which are provided in IRAF[1]. The data reduction includes bias and sky subtraction, flatfield calibration, interpolation over bad pixels, cosmic-ray removal, spatial rectification and wavelength and flux calibration with arc lamp exposures. After the data reduction, we merged eleven individual science frames into a final data cube to increase the flux of the spaxels and thus the signal-to-noise ratio (S/N). The science frames had to be re-centered to a chosen reference frame by determining their relative shifts to each other and calibrated to the same wavelength range and pixel sampling. According to the method presented in Krajnović et al. (2009), the re-centering was performed by comparing and re-aligning the science frame's isophotes. The isophotes could not always be matched perfectly as in some cases the outer and inner isophotes were not concentric. This inconsistency can result from uncertainties in the adaptive optics correction. While the inner isophotes are more strongly influenced by the point spread function (PSF), the outer isophotes contain less flux and are more affected by statistical uncertainties. Therefore, we used a compromise between the geometrically more robust outer isophotes and the more flux-significant inner isophotes to deduce the relative shifts. Using the determined shifts, all of the frames were aligned to the reference frame. Finally, the frames were merged with a sigma-clipping pixel reject algorithm to create the final data cube. A new square pixel grid of 0.05″ scale was defined, individual science frames were interpolated to this grid and the flux values of the final data cube calculated as the median flux values of the single data frames as in Krajnović et al. (2009).

Before extracting kinematics from a data cube a high S/N has to be guaranteed; typically S/N $\geq$ 40 (van der Marel & Franx 1993; Bender et al. 1994), as the higher-order moments of the line-of-sight velocity distribution (LOSVD) are very sensitive to noise effects. To keep a roughly constant, high S/N, we used the Voronoi adaptive binning technique[2] introduced by Cappellari & Copin (2003). As the size of the Voronoi bins varies according to the local S/N, a high spatial resolution can be retained in the central pixels. An initial estimate of the noise N of the unbinned spectra was determined by smoothing each galaxy spectrum over 30 pixels and then taking the standard deviation of the residual between the respective galaxy spectrum and the smoothed spectrum. According to our initial S/N estimate, the critical S/N threshold was chosen to be 60. Using the Voronoi binning method, adjacent pixels of our data were binned together into 1546 bins. The single spectra of the binned pixels were co-added to provide a S/N $\geq$ 60. Then, we computed the residual-noise (rN) of each bin as the standard deviation of the difference between the observed galaxy spectrum and the kinematic model (see Sect. 3). The final signal-to-residual-noise S/rN lies between 35 and 85, with lower values at the edges of the FoV.

[1] http://www.gemini.edu/sciops/instruments/nifs/data-format-and-reduction
[2] http://purl.org/cappellari/software

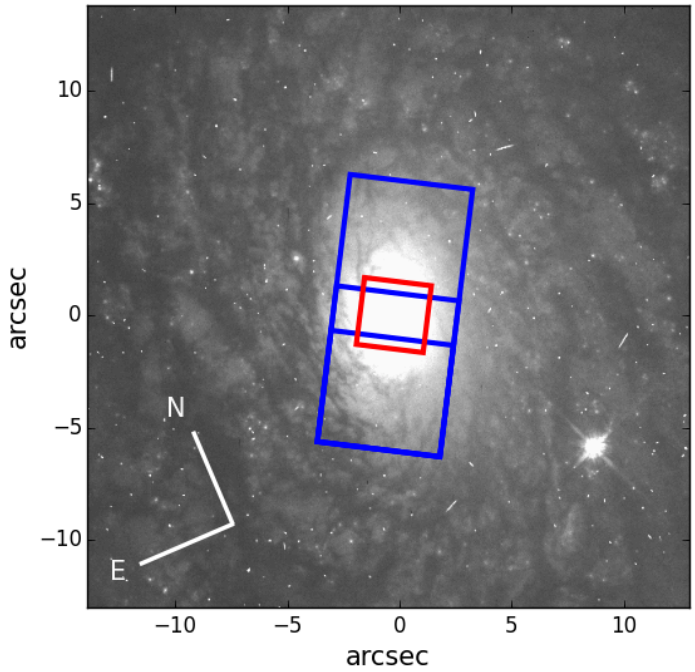


**Figure 2.1 —** Schematic overplot of the NIFS (red) and GMOS (blue) field-of-view on the WFPC2 F606 image. The kinematic data only map the very core of NGC 4414 which is not polluted by dust. The orientation of the NIFS data is 150° and that of the GMOS data is 60° counterclockwise from north. The star in the south-western part of the bulge served as a natural guide star for our observations.

## 2.3 GEMINI GMOS-N data

Parallel IFU observations were conducted with the GMOS instrument (Allington-Smith et al. 2002) at the Gemini Observatory to cover the complete bulge of NGC 4414 (science program GN-2007A-Q-45). The GMOS observations were performed with the *B*600 grating in the *g*_*G*0301 filter and with two pointings keeping the target nucleus in both. The combined FoV covers $5.5'' \times 12''$ which enables us to further constrain the bulge of our target. In total, NGC 4414 was observed $5 \times 1800$ seconds (2.5 hours) at two different wavelengths (475 and 483 nm). Figure 2.1 displays the FoV and the orientation of the NIFS and GMOS data relative to each other and to the extent of the galaxy. Different routines of the IRAF package (see footnote 1) were used for the data reduction of the GMOS data, which consisted of bias subtraction, correction of the spectrum-pixel-association, flat-fielding, wavelength-calibration, and cosmic ray removal. The wavelength-calibration was carried out by comparing the GMOS spectral lines with reference spectral lines of a copper-argon lamp. In addition, a bad pixel correction was applied. One of the blue fiber bundles of the GMOS spectrograph had reduced flux passage resulting in two columns of bad pixels in the science frames. Depending on whether the bad columns lay inside or outside of the observed galaxy nucleus, two different corrections were applied. Due to symmetry, bad pixels inside the galaxy nucleus were corrected by mirroring the flux level of the opposite side of the galaxy nucleus. On the other hand, outside the galaxy nucleus, bad pixels were corrected by interpolating the horizontally adjacent pixels. This correction only affects the absolute flux level of the bad pixels, but does not influence the absorption lines, and, therefore, does not alter the kinematics. In total, nine science frames were merged with the method described in Sect. 2.2 to create a final GMOS data cube. As the central region of NGC 4414 was mainly probed with the better resolved NIFS data, we Voronoi binned adjacent spaxels together to achieve a S/N $\geq$ 60 for each spaxel. The final S/rN of the GMOS data lies between 40 and 100.

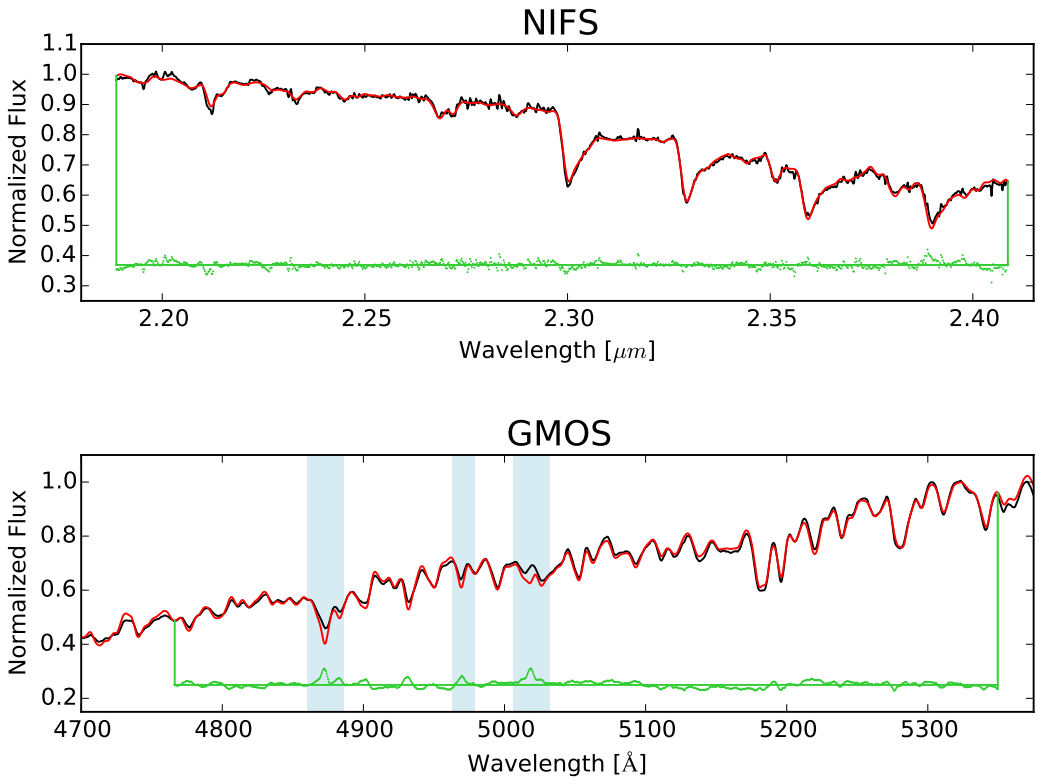


**Figure 2.2 —** Optimal template for NIFS (top) and GMOS (bottom) observations. The black line represents the total galaxy spectrum, which is composed of the spectra of all single spatial pixels, the red line shows the optimal template, which is fitted to the total galaxy spectrum. The fitting residuals are presented as green dots spread around the residual=0-line (green solid line), where both are shifted upwards by an arbitrary amount. The shaded regions contain emission lines and are not included in the fit.

## 2.4 Imaging data

In order to construct dynamical models, appropriate imaging data of NGC 4414 is required to measure the surface brightness and determine the gravitational potential of the stellar component. The imaging data must have a large FoV to cover the light of the whole galaxy and a sufficient spatial resolution in the very central regions where the central mass dominates the galaxy potential. Therefore, we retrieved Wide Field and Planetary Camera 2 (WFPC2) imaging data in F606W from the ESA Hubble Science Archive, which generates automatically reduced and calibrated data. Except for F606W, all WFPC2 images of NGC 4414 were saturated in the center and were therefore not usable for our modeling. The prior data calibration process involved the steps of masking bad pixels, performing an analog-to-digital (A/D) correction and the correction of bias, dark and shutter shading (WFPC2 Handbook[3]). Because of the central saturation of most of the WFPC2 images, it was not possible to remove cosmic rays by comparing the different images. That is why we corrected the images for cosmic rays by determining pixels (at least five pixels beyond the center) that had a large count gradient towards their neighbors and masked these pixels prior to the fitting of the light distribution (Sect. 4.1). We also masked pixels which were significantly affected by dust extinction. These pixels were determined by the method described in Sect. 1.1. In order to fulfill the large FoV criteria, we used ground-based SDSS

[3]http://documents.stsci.edu/hst/wfpc2/documents/handbooks/dhb/wfpc2_dhb.pdf

imaging data in the g-, r- and i-band as our second source. We used the Montage-based online tool Image Mosaic Service[4] provided by NASA and Caltech to create a $0.2 \times 0.2$ square degrees mosaic centered on NGC 4414. Image Mosaic Service uses the individual SDSS images and overlaps them by preserving the fluxes and astrometry.
Dust can have a significant effect on the accuracy and reliability of photometric models as it alters the apparent shape of the galaxy and dims the light due to the wavelength dependent extinction. The images of NGC 4414 indicate large dust and gas patterns in the disk of the galaxy, which obscure the attained light of the galaxy in the SDSS r-band images such that the actual surface brightness is not observable. Using a method described in Cappellari et al. (2002) we corrected the SDSS r-band large FoV image for these extinction effects in order to be able to fit the underlying surface brightness profile. The details of the dust correction are outlined in 1.1. The largest correction was around 25% of the measured flux (see Fig. 2.13). After the correction, the disk region of NGC 4414 shows a more homogeneous flux distribution than before with a larger dust correction on the eastern side of the galaxy.

[4]http://montage.ipac.caltech.edu/

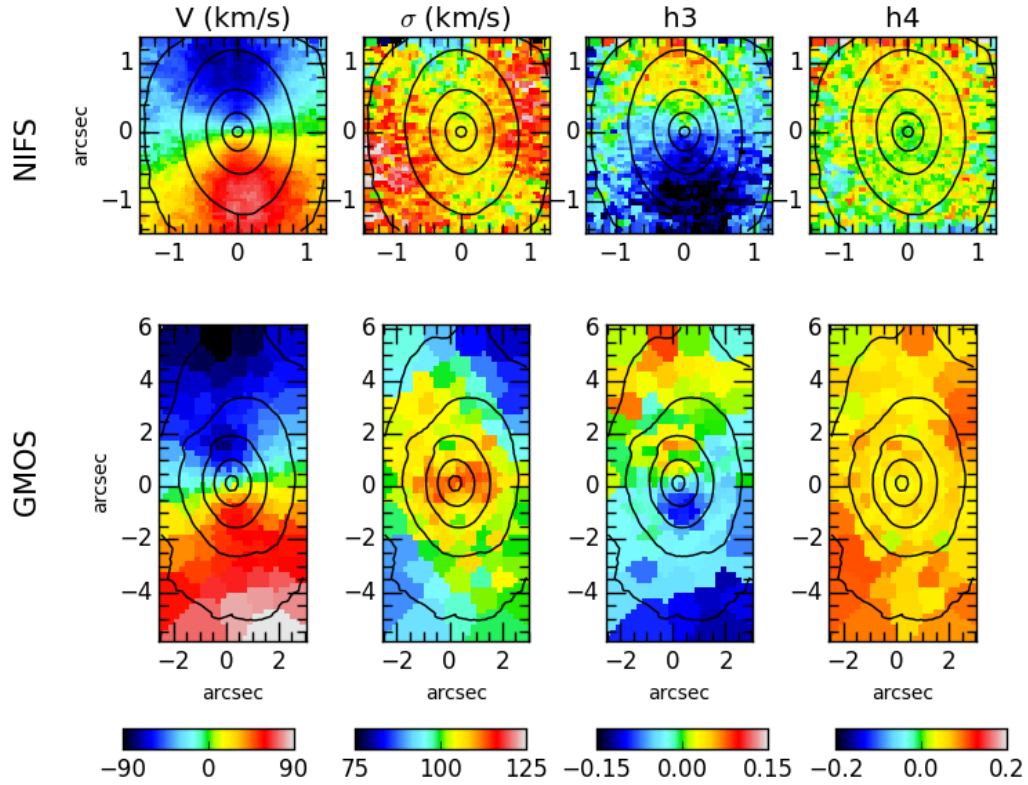


**Figure 2.3 —** Kinematic maps of NGC 4414 derived from NIFS (top) and GMOS (bottom) observations. From left to right the maps show: the mean velocity V, the velocity dispersion $\sigma$ and the Gauss-Hermite moments: $h_3$ and $h_4$. The maps are aligned such that the northern side of the galaxy is at the top.

# 3 Stellar kinematics

## 3.1 Method

The observed spectrum of a galaxy is the convolution of the integrated spectrum of its stellar population with the instrumental broadening and the LOSVD. In order to extract the kinematics from the galaxy absorption line spectra, we used the penalized Pixel-fitting method (pPXF (see footnote 2); Cappellari & Emsellem 2004). pPXF fits the observed spectrum by convolving a template spectrum with the LOSVD which is parametrized by the mean velocity V, the velocity dispersion $\sigma$ and Gauss-Hermite polynomials (Gerhard 1993; van der Marel & Franx 1993). The success of pPXF depends critically on the provision of a good set of template stellar spectra that match the galaxy spectrum as closely as possible. In order to avoid a template mismatch, an 'optimal template' is created as a linear combination of spectra taken from a stellar template library covering the observed wavelength region. The stellar templates used for GMOS and NIFS were the Medium resolution INT Library of Empirical Spectra (MILES; Sánchez-Blázquez et al. 2006) and the Winge et al. (2009) compendium of Gemini Near Infrared Spectrograph (GNIRS) and NIFS observed stars, respectively.

We applied the same general procedure to both data sets: assuming that the whole galaxy consists of the same stellar population, we first determined the optimal template by fitting the stellar template library to a composite spectrum which was created by adding all spectra of the galaxy data cube. During the later application of pPXF, this optimal template was fitted to each bin of the data cube in order to determine the LOSVD of each spatial bin. We specified the LOSVD

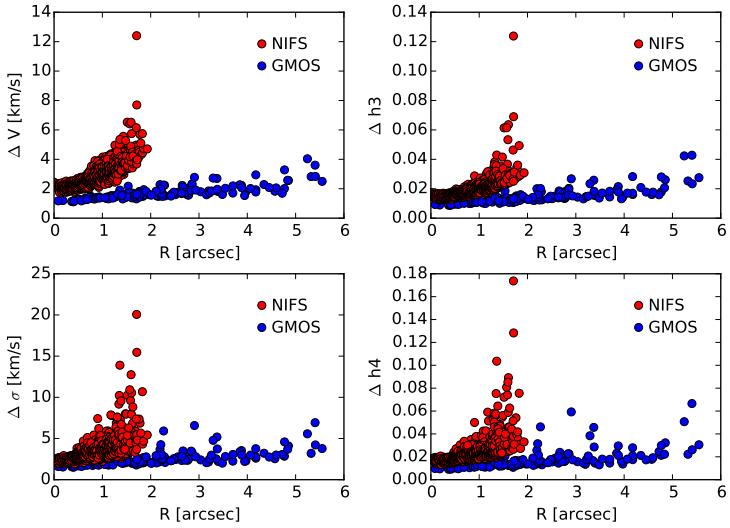


**Figure 2.4 —** Radial distribution of kinematic errors of the NIFS (red) and GMOS (blue) observation. Shown are the errors of the mean velocity $\Delta V$, velocity dispersion $\Delta\sigma$, $\Delta h_3$ and $\Delta h4$. The errors are uniformly low in the central regions and increase towards the edges of the maps.

with the V, $\sigma, h_3$ and $h_4$ moments and included a fourth degree additive polynomial in order to correct the shape of the underlying continuum. From the pPXF fitting we obtained the values of the moments for each spatial bin. We then checked each spectrum visually for template mismatch and for the quality of the fitting, but no peculiarities were found.

The uncertainties of the stellar kinematics were determined by using Monte Carlo simulations. Therefore, we applied the following procedure to the spectrum of each Voronoi bin: we determined the standard deviation between the spectrum and the pPXF fit and perturbed the spectrum 100 times by adding an appropriate random Gaussian noise at the order of the standard deviation. For each of the 100 realizations, the LOSVD was determined. Finally, we took the standard deviation of the derived LOSVD moments.

The following two sections explain the particular specifications for the two data sets and the results from the kinematic fits are presented in Sect. 3.4.

## 3.2 NIFS specifics

As NIFS provides spectra in the near-infrared regime, a stellar template catalog in the K-band is required. Therefore, we used two stellar template libraries[5] by Winge et al. (2009) which consist of G-, K- and M-stars with spectra centered at 2.2 $\mu$m and a spectral resolution of approximately 3.2 Å. One template archive was observed with GNIRS (23 stars), the other with NIFS (31 stars). In order to work with the GNIRS stellar library it was necessary to take the different instrumental resolutions into account. By fitting ten characteristic lines of the sky observation, we determined the spectral resolution of NIFS to be $\sigma_{\mathrm{NIFS}} = 3.2$ Å compared to GNIRS with $\sigma_{\mathrm{GNIRS}} = 2.9$ Å. Therefore, we had to convolve the GNIRS templates with the quadratic difference in resolution. Furthermore, we used the spectrum to the interval shown in Fig. 2.2 to mitigate edge effects and possible contamination from emission lines. The most significant features in the NIFS spectra are the four CO absorption lines which are well fitted by pPXF.

[5]http://www.gemini.edu/sciops/instruments/nearir-resources/spectral-templates

## 3.3 GMOS specifics

For the optical GMOS data, we used the stellar templates from the MILES library, which covers a wavelength range from 3525 Å to 7500 Å and consists of 985 stars in total. Similarly to the NIFS preparations, the difference between the stellar template resolution and the instrumental resolution has to be taken into account when comparing the different data sets. The instrumental resolution of GMOS was derived by applying the pPXF routine on an extracted twilight exposure and measuring the mean velocity dispersion by using a solar template. Thus, we achieved the spectral resolutions of $\sigma_{\mathrm{GMOS}} = 2.16$ Å compared to $\sigma_{\mathrm{MILES}} = 2.5$ Å (Falcón-Barroso et al. 2011). As both instrumental resolutions are similar, we did not convolve the GMOS spectra to lower resolution in order to retain important kinematic information. We analyzed the effect of not taking the convolution into account by using a well-defined sub-sample (in total 52 spectra) of the Indo-US stellar library (Valdes et al. 2004) which covers a wavelength range of 3460 to 9464 Å and a spectral resolution of $\sigma_{\mathrm{Indo-US}} = 1.35$ Å (Beifiori et al. 2011). We extracted the kinematics of GMOS based on the Indo-US library, but this time taking the difference in resolution into account. The resulting kinematic maps show the same general features and trends as the kinematic maps which are based on the MILES template and without accounting for convolution. However, the comparison revealed systematic offsets in the even LOSVD moments of $\sigma \approx +8$ km/s and $h_4 \approx 0.02$. These offsets are in the order of a factor of 3 and 2 times the corresponding errors for the central and 2 and 0.5 times the errors for the outer spaxels. Differences between the kinematic results could be inferred from a template mismatch in the Indo-US library since we build our optimal template from only 52 stellar spectra. Therefore, we decided to use the MILES spectral library in the further analysis, whilst keeping the offsets in the even velocity moments as additional uncertainty.

## 3.4 Kinematic results

The two-dimensional kinematic maps for NIFS (top) and GMOS (bottom) are presented in Fig. 2.3. The two panels on the left show the rotational velocity of NGC 4414 for the NIFS and GMOS observations. Both observations are consistent with each other and show regular rotation patterns without any major asymmetries. The northern part of NGC 4414 moves towards us, while the southern part is the receding side. After subtraction of the systemic velocity, the extreme values are approximately ±77 km/s for the NIFS observation and ±90 km/s for GMOS. The velocity dispersion map shows an elongated dip down to approximately 105 km/s in the central region of the NIFS data which is orientated along the major axis. This dip is not distinctly visible in the GMOS data due to the limited spatial resolution and the large Voronoi bins in the center. Instead, the GMOS data shows a dumbbell-shaped central increase with peculiar lobes along the minor axis of approximately 114 km/s. Both the extended maximum of the GMOS velocity dispersion and the elongated minimum of the NIFS velocity dispersion coincide with the photometric center of NGC 4414. The third Gauss-Hermite moment $h_3$, which is loosely related to the skewness of the distribution, is strongly anti-correlated to the rotational velocity. The $h_4$ map, which relates to the kurtosis, shows a dip in the central 2 arcsec of the GMOS data, while it is uniformly distributed over the NIFS $h_4$ map (with an underlying gradient from blue to red towards the northern side).

The radial distribution of the errors derived from the Monte Carlo simulations are illustrated in Fig. 2.4. The NIFS errors are uniformly low in the central 1 arcsec, but increase sharply towards the edges of the map and thus follow the S/rN of the observation. A similar behavior is seen in the GMOS errors. However, the GMOS errors are lower as the spectra were binned to a higher S/rN. Apart from the central region of the velocity dispersion map, the overall comparison

**Table 2.2 —** Parameters of the double Gaussian fits for the NIFS and GMOS PSF. Given is the full width at half maximum $\mathrm{fwhm}_{PSF}$ of the two Gaussians and the relative flux $f_1$ of the first Gaussian.

| Data | NIFS (arcsec) | GMOS (arcsec) |
|---|---|---|
| $\mathrm{fwhm}_1$ | 0.126 | 1.05 |
| $\mathrm{fwhm}_2$ | 1.19 | - |
| $f_1$ | 0.7 | 1 |

between the NIFS and GMOS data shows good agreement. This allows a combination of both data sets in the latter sections of this chapter.

## 3.5 Spatial resolution of NIFS and GMOS

A key parameter for characterizing the quality of the data is the effective spatial resolution expressed as the width of the PSF of the reconstructed unbinned data cube. A precise measurement is not only important to estimate the seeing conditions during the observations but also to determine how far the dynamics in the center of the galaxy can be probed. In order to measure the NIFS PSF, we convolved the HST data with the sum of two concentric circular two-dimensional Gaussians such that it matched the NIFS data (as done e.g., by McDermid et al. 2006; Davies 2008; Krajnović et al. 2009). The GMOS PSF was determined by convolving the HST data with only a single Gaussian such that it matched the GMOS data. Both PSFs are parametrized by the full width at half maximum $\mathrm{FWHM}_{PSF}$ of each Gaussian component and their relative fluxes. Details of the fitting and the (double) Gaussian fits are given in Sect. 2.2 of the Appendix and the parameters are given in Table 2.2. The NIFS PSF is comparable to measurements from other papers which use laser guide star adaptive optics (Krajnović et al. 2009; Walsh et al. 2015). In addition, we used the narrow component of the NIFS PSF to determine the Strehl ratio which yields 30.8% (details are given in Appendix 2.3).

## 3.6 The effective stellar velocity dispersion $\sigma_\mathrm{e}$

A prediction for $M_\mathrm{BH}$ in NGC 4414 can be achieved by inserting its effective stellar velocity dispersion $\sigma_\mathrm{e}$ into the $M_\mathrm{BH} - \sigma_\mathrm{e}$ relation. The effective stellar velocity dispersion is the integrated velocity dispersion within one bulge effective radius and can be determined from our spectral data. Unfortunately, the GMOS data does not completely cover the bulge effective radius $R_\mathrm{e}$ of NGC 4414, which is approximately $3.9 \pm 1.4''$ (Fisher et al. 2009). Consequently, it was necessary to extrapolate the measured integrated velocity dispersion towards $\sigma_\mathrm{e}$. We considered two different methods for determining $\sigma_\mathrm{e}$: 1) extrapolating $\sigma$ to the desired value on the basis of typical velocity dispersion profiles and 2) extracting a velocity dispersion map from Jeans Anisotropic Modelling (JAM; Cappellari 2008, (see footnote 2)) models.

Based on galaxy velocity dispersion profiles of the CALIFA sample (Sánchez et al. 2012), Falcón-Barroso et al. (2017) provide an extrapolation of $\sigma_\mathrm{e}$ for late-type galaxies and extend the work of Cappellari et al. (2006) on early-type galaxies. They show that the velocity dispersion profile for galaxies follows a power-law which has the form $(\sigma_\mathrm{R}/\sigma_\mathrm{e}) = (R/R_\mathrm{e})^\alpha$ where $\sigma_R$ denotes the velocity dispersion at a given radius R. The exponent $\alpha$ is positive for late-type galaxies ($\alpha_\mathrm{LTG} = 0.077$) and negative for early-type galaxies ($\alpha_\mathrm{ETG} = -0.055$). While NGC 4414 is a late-type galaxy, its GMOS $\sigma$ map shows a decreasing trend with radius which is why we also tested the power-law with a negative exponent for our data. In order to measure $\sigma_R$ from the GMOS data, we first co-added the spectra of each spaxel within an elliptical aperture of

radius 2 arcsec. The resulting spectrum equals a spectrum that would have been observed with a single aperture having a semi-major axis of $R_1 = 2'' \approx 1/2\,R_e$. Applying pPXF to the composed spectrum provides $\sigma_{R,1}$ =121.5 km/s. We used that value in the power-law equations and obtained $\sigma_{e,LTG}$ = 127.9 ±4 km/s and $\sigma_{e,ETG}$ = 117.1 ± 3 km/s. Using $\alpha = -0.066$ (Cappellari et al. 2006) results in $\sigma_{e,ETG}$ = 116.3 ± 3 km/s. The results diverge by approximately 10%. It must be noted that the velocity dispersion profiles generally show a very large scatter with different galaxies (see Cappellari et al. 2006, Falcón-Barroso et al.). We therefore also decided to derive $\sigma_e$ using another method.
JAM can be used to predict $V_{RMS}$, V and $\sigma$ maps of $10'' \times 10''$ size, sufficiently enough to contain the effective radius of 3.9″. We used the luminous mass model (for details see Sect. 4.1, 4.2) and constrained the JAM model with the GMOS FoV. This model reproduced the general features (increased sigma lobes in the center, decreasing velocity dispersion with increasing radius) of the GMOS velocity dispersion map quite well. The value for $\sigma_e$ was then derived by adding up the luminosity-weighted pixel values within an aperture radius of the effective radius of the bulge of 3.9 ± 1.4 arcsec. This method yielded an effective stellar velocity dispersion of 113 ± 5 km/s.
Previous measurements predict that the central velocity dispersion for NGC 4414 in a rectangular aperture of size $2'' \times 4''$ yields $\sigma_c$ = 117 ± 4 km/s (Barth et al. 2002; Ho et al. 2009). This value is consistent with the effective stellar velocity dispersion based on the JAM model and from the power-law extrapolation for early-type galaxies. As a result of the given analysis we conclude the effective stellar velocity dispersion of NGC 4414 to have an averaged value of 115.5 ± 3 km/s.

# 4 Dynamical modeling

In this Section, we present the dynamical models which were constructed to measure the mass of the central black hole. In order to assess the robustness of the results, we used two methods which contain different assumptions and therefore provide independent results. The first method is the predefined JAM method Cappellari (2008, (see footnote 2)) which is based on the Jeans equations (Jeans 1922). In the second method, we applied the more general Schwarzschild orbit superposition method (Schwarzschild 1979; Cretton & van den Bosch 1999; van der Marel et al. 1998; Gebhardt et al. 2003; Cappellari et al. 2007; Onken et al. 2014) which is a complex numerical realization of the central galactic orbits. Both methods are further described in their allocated sections. A common requirement for both methods is the determination of the stellar gravitational potential which can be derived from the stellar luminosity of the galaxy combined with its $M/L$, which is discussed in the following Section.

## 4.1 The luminous mass model

We modeled the dust-corrected galaxy surface brightness by using the Multi-Gaussian Expansion (MGE) introduced by Monnet et al. (1992) and Emsellem et al. (1994) . In order to simplify the convolution and deprojection calculations the projected surface brightness is parametrized as a sum of two-dimensional concentric Gaussians

$$\Sigma(x', y') = \sum_{j=1}^{N} \frac{L_j}{2\,\pi\sigma_j'^2\,q_j'} \exp\left[-\frac{1}{2\sigma_j'^2}\left(x'^2 + \frac{y'^2}{q_j'^2}\right)\right], \tag{2.1}$$

where N is the number of Gaussians with each having the total luminosity $L_j$, an observed axial ratio between $0 \leq q_j' \leq 1$ and a dispersion $\sigma_j'$ along the major axis.
We performed our MGE modeling of NGC 4414 by using the software and method developed for general application on galaxies by Cappellari (2002, see footnote 2). A well-constructed

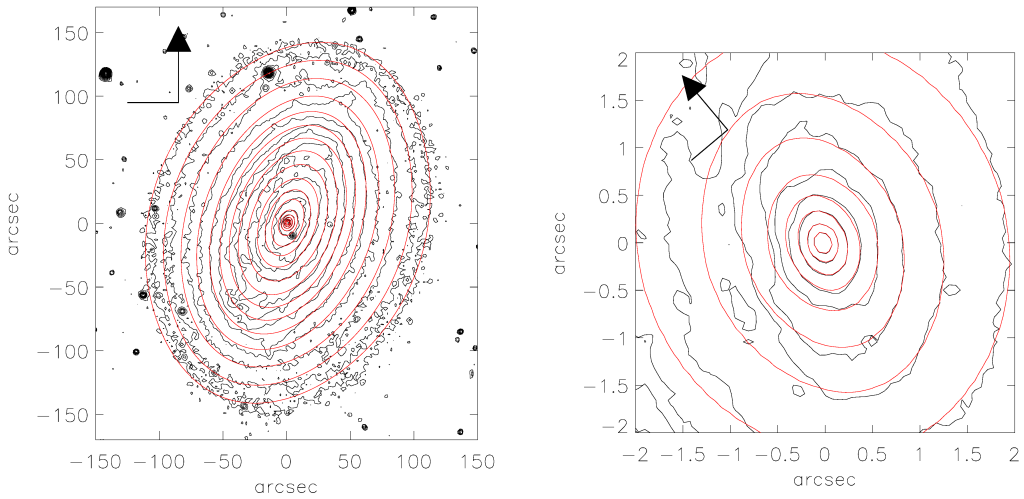


**Figure 2.5 —** Comparison between the r-band isophotes of NGC 4414 (black) and the MGE surface brightness model (red) from the combination of the HST F606W and the SDSS r-band image. The upper panel shows a wide-field view with isophotes from the SDSS r-band image, the lower panel shows a magnification to the central $4 \times 4''$ region based on the HST F606W isophotes. Foreground stars and strong dust patterns were masked during the MGE fit. The upper panel is orientated such that north is at the top and east is on the left of the image, the lower panel is orientated as in Fig. 2.1.

dynamical model requires the combination of deep imaging of large FoV data with high-resolution data in the center of the galaxy. This provides a good estimate of the $M/L$ in the outskirts and also reveals the nuclear morphology of the galaxy. In order to properly decompose the components of the light profile, we used the MGE routine on the ground-based wide-field SDSS r-band ($12' \times 12'$) and high-resolved HST/WFPC2 F606PC ($36.4'' \times 36.4''$) image simultaneously. Due to the large amount of dust, we used the HST image only to fit the innermost isophotes ($R \leq 5''$) and the dust-corrected SDSS r-band to measure the shape of the outer-disc isophotes. For the inner and outer regions, we kept the same constraints for the axial ratio of the two-dimensional Gaussians. As the dust attenuation significantly changes the shape and the amount of measured light, we applied a dust mask to the contaminated regions (see Appendix 1.2). Before the MGE model of equation 2.1 can be compared with the observed surface brightness, the instrumental and atmospheric PSF have to be taken into account. We obtained a model of the HST/ WFPC F606PC PSF at the center of the galaxy using the Tiny Tim HST PSF modeling tool (Krist & Hook 2001) and parametrized it with a circular MGE model (see Appendix 2.1).

The final MGE model is composed of eleven concentric Gaussians. Except for the dust structures on the eastern side of the galaxy and the spiral arms, the MGE model reproduces the shape of the isophote contours very well (Fig. 2.5). The best fitting MGE parameters of NGC 4414 in physical units are listed in Table 3 following prescriptions in Cappellari (2002).

We then de-projected the derived MGE model by using the MGE formalism to retrieve the three-dimensional intrinsic galaxy luminosity density. The de-projection provides non-unique solutions (Rybicki 1987) from which the MGE fit then chooses a density profile which is consistent with the observed photometry.

Finally, the galaxy luminosity density can be converted to the galaxy total mass density by multiplication with the galaxy's stellar ($M/L$), which can be different for each Gaussian. In our models, we assume a constant $M/L$. The luminosity density is used in the next sections to construct dynamical models of NGC 4414.

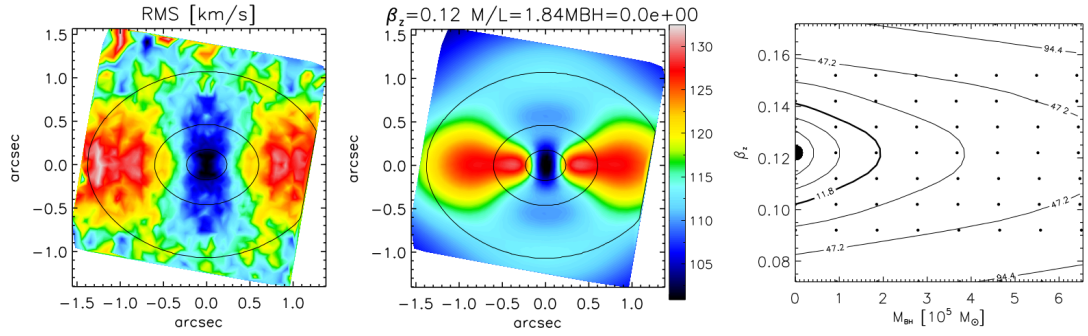


**Figure 2.6 —** Results of the JAM modeling method. The left panel shows the bi-symmetrized $V_{\rm rms}$ observed with NIFS. The middle panel shows the JAM model for the upper limit of the mass of the central SMBH $M_{\rm BH} = 0\,M_\odot$ and the best fitting anisotropy parameter $\beta = 0.12$. It is clearly visible that the model cannot reproduce the NIFS $V_{\rm rms}$ very well. The right panel shows the grid of computed models (black points) overplotted with smoothed $\Delta\chi^2$ contour lines to find the best fitting model (larger black dot). The smoothing was applied by a minimum curvature algorithm. The thick contour line denotes the $3\sigma$ threshold.

## 4.2 Jeans anisotropic model

The first method to derive the mass of the central black hole is based on the Jeans (1922) equations which follow on from the steady-state collisionless Boltzmann equation. The Jeans equation relates the galactic gravitational potential to the second velocity moment and the galaxy luminosity density (Binney & Tremaine 2008). The additional anisotropy parameter $\beta_z$ measures the anisotropy of the velocity distribution and therefore the orbital distribution in the galaxy. The solution of the line-of-sight integral over each Gaussian component is given by equation (28) in Cappellari (2008). The second velocity moment is well approximated by the observable quantity

$$V_{\rm rms} = \sqrt{V^2 + \sigma^2}, \tag{2.2}$$

where V is the stellar mean velocity and $\sigma$ the velocity dispersion which parametrize the LOSVD and were measured in Section 3. Cappellari (2008) provide the JAM software (see footnote 2) which allows us to construct a model of the central dynamics of NGC 4414 based on the Jeans formalism. Although the JAM method does not allow for a general anisotropy and could, in principle, produce biased results, it was shown to provide results in agreement with more general techniques in the cases where it was compared (Cappellari et al. 2010; Seth et al. 2014; Drehmer et al. 2015). Of particular interest is the case of the black hole in NGC 1277, where the Schwarzschild's model of van den Bosch et al. (2012) indicated a significantly larger black hole than the models by Emsellem (2013), based on an N-body realization having the same 1st and 2nd moments of a JAM model (computed via Eqs. 19 to 21 in Cappellari (2008)), which generalizes the MGE formalism. The latter black hole estimate turned out to be confirmed by subsequent work (Walsh et al. 2016) using high-resolution IFU data. This illustrates the usefulness of comparing black hole determination using different techniques based on different assumptions.

From the derived MGE surface brightness we constructed several axisymmetric models. The models have three free parameters which are 1) the anisotropy parameter $\beta_z$, 2) the mass of the black hole $M_{\rm BH}$ and 3) the dynamical mass-to-light ratio $M/L$. We fixed the inclination of the galaxy to that of the large-scale atomic and molecular gas disk (Vallejo et al. 2002; Wong et al. 2004, Sect.5 of this chapter).

In total, we constructed 54 dynamical models in a grid of $\beta_z = [0.07, 0.17]$ and $M_{\rm BH} = [0, 3 \times 10^5\,M_\odot]$. The formally best fitting model parameters could be determined by minimizing $\chi^2$

between model $V_{\rm rms,model}$ and the NIFS observation $V_{\rm rms,obs}$. Figure 2.6 illustrates the $\beta_z - M_{\rm BH}$ grid of our constructed models. The JAM models are plotted as black points. In order to describe the agreement between the JAM models and the observed $V_{\rm rms}$, we overplotted the contours of $\Delta\chi^2 = \chi^2 - \chi^2_{\rm min}$ on the model grid with $\chi^2_{\rm min}$ defined by the best fitting model. The mass of the black hole is not constrained resulting in an upper limit measurement of $M_{\rm BH} = 1.5 \times 10^5 M_\odot$ (for one degree of freedom, marginalizing over $\beta_z$) and $M_{\rm BH} = 2 \times 10^5 M_\odot$ (for two degrees of freedom, see Fig. 2.6,) at 3 $\sigma$ significance obtained solely from the NIFS observations and the JAM models. This is approximately 50 times lower than that predicted by the $M_{\rm BH} - \sigma_{\rm e}$ relation (e.g. Greene et al. 2016, late-type). In addition, JAM provides the dynamical $M/L$ of the best-fitting model of $M/L = 1.84 \pm 0.04$.

For a visual comparison, we show the $V_{\rm rms}$ data and the best fitting JAM model in Fig. 2.6. Formally the best fitting dynamical model is given by $M_{\rm BH} = 0\, M_\odot$ and $\beta = 0.12$. We note that the JAM models generally do not reproduce the observations very accurately, but resemble the observed $V_{\rm rms}$. However, while the actual shape of the $V_{\rm rms}$ cannot qualitatively be reproduced by the JAM models, the distinct $V_{\rm rms}$ drop from the center of the observations is also present in the models. This drop is very crucial as it provides important implications on the central black hole. Models with higher black hole masses fail more distinctly to reproduce this drop in the $V_{\rm rms}$ (see Sect.5.2 and Fig. 2.11).

## 4.3 Schwarzschild model

We constructed dynamical models based on the Schwarzschild (1979) method, generalized to fit stellar kinematics (Richstone & Tremaine 1988; Rix et al. 1997; van der Marel et al. 1998). The implementation we use was optimized for integral-field observations and is described in Cappellari et al. (2006). Briefly, the first step of the method is a construction of a library of orbits which evenly sample the space of three integrals of motion: energy $E$, vertical projection of the angular momentum $L_z$ and the third integral, $I_3$. Energy is sampled at 41 logarithmically spaced points specifying the representative radius of the orbit, while at each energy we used eleven radial and eleven angular points for sampling $L_z$ and $I_3$, respectively. Each model library comprises a total of 2143150 prograde and retrograde orbits bundled in groups of $6^3 = 216$ orbits with adjacent initial conditions. The orbits are integrated in the potential defined by the MGE parametrisation of the light distribution (Section 4.1), which was projected at an inclination of 55 degrees, while assuming axisymmetry. The two free parameters which define the total potential are the mass-to-light ratio ($M/L$) and the mass of the black hole. Once the orbits are integrated, they can be projected onto the observable space (position in the sky and the LOSVD parameters), while taking into account the PSF and the Voronoi bins. Each orbit is assigned a weight in a non-negative least-squared fit (Lawson & Hanson 1974), and when combined they reproduce the observed stellar density and kinematics in each bin. Both NIFS and GMOS kinematic data are used to constrain the models, however we exclude the GMOS data from the central 0.8 arcscec (we verified that including the GMOS data does not change the results). As our Schwarzschild model is axisymmetric by construction, we first symmetrized the kinematics ($V$, $\sigma$, $h_3$ and $h_4$ maps) using point-(anti)symmetry around the photometric major axis, averaging at positions: [($x$,$y$),($x$,$-y$),($-x$,$y$), ($-x$,$-y$)], while keeping the original errors in each bin. Finally, when running the linear orbital superposition, we used two levels of regularization, a moderately low $\Delta = 10$ and a high one $\Delta = 4$ (as defined in van der Marel et al. (1998)). Both regularizations gave equivalent results and we present the one with moderate regularization.

Grids of 441 dynamical models are presented in Fig. 2.7. The contours show the $\Delta\chi^2$ levels, which are calculated for a two-parameter distribution, while the thick contour displays the $3\sigma$ level. In the left hand panel there is a discontinuity of the $3\sigma$ $\Delta\chi^2$ level at lower masses,

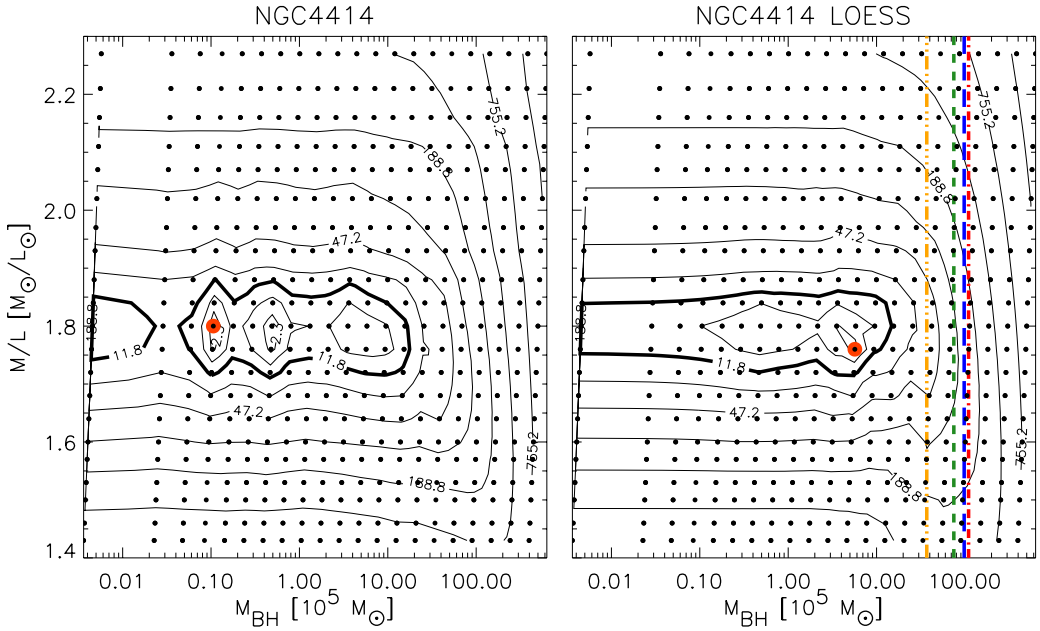


**Figure 2.7 —** Grids of Schwarzschild dynamical models (round symbols) with different mass-to-light ratios and black hole masses. Contours are the $\Delta\chi^2 = \chi^2 - \chi^2_{\rm min}$ levels. The thick contours are the $3\sigma$ levels. Both panels are for regularization parameter of $\Delta = 10$, while the right hand panel shows smoothed $\Delta\chi^2$ contours using the local non-parametric regression LOESS algorithm (Cleveland 1979; Cappellari et al. 2013b), with the local polynomial set to quadratic. The large red circle shows the model with the formal $\chi^2$ minimum. The LOESS smoothed $\chi^2$ contours indicate that no $\chi^2$ minimum is reached within our grid when models are marginalized over all $M/L$ ratios. The dashed (green) line indicates the values of $M_{\rm BH}$ for which the sphere of influence is three times smaller than the resolution of our NIFS data (this value is also close to the prediction based on the McConnell & Ma (2013) $M_{\rm BH} - \sigma_{\rm e}$ scaling relation). The dashed-double dotted (orange), long-dashed (blue) and dashed-dotted (red) vertical lines indicate predictions for $M_{\rm BH}$ of the van den Bosch (2016), Saglia et al. (2016) and Greene et al. (2016) scaling relation (for all galaxies in their samples), respectively.

suggesting the possibility of also constraining the lower limit of $M_{BH}$. However, this is not real and likely a spurious result of the models. Running a smaller orbital library constructed by sampling the three integrals ($E$, $L_z$, $I_3$) with (21,7,8) starting conditions, results in several of these local minima in the region below $M_{BH} < 10^6$ $M_\odot$. Regularizing the Schwarzschild models does not significantly improve the grid of $\Delta\chi^2$ values. The grid of $\Delta\chi^2$ becomes, however, significantly smoother when the size of the orbital library is increased, as shown here. A further increase of the library size would likely remove the present discontinuity. As the increase in the orbital library is expensive in terms of computing, we examined the difference between these models in Fig 2.8. Next to the observed velocity dispersion (NIFS), we plot two models with the lowest $M_{BH}$ and the model of the formal best fit from the left hand panel on Fig 2.7. It is obvious that these models are not different in any significant way, even though the formal $\chi^2$ value is sufficiently higher for the model in the middle to exclude it from the three-sigma uncertainty level. The differences between the models are at the level of the systematic errors affecting the data, and this is likely connected to the size of the orbital library and intrisinc degeneracies such as the deprojection at a relatively low inclination (see Krajnović et al. (2005) for a similar situation related to the degeneracy in recovering the inclination and van der Marel et al. (1998) for a discussion on the topology of $\Delta\chi^2$ contours due to finite numerical accuracy of the models).

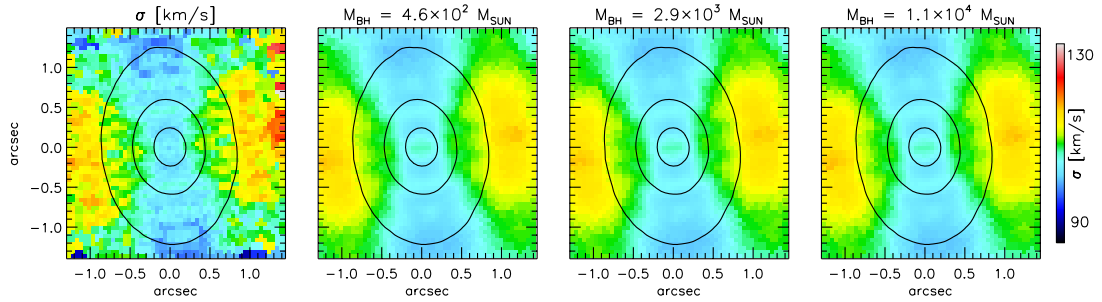


**Figure 2.8 —** Comparison between the observed NIFS velocity dispersion map and three low $M_{\rm BH}$ Schwarzschild models, all at the same $M/L$=1.80. From left to right: the data, the model with the lowest $M_{\rm BH}$ used in this work, a model which is formally outside the three-sigma uncertainty level, and the formal best fit model from Fig. 2.7 left panel. The $M_{\rm BH}$ values are given above the maps. There are no significant differences between these three models, and the differences with the data are on the level of systematics, arguing that the the three-sigma uncertainty level on the left hand panel of Fig 2.7 should be continuous and no lower limit to the $M_{\rm BH}$ is found in NGC 4414.

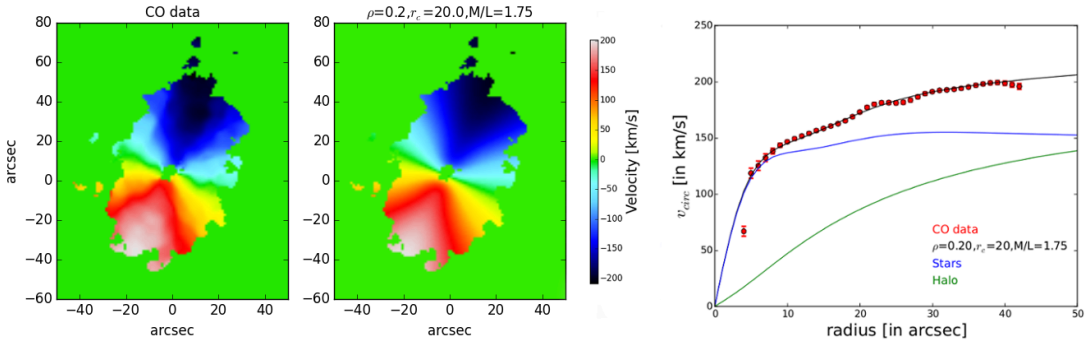


**Figure 2.9 —** Comparison between the CO observations and our convolved two-dimensional velocity model. The left and middle panel show the CO data obtained by Wong et al. (2004) and our model which best describes the CO data. The right panel shows the rotation curves of the CO observations (red points) and the best-fitting model (black solid line). We also separately plot the rotation curves from the stellar (blue solid line) and dark matter (green solid line) potential. All model curves are convolved with the kernel by Qian et al. (1995).

Fig. 2.8 suggests that one could apply a moderate level of smoothing to improve the topology of $\Delta\chi^2$ contours (e.g. Gebhardt et al. 2003). For the right hand plot of Fig. 2.7 we adaptively averaged $\Delta\chi^2$ contours using the local regression smoothing algorithm LOESS Cleveland (1979), adapted for two dimensions (Cleveland & Devlin 1988) as implemented by Cappellari et al. (2013a) (see footnote 3). We used a limited number of points for the LOESS kernel with the fraction (of total number of points) equal to 0.2, and a local quadratic approximation, as the location of the $\chi^2$ minimum is similar to a quadratic function. This produces a smooth $\Delta\chi^2$ with a well-defined upper limit, fully consistent with the original grid. The formal best fit now has a somewhat larger $M_{\rm BH}$, and a slightly smaller $M/L$, but these should not be taken literally as there is no sufficient difference between the models within the three-sigma uncertainty level (see also the first model on Fig. 2.11).

The Schwarzschild models constrain the mass-to-light ratio to $M/L = 1.80 \pm 0.09$, in good agreement with other estimates (Section 5.1 and Table 2.3). As discussed, we do not constrain the lower mass limit of $M_{\rm BH}$ at $3\sigma$ level, while the upper mass limit is $1.56 \times 10^6\, M_\odot$. In

Appendix 8 we show the comparison between a representative Schwarzschild model within the three-sigma uncertainity level having $M/L = 1.80$ and $M_{\rm BH} = 5.81 \times 10^5\ M_\odot$, and the kinematics from GMOS and NIFS observations.

# 5 Discussion

Both the Jeans and the Schwarzschild models from our previous analysis provide consistent results for the black hole mass of NGC 4414, constraining only the upper limit value. These upper limits mark the mass boundary of where the models start to become clearly inconsistent with our data. Below we carry out a comprehensive error analysis of our measurements, discuss our results with respect to the resolution limit and place the galaxy on the most recent and relevant $M_{\rm BH}$-host galaxy relations.

## 5.1 Error budget

Many assumptions and uncertainties go into the dynamical models to determine the mass of the central black hole. While the statistical errors given in the previous sections account for the uncertainties of the models, it is also important to take a closer look at systematic effects which can drastically change the results. In this section, we evaluate the importance and effects of dust contamination, distance accuracy, dark matter contribution, variation in $M/L$ with radius, and kinematical tracers.

*Dust Contamination:* A large amount of dust pollutes the facing side of NGC 4414 (see Fig. 2.13, Fig. 2.14). This especially affects the visible light WFPC2 F606W PC and SDSS r-band images, less so images in the infrared. Therefore, we corrected both images before modeling the surface brightness (see Appendix 1.2). We checked the effect of the dust-correction by also creating MGE models from the WFPC2 F606W image in combination with different dust masks and even without a dust mask. Constructing dynamical models for these modified MGE models, however, revealed no significant change in the upper limit measurement, but the models represented the data less well.

*Distance:* NGC 4414 has approximately 40 distance measurements based on Cepheids and Tully-Fisher methods which span a range between 5 and 25 Mpc. Taking only distances into account that have a conservative error below 1 Mpc, the distance span lowers to between $16.6 \pm 0.3$ and $21.1 \pm 0.9$ Mpc (Kanbur et al. 2003; Paturel et al. 2002). This gives a difference of [-1.7,+4.0] Mpc to our applied distance value of 18.0 Mpc. In our dyncamical models, the distance operates as scaling factor and is directly proportional to the mass of the black hole and anti-proportional to the $M/L$. This means the uncertainty from the distance is around 20%. Taking the distance uncertainty into account for our models, we get $M_{\rm BH} \leq 1.85 \times 10^6\ M_\odot$ and $M/L = 1.8 \pm 0.35$.

*Dark Matter*: Both dynamical modeling methods do not explicitly take dark matter (DM) into account. Consequently, the models are only reliable when the shape of the total density distribution is well approximated by the stellar density distribution within the region where we fit the kinematics. However, different studies (Gebhardt & Thomas 2009; Schulze & Gebhardt 2011; Rusli et al. 2013b) report a change in black hole mass measurements when including the presence of dark matter in the region covered by the kinematic data. This happens when the dynamical models include kinematics at sufficiently large radii that the difference between the slope of the total and stellar density becomes significant. The reported effect of accounting for dark matter in the dynamical modeling method is a factor between 1.2 and 2 in the black hole mass and results from the degeneracy between the dark matter halo mass, the stellar mass-to-light ratio and the black hole mass. Therefore, neglecting the dark matter component increases the $M/L$ leading to a smaller $M_{\rm BH}$ to fit the observed kinematics. Vallejo et al. (2003) fit a Navarro-Frenk-White

halo (Navarro et al. 1996) to the rotation curve of NGC 4414 and report a low-mass DM halo in the central region of the galaxy. As the low-DM assumption is important for the black hole measurement, we further validated our dynamical results by deriving the dark matter fraction within the observed region of NGC 4414.

Therefore, we constructed a model circular velocity map and compared it to CO observations deriving the stellar mass-to-light ratio and probing the existence of dark matter in the center of the galaxy. The CO velocity fields were derived by Wong et al. (2004) from mm-interferometric observations, which cover the CO emission for a large portion of the visible galaxy ($R \approx 50''$). By fitting Gaussians to the spectrum of each pixel, using a customized version of the MIRIAD task GAUFIT, the authors derived the velocity map of their data. We used the mass model from Section 4.1 to derive the circular velocity profile along the galaxy major axis $v_{\rm mj}$. The central DM contribution was parametrized with a pseudo-isothermal sphere which predicts the following circular velocity for the DM component:

$$V^2_{\rm c,DM}(r) = 4\pi G\rho_0 r_c^2 \left[1 - \frac{r_c}{r}\arctan(\frac{r}{r_c})\right], \tag{2.3}$$

where $\rho_0$ denotes central mass density of the sphere and $r_c$ is the core radius. We added the contribution of the pseudo-isothermal sphere quadratically to the stellar circular velocity. Using the standard projection formula

$$v_{\rm c,stars}(x,y) = v_\phi\left(\frac{x\sin i}{r}\right) = v_{mj}\left(\frac{x}{r}\right), \tag{2.4}$$

with the radius $r^2 = x^2 + (y/\cos i)^2$ and galaxy inclination $i$, it is possible to construct an axisymmetric two-dimensional velocity map model from the velocity profile (Krajnović et al. 2005). The Wong et al. (2004) CO velocity field is sampled on square pixels of 1 arcsec size, while the observations had a beam of $6.53 \times 4.88$ arcsec. We convolved our model velocity field with the circular beam size of 6.53 arcsec using the kernel of Qian et al. (1995). The constructed velocity field is a function of stellar $M/L$, galaxy inclination $i$, central DM density $\rho_0$ and core radius $r_c$. In order to find the velocity field model which best represents the CO data, we tested different parameter grids and finally obtained $M/L = 1.75$, $i = 55°$, $\rho_0 = 0.2$ and $r_c = 20''$. The degeneracy between stellar mass-to-light ratio and dark matter was clearly visible while constructing the different models. The derived value for the $M/L$ is consistent with the other measurements in this chapter. In Figure 2.9, we present the CO data, the best matching two-dimensional velocity field and a cross section of our velocity field model (black line) and the CO data (red dots) along the major axis. Except for the most central point of the CO data, our model reproduces the entire CO data very well. However, this outlier is tightly related to the CO emission hole in the center of NGC 4414. Figure 2.9 also illustrates the stellar and dark matter contribution of the velocity profile separately. We note that, for $r < 10''$, which is probed by the NIFS and GMOS data, the dark matter contribution is small; approximately 10% of the total mass.

We also tested the DM content of NGC 4414 by running another set of dynamical JAM models, this time adding a spherical dark halo component, modeled as generalized Navarro-Frenk-White profile (Navarro et al. 1996) with fixed $r_s = 20$ Kpc, to the galaxy potential. We then calculated a parameter grid of $M_{\rm BH}$, $M/L$, the halo density $\rho_s$ at $r_s$ and the dark halo slope $\gamma$ for $r \ll r_s$. These models showed consistent results with the CO data. Therefore, the no-dark-matter assumption is acceptable for the dynamical models of the central region of NGC 4414. This is consistent with other findings (Vallejo et al. 2003; Cappellari et al. 2013a).

*Stellar $M/L$ Variation:* Our dynamical models assume that the $M/L$ stays constant for different radii. However, stellar population changes can result in different $M/L$. Various observations

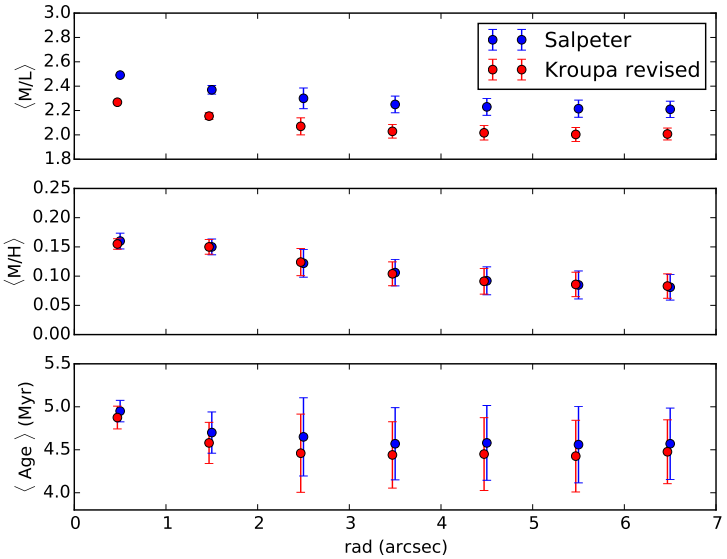


**Figure 2.10 —** Radial trends of the stellar $M/L$, the mass-weighted metallicity and the mass-weighted age of NGC 4414 derived from pPXF. The given radius is the radius of a circular aperture around the galaxy center which defines the spectra used for the respective composite spectrum. We tested the Salpeter IMF (blue) as well as the Kroupa revised IMF (red). For improved clarity, the red points have been shifted very slightly to the left.

**Table 2.3 —** Summary of the derived $M/L$ in NGC 4414

| Method | $M/L$ | Radius ["] |
|---|---|---|
| JAM + NIFS | 1.84 ± 0.04 | 1.5 |
| JAM + GMOS | 2.14 ± 0.04 | 5.5 |
| Schwarzschild | 1.8 ± 0.09 | 5.5 |
| Stellar populations | 2.15 ± 0.03 | 1.5 |
| Stellar populations | 2.0 ± 0.06 | 5.5 |
| CO map + DM | 1.75 ± 0.02 | 40 |

and models suggest that different evolutionary histories in different regions of spiral galaxies lead to variations in the stellar $M/L$ (Bell & de Jong 2001), which can affect the results of the dynamical models (Portinari & Salucci 2010). We tested the $M/L$ variation by applying pPXF to our GMOS data and fitting a linear combination of Simple Stellar Population (SSP) model spectra to the galaxy spectrum.

In order to cover the optical wavelength range of the GMOS spectrum, we used the model spectra from the MILES SSP model library (Vazdekis et al. 2010) which spans an equally spaced $50 \times 7$ grid of age ranging from 0.06 to 17.78 Gyrs and metallicities between [Z/H]= -2.32 and 0.22. As initial mass function (IMF) we assumed the standard Salpeter (1955) IMF and the Kroupa (2001) revised IMF. We used the method described in McDermid et al. (2015); Shetty & Cappellari (2015) to determine the stellar population of NGC 4414, by applying weights to the different SSP model spectra and constrain these with the pPXF built-in regularization option which specifies the penalization of the $\chi^2$. Models with similar ages and metallicities were assigned smoothly varying weights until difference in $\chi^2$ between the current and non-regularized solution satisfied the following criteria $\Delta\chi^2 \approx \sqrt{2N}$, where N is the number of pixels fitted in the spectrum (Press

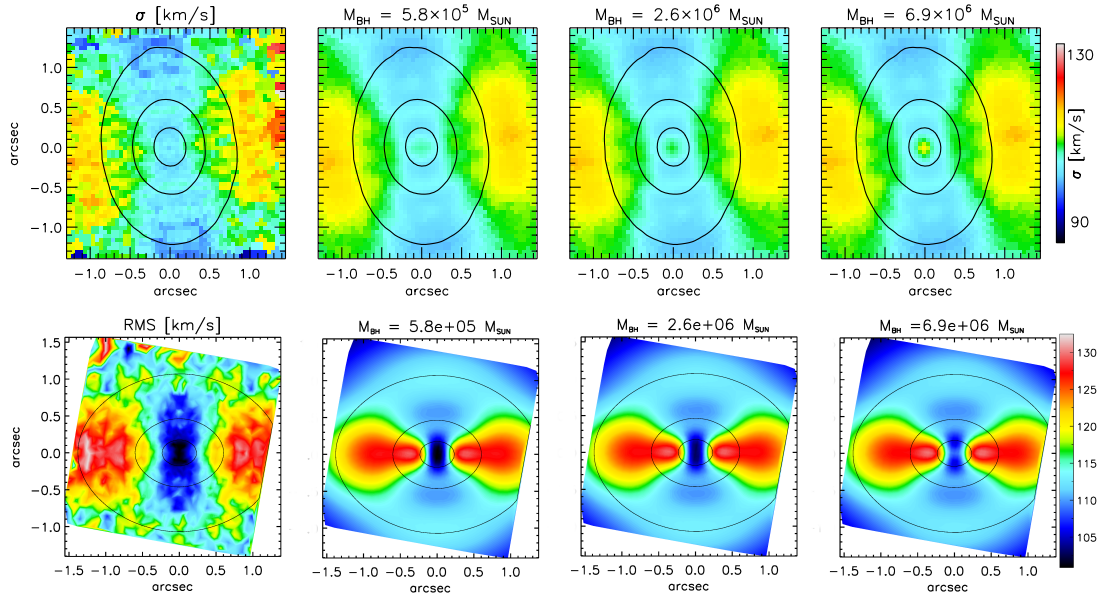


**Figure 2.11 —** Comparison between the observed NIFS velocity dispersion map and three representative Schwarzschild models, all at the same $M/L$=1.80 and with different black hole masses. From left to right: the data, the formal best fit $M_{BH}$ (using LOESS) model, a model with $M_{BH}$ a factor of five higher than the previous one (70% higher than the derived upper limit), and the model with $M_{BH}$ for which the sphere of influence is the same as our spatial resolution. The $M_{BH}$ values are given above the maps. Note the appearance of the central velocity dispersion peak for models above the formal upper limit. The same comparison is given for the JAM $V_{rms}$ models in the lower panels.

2007).

We analyzed the stellar populations using two different approaches. In the first approach, we fitted the SSP models to the composite spectrum of the entire GMOS cube from which we determined the mass-weighted age of NGC 4414 to be approximately 4.5 Gyrs and the mass-weighted metallicity of $\langle[M/H]\rangle = 0.0975$ for Salpeter as well as 4.5 Gyrs and $\langle[M/H]\rangle = 0.0812$ for Kroupa. The derived stellar population provides the mass-weighted $M/L$, calculated as

$$(M/L) = \frac{\sum_j w_j M_{*,j}}{\sum_j w_j L_{r,j}} \quad , \tag{2.5}$$

where $w_j$ denotes the weight given by the pPXF fit to the $j$th template, $M_{*,j}$ is the mass of the $j$th template given in stars and stellar remnants, and $L_{r,j}$ is the r-band (AB) luminosity of the template. We determined a $M/L = 2.1$ from the stellar population. In our second approach we were interested in the strength of the $M/L$ gradient for NGC 4414. Therefore, we co-added the spectra in circular apertures of different radii and applied pPXF to these composite spectra. Figure 2.10 shows the radial trends for the derived stellar $M/L$, the mass-weighted metallicity and the mass-weighted age for the two different assumed IMFs.The difference in IMF solely introduces an offset between the results. Clear evidence for a gradient in $M/L$ is visible in Fig. 2.10, however, the stellar $M/L$ only changes by 10% between 0.5 arcsec and 6.5 arcsec. The uncertainty in the black hole mass due to the stellar $M/L$ variation also yields approximately 10%. Therefore, we conclude that within the level of precision achievable with our dynamical modeling methods, $M/L$=const. is an adequate assumption. By keeping the dynamical $M/L$ constant, we are also able to account for the small amount of dark matter found in the center of the galaxy (McConnell et al. 2013).

Table 2.10 gives an overview of the $M/L$ measurements of NGC 4414 which we determined with very different methods. The measurements show great consistency with each other. However, the stellar $M/L$ values derived from the stellar populations show noticeably higher trends than the dynamical $M/L$. The dynamical $M/L$ measurements are strongly dependent on the distance accuracy of NGC 4414. As noted above, this distance uncertainty increases the measured dynamical $M/L$ uncertainty by 10%. Thus, assuming a distance of 16 Mpc instead would increase the Schwarzschild $M/L$ to 2.0 ± 0.1 which is more consistent with the stellar $M/L$. Therefore, we conclude that the different $M/L$ ratios result from uncertainties in the different methods.

*Kinematic Tracer:* In order to construct dynamical models, we would ideally use a luminosity density which was observed in a similar band to the kinematical tracer. Using a luminosity density in the r-band while probing the central kinematics in the K-band could lead to tracking different stellar populations. Therefore, we tested the compatibility between the r-band and K-band surface brightness of NGC 4414. Figure A.4 provides initial evidence of how well the the HST data matches the NIFS K-band image. After convolution with the NIFS PSF, the HST data fits the center of the collapsed NIFS data very well and discrepancies arise at the edges of the NIFS data where dust begins to emerge. In a second attempt to compare both tracers, we constructed a MGE model from the combination of the reconstructed NIFS image, the WFPC2 F606W image and the SDSS r-band image. We used the reconstructed NIFS image to probe the central 1.2 arcsec of NGC 4414, HST between 1.2 arcsec $< r <$ 5 arcsec and SDSS for the remaining extent of the galaxy. We then constructed dynamical Jeans models from this new MGE in combination with NIFS kinematics. From this test, we determined the best-fitting model parameters to be $M_{\rm BH} = 0 M_{\odot}$ and $M/L = 1.79$. Within $3\sigma$ statistical uncertainty the $\chi^2$criterion provides an upper limit of $2.4 \times 10^5 M_{\odot}$, which is consistent with our r-band image-only MGE model results. Therefore, inaccuracies in the tracer distribution do not affect our final results.

## 5.2 Bridging the resolution limit

The case of NGC 4414 provides important conclusions relating to the resolution limit of black hole measurements. In this study, we are able to constrain the black hole upper mass limit of NGC 4414 to a significantly lower value than the resolution limit given by our high-resolution NIFS data.

The vertical lines in Fig. 2.7 show expected values for the $M_{\rm BH}$ in NGC 4414, based on the predictions from recent $M_{\rm BH} - \sigma_{\rm e}$ scaling relations (McConnell & Ma 2013; Saglia et al. 2016; Greene et al. 2016) and the $M_{BH}$-size-mass relation proposed by van den Bosch (2016). The closest to the derived upper limit is the $M_{BH}$-size-mass relation by van den Bosch (2016), which predicts $M_{\rm BH} = 3.66 \times 10^6\ M_{\odot}$ based on the galaxy effective radius (Davis et al. 2012) and the total galaxy mass (which we obtained from JAM) . This prediction is followed by the McConnell & Ma (2013) relation for all galaxy types, which, assuming the velocity dispersion of NGC 4414 within the effective radius, predicts $M_{\rm BH} = 9.4{\times}10^6\ M_{\odot}$, approximately five times larger than our formal upper limit. A similar mass is obtained if one looks for the lower $M_{\rm BH}$ limit that we should have been able to detect, assuming that the black hole sphere of influence is three times smaller than the resolution of NIFS data (0.13 arcsec). Krajnović et al. (2009) showed that it is not necessary to resolve the sphere of influence to estimate $M_{\rm BH}$ if one has IFU data covering approximately one effective radius of the galaxy as well as the high resolution adaptive optics assisted IFU observations of the nucleus. With such data it is feasible to estimate $M_{\rm BH}$ for black holes when the sphere of influence is up to three times that of the spatial resolution of the data (see also Cappellari et al. 2010). For our observations of NGC 4414, this lower $M_{\rm BH}$ limit is $7.5 \times 10^6 M_{\odot}$. Given these limits, the quality of the data presented here, and predictions from

the latest estimates of the scaling relations for late-type galaxies (e.g., $9.8 \times 10^6$ $M_\odot$; Greene et al. 2016, late-type) or low mass galaxies, we would have been able to measure $M_{\rm BH}$, if it were as predicted by the $M_{\rm BH} - \sigma_e$ relation. However, the upper limit obtained from Schwarzschild models is still several factors smaller than the expected $M_{\rm BH}$, which suggests that the NGC 4414 has an under-massive central black hole, if any at all.

Furthermore, Fig 2.11 shows that the models start significantly departing (such that it is visually easy to see the differences) from the observed data for $M_{\rm BH}$ a few times larger than the formal upper limit. The velocity dispersion map of the highest mass black hole in this figure is obviously very different from the observed velocity dispersion. The central peak is completely absent in the data. This peak decreases with smaller $M_{\rm BH}$, and is not visible for the models within the $3\sigma$ confidence level. The kinematically cold nuclear structure essentially limits the mass of the central black hole to a few times $10^6$ $M_\odot$, a factor of ten smaller than expected from the latest scaling relations (e.g., Saglia et al. 2016; Greene et al. 2016). The same results can be recovered from less general JAM models as well (constrained using only the high resolution data).

Crucially, this suggests that when one uses high quality IFU data, the predicted sphere of influence should be taken only as a very rough guide for the possible $M_{\rm BH}$ one could measure. In the case of NGC 4414, the sphere of influence for the black hole of $10^6$ $M_\odot$ is approximately 0.004 arcsec, while the resolution of the NIFS data is approximately 0.1 arcsec, a factor of 25 lower. Nevertheless, in this case, the models are able to rule out $M_{\rm BH} \geq 2 \times 10^6$ $M_\odot$, as visually confirmed on Fig. 2.11.

The measured upper limit for the black hole mass is approximately five times lower than the black hole we would formally be able to measure based on the sphere of influence criterion only. Constraining dynamical models with high quality IFU data and imaging (high-resolution and having a large field-of-view in both cases), can therefore bring down the measurement of black holes for at least this factor compared to the prediction based on the formal resolution limit and the sphere of influence argument. This implies that not being able to resolve the sphere of influence is not a hard limit which prohibits the detection of the corresponding massive black hole in future observations. The sphere of influence should be taken only as a rough indicator for black hole mass measurements. High Strehl ratio IFU data (covering a large area of the galaxy) can be, however, trusted to provide constraints for SMBHs several factors lower than predicted by the simple sphere of influence argument.

## 5.3 Black hole - host galaxy scaling relations

The $M_{\rm BH} - \sigma_{\rm e}$ relation (Ferrarese & Merritt 2000; Gebhardt et al. 2000; Tremaine et al. 2002) can be described by a single power law over a wide range in effective stellar velocity dispersion (Graham et al. 2011; McConnell & Ma 2013; Kormendy & Ho 2013). Its effective stellar velocity dispersion of $\sigma_{\rm e} = 115.5 \pm 3$ km/s (Sect. 3.6) indicates that NGC 4414 contributes to the low-mass end of the $M_{\rm BH} - \sigma_{\rm e}$ correlation, which is poorly populated. Figure 2.12 shows a reconstruction of the most recent version of the $M_{\rm BH} - \sigma_{\rm e}$ relation (McConnell & Ma 2013; Saglia et al. 2016; Greene et al. 2016) for spirals and all galaxies. We created the diagram with the SMBH sample from the compilation of Saglia et al. (2016) and added a number of spiral galaxies and previous outlier upper-limit measurements (Verdoes Kleijn et al. 2002; Greene et al. 2010; Coccato et al. 2006; De Lorenzi et al. 2013; den Brok et al. 2015; Walsh et al. 2015, 2016; Greene et al. 2016; Thomas et al. 2016; Bentz et al. 2016). The location of NGC 4414 in the $M_{\rm BH} - \sigma_{\rm e}$ relation is indicated by a red star. It is clearly visible that our $M_{\rm BH}$ measurement lies below the shown scaling relations, but is possibly located within the region of late-type galaxies. Comparing our upper limit result with the SMBH masses derived from the scaling relations, we find a deviation of $1\sigma$ for Saglia et al. (2016), $1.5\sigma$ for McConnell & Ma (2013) and $2.5\,\sigma$ for

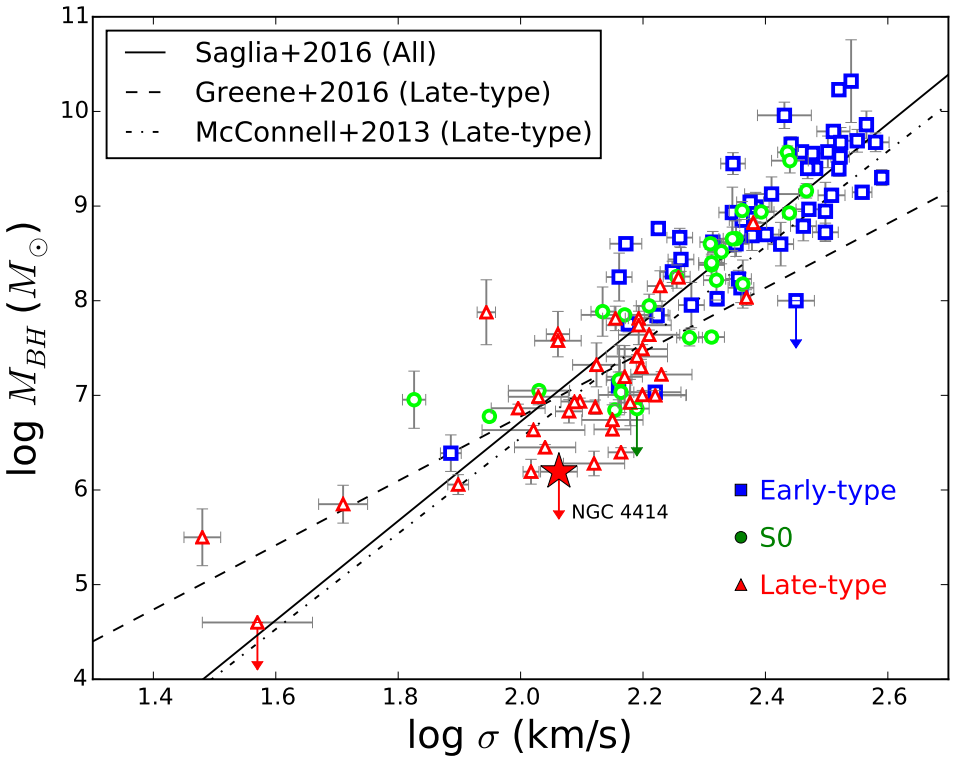


**Figure 2.12 —** Location of the upper limit mass measurement of NGC 4414 in the $M_{\rm BH} - \sigma_{\rm e}$ relation. The data points were taken from the BH compilation of Saglia et al. (2016) in addition to measurements by Verdoes Kleijn et al. (2002); Greene et al. (2010); Coccato et al. (2006); De Lorenzi et al. (2013); den Brok et al. (2015); Walsh et al. (2015, 2016); Greene et al. (2016); Thomas et al. (2016); Bentz et al. (2016) and divided into early-type galaxies (blue), S0 type (green) and late-type galaxies (red). Our upper-limit measurement is indicated by a red star. We have also added the scaling relations by Saglia et al. (2016) for all types of galaxies (solid) and Greene et al. (2016); McConnell & Ma (2013) for late-type galaxies (dashed,dashed-dotted).

Greene et al. (2016) whereas Greene et al. (2016) assumes much smaller errors. Therefore, NGC 4414 could be located in the region spanned by the scatter of the relations, if not even lower. This scatter is generally very wide in the $\sigma_{\rm e}$ scaling relations, both in the low and also the upper end. NGC 4414 is not the only galaxy, which shows a significant divergence from the black hole scaling relations. Many outliers can be found in the upper-mass end of the relations, but a number of galaxies have also been found for which the dynamical models predict an upper limit to the black hole mass, putting them below the $M_{\rm BH} - \sigma_{\rm e}$ scaling relation (Sarzi et al. 2001; Merritt et al. 2001; Gebhardt et al. 2001; Valluri et al. 2005; Coccato et al. 2006). Below the scaling relation there are three upper limits of which only NGC 4414 is obtained from stellar kinematics. Vittorini et al. (2005) suggest these objects could likely be 'laggard' galaxies (e.g., Vittorini et al. 2005; Coccato et al. 2006) that could not yet completely develop their massive black holes. These galaxies have spent most of their lifetime isolated in 'the field', where encounters are so rare that gas fueling of the galactic center is slowed down causing a limited growth of the black hole mass.

NGC 4414 seems to continue the trend seen in the late-type galaxies of Greene et al. (2016) and more work in this $\sigma$ range is necessary to better constrain the slope of the black hole scaling relations.

## 6 Conclusions

We obtained high-resolution NGS adaptive optics-assisted Gemini NIFS and large-scale Gemini GMOS IFU observations of the spiral galaxy NGC 4414 to map its kinematics which trace the gravitational potential of the central SMBH. The stellar kinematic maps reveal a regular rotation with a maximum of ±90 km/s and an elongated central velocity dispersion drop decreasing down to 105 km/s. We combined the kinematics data with a luminous mass model from dust-corrected HST WFPC2 F606W and SDSS r-band images and constructed dynamical JAM and Schwarzschild models from the light model and the kinematic information. The dynamical models cannot constrain the lower mass of the central mass hole and only predict an upper limit mass. The JAM models provide $M_{\rm BH} < 1.5 \times 10^5 M_\odot$ and a $M/L$= 1.84 ± 0.04 , while the more sophisticated orbit-based Schwarzschild models state $M_{\rm BH} < 1.56 \times 10^6 M_\odot$ and a $M/L$= 1.8 ± 0.09 at $3\sigma$ significance. This upper limit measurement is $1\sigma$ below the Saglia et al. (2016) and $2.5\,\sigma$ below the Greene et al. (2016) $M_{\rm BH} - \sigma_{\rm e}$ relation assuming $\sigma_{\rm e}$ = 115.5 ± 3 km/s. In order to analyze the robustness of the measurements, we tested how various systematic uncertainties, such as dark matter content, dust attenuation, $M/L$ variation, distance uncertainty and kinematic tracer variation, influence the results. Taking the different uncertainties into account, we remain in the black hole uncertainty given by the $3\,\sigma$ significance of the $\chi^2$ criteria. We are able to accurately constrain the black hole upper limit to approximately five times less than the black hole mass predicted by the resolution of our instruments. This result shows that AO-supported IFU data permits us to look for black holes with masses significantly below the resolution limit. This is especially important in the low-mass black hole regime, which is still largely underpopulated in the black hole-host galaxy relations. While our measurement of NGC 4414 provides a new measurement in this undersampled black hole domain, additional black hole mass measurements are needed in order to find a consensus on what happens in the low-mass end of the scaling relations.

# 7 Dust-corrected images

Before deriving the MGE model from the SDSS image, we corrected it for the effects of dust absorption based on the method described in Cappellari et al. (2002) and Scott et al. (2013a). The degree of the correction is shown in Figure 2.13. We also applied a dust-mask to the HST image, which is shown in Figure 2.14. Details of the dust-correction and dust masking are described in Section 1.1 of the Appendix.

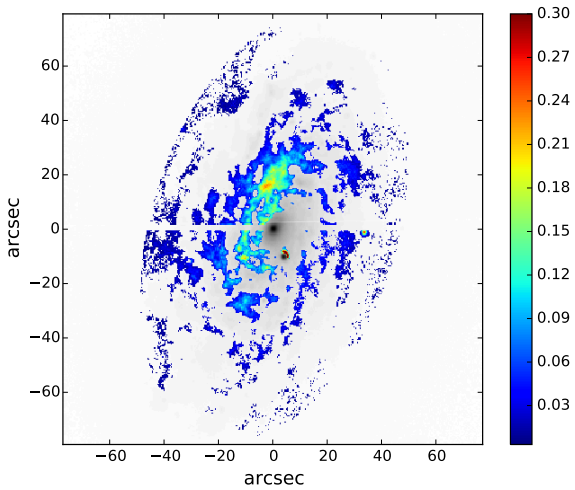


**Figure 2.13 —** Dust-corrected central region of the observed SDSS r-band image. The correction was only applied within a major axis radius of 80″ (see caption of Fig. A.1). The over-plotted color coding indicates the degree of the correction where 0.1 means that the observed flux increased by 10 %. The lines in the center of the image are edge artifacts from assembling the single SDSS images to a large FoV montage.

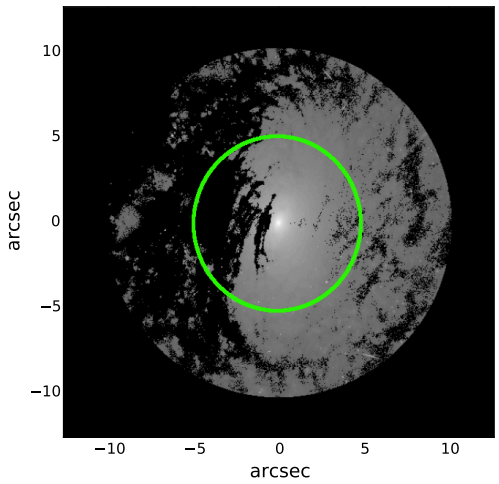


**Figure 2.14 —** Dust masked region of the HST/F606W image. The black parts of the image are the regions which were masked to account for dust attenuation. The green circle marks the region which was used in the MGE modeling ($r < 5''$).

## 8 Comparison of Schwarzschild models and velocity moments for NIFS and GMOS

Dynamical models do not constrain the lower mass limit for a SMBH in NGC 4414, with the formal best fit model being at the edge of our grid in $M_{\rm BH}$. Therefore we present here a representative model close to the upper mass limit given by the $3\sigma$ uncertainty level. The model reproduces most of the kinematics features both on NIFS and GMOS data. For the NIFS data, the major difference is an over prediction of the central velocity dispersion and under prediction of $h_4$ Gauss-Hermite coefficient at approximately two and one sigma level. For GMOS data the models reproduce the kinematics maps to a similarly good standard with the exception of the central regions on the velocity dispersion and the $h_4$ maps. Note that the central one arcsec was not fitted for the GMOS data, which partially explains the over-prediction of the velocity dispersion and the under-prediction of $h_4$ at approximately the two sigma level.

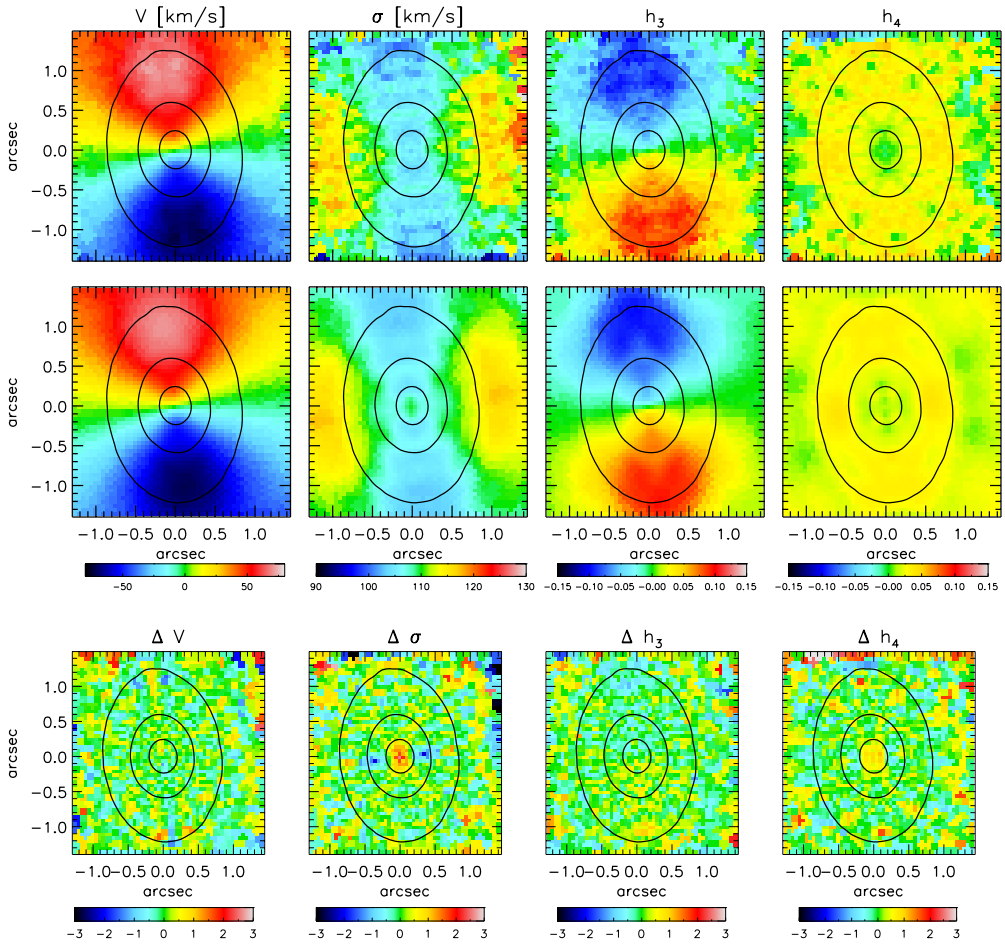


**Figure 2.15 —** Top row: Symmetrized NIFS maps showing (from left to right) the mean velocity, the velocity dispersion and $h_3$ and $h_4$ Gauss-Hermite moments. Middle row: Schwarzschild dynamical models for $M/L = 1.80$ and $M_{\rm BH} = 5.81 \times 10^5\ M_\odot$. The maps show the same quantities as in the row above. Bottom row: the difference between the Schwarzschild model predicted and the observed kinematics, divided by the observational errors.

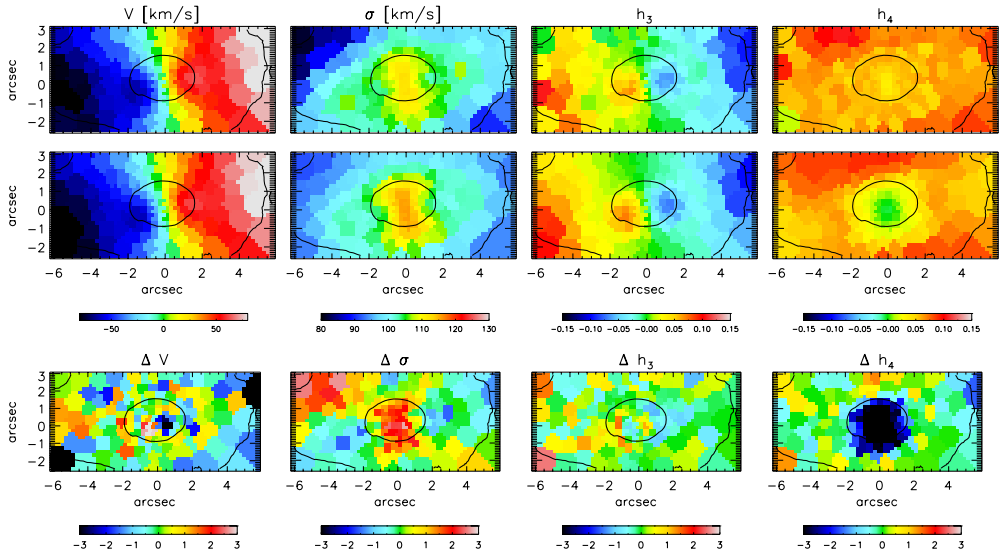


**Figure 2.16 —** As in Fig. 2.15 but for GMOS data.

# 3 Six new supermassive black hole mass determinations from adaptive-optics assisted SINFONI observations

**Sabine Thater, Davor Krajnović, Michele Cappellari, Timothy A. Davis, Tim de Zeeuw, Richard M. McDermid, Marc Sarzi**

— A version of this chapter is published as S. Thater et al., 2019, A&A, 625, A62 —

Abstract

Different massive black hole mass - host galaxy scaling relations suggest that the growth of massive black holes is entangled with the evolution of their host galaxies. The number of measured black hole masses is still limited and additional measurements are necessary to understand the underlying physics of this apparent coevolution. We add six new black hole mass ($M_{\rm BH}$) measurements of nearby fast rotating early-type galaxies to the known black hole mass sample, namely NGC 584, NGC 2784, NGC 3640, NGC 4570, NGC 4281, and NGC 7049. Our target galaxies have effective velocity dispersions ($\sigma_{\rm e}$) between 170 and 245 km s$^{-1}$, and thus this work provides additional insight into the black hole properties of intermediate-mass early-type galaxies. We combined high-resolution adaptive-optics SINFONI data with large-scale MUSE, VIMOS and SAURON data from ATLAS$^{\rm 3D}$ to derive two-dimensional stellar kinematics maps. We then built both Jeans Anisotropic Models and axisymmetric Schwarzschild models to measure the central black hole masses. Our Schwarzschild models provide black hole masses of $(1.3 \pm 0.5) \times 10^8$ $M_\odot$ for NGC 584, $(1.0 \pm 0.6) \times 10^8$ $M_\odot$ for NGC 2784, $(7.7 \pm 5) \times 10^7$ $M_\odot$ for NGC 3640, $(5.4 \pm 0.8) \times 10^8$ $M_\odot$ for NGC 4281, $(6.8 \pm 2.0) \times 10^7$ $M_\odot$ for NGC 4570, and $(3.2 \pm 0.8) \times 10^8$ $M_\odot$ for NGC 7049 at $3\sigma$ confidence level, which are consistent with recent $M_{\rm BH}$ - $\sigma_{\rm e}$ scaling relations. NGC 3640 has a velocity dispersion dip and NGC 7049 a constant velocity dispersion in the center, but we can clearly constrain their lower black hole mass limit. We conclude our analysis with a test on NGC 4570 taking into account a variable mass-to-light ratio ($M/L$) when constructing dynamical models. When considering $M/L$ variations linked mostly to radial changes in the stellar metallicity, we find that the dynamically determined black hole mass from NGC 4570 decreases by 30%. Further investigations are needed in the future to account for the impact of radial $M/L$ gradients on dynamical modeling.

# 1 Introduction

Most massive galaxies harbor a supermassive black hole (SMBH) in their centers. While black holes are invisible by their nature, their mass can be estimated using the motion of dynamical tracers (i.e., stars or gas) in combination with sophisticated dynamical models. The literature contains more than 100 robust dynamical black hole mass determinations, slowly growing into a statistically significant sample. Relating these measured black hole masses ($M_{\rm BH}$) to different host galaxy properties, such as bulge stellar mass, bulge velocity dispersion $\sigma_e$, Sérsic index n, and star formation, revealed several noticeably tight correlations, for example, $M_{\rm BH} - L$ (Kormendy & Richstone 1995; Magorrian et al. 1998), $M_{\rm BH} - \sigma_e$ (Ferrarese & Merritt 2000; Gebhardt et al. 2000), and $M_{\rm BH}$−n (Graham et al. 2001). Connecting vastly different scales these relations raise the question whether the growth of the black hole and the evolution of the host galaxy are entangled with each other (see recent reviews by Kormendy & Ho 2013 and Graham 2016). Current explanations suggest that black holes grow via two main processes: self-regulation by accretion of gas onto the black hole, facilitated by galaxy merging or accretion of gas (Silk & Rees 1998; Fabian 1999; Di Matteo et al. 2008; Volonteri 2010) and by mergers of black holes, following dry major mergers. Kulier et al. (2015) and Yoo et al. (2007) showed that accretion is the main channel of black hole growth, but galaxy mergers become relevant for more massive galaxies (see also Graham 2012, Graham & Scott 2013, and Krajnović et al. 2018a). Based on the scaling relations we can see a clear trend that the more massive the galaxy is, the more massive its central black hole seems to be. The exact shape of the various scaling relations is however still under debate. While early studies suggested a single power law (Kormendy & Ho 2013), it is nowadays debated whether the fundamental relation between black hole and host galaxy properties scales as a double power law (Graham & Scott 2013) or has to be described by a three-parameter plane (van den Bosch 2016; Saglia et al. 2016). Moreover, Krajnović et al. (2018a) and Mezcua et al. (2018) recently reported an up-bending of the scaling relations with higher galaxy mass questioning the existence of one universal scaling relation. The search for a fundamental relation is made even more difficult by an increased internal scatter in both the low- and high-mass regime of the scaling relations. In order to understand and reduce the increased scatter, different observational strategies need to be developed. It is important to understand the different measurement methods with their associated systematic uncertainties by obtaining multiple $M_{\rm BH}$ measurements with different methods for individual galaxies as was done, for example, in Walsh et al. (2010), Barth et al. (2016), Davis et al. (2017b), Davis et al. (2018b), and Krajnović et al. (2018b). On the other hand, it is also important to figure out the intrinsic scatter due to different galaxy formation scenarios by obtaining more and more homogeneous measurements over the complete SMBH mass range to strengthen current theories and ideas.

Our SMASHING sample (see Section 2 for details) was created to exploit the capabilities of natural guide star (NGS) and laser guide star (LGS) adaptive optics (AO) systems at 8m ground-based telescopes. Its purpose is to fill up the scaling relations with additional $M_{\rm BH}$ measurements of early-type galaxies. By the time of the creation of the project in 2009, the $M_{\rm BH}$ measurements were almost exclusively populated by Hubble Space Telescope (HST) measurements with the exception of Nowak et al. (2008) and Krajnović et al. (2009) who pioneered a new method to measure $M_{\rm BH}$ using ground-based spectroscopy in combination with AO systems, LGS and NGS, respectively. The SMASHING survey was planned to expand the AO method to a wide range of early-type galaxies with different velocity dispersions, from the low ($\approx 100$ km s$^{-1}$) to the high ($\approx 300$ km s$^{-1}$) end. The first results, based on observations with the Gemini-North's Near-Infrared Integral Field Spectrometer (NIFS) and the Gemini Multi-Object Spectrograph (GMOS), were published in Chapter 2 and Krajnović et al. (2018b). Unlike many other $M_{\rm BH}$

measurements in the literature, we used both small (high spatial resolution) and large-field integral field spectroscopic (IFU) data for our measurements. High-resolution kinematics are crucial to probe the orbital structure in the vicinity of the SMBH and outside of its sphere of influence (SoI) as well; large-scale kinematics are needed to constrain the global dynamical mass-to-light ratio ($M/L$) and to trace the influence of the stars on radial orbits. These orbits pass close to the SMBH, but spend most of the time at large radii. Including both data sets provides more robust $M_{\rm BH}$ measurements, especially if the SoI is hardly resolved.

This paper is the first of a series of papers based on observations with the INtegral Field Observations in the Near Infrared spectrograph (SINFONI). We present AO-assisted, near-infrared IFU data for six fast-rotating axisymmetric early-type galaxies to study the stellar kinematics in the vicinity of their central black hole. We begin by introducing the sample and its selection in Section 2, followed by the data acquisition and reduction in Section 3. In Section 4, we describe the extraction of the stellar kinematics from the near-infrared SINFONI and optical Multi Unit Spectroscopic Explorer (MUSE) and VIsible Multi Object Spectrograph (VIMOS) IFU data. In addition to the kinematics, we combine high-resolution HST and Sloan Digital Sky Survey (SDSS) data to model the stellar surface brightness and thus examine the stellar brightness density of our target galaxies. In Section 5, we present the dynamical models that were constructed using two different and independent methods: Jeans Anisotropic Modeling (Cappellari 2008) and Schwarzschild (1979) orbit superposition modeling. We analyze our assumptions for the dynamical modeling with particular attention to $M/L$ variations and discuss our results in the context of the $\mathrm{M_{BH}} - \sigma_{\rm e}$ relation in Section 6, and finally, conclude in Section 7.

**Table 3.1 —** Sample

| Galaxy | Type | Distance (Mpc) | Linear scale (pc arcsec$^{-1}$) | $M_K$ (mag) | $r_e$ (arcsec) | $\sigma_e$ (km s$^{-1}$) | $\sigma_0$ (km s$^{-1}$) | $\log(M_{bulge})$ $\log(M_\odot)$ | $i$ (°) | Large Scale |
|---|---|---|---|---|---|---|---|---|---|---|
| (1) | (2) | (3) | (4) | (5) | (6) | (7) | (8) | (9) | (10) | (11) |
| NGC 584 | S0 | 19.1 ± 1.0 | 93 | −24.19 | 33.0 | 189 ± 5 | 216 | 10.48 | 51 | MUSE |
| NGC 2784 | S0 | 9.6 ± 1.8 | 47 | −23.31 | 40.2 | 188 ± 8 | 243 | 10.44 | 66 | VIMOS |
| NGC 3640 | E3 | 26.3 ± 1.7 | 128 | −24.60 | 38.5 | 176 ± 8 | 173 | 11.00 | 68 | SAURON |
| NGC 4281 | S0 | 24.4 ± 2.2 | 118 | −24.01 | 24.5 | 227 ± 11 | 314 | 10.88 | 71 | SAURON |
| NGC 4570 | S0 | 17.1 ± 1.3 | 83 | −23.48 | 17.9 | 170 ± 8 | 209 | 10.18 | 88 | SAURON |
| NGC 7049 | S0 | 29.9 ± 2.6 | 145 | −25.00 | 35.4 | 245 ± 8 | 266 | 11.02 | 42 | VIMOS |

**Notes** – Column 1: Galaxy name. Column 2: Morphological type (de Vaucouleurs et al. 1991). NGC 584 had been misclassified in the earlier work and we adopt the classification by Huang et al. (2013) in this work. Column 3: Distance to the galaxy (taken from Cappellari et al. (2011) for SAURON/ATLAS$^{3D}$ galaxies or NED for VIMOS and MUSE galaxies); the uncertainties were calculated by dividing the NED standard deviations by $\sqrt{N}$, where N is the number of measurements. Column 4: Linear scale derived from the distance. Column 5: 2MASS total K-band magnitude (Jarrett et al. 2000). Column 6: Effective radius derived from B-band (CGS) or r-band (ATLAS$^{3D}$) imaging data. The values were taken from Ho et al. (2011) or Cappellari et al. (2013a) for ATLAS$^{3D}$ galaxies. Column 7: Effective velocity dispersion derived by co-adding the spectra of the large-scale optical IFU data in elliptical annuli of the size of the effective radius. For ATLAS$^{3D}$ galaxies taken from Cappellari et al. (2013a). Column 8: Central velocity dispersion derived by co-adding the spectra of the high-spatial-resolution SINFONI IFU data in elliptical annuli within one arcsec. Column 9: Bulge mass calculated by multiplying the bulge-to-total ratios from Krajnović et al. (2013) for ATLAS$^{3D}$ galaxies or Gao et al. (2018) for the remaining galaxies with the total dynamical mass from Cappellari et al. (2013a) or this paper. Column 10: Inclination from Cappellari et al. (2013a) for ATLAS$^{3D}$ galaxies and Ho et al. (2011) for remaining galaxies. For NGC 584 from Laurikainen et al. (2010). Column 11: Large-scale kinematics data that is used for the Schwarzschild dynamical models. The SAURON data comes from the ATLAS$^{3D}$ galaxy survey.

## 2 Sample

The six galaxies analyzed in this paper belong to our SMASHING galaxy sample to dynamically determine black hole masses in the nearby universe. Three of our target galaxies were selected from the ATLAS$^{3D}$ volume-limited galaxy sample (Cappellari et al. 2011), from which one galaxy had already been observed in the SAURON project (de Zeeuw et al. 2002). The three remaining galaxies were observed with the VIMOS or MUSE instruments. Additional high spatial resolution data was obtained with the near-infrared SINFONI instrument to probe the direct vicinity of the SMBH. Based on their velocity dispersion, the sample galaxies are expected to be located in the intermediate $M_{\rm BH}$ range. The main properties of our six sample galaxies are summarized in Table 4.1.

Our target galaxies were selected based on a number of requirements for a successful $M_{\rm BH}$ determination. An important criterion for a robust black hole mass determination is the need to resolve the SoI of the black hole within which the SMBH dominates the galaxy potential. The SoI depends on the mass of the black hole $M_{\rm BH}$ and the velocity dispersion of the galaxy within an effective radius $\sigma_{\rm e}$ and is defined as $r_{\rm SoI} = G\,M_{\rm BH}/\sigma_{\rm e}^2$, where $G$ is the gravitational constant. We calculated an estimated value for $r_{\rm SoI}$ using black hole masses based on the $M_{\rm BH} - \sigma_{\rm e}$ relation from Tremaine et al. (2002)[1] and the ATLAS$^{3D}$ velocity dispersions from Cappellari et al. (2013b). Using the large set of information from both large-scale and high-resolution IFUs, we can probe SoIs that are two to three times lower than the spatial resolution (Krajnović et al. 2009, see also Chapter 2). With the goal of gaining the best possible resolution, we used the AO mode from the SINFONI instrument if possible using a NGS or a LGS to correct for unstable seeing conditions.

Furthermore, archival HST imaging was needed for the galaxies of our sample to build detailed light models of the centers of the galaxys. We also ensured that the selected galaxies would not include any obvious bars or merger features indicating a non-relaxed galactic potential, which would make the galaxies unsuitable for dynamical modeling with static potential models, as used in this work.

## 3 Observations

The mass measurement of massive black holes requires a large variety of data sets. Both high spatial resolution kinematic information of the central galaxy region to constrain the wide range of different stellar orbit families and large-scale IFU data to constrain the global galaxy characteristics are essential for a precise measurement. The IFU data is complemented by imaging data from HST and ground-based telescopes to construct a detailed mass model of the host galaxy. In the following section, we present different observations from the IFUs toward the imaging data.

[1]The data acquisition process for this project started in 2008. At that time Tremaine et al. (2002) was one of the best representations of the black hole - host galaxy scaling relations. Tremaine et al. (2002) is very similar to the scaling relations that we show in Fig. 10. The selection based on the scaling relation by Tremaine et al. (2002) was only to select galaxies that were most likely to provide robust $M_{\rm BH}$ estimates. However, the required observing time and obtaining useful data in the near-infrared with LGS AO trimmed the sample more significantly than any scaling relation.

**Table 3.2 —** Details of the SINFONI observing runs

| Galaxy | Date | PID | Pixel scale (mas) | N of exp. | N comb. exp. | $T_{exp}$ (h) | AO mode |
|---|---|---|---|---|---|---|---|
| (1) | (2) | (3) | (4) | (5) | (6) | (7) | (8) |
| NGC 584 | 2007 Jul 23,24 | 079.B-0402(A) | 100 | 3 | 3 | 0.75 | NGS |
| NGC 2784 | 2007 Dec 12,29, 2008 Jan 01,02 | 080.B-0015(A) | 100 | 9 | 9 | 4.5 | NGS |
| NGC 3640 | 2010 Apr 08,09 | 085.B-0221(A) | 100 | 13 | 12 | 3.16 | LGS |
| | 2013 May 08,09, May 09 | 085.B-0221(A) | 100 | 8 | 7 | 3.16 | LGS |
| | 2013 Dec 27, 2014 Jan 07,24 | 291.B-5019(A) | 100 | 14 | 12 | 3.16 | LGS |
| NGC 4281 | 2010 Sep 04 | 085.B-0221(A) | 100 | 4 | 3 | 2.25 | LGS |
| | 2012 Mar 20 | 085.B-0221(A) | 100 | 4 | 4 | 2.25 | LGS |
| | 2013 May 09,11 | 091.B-0129(A) | 100 | 19 | 16 | 2.25 | LGS |
| NGC 4570 | 2013 May 07 | 091.B-0129(A) | 100 | 16 | 15 | 2 | LGS |
| NGC 7049 | 2005 Jun 08,09,10,14,19 | 075.B-0495(A) | 100 | 20 | 16 | 6.25 | NGS |
| | 2005 Jun 27, Jul 02,03,07 | 075.B-0495(A) | 100 | 12 | 9 | 6.25 | NGS |

**Notes.** Column 1: Galaxy name. Column 2: Dates of the observations. Column 3: Identification number of the Proposal. Column 4: Spatial pixel scaling of the observation. Column 5: Number of available single exposure frames. Column 6: Number of single exposure frames in the combined data cube. Column 7: Combined exposure time in hours. Column 8: AO mode applied for the data, either using a NGS or a LGS.

## 3.1 SINFONI IFU data

The near-infrared portion of our IFU data was obtained between 2005 and 2013 with the SINFONI instrument mounted on UT4 (Yepun) of the Very Large Telescope (VLT) at Cerro Paranal, Chile. The SINFONI instrument consists of the Spectrometer for Infrared Faint Field Imaging (SPIFFI) assisted by the AO module, Multi-Application Curvature Adaptive Optics (MACAO) (Eisenhauer et al. 2003; Bonnet et al. 2004). We observed each galaxy at K-band grating (1.94 - 2.45 $\mu$m) providing a spectral resolution of $R \sim 4000$ and a pixel scaling of 100 mas leading to a total field of view (FoV) on the sky of about $3.2 \times 3.2''$ per pointing. Details of the observing runs for each galaxy are provided in Table 4.2. For each of our observations, we made use of the AO mode, either using a NGS or an artificial sodium LGS to correct for the ground-layer turbulence and achieve the highest spatial resolution possible. In the ideal case, the LGS mode still requires a NGS to correct for the tip-tilt disturbances in the wavefront, which are not sensed by the LGS. However, we often did not have a suitable tip-tilt star close to the galaxy and tip-tilt on the nucleus was not always possible, such that we applied the SINFONI Seeing Enhancer mode, which provided a slight improvement to the natural seeing. Our observations show typical Strehl ratios of about 10 % (see Table 4.3). The observations were performed using the object-sky-object nodding scheme. At the beginning and end of each observing block, the respective standard star was observed at a similar airmass and with the same optical setup to correct for the telluric features at similar atmospheric and instrumental conditions. We used the SINFONI reduction pipeline to reduce the data and reconstruct the data cubes of the individual observations. This science frame contains spatial information in the X and Y directions and spectral information in the Z direction. As the data reduction was extensive, we mention a number of steps individually in the next subsections.

### Data reduction and sky correction

The data reduction mostly followed the steps that are described in the SINFONI instrument handbook. The observations were reduced using the ESO SINFONI pipeline (version 2.4.8, Modigliani et al. 2007) in combination with additional external corrections to optimize the resulting data cubes. The ESO pipeline includes the bias-correction, dark-subtraction, flat-fielding, non-linearity correction, distortion correction, and wavelength calibration (using a neon arc lamp frame) for each observation of target and standard star. The nearest sky exposure was used to remove the night-sky hydroxyl (OH) airglow emission using the method described by Davies (2008). In the last step of the data reduction, each observation was reconstructed into a three-dimensional data cube.

### Telluric and heliocentric velocity correction

A significant part of the data correction in the near-infrared regime is the correction for telluric absorption that originates in the Earth's atmosphere (mainly ozone, gaseous oxygen, and water vapor). Telluric absorption lines are exceptionally deep at the blue end of the K band and may vary over the time of the observation. Therefore, it is necessary to correct each science frame individually. Standard stars with known spectra are typically used to remove these atmospheric absorption features from science cubes.
For the telluric correction of the near-infrared spectra, we wrote a Python script to apply the same method as described in Krajnović et al. (2009). In most of the observation nights, two telluric stars were observed which gave us the opportunity to choose the telluric stars with a similar airmass to our science target. The telluric stars were either solar-like G0-2V stars or hotter B2-5V stars in an unsystematic order. We used the Python version 6.06 of the penalized

Pixel fitting software[2] (pPXF, Cappellari & Emsellem 2004) as upgraded in Cappellari (2017) to fit a stellar template showing the characteristic features of the telluric star. For the solar-like G-type stars, we use a high-resolution solar template (Livingston & Wallace 1991)[3] and in the case of spectrally almost featureless B-type stars we fitted a blackbody spectrum.
The telluric absorption corrected spectra were then corrected for the Doppler shifts due to the motion of the earth around the Sun, commonly known as heliocentric correction. As some of our targets were observed at different times of the year, the velocity shifts in the observed spectra could be between 10-40 km $s^{-1}$, which is on the order of the line-spread function (LSF). We used our own python routine to correct the wavelength into the heliocentric frame of reference. The corrected wavelength is defined by $\lambda_{\text{corrected}} = (1 + v_{\text{helio}}/c) \times \lambda_{\text{uncorrected}}$, where c is the speed of light and $v_{\text{helio}}$ is the projected heliocentric velocity that was calculated from the ESO pipeline for each data frame. The heliocentric correction was necessary for NGC 3640, NGC 4281, and NGC 7049, as in these cases the different observing blocks were spread widely throughout the year. We had to apply the heliocentric correction to each spaxel of each of our science frames individually.

### Merging of the data cube

The individual frames of the observations from the different observing blocks were then combined spatially using the position of the center of the galaxy as reference. This position changed for each of our science frames as a dithering pattern of a few pixels was applied for each subsequent observation to ensure that the galaxy would not always fall onto the same pixels of the detector and thus adding systematic uncertainties. It was possible to identify the center of the galaxy with an accuracy of about one pixel (=0.05″) by comparing the isophotes of the reconstructed images and recenter them. In this step, we also excluded science frames with a bad point spread function (PSF). Bad PSFs can be the result of poor seeing or an insufficient AO correction. In Table 4.2 we specify how many science frames were excluded for each galaxy. After the recentering, we applied a sigma-clipping pixel reject algorithm to align the single science frames and created the final data cubes as in Krajnović et al. (2009) and Chapter 2. The algorithm defines a new square pixel grid and interpolates the science frame to this grid. Flux values of the final data cubes were calculated as median flux values of the single data frames. Finally, we obtained $3 \times 3''$ data cubes with 0.05″ pixel scale for the 100 mas SINFONI observations.

### Correction of line-spread function inhomogeneities

In order to compare the spectra of the IFU with template spectra, which is needed for the extraction of the stellar kinematics (see Section 4.1), it is necessary to quantify the intrinsic dispersion of the SINFONI instrument. Therefore, we determined the spectral resolution of the SINFONI data from strong arc lines. While attempting to determine the spectral resolution of the SINFONI data, we encountered a problem: The spectral resolution over the full $64 \times 64$ spaxel FoV was very inhomogeneous (see Figure 3.1), which was also recognized by Nguyen et al. (2018) and Voggel et al. (2018). In order to better characterize the shape and inhomogeneity of the LSF for the merged cubes, we applied the same data reduction routines to the respective arc lamp (except for the sky subtraction). We then built an arc line data cube by combining the reduced arc lamp frames. We used the same dither pattern as for the science frames to ensure that the arc line cube would fully resemble the data cube of the science object. From the combined arc line cube we then measured the LSF using six isolated, strong arc lamp lines

[2]http://purl.org/cappellari/software
[3]http://www4.nso.edu/staff/wcl/atlases.html

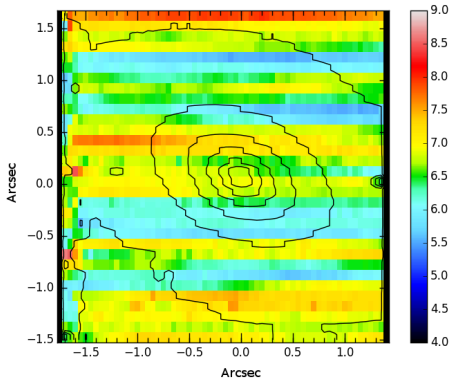


**Figure 3.1 —** Example of the spectral resolution inhomogeneity across the SINFONI detector. The spectral resolution for each spaxel was derived from arc line observations of NGC 584. The spectral resolution varies significantly in the vertical direction of the detector with values ranging from 5.5 Å to 7.7 Å FWHM.

for each spaxel. This LSF cube was later used when fitting each spaxel with a stellar template (details in Section 4.1). The spectral resolution across the FoV has a median value of 6.8 Å full-width at half maximum (FWHM) ($\lambda/\Delta\lambda = 3820$) with values ranging from 5.5 Å to 7.7 Å FWHM.

### Voronoi binning

The last step before determining the stellar kinematics was to ensure a sufficient and spatially uniform signal-to-noise (S/N) by spatially binning the final SINFONI data cubes with the adaptive Voronoi binning method[4] (Cappellari & Copin 2003), Python version 3.1.0. In this method, based on the initial S/N estimate, spaxels are co-added while keeping the geometrical constraint of nearly round bins. An initially approximated noise estimate was obtained by median smoothing each spectrum with a kernel of 30 pixels width and calculating the standard deviation of the difference between the smoothed and the original spectrum. This initial estimate was then passed on as input S/N to the Voronoi binning script. The input S/N was systematically chosen between 50 and 70, thereby balancing the desire to keep the central spaxels (if possible) unbinned to ensure a sufficiently high resolution in the center while increasing the quality of the outward spectra for the extraction of the kinematics. In our final binning scheme, we established typical bin sizes of $< 0.1''$ in the center, while 0.3-0.4″ diameter for bins at a radius larger than 1″.

### SINFONI spatial resolution

The quality of our black hole mass measurements is indicated by the spatial resolution of the AO-corrected SINFONI data. We determined the spatial resolution by convolving high-resolution HST images with a double Gaussian model PSF and compared it to the collapsed image of the SINFONI IFU data. A detailed description of how we derived the spatial resolution is given in Appendix 2.2. The resulting parameters are given in Table 4.3.

[4]See footnote 2

**Table 3.3 —** SINFONI spatial resolution

| Galaxy | $FWHM_N$ (arcsec) | $FWHM_B$ (arcsec) | $f_N$ | Strehl |
|---|---|---|---|---|
| (1) | (2) | (3) | (4) | (5) |
| NGC 584 | 0.20 ± 0.02 | 0.74 | 0.54 | 13 % |
| NGC 2784 | 0.21 ± 0.02 | 0.50 | 0.74 | 11 % |
| NGC 3640 | 0.19 ± 0.02 | 0.56 | 0.41 | 14 % |
| NGC 4281 | 0.22 ± 0.04 | 0.90 | 0.86 | 10 % |
| NGC 4570 | 0.18 ± 0.02 | 0.58 | 0.47 | 15 % |
| NGC 7049 | 0.20 ± 0.03 | 0.61 | 0.67 | 13 % |

**Notes.** The SINFONI PSF of the data was parametrized by a double Gaussian with a narrow and broad component. The parameters are given in the following columns. Column 1: Galaxy name. Column 2: FWHM of the narrow Gaussian component. Column 3: FWHM of the broad Gaussian component. Column 4: Relative intensity of the narrow component. Column 5: Strehl ratio of the data.

## 3.2 Large-field data

### MUSE IFU data

The MUSE (Bacon et al. 2010) data of NGC 584 was taken on July 1, 2016 under the science program 097.A-0366(B) (PI: Hamer). They obtained a total exposure time of 2700s divided into three 900s on-source integrations each yielding a FoV of $60 \times 60''$($\approx$ two effective radii of NGC 584). In addition, there was an off-source exposure of a blank field, which can be used to estimate the sky. The fields were oriented such as to map the galaxy along the major axis with a large overlap, as every frame contained the nucleus of the galaxy. We reduced the data using the MUSE data reduction pipeline (Weilbacher et al. 2015), version 1.6. The reduction followed the standard steps, first producing master calibration files (bias, flat, and skyflat), the trace tables, the wavelength solution, and the LSF for each slice. Each on-target observation was reduced using these calibration files and closest in time illumination flats to account for temperature variations. In addition, a separate sky field and a standard star were reduced in the same way. From these, we extracted a sky spectrum and its continuum, as well as the flux response curve and an estimate of the telluric correction. The sky spectrum was applied to all three on-target frames, where we let the pipeline model the sky lines based on the input sky spectrum and the LSF. As all on-source frames contained the nucleus, we recorded its relative positions between the frames and applied the offsets with respect to the first one, prior to merging with MUSE pipeline merging procedure. In the final cube each pixel has a size of $0.2'' \times 0.2''$ and a spectral sampling of 1.25 Å per pixel. For our $M_{BH}$ determination we only needed the high S/N central $30'' \times 30''$ of the MUSE data cube and cut this region out. We then Voronoi-binned the cut central region to a target S/N of 60, resulting in bin diameter sizes of $0.5''$ in the center and $3''$ at radii larger than $12''$.

### VIMOS IFU data

The large-field data for NGC 2784 and NGC 7049 were obtained between October 2006 and August 2007 using the VIMOS instrument (Le Fèvre et al. 2003) mounted on UT3 Melipal under the science programs 078.B-0464(B) and 079.B-0402 (B) (PI: Cappellari).
The VIMOS data reduction was performed by Lagerholm et al. (2012) making use of the ESO

pipeline[5] (version 2.3.3) and some Image Reduction and Analysis Facility (IRAF) tasks. This data reduction process includes bias and sky subtraction, flatfield calibration, interpolation over bad pixels, cosmic-ray removal, spatial rectification, wavelength with HeArNe lamp exposures, flux calibration with standard stars, and fringe-like pattern removal. As described in Lagerholm et al. (2012), they also corrected the fringe-like pattern in the spectral and the intensity variations in the imaging domain, which were dominating the raw data. After the data reduction, they merged the individual science frames into final data cubes. In the same manner as for the SINFONI and MUSE data, we also Voronoi-binned the VIMOS data to a target S/N of 60, obtaining bin sizes of 0.5″in the galaxy center and 2-3″at radii larger than 7.5″.

#### SAURON IFU data

NGC 3640, NGC 4281, and NGC 4570 are part of the ATLAS$^{3D}$ galaxy survey (Cappellari et al. 2011). The observations were obtained with the Spectrographic Areal Unit for Research on optical Nebulae IFU (SAURON, Bacon et al. 2001) at the 4.2 m William Herschel Telescope of the observatorio del Roque de los Muchachos on La Palma and reduced with the XSAURON software (Bacon et al. 2001) . The SAURON IFU has a FoV of $33'' \times 41''$ with a sampling of $0.94'' \times 0.94''$ square pixels, covering about 1-2 effective radii of our target galaxies. A detailed description of the stellar kinematics extraction of the ATLAS$^{3D}$ sample is given in Cappellari et al. (2011). The resulting velocity maps of NGC 3640, NGC 4281, and NGC 4570 were already presented in Krajnović et al. (2011), and we show the full kinematic set of these galaxies in Figure 4.10. In addition, NGC 4570 is part of the SAURON survey (de Zeeuw et al. 2002) and was presented in Emsellem et al. (2004). In this paper, we use the homogeneously reduced publicly available ATLAS$^{3D}$ data[6], which was binned to a target S/N of 40.

### 3.3 Imaging data

For the high-resolution central imaging of our target galaxies, we downloaded HST archival data. We obtained either Wide-Field Planetary Camera (WFPC2; Holtzman et al. 1995) or Advanced Camera for Survey (ACS; Ford et al. 1998) data from the ESA Hubble Science Archive, which generates automatically reduced and calibrated data. Cosmic rays were removed by taking the median of the aligned single CR-SPLIT images. Owing to an unsuccessful sky subtraction in the archival data, the ACS image was reprocessed by applying the DRIZZLEPAC[7] package of the Astroconda distribution. For the large FoV imaging of our targets of the southern hemisphere, NGC 584, NGC 2784, and NGC 7049, we used images of the Carnegie-Irvine Galaxy Survey (CGS; Ho et al. 2011; Li et al. 2011; Huang et al. 2013). For the other three targets we used SDSS DR7 r-band images (Abazajian et al. 2009), which we received from the ATLAS$^{3D}$ collaboration (Scott et al. 2013a).

## 4 Stellar kinematics

### 4.1 Method

For each instrument, we independently measured the light-weighted stellar kinematics from the galaxy absorption line spectra using the Python implementation of the penalized Pixel Fitting method[8] (pPXF; Cappellari & Emsellem 2004; Cappellari 2017). The pPXF routine fits the

[5]http://www.eso.org/sci/software/pipelines/
[6]http://purl.org/atlas3d
[7]http://www.stsci.edu/hst/HST_overview/drizzlepac
[8]See footnote 2

**Table 3.4 —** HST archival data

| Galaxy (1) | PID (2) | Instrument (3) | Filter (4) |
|---|---|---|---|
| NGC 584 | 6099 | WFPC2 | F555W |
| NGC 2784 | 8591 | WFPC2 | F547M |
| NGC 3640 | 6587 | WFPC2 | F555W |
| NGC 4281 | 5446 | WFPC2 | F606W |
| NGC 4570 | 6107 | WFPC2 | F555W |
| NGC 7049 | 9427 | ACS | F814W |

**Notes.** Column 1: Galaxy name. Column 2: programme identification number. Column 3 and 4: Camera on HST and the filters in which the data were taken.

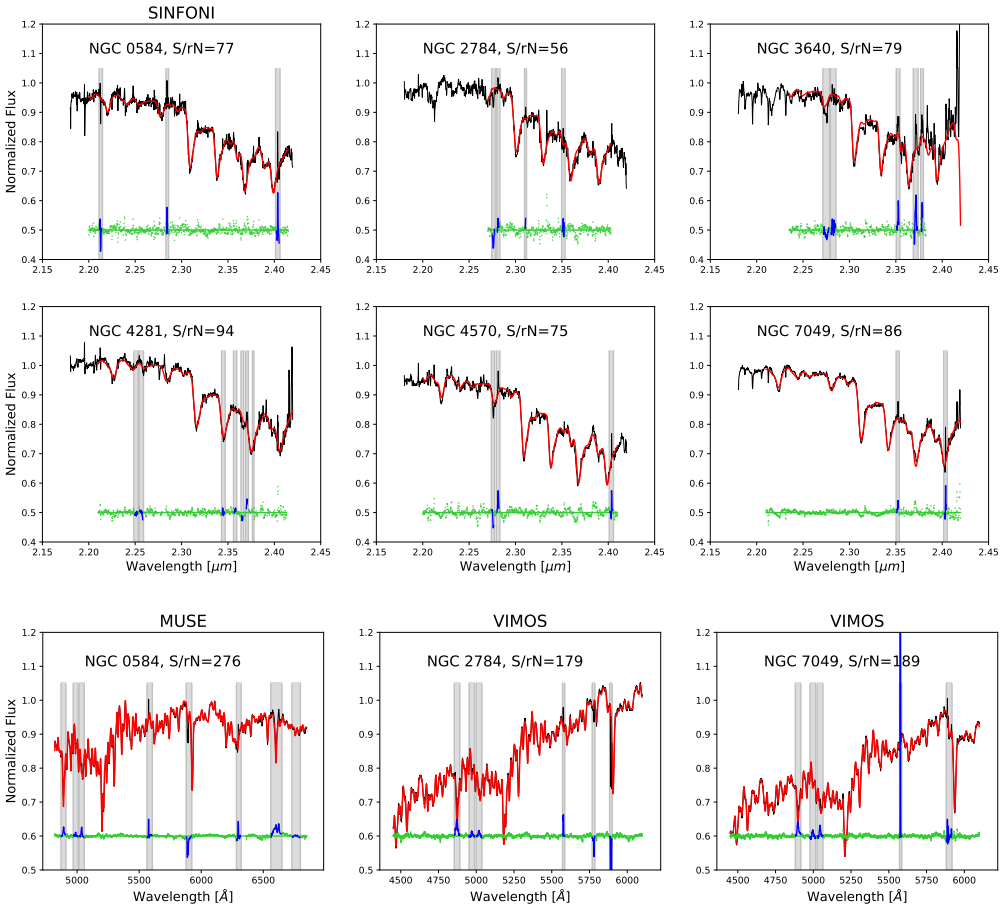


**Figure 3.2 —** Integrated SINFONI, MUSE, and VIMOS spectra and pPXF fits of our target galaxies. The integrated spectra (black solid lines) were obtained by summing up all spectra of the IFU data cubes and fitted using the pPXF routine (red lines) to derive an optimal template. The fitting residual between spectrum and best-fitting model are shown as green dots and are shifted up by 0.5 (0.6 for the bottom panels). Regions that were masked in the fit (often because of emission lines or insufficient sky subtraction) are indicated as gray shaded regions and their residuals are indicated in blue.

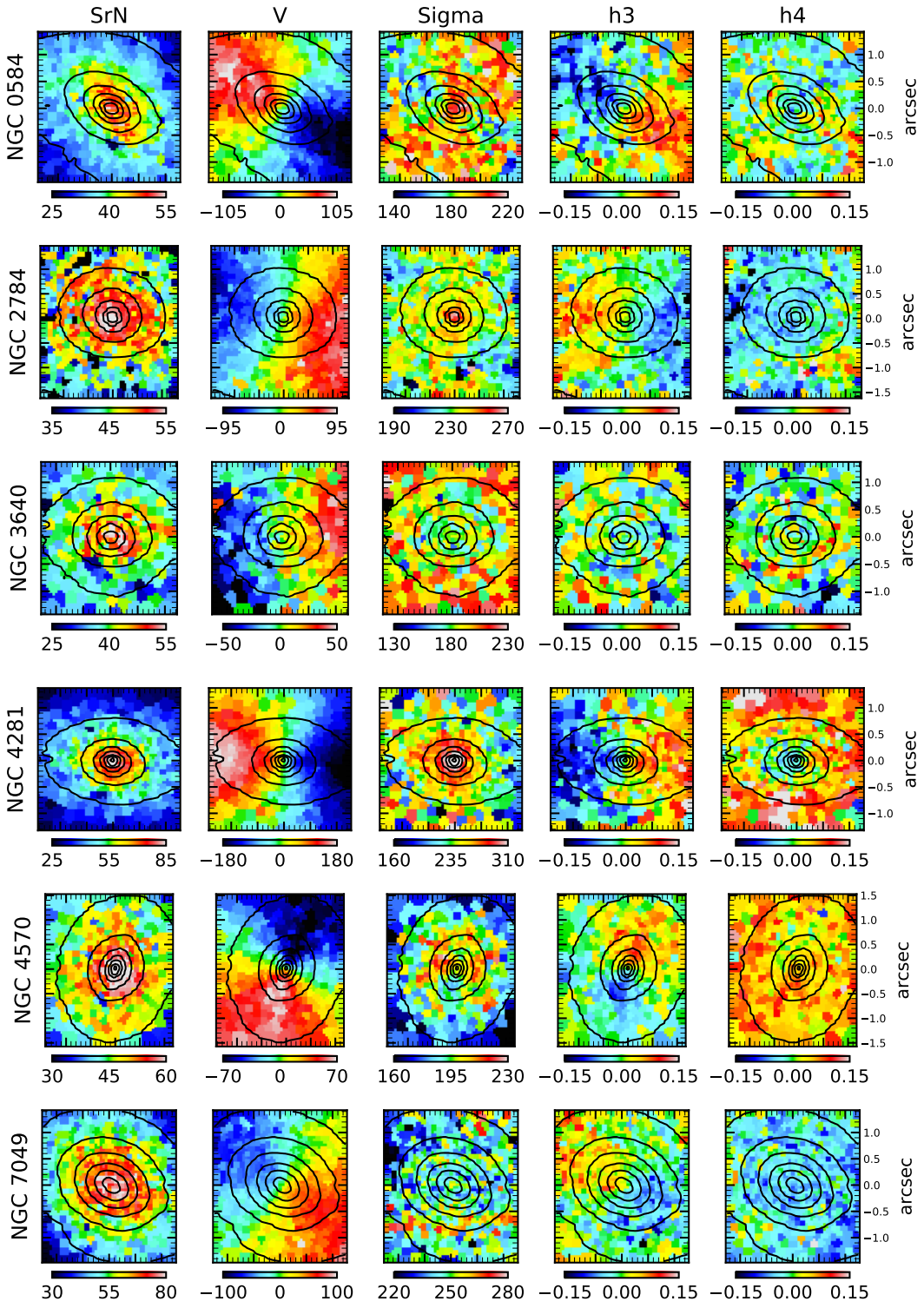


**Figure 3.3 —** SINFONI stellar kinematics (derived from CO band-head spectroscopy) of our target galaxies (from top to bottom) NGC 584, NGC 2784, NGC 3640, NGC 4281, NGC 4570, and NGC 7049. From left to right the panels show maps of signal-to-residual noise (S/rN), mean velocity ($V$), velocity dispersion ($\sigma$), and the Gauss-Hermite moments $h_3$ and $h_4$. The black contours indicate the galaxy surface brightness from the collapsed data cube. North is up and east to the left.

galaxy spectrum by convolving a stellar spectrum template with the corresponding stellar line-of-sight velocity distribution (LOSVD), which is parametrized by Gauss-Hermite polynomials (Gerhard 1993; van der Marel & Franx 1993). In detail, the LOSVD is then specified by the mean velocity $V$, the velocity dispersion $\sigma$, and two additional quantities to describe asymmetric ($h_3$) and symmetric ($h_4$) deviations from a simple Gaussian. As the higher Gauss-Hermite polynomials are strongly coupled to the simple Gaussian moments, their relative weights are controlled by the so-called BIAS parameter, which is dependent on the S/N of the data (Cappellari & Emsellem 2004; Emsellem et al. 2004). For low S/N data, the BIAS parameter prevents spurious solutions by biasing the derived LOSVD toward a simple Gaussian.
We analogously derived a second set of kinematics for each of our sample galaxies where we parametrized the LOSVD with the first two moments ($V$, $\sigma$) only. In this case, the BIAS keyword is not used by the code. This set of kinematics was needed to construct the Jeans Anisotropic Models (Section 5.2), which only take into account the lower order moments of the LOSVD.

The usage of pPXF is twofold in order to minimize statistical variations across the field and reduce the computational expense. The first step is the creation of an optimal template by running pPXF on the global galaxy spectrum. The optimal template is a non-negative linear combination of the stellar library and consisted of typically 2-5 stars for the SINFONI data and about 30 stars for the large-scale data. Depending on the spectral range of the observed data, we used either MILES (Sánchez-Blázquez et al. 2006), Indo-US (Valdes et al. 2004) optical, or the Gemini Spectral Library of Near-IR Late-Type (Winge et al. 2009) stellar template library spectra, which are further described in the following two subsections. The optimal template is then used to fit the spectra from each Voronoi bin using $\chi^2$ minimization. While running pPXF on our spectra, we also added an additive polynomial to account for the underlying continuum. Furthermore, emission lines and regions of bad sky subtraction were masked during the fit. We then compared the fitted spectrum with the original spectrum for each bin. The standard deviation of the residuals (i.e., shown as green points in Fig. 5.5) was used to derive a final signal-to-residual noise (S/rN), which measures both the quality of the data and the precision of the fit.

The errors of the recovered kinematics were derived with Monte Carlo simulations, the standard approach for LOSVD extractions. The complete measurement process is repeated for a large number of data realizations (500), where each realization is the original spectrum perturbed by adding noise in the order of the standard deviation of the pPXF residuals. Applying pPXF (with BIAS parameter set to zero) on each realization (with the same optimal template) provides 500 measurements of the LOSVD. The final error of each bin is then the standard deviation of the LOSVD distributions of these 500 realizations. The kinematic errors are spatially anticorrelated with the S/rN distribution: low in the center and larger in the outer regions. Mean errors are shown in Figure 4.3, where we compare the large- and small-scale kinematics with each other. We note that the large-scale kinematics have much smaller errors than the SINFONI data (velocity: $\approx 2.5-5\,\mathrm{km\,s^{-1}}$ versus $\approx 5-10\,\mathrm{km\,s^{-1}}$ and velocity dispersion: $2.5-6\,\mathrm{km\,s^{-1}}$ versus $6-12\,\mathrm{km\,s^{-1}}$).

## 4.2 SINFONI specifics

The SINFONI spectrograph in combination with AO provides spatially highly resolved spectra in the near-infrared regime yielding significant information about the motion of the stars surrounding the central black hole due to its dust transmissivity and high resolution. A significant feature in the near-infrared is the CO absorption band head at about $2.3\,\mu$m, which can be used to gain robust

measurements of the LOSVD. We used the stellar template library by Winge et al. (2009), which consists of 23 late-type stars observed with the Gemini Near-Infrared Spectrograph (GNIRS) and 31 late-type stars observed with the Gemini Near-Infrared Integral Field Spectrometer (NIFS) to fit the SINFONI spectra in the range 2.29 to 2.41 $\mu$m. Excluded from the fit were emission lines and incompletely reduced sky lines that especially contaminated the third and fourth absorption line of the band head. Furthermore, to mitigate template mismatch effects in our kinematics extraction, we tested including both GNIRS and NIFS template stars as well as the restriction to only one instrument's template stars. While all three attempts gave generally consistent results, the NIFS template stars could not always reproduce the calcium line (at $\sim 2.25\,\mu$m) very well. This slight template mismatch often led to systematically lower velocity dispersions (but within the statistical errors). During the fitting procedure, we carefully examined and compared all three template library combinations and always chose the one that gave the best fit to the SINFONI spectra.

In order to recover reliable LOSVD measurements, we had to ensure that both the stellar templates and the SINFONI observations had a comparable spectral resolution before the fitting procedure. As the NIFS and GNIRS stellar spectra are provided at a better resolution than the SINFONI galaxy spectra, we had to degrade the template spectra to the same resolution as the SINFONI observations. Therefore, we convolved the template spectra ($\sigma_{\rm temp} \approx 2.9 - 3.2$ Å) with a Gaussian having the dispersion of the difference between the dispersion of the Gaussian assumed LSF of the data and the stellar template. Our final pPXF fits reproduce the observed galaxy spectra very well as illustrated in Figure 5.5. For NGC 2784, NGC 3640, and NGC 4281, we also excluded the region around the NaI atomic absorption line at $\sim 2.2\,\mu$m as none of our stellar templates could match the line strength fully. As Silva et al. (2008) point out this is an often seen discrepancy between pure old galaxies and Galactic open cluster stars. We extended the masked regions because the blue part of the spectrum is very noise-polluted and biases the kinematics to a more noisy solution. Including or excluding this region, the changes in the four moments stay within the derived kinematical errors.

## 4.3 VIMOS and MUSE specifics

The kinematic extraction of the optical VIMOS and MUSE data was performed similarly to the ATLAS$^{3D}$ kinematic extraction. We re-extracted the kinematics for VIMOS data as the Lagerholm et al. (2012) extraction did not contain kinematic errors for each spaxel.
The optical IFU data matching stellar templates were taken from the medium-resolution Isaac Newton Telescope library of empirical spectra (MILES; Sánchez-Blázquez et al. 2006; Falcón-Barroso et al. 2011) stellar library[9] (version 9.1). We used the full sample consisting of 980 stars that span the wavelength range 4760-7400 Å and fitted the wavelength range from 3800-6500 Å in the galaxy spectra. As already mentioned, we also had to ensure that the instrumental resolution of the stellar templates and the optical data had comparable values. Beifiori et al. (2011) and Falcón-Barroso et al. (2011) reported the instrumental dispersion of the MILES template library to be $\sigma_{\rm MILES} = 2.51$ Å. The MUSE spectral resolution was carefully measured by Guérou et al. (2017) based on sky emission lines and the authors found a variation of the LSF with wavelength. In the wavelength range from 4800 Åto 6800 Å, the spectral resolution changes from 2.5 Åto 2.9 Å. We performed a kinematics extraction using the extreme values of 2.5 Åand 2.9 Åto test the significance of this spectral resolution variation on our stellar kinematics measurement. The velocity dispersion changed in average by only 5 km s$^{-1}$, which is within the kinematic error range, and we decided not to downgrade the MILES template library to the MUSE resolution.

[9] http://miles.iac.es/

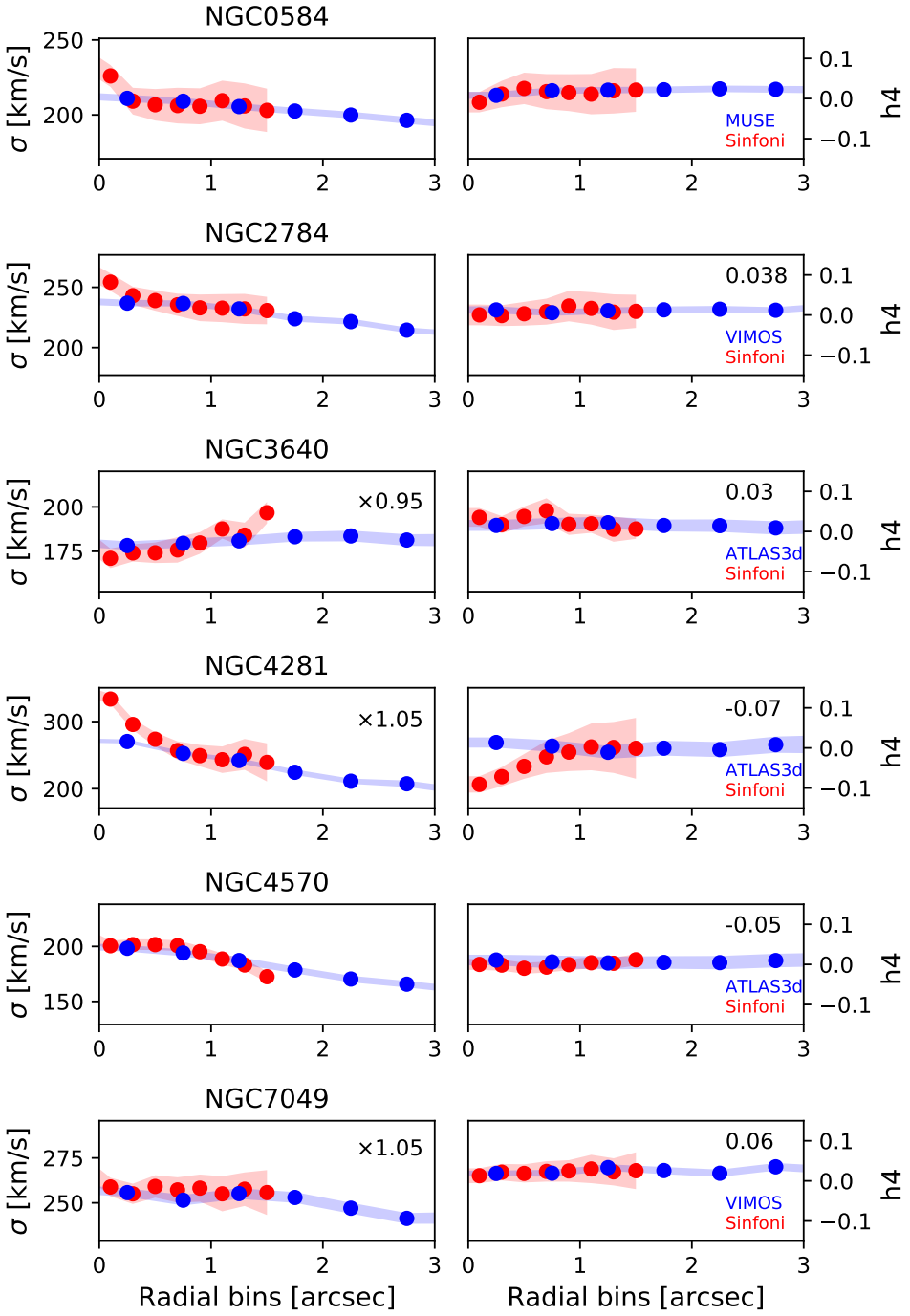


**Figure 3.4 —** Comparison of velocity dispersion and $h_4$ profiles for the SINFONI (red) and the respective large-scale data (blue). The values were averaged within circular annuli around the kinematic center. The error range of the averaged values in the radial bins are calculated via error propagation and are shown as shaded regions. Applied shifts in the SINFONI maps are denoted by the values in the upper right corner of each panel.

On the other hand, the VIMOS data have an instrumental dispersion of $\sigma_{\rm VIMOS} = 2.1$ Å (Rawle et al. 2008). Theoretically, a downgrading of the observed galaxy spectrum would be necessary in this case. As both instrumental spectral resolutions were relatively similar and we did not want to smooth relevant kinematic information, we did not convolve the VIMOS spectra to the lower resolution. All velocity dispersions are $\sigma > 150$ km s$^{-1}$, so the effects of the slightly different resolutions on the derived kinematics are negligible. However, just as in Chapter 2, we tested the effect of not downgrading the VIMOS spectra via a well-defined subsample of the Indo-US stellar library (Valdes et al. 2004) as stellar template in the pPXF fit. Our subsample of the Indo-US stellar library consists of 52 spectra and covers a wavelength range from 3460 Å to 9464 Å at a spectral resolution of $\sigma_{\rm Indo\text{-}US} = 1.35$ Å (Beifiori et al. 2011). A comparison between the Indo-US kinematic extractions with the MILES extractions showed that the extracted kinematical maps displayed the same general features and trends. We could, however, discern a difference in the extracted values between the two stellar templates with the MILES velocity dispersions being systematically lower (10-20 km s$^{-1}$) and thus, more consistent with the stellar kinematics extraction from SINFONI. We furthermore recognized that the spectral fits were worse for the Indo-US fits such that we expected a template mismatch from the relatively small number of Indo-US template stars. Comparing our kinematic extraction with the extraction by Lagerholm et al. (2012) proved consistent results. We, therefore, decided to keep the MILES library for the rest of this work.

## 4.4 Kinematic results

In Figure 4.2, we present the high-resolution SINFONI kinematic maps of the central 3×3 arcsecs of the galaxies resulting from the pPXF fits. The first column shows the S/rN map, which we derived from the comparison between the pPXF fit and the input spectra (after applying the Voronoi binning). This map visualizes well the quality of the pPXF fit and the quality of the data, as the S/rN is directly related to the errors of the kinematics because they are large in the center and monotonically decrease with radius. The S/rN maps show that our kinematics extraction works well (S/rN > 30) within 1 arcsec, which is the region that we used for our dynamical modeling. The next four columns show the velocity, velocity dispersion, and $h_3$ and $h_4$ maps for each of our galaxies.

As expected from our selection criteria, the derived kinematics show mainly regular features. For each of our six galaxies, a clear rotation pattern is visible with maximal relative velocities ranging from 50 to 180 km s$^{-1}$ (after subtracting the systemic velocity). The velocity dispersions show various patterns for the different galaxies. NGC 2784 and NGC 4281 contain a clear sigma increase within the isophotal center. The sigma peak in NGC 2784 has a size of about 0.3″ and goes up to 275 km s$^{-1}$, while we find a larger sigma peak in NGC 4281 ($\sigma \approx 310$ km s$^{-1}$). In NGC 3640 another clear feature is apparent: a slightly asymmetric velocity dispersion decrease in the center (down to 175 km s$^{-1}$) that spans the complete central region ($r < 0.7''$). This dip velocity is consistent with early work by Prugniel et al. (1988) and Davies et al. (1987). Prugniel et al. (1988) also pointed out that this galaxy might be in an advanced merger state, which would significantly affect our dynamical models. Large-scale signatures of this merger (such as shells) are also visible in the MATLAS images from Duc et al. (2015), also shown in Bonfini et al. (2018). However, Krajnović et al. (2011) analyzed the ATLAS$^{3D}$ kinematics of NGC 3640 with the KINEMETRY routine (Krajnović et al. 2006) and found only very small residuals and a very regular shape within one $R_e$, indicating that the center of NGC 3640 is relaxed now. We, therefore, believe that our $M_{\rm BH}$ measurement is robust and not likely to be affected by the advanced merger state (Prugniel et al. 1988). The velocity dispersion map of NGC 584 shows an hourglass-shape that can be attributed to a dynamically cold disk component

(low velocity dispersions). Also, NGC 4570 shows signatures of a central disk. Its velocity dispersion goes up to 230 km $s^{-1}$, and we see maximal rotational velocities of 60 km $s^{-1}$, which is fully consistent with the HST/Faint Object Spectrograph kinematics from van den Bosch et al. (1998). The velocity dispersion map of NGC 7049 is very unusual: it shows a very flat velocity dispersion profile without a clear sigma rise visible in the kinematics of this galaxy.
The $h_3$ Gauss-Hermite moment maps show the typical anticorrelation to the velocity for each galaxy. The $h_3$ map of NGC 3640 may look chaotic at first glance, but the anticorrelation trend is also slightly visible here.

The visual comparison of the near-infrared central kinematic maps with the optical large-scale maps (Appendix: Fig. 4.10, 3.14) shows globally consistent results and similar trends even though we probe both very different scales and very different wavelength regions. The kinematic details of the SINFONI maps are generally not present on the large-scale kinematic maps, as the spatial resolution of the latter is comparable to the SINFONI FoV. In a second more quantitative comparison, we compared the Gauss-Hermite profiles from the four-moment pPXF fit of the two data sets. For the "point-symmetric" velocity dispersion and $h_4$ moment, we averaged the bins within concentric circular annuli around the kinematic center and repeated this process with growing radius. The bins were chosen such that the luminosity-weighted center was within the respective annulus. We present the comparison in Figure 4.3. For some cases, we had to slightly shift the velocity dispersion and $h_4$ values of the SINFONI data (values are shown in Figure 4.3) to perfectly match the large- and small-scale data. The shifts are about 5 % for three of our galaxies and there are no shifts for the remaining galaxies. Even before the shifts, all measured SINFONI velocity dispersions and most $h_4$ profiles were in very good agreement with the large-scale data. Some discrepancy can be seen in the $h_4$ profile of NGC 4281, which has a positive gradient for SINFONI and constant value for ATLAS$^{3D}$. We believe that this discrepancy arises from the ATLAS$^{3D}$ spatial resolution, which flattens out the central features of the $h_4$ moment. Krajnović et al. (2018b) have tested the significance of the shifting with respect to the measured black hole mass and they noticed that the uncertainty increases by about 80% of the measured black hole mass by shifting the velocity dispersion up by about 8%. This means that we possibly add an uncertainty of 50% in mass for NGC 3640, NGC 4281, and NGC 7049.

# 5 Dynamical modeling

We derived the central black hole masses of our target galaxies using two different and independent dynamical modeling methods: Jeans Anisotropic Models (JAM; Cappellari 2008) for constraining the parameter space and three-integral Schwarzschild (1979) orbital superposition models for deriving the final black hole masses. In the past, the Schwarzschild method has successfully been used to reproduce detailed models for spherical, axisymmetric, and triaxial nearby galaxies. On the other hand, the JAM method is less general than orbit-based methods but far less computationally time consuming. Furthermore, it provides a good description of galaxies based on two-dimensional stellar kinematics. Previous works on almost 40 galaxies have shown that, although the models start from different assumptions, both techniques provide generally consistent $M_{BH}$ results (Cappellari et al. 2010; Seth et al. 2014; Drehmer et al. 2015; Feldmeier-Krause et al. 2016; Krajnović et al. 2018b; Ahn et al. 2018, , but see also Chapter 2), such that modeling the observed stellar kinematics with both independent methods provides a more robust measurement. Recently, Leung et al. (2018) compared the results from both Schwarzschild and JAM models against circular velocities derived from molecular gas for 54 galaxies with CALIFA (Sánchez et al. 2012) integral-field stellar kinematics. These

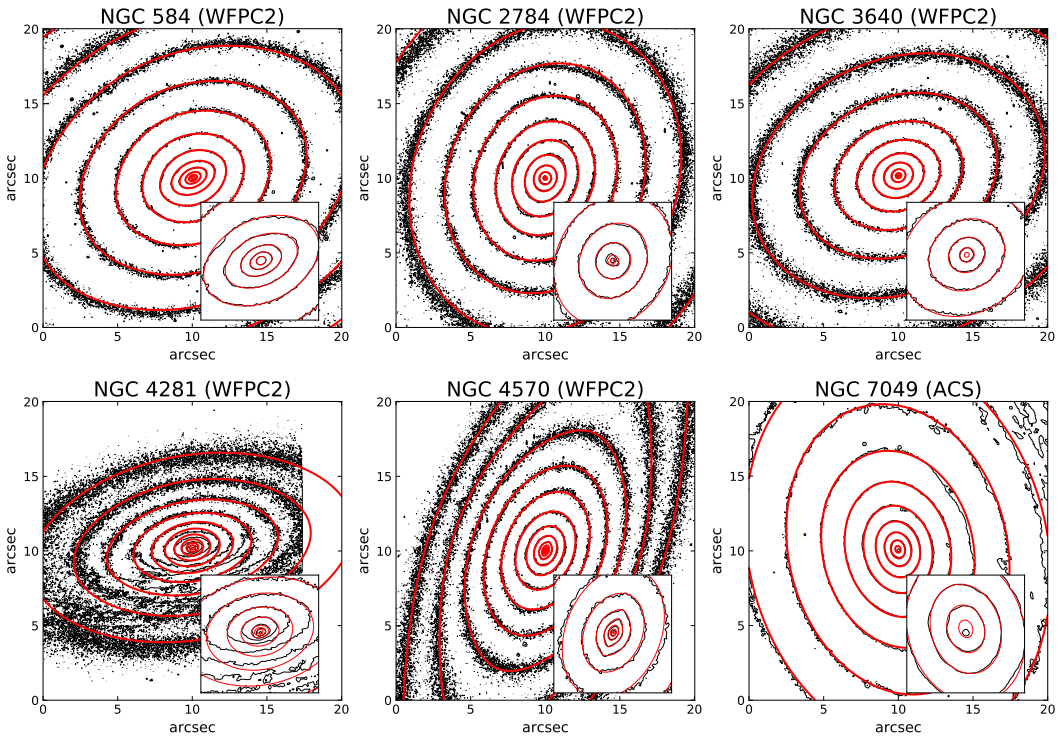


**Figure 3.5 —** Isophotal maps of the WFPC2 and ACS images of our target galaxies within a FoV of $20 \times 20''$. In the bottom right of each panel we show a cut out of the central $3 \times 3''$. The contours of our best-fitting MGE model (red) are superimposed on the HST images. For the models, foreground stars and close galaxies were masked. For NGC 2784, NGC 4281, and NGC 7049 a dust correction of the internal dust rings had to be applied before MGE modeling their surface brightness. The MGE models were build from the combined photometric information of HST ($r < 10''$) and wide FoV data ($r > 10''$) from ATLAS$^{3D}$ and the CGS (Ho et al. 2011) survey.

authors found that JAM and Schwarzschild recover consistent mass profiles (their Fig. D1). Moreover, JAM was found to recover more reliable circular velocities than the Schwarzschild models, especially at large radii where the gas velocities are more accurate (their fig. 8). Their study illustrates the fact that the reduced generality of the JAM method, with respect to the Schwarzschild method, is not necessarily a weakness and highlights the usefulness of comparing both methods as we do in this work.

## 5.1 Mass model

The gravitational potential of the galaxy is a composition of the potential of the stars, the potential from the central black hole that is assumed as a point mass, and the potential of dark matter. In order to find the mass of the central black hole, it is crucial to determine the stellar and dark matter contribution of the total galaxy mass as precisely as possible. The stellar mass density of the galaxy can be inferred from the galaxy luminosity density multiplied by the stellar $M/L$, which itself can be derived by modeling the stellar surface brightness of the galaxy. An efficient tool to provide an analytical description of the surface brightness of galaxies is the Multi-Gaussian Expansion (MGE) developed by Emsellem et al. (1994) and Cappellari (2002) in which a sum of two-dimensional concentric Gaussians parametrizes the galaxy surface brightness.

We performed the MGE modeling simultaneously on highly resolved HST and deep wide-field ground-based SDSS (presented by Scott et al. 2013a) or CGS (Ho et al. 2011) imaging

data via the MgeFit Python package[10] Version 5.0 of Cappellari (2002). Except for NGC 7049, the SDSS images were in the r band, while from HST we chose images taken with the WFPC2 camera in bands that matched the SDSS r band best. NGC 7049 was only observed with the ACS camera in the F814W filter and we matched it with I-band data from the CGS survey. We aligned the surface brightness profiles by rescaling the large FoV imaging data to the central HST profiles and used the HST imaging for the photometric calibration. Foreground stars and nearby galaxies were carefully masked before applying this procedure. Furthermore, we had to apply a dust correction to NGC 4281 and NGC 7049 to improve the modeling of the underlying galaxy surface brightness. Dust can have a significant effect on the stellar mass model as it alters the shape of the stellar surface brightness and dilutes the observed galaxy light. A careful dust correction is necessary to optimize the reproducibility from the model and the actual shape of the galaxy. We used the same method as in Cappellari et al. (2002) and Scott et al. (2013a) to dustcorrect the SDSS and CGS images and the dust-masking method outlined in Chapter 2 to mask dust rings visible in the HST images, which had only a single image available (for details see Appendix 8). We also visually inspected the HST images of our galaxies for nuclear star clusters, but could not find any evidence. This is expected as galaxies with a mass of more than $10^{11}$ $M_{\odot}$ usually do not harbor nuclear star clusters (Ferrarese et al. 2006; Wehner & Harris 2006; Seth et al. 2008; Graham & Spitler 2009).

The final MGE fits converge for between 10-12 Gaussian components centered on the galaxy nucleus and with the major axis aligned with the galaxy photometric major axis. For most of our lenticular galaxies, we can see a clear trend of the axial-ratio change with radius. These galaxies show rather round isophotes in the central bulge region and flattened and disk-like isophotes for larger radii from the outer disk.

We converted the MGE parameters from pixel-space into physical units of $L_{\odot}$ pc$^{-2}$ following the guideline given by the MGE readme and Holtzman et al. (1995). For the transformation we needed to account for the absolute Vega magnitude of the Sun[11] $M_{F555W} = 4.85$, $M_{F606W} = 4.66$ and $M_{F814W} = 4.15$. Furthermore, we corrected for the foreground Galactic Extinction applying the values found in the NASA/IPAC Extragalactic Database[12] which were derived by Schlafly & Finkbeiner (2011). The final MGE parameters are presented in Table 3: for each galaxy, we list the index of the Gaussian component, surface brightness in units of $L_{\odot}$ pc$^{-2}$, Gaussian dispersion $\sigma_j$ in arcseconds, and axial ratios $q_j$. In Figure 3.5, we show a comparison of our resulting best-fit MGE models and the observed HST WFPC2 and ACS images. Except for nuclear dust patterns (NGC 2784, NGC 4281, NGC 7049), the modeled MGE surface brightness are in good agreement with the surface brightness of each of the six galaxies. Especially for NGC 4281 a large dust mask had to be applied to correct the MGE model for the large amount of dust in this galaxy.

The next step for determining the mass model is the deprojection of the surface brightness into a three-dimensional luminosity density. Therefore, it is necessary to impose an assumption on the structure of the potential. For each of our target galaxies we adopted the assumption of an axisymmetric potential, such that assuming a given inclination ($i > 0$), the luminosity density can directly be deprojected from the MGE model. We used the built-in MGE regularization to bias the axial ratio of the flattest Gaussian to be as large as possible to prevent strong variations in the mass density of the MGE model. The MGE deprojection assumption does not remove the intrinsic degeneracy of the deprojection (Rybicki 1987; Gerhard & Binney 1996), which, especially at low inclination, can lead to major uncertainties and constitutes a fundamental

[10] See footnote 2

[11] http://mips.as.arizona.edu/ cnaw/sun.html

[12] https://ned.ipac.caltech.edu/

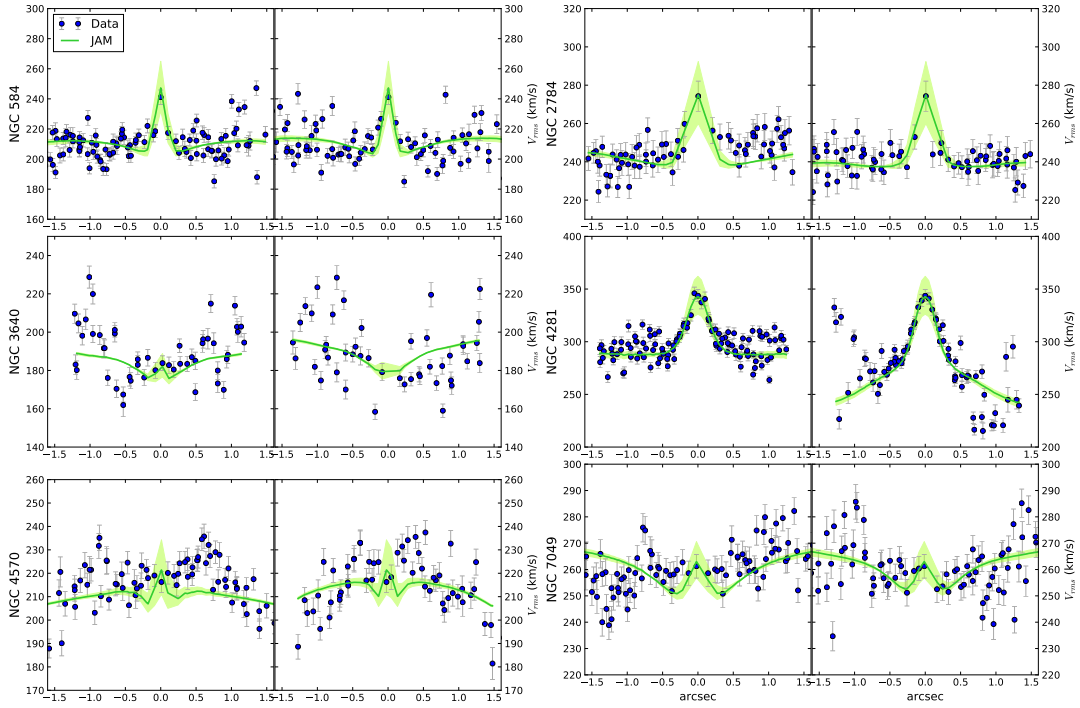


**Figure 3.6 —** Comparison of the $V_{\rm rms}$ profiles between the SINFONI data (blue) and best-fitting JAM models (green) along the major (left) and minor (right) axis. The green shaded region shows JAM models with varying black hole mass by a factor of 1.3 either larger or smaller than the best-fitting mass.

limitation to the accuracy of any dynamical model (e.g., Lablanche et al. 2012). In the center of the galaxies, which is probed by our data, stars mainly contribute to the mean potential of the galaxy. This means that the galaxy mass density $\rho$ can simply be described as the product of the galaxy luminosity density and a dynamical $M/L$. The gravitational potential generated by this mass density can then be obtained with the Poisson equation, $\nabla^2\Phi = 4\pi G\rho$, and is one of the ingredients for the dynamical models in the next two sections. For further details regarding the MGE deprojection, we refer to the original work by Emsellem et al. (1994) and Cappellari (2002).

## 5.2 Jeans anisotropic models

The motion of a collection of stars in a gravitational field can be described by the Jeans (1922) equations. They provide the basis for the JAM method (Cappellari 2008), which predicts the second velocity moment by solving the Jeans and Poisson equations for the mass density derived from the MGE model. Projected along the line of sight of the model, the second velocity moment is a function of four free parameters: the mass of the black hole $M_{\rm BH}$, the anisotropy parameter $\beta_z$, the $M/L$, and inclination angle i. The anisotropy parameter describes the orbital distribution by relating the velocity dispersion parallel to the rotation axis and in the radial direction: i.e., $\beta_z = 1 - \sigma_z^2/\sigma_R^2$ assuming that the velocity ellipsoid is aligned with cylindrical coordinates. We used the JAM method to model the second velocity moment in the potential defined by our MGE models, which is assumed to be axisymmetric. The modeled second velocity moment was then compared to the observed $V_{\rm rms} = \sqrt{V^2 + \sigma^2}$, where $V$ is the mean velocity and $\sigma$ the velocity dispersion that was measured from the high-resolution SINFONI stellar kinematics (assuming a parametrization of the LOSVD of a simple Gaussian). Unlike the Schwarzschild models (Section 5.3), we only fit the innermost high-resolution SINFONI kinematics to be robust

against possible gradients in the $M/L$ or the anisotropy.

We found the posterior distributions and the best-fitting values of the JAM parameters by applying a Bayesian framework in the form of Markov chain Monte Carlo (MCMC) inference method (Hastings 1970). We used the emcee software package Foreman-Mackey et al. (2013) which is a python implementation of the Goodman & Weare (2010) affine invariant MCMC ensemble sampler[13]. Generally, JAM is fit to the data using Bayesian approaches and MCMC as this makes it easy to detect degeneracies between parameters and marginalize over uninteresting parameters (e.g., Cappellari et al. 2012; Barnabè et al. 2012; Cappellari et al. 2013b; Watkins et al. 2013; Cappellari et al. 2015; Mitzkus et al. 2016; Poci et al. 2016; Kalinova et al. 2017; Li et al. 2017a; Bellstedt et al. 2018; Leung et al. 2018), and in the context of massive black hole determination by Krajnović et al. (2018b) and Ahn et al. (2018). For our dynamical JAM modeling, we followed a similar approach as Cappellari et al. (2013a). In the burn-in phase, a set of walkers explores the predefined parameter space, where each successive step is evaluated based on the likelihood of each walker. We used 100 walkers and tracked them for 200 steps until the fit converged. After the exploration of the parameter space, we continued the MCMC for 500 steps (post-burn-phase) and used the final walker positions to generate posterior distributions and model properties.
We built models with the four free parameters ($\log M_{\rm BH}, \beta_z, M/L, i$) and compared them with the observed $V_{\rm rms}$ using a $\chi^2$-statistic. The logarithmic likelihood probability of our data is defined as

$$\log P\left(V_{\rm rms} \,|\, i,\ M/L,\ \beta_z,\ \log M_{\rm BH}\right) \propto -\frac{1}{2} \sum_n \underbrace{\left( \frac{V_{\rm rms} - \langle v_{\rm los}^2 \rangle^{1/2}}{\delta V_{\rm rms}} \right)^2}_{\chi^2} \tag{3.1}$$

which is a sum over all good spaxels and where $\delta V_{rms}$ are the errors derived by the Monte Carlo simulations of the kinematic data and error propagation. In order to ensure that the fitting converges, we set reasonable priors on the parameters. We used uninformative priors (assumption of maximal ignorance) for the different parameters, which are uniform within the bounds of the likelihood function: $\log M_{\rm BH} \in [4.8, 9.8]$, $\beta_z \in [-1, +1]$, $M/L \in [0.1, 20]$ and the inclination was allowed to vary over the full physical range, being only limited by the flattening parameter $q_{\rm min}$ of the flattest Gaussian of the MGE model $\cos^2 i = q^2$. We made sure that the MCMC chain converges by visually checking our burn-in plots and running several Markov chains.

In Appendix E (Figure A.7), we present the MCMC posterior probability distributions of the various JAM model parameters for each galaxy. The contour plots show the projected two-dimensional distributions for each parameter combination and the histograms show the one-dimensional distributions for each parameter. As clearly indicated by the contour plots, our $M_{BH}$ and $\beta_z$ parameters are not degenerate for NGC 584, NGC 2784, NGC 3640, and NGC 4570, which shows that these measurements are robust. The $\beta_z$ parameters and the inclinations are naturally correlated but do not affect the black hole mass measurement. Generally, the derived inclinations are not well constrained and tend to be larger than expected from the literature. This is expected behavior as we only fit the central kinematics of our galaxies. That is why we decided to use the literature inclinations for the Schwarzschild modeling analysis. Furthermore, NGC 4281 and NGC 7049 show a degeneracy but still clearly constrain the black hole mass. We used the posterior probability distributions to calculate the best-fit value and their corresponding $3\sigma$ uncertainties. The median values of the posterior distribution are given in Table 4.5. A visual

[13] http://dfm.io/emcee/current/

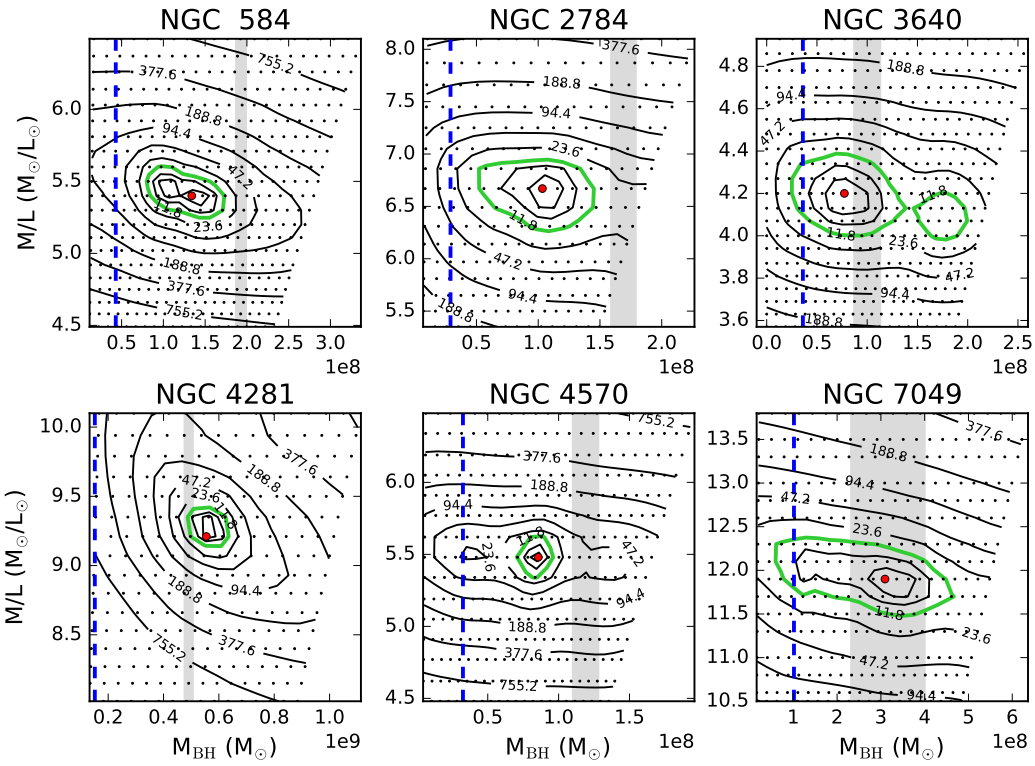


**Figure 3.7 —** Grids of Schwarzschild models (indicated by the black dots) over various $M/L$s and black hole masses $M_{\rm BH}$. The best-fitting model, derived as the minimum of $\chi^2$, is indicated by a large red circle. The contours indicate the $\Delta\chi^2 = \chi^2 - \chi^2_{\rm min}$ levels; the thick green contour shows the $3\sigma$ level of the two-dimensional distribution. In addition, we added the $3\sigma$ limits on the best-fitting black hole masses of the JAM models (gray shaded regions). The dashed blue line indicates the mass of the black hole which has the radius of the SoI of half the resolution of our LGS AO data (inferred from the narrow component of the AO PSF); this is approximately the lowest black hole measurement that we expect to be detectable based on our data.

comparison between the observed $V_{rms}$ profiles and the best-fit jam models of the MCMC routine are presented in Figure 3.6. In all cases the derived models reproduce the central peak of the observed $V_{\rm rms}$ well, while the outer kinematics often suffer from scatter. Our derived best-fitting JAM $M_{\rm BH}$ and $M/L$s were used as an initial guess to constrain the Schwarzschild models.

## 5.3 Schwarzschild models

In our second dynamical modeling approach, we used the axisymmetric Schwarzschild code which was optimized for two-dimensional IFU data and described in Cappellari et al. (2006). The method is based on the numerical orbit-superposition method originally invented by Schwarzschild (1979) and further developed to fit stellar kinematics (Richstone & Tremaine 1988; Rix et al. 1997; van der Marel et al. 1998; Cretton et al. 1999). The basic idea of the Schwarzschild method is that the mass distribution of the galaxy is well described by the sum of time-averaged orbits in a stationary galaxy potential. The method basically consists of two steps which are repeated for each modeled black hole mass, respectively. First, assuming a stationary galaxy potential, a representative orbital-library is constructed from the galaxy potential, which itself is derived from the mass density from Section 5.1. Regular orbits in axisymmetric potentials

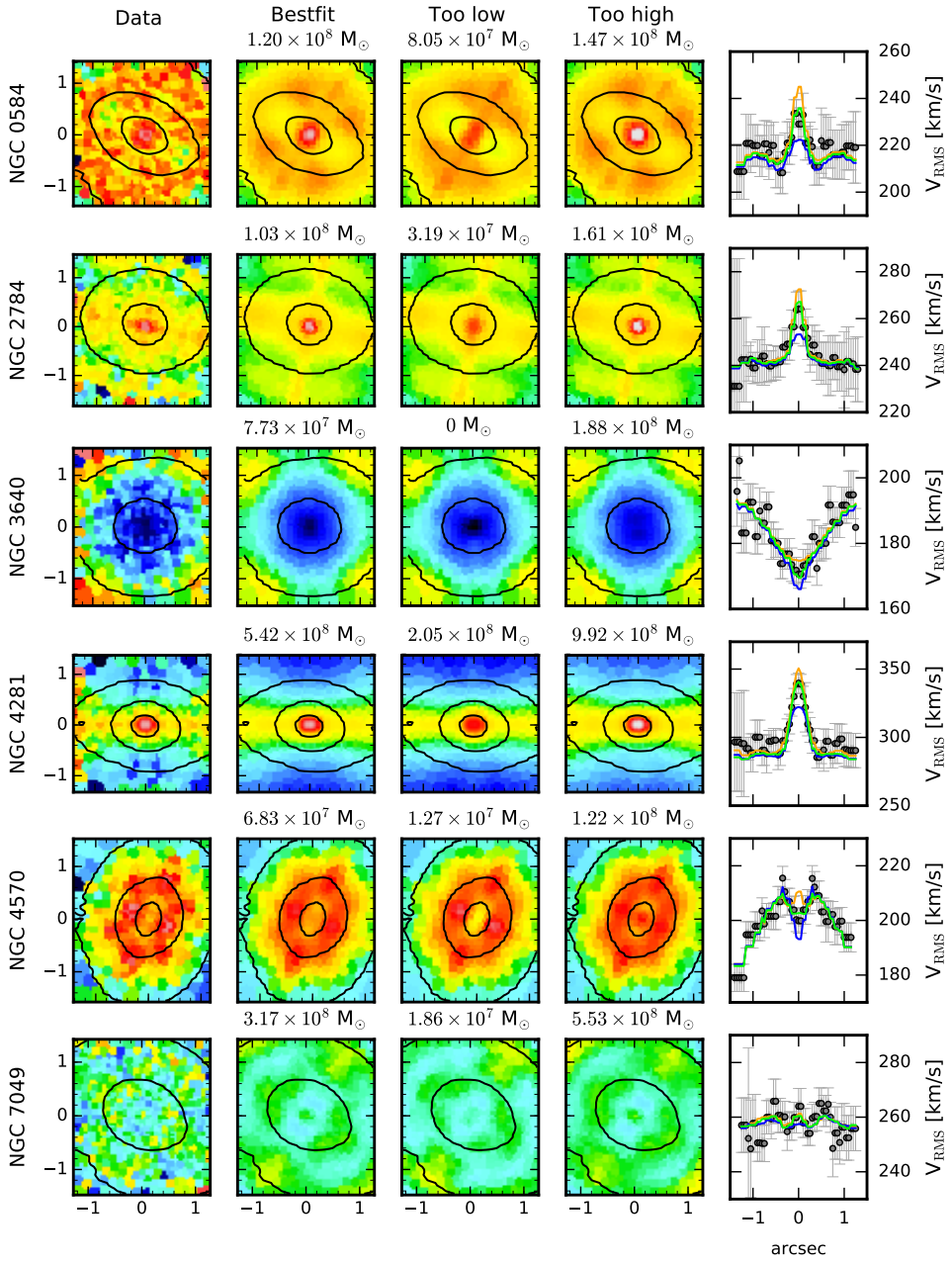


**Figure 3.8 —** Comparison of the $V_{\rm rms} = \sqrt{V^2 + \sigma^2}$ maps from the SINFONI data and the Schwarzschild models. Each row shows the maps of one galaxy, respectively. From left to right we present the observed symmetrized $V_{\rm rms}$ from the SINFONI data, and the $V_{\rm rms}$ maps of the Schwarzschild models from the best fitting, a too low and a too high $M_{\rm BH}$ as well as the profiles along the x=0 axis. The too low (blue) and too high (orange) black hole masses are chosen to be just outside of the $3\sigma\chi^2$ contours. All models are shown at the respective best-fitting $M/L$. The high- and low-mass models are clearly ruled out for all galaxies.

are characterized by three integrals of motion: the binding energy E, the vertical component of the angular momentum $L_z$, and a non-classical third integral $I3$ introduced by Ollongren (1962), see also Richstone (1982) , which are equally sampled by the orbit library. We typically trace each orbit for 200 oscillations through the system to have a representative characteristic within the entire equilibrium phase of the galaxy.
In a second step, each orbit is projected into the plane of the observables and the complete set of

orbits is combined to match the light distribution and the LOSVD of the galaxy by assigning a weight in a non-negative least-squared (NNLS) fit (Lawson & Hanson 1974). Compared to the JAM models, where we approximated the velocity second moments as the dispersion of a Gaussian, the Schwarzschild modeling method fits the full LOSVD.

We constructed the Schwarzschild models along a grid of radially constant dynamical $M/L$s and the mass of the black hole $M_{\rm BH}$. We began the modeling procedure by running coarse parameter grids centered on the best-fitting parameters ($M_{\rm BH}$, $M/L$) derived from the JAM models in Section 5.2. These models were improved iteratively by running finer and finer grids centered on the respective $\chi^2$ minimum of the coarse grid. Our final grids were then built with 21 $M_{\rm BH}$ and 21 $M/L$ equally spaced values for each galaxy. We only had to compute the orbit libraries for the different black hole masses as the orbits depend on the shape of the galaxy potential. The different $M/L$ values only scale the potential and thus the orbit libraries can be rescaled to match the different $M/L$ a posteriori. Each orbit library consists of $21 \times 8 \times 7 \times 2$ orbit bundles, which are composed of $6^3$ dithers, making in total 508 032 orbits per black hole mass. These orbit libraries were then fitted to the symmetrized stellar kinematics and to the photometric model in a NNLS fit and $\chi^2$ values were calculated by fitting our Schwarzschild models to both small- and large-scale kinematics. We excluded the large-scale kinematics in the central $0.8''$ such that in the central regions only the more reliable high-resolution data was fitted. For the NNLS fitting, we applied a regularization of $\Delta = 10$ (analogous to Krajnović et al. 2009 and van der Marel et al. 1998) to impose an additional smoothing on the distribution function of the orbit weights. We present our final grids of Schwarzschild models for each of our six galaxies in Figure 4.6. Plotted on the grid is the $\chi^2$ distribution as a function of $M_{BH}$ and dynamical $M/L$ from which we deduced the best-fitting parameters within $3\sigma$ significance ($\Delta\chi = 11.8$). To smooth the topology of the $\chi^2$ contours, we applied the local regression smoothing algorithm LOESS Cleveland (1979), adapted for two dimensions (Cleveland & Devlin 1988) as implemented by Cappellari et al. (2013a, see footnote 3).

**Table 3.5 —** Summary of dynamical modeling results

| Galaxy | JAM $M_{BH}$ ($\times 10^8\ M_\odot$) | $M/L$ ($M_\odot/L_\odot$) | $\beta$ | $i$ (°) | $\chi^2/DOF$ | Schwarzschild $M_{BH}$ ($\times 10^8\ M_\odot$) | $M/L$ ($M_\odot/L_\odot$) | $\chi^2/DOF$ | $r_{SoI}/\sigma_{PSF}$ |
|---|---|---|---|---|---|---|---|---|---|
| (1) | (2) | (3) | (4) | (5) | (6) | (7) | (8) | (9) | (10) |
| NGC 584 | $1.93^{\pm 0.06}$ | $5.4^{\pm 0.1}$ | $0.05^{\pm 0.01}$ | $89^{\pm 3}$ | 4.35 | $1.34^{\pm 0.49}$ | $5.4^{\pm 0.2}$ | 0.99 | 1.6 |
| NGC 2784 | $1.69^{\pm 0.1}$ | $7.7^{\pm 0.3}$ | $0.04^{\pm 0.04}$ | $77^{\pm 13}$ | 1.86 | $1.03^{\pm 0.54}$ | $6.7^{\pm 0.7}$ | 1.08 | 1.8 |
| NGC 3640 | $0.99^{\pm 0.13}$ | $4.2^{\pm 0.1}$ | $0.14^{\pm 0.04}$ | $85^{\pm 9}$ | 13.90 | $0.77^{\pm 0.51}$ | $4.2^{\pm 0.2}$ | 1.65 | 1.1 |
| NGC 4281 | $4.91^{\pm 0.15}$ | $12.5^{\pm 0.2}$ | $-0.03^{\pm 0.02}$ | $75^{\pm 9}$ | 9.93 | $5.42^{\pm 0.80}$ | $9.3^{\pm 0.3}$ | 3.98 | 2.1 |
| NGC 4570 | $1.19^{\pm 0.09}$ | $6.6^{\pm 0.1}$ | $0.22^{\pm 0.02}$ | $74^{\pm 1}$ | 3.98 | $0.68^{\pm 0.20}$ | $5.5^{\pm 0.1}$ | 1.87 | 1.1 |
| NGC 7049 | $3.16^{\pm 0.84}$ | $11.4^{\pm 0.4}$ | $0.04^{\pm 0.04}$ | $44^{\pm 10}$ | 3.18 | $3.17^{\pm 0.84}$ | $11.9^{\pm 0.3}$ | 1.38 | 1.6 |

**Notes.** Column 1: Galaxy name. Column 2-6: Parameters of the JAM models (black hole mass, mass-to-light ratio, velocity anisotropy parameter, inclination of the galaxy and $\chi^2$ of the best-fitting model). Column 7-9: Parameters of the Schwarzschild models (black hole mass, mass-to-light ratio in the HST band specified in Table 3.4 and $\chi^2$ of the best-fitting model). Column 10: Comparison of the black hole sphere-of-influence (calculated with the central velocity dispersion $\sigma_0$) and the spatial resolution of the observations (measured by the narrow component of the AO PSF).

For each galaxy, we can constrain the upper and lower limit of the black hole masses. The best-fit values are presented in Table 4.5. Figure 4.6 also includes our JAM black hole mass measurements ($M_{\rm BH}$ values within 99.7% intervals from posterior, namely $3\sigma$) as gray shaded regions and the lowest possible black hole measurement based on the data resolution in combination with the SoI argument (blue dashed line). NGC 3640, NGC 4281, and NGC 7049 have a clear overlap between the $3\sigma$ uncertainties of the JAM and Schwarzschild models meaning they are fully consistent with each other. For the remaining galaxies we measure slightly smaller black hole masses than with the JAM method. We note that the presented uncertainties on our black hole mass measurements are predominantly formal random errors from the dynamical modeling and as such they underestimate the fuller systematic uncertainties, which we discuss in Section 6.1. In Figure 3.8, we compare the $V_{RMS}$ maps between the SINFONI data and the Schwarzschild models for the best-fit, a lower and higher $M_{\rm BH}$ (just outside the $3\sigma$ contours), as well as the profiles along the x-axis. The different models are even visually very different, such that we can clearly constrain the upper and lower limit of the black hole mass. A full comparison between our observed (symmetrized) kinematic maps and the best-fitting Schwarzschild models with all our LOSVD parameters for both the SINFONI and large-scale data is shown in Appendix 5. The models can reproduce all of the kinematic features very well, both on the high-resolution SINFONI data and the large-scale data.
NGC 4281 and NGC 7049 have an unusually large $M/L$, but roughly comparing the derived value of NGC 4281 (F606W band) with the value from Cappellari et al. (2013a) who derived a value of 9.1 for the r band by applying dynamical JAM models on the ATLAS$^{3D}$ data only, our value is fully consistent.

# 6 Discussion

The results that we recovered from our dynamical models are only robust when the assumptions on the models are valid. Therefore, we further investigated a number of systematic error sources that could have affected our results. In that respect, the choice of distance D does not influence our conclusions but sets the scale of our models in physical units. Specifically, lengths and masses are proportional to D, while $M/L$ scales as $\mathrm{D}^{-1}$.

## 6.1 Systematic uncertainties

**Variations in stellar populations**

Various radial gradients have been found for different stellar population properties in early-type galaxies. For instance, early-type galaxies typically show color gradients because the central regions are redder than the galaxy outskirts (Peletier et al. 1990; Wu et al. 2005). Metallicities often follow a negative trend with radius (i.e., the metallicity decreases when the radius increases), while the age gradient is moderately flat (Kuntschner et al. 2010; Li et al. 2017a). The mentioned gradients imprint their signature on the stellar $M/L$, which is thus expected to increase toward the center. Furthermore, variations in the stellar initial mass function (IMF) corresponding to a larger percentage of low-mass stars can have an additional effect on the $M/L$ variation. Negative stellar $M/L$ gradients were observationally confirmed for local early-type galaxies (e.g., recently in Boardman et al. 2017; Sarzi et al. 2018; Vaughan et al. 2018). In the previous section, we assumed the $M/L$ to be constant for simplicity and this is possibly problematic. However, ignoring the stellar $M/L$ gradients can lead to overestimating the dynamical $M/L$ and therefore also the central black hole mass (McConnell et al. 2013; Krajnović et al. 2018a). On the other hand, the stellar $M/L$ usually runs contrary to the dark matter content, which is low in the center

but increases toward the outskirts of the galaxy. Therefore, including a nearly constant dynamical $M/L$ must not always be a bad assumption in dynamical modeling (see Chapter 2) in particular, when modeling the stellar kinematics observed over a wide range of radial scales.

In our first dynamical modeling attempt, we assumed a constant dynamical $M/L$ for both Jeans and Schwarzschild dynamical models. Comparing the dynamical $M/L$ derived from the JAM models (where we only used the central kinematics <1.5″) and the Schwarzschild models, we noticed a significant (>10%) difference for half of our sample: NGC 2784, NGC 4281, and NGC 4570. We considered that the dynamical $M/L$ difference could be caused by stellar population variations. In order to study the effect of spatial variations in the stellar populations, we followed the same method as in McDermid et al. (2015) and Chapter 2 and applied a mass-weighted stellar population synthesis for NGC 4570. We chose NGC 4570 for this test as its data had the best S/N and it did not suffer from dust contamination.

The ATLAS$^{3D}$ IFU spectra of NGC 4570 were co-added in growth curves with increasing circular aperture sizes having radii between 0.5 and 25 arcsec and then fitted with a linear combination of MILES simple stellar population (SSP) model spectra (Vazdekis et al. 2010) using the pPXF routine. We used two different sets of template model spectra assuming either a unimodal IMF of slope 1.30, which equals a Salpeter (1955) IMF, or a Kroupa (2001) revised IMF. For each IMF choice, we used 350 SSP template spectra spanning a grid of 50 ages logarithmically spaced between 0.06 to 17.78 Gyr and 7 metallicities [Z/H] = [-2.32, -1.71, -1.31, -0.71, -0.40, 0.00, 0.22]. In addition, we also kept track of the stellar and stellar remnant mass $M_*$ and the r-band luminosity of each stellar model of the template library. Each of the template SSP spectra is assigned weights in the pPXF fit, which are smoothed out for models having similar ages and metallicities to ensure a smooth star formation history solution and suppress the noise in the final weights distribution. The smoothing is applied by adding a linear regularization to the pPXF fit, which is chosen such that the difference in $\chi^2$ between regularized and non-regularized fit equals $\sqrt{2N}$, where N is the number of good pixels in the spectrum. We then calculated the mass-weighted stellar $M/L$ for each radial bin using the tracked stellar mass and r-band luminosity from the SSP models and using equation (5) from Chapter 2.

The derived $M/L$ profiles of NGC 4570 for the two different IMFs, the metallicity and age profiles are shown in Figure 3.9. Within the effective radius, a negative $M/L$ gradient on the order of 10-20 % of the central $M/L$ is clearly visible, which has to be accounted for in the dynamical models. The gradient is very strong between 3″and 10″and flattens out for larger distances. Furthermore, while the shape of the $M/L$ profile does not depend on the choice of the IMF, we note that their values differ by about 0.66 $M_\odot/L_\odot$ owing to the ratio of high-mass to low-mass stars within the different IMFs. Recent papers have suggested a trend in IMF with $\sigma_e$, in such a way that low $\sigma_e$ (<250 km s$^{-1}$) typically follow Kroupa-like IMFs, while galaxies with large $\sigma_e$ follow Salpeter-like or heavier IMFs (e.g., Cappellari et al. 2012, 2013a; Posacki et al. 2015; Li et al. 2017a). Having velocity dispersions between 170 km s$^{-1}$ and 245 km s$^{-1}$ our sample galaxies thus would likely follow a Kroupa-like IMF but are located in the transition zone. In addition, IMF gradients have been found to follow the radial trend of the stellar metallicity (e.g., Martín-Navarro et al. 2015; Sarzi et al. 2018) which gives even more reasons to consider bottom-heavy IMF forms as well. That is why we decided to derive the $M/L$ for both IMFs and test them in our dynamical models.
The derived $M/L$ values were then multiplied with the luminosity model MGE at the respective distance from the galaxy center (assuming an aperture size on the order of MGE $\sigma_j$ from Section 5.1) and included in the dynamical Schwarzschild models as mass density. We emphasize

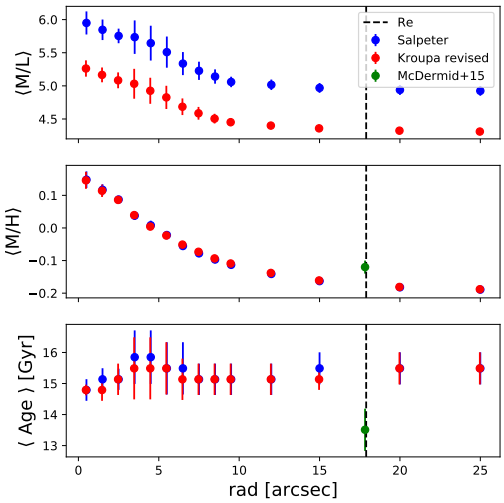


**Figure 3.9 —** Profiles of $M/L$ derived from stellar population analysis of the SAURON spectra combined over different aperture sizes between 0.5 and 25″. The two colors specify whether the MILES stellar templates were created based on a Salpeter IMF ($\alpha$=1.3) (blue) or a revised Kroupa IMF (red). The dashed line denotes the effective radius of the galaxy where we compare our measurements with measurements from McDermid 2015 as a consistency check. The discrepancy between the measurements (lower age and larger metallicity) arises because those authors capped their MILES library at 14 Gyrs and thus, used a different stellar library.

that we only included the $M/L$ gradients in the Schwarzschild models as the JAM models only trace the galaxy potential within 1.5″where the stellar $M/L$ is approximately constant. However, when constructing the Schwarzschild models, we also include stellar orbits from greater distances, which could feel the effect of the observed $M/L$ gradient. In order to account for the two possible IMFs, we ran the Schwarzschild grid for the two $M/L$ profiles independently. We present the final black hole masses derived from the Schwarzschild models in combination with a variable $M/L$ in Table 3.6. We find two main results from this analysis: First, both IMFs give very consistent results, which was expected as the shape of their $M/L$ gradient is very similar; second, including $M/L$ variations in the Schwarzschild models reduces the derived black hole mass by about a factor of 1.5 (30%). The mass of the SMBH is decreased as more mass is included in the stellar component and the impact on the black hole mass may have been even more important if we could have accounted for stellar population gradients down to the resolution of our SINFONI data. Our test agrees with McConnell et al. (2013) who noticed that the SMBH mass decreases by about 20-30% by taking $M/L$ gradients into account. On the other hand, Cappellari et al. (2002) only found negligible variations when allowing for $M/L$ gradients which were within the statistical uncertainties. While this test provides an interesting implication on the SMBH scaling relations, we will postpone a more detailed discussion for a future paper in the series when we can apply a detailed test to all 18 galaxies of the sample. This test will be crucial for the three galaxies of our sample that contain nuclear disks that are often accreted and thus likely have different stellar populations and varying $M/L$ gradients. Furthermore, it will be interesting to test if our dusty galaxies follow positive $M/L$ gradients due to ongoing star formation and how much these gradients will affect the derived black hole measurements. A solution to the uncertainties introduced by possible unknown population gradients consists of allowing the total mass profile to differ from the distribution of the tracer population producing the kinematics (as done, e.g., in Mitzkus et al. 2016; Poci et al. 2016; Li et al. 2017a). In black hole studies, this is generally carried out by allowing for a dark matter profile in addition to a stellar component (see Sec. 6.1.2), but the very same approach will account for gradients in the stellar $M/L$ as well.

**Table 3.6 —** Schwarzschild dynamical modeling results with variable $M/L$

| Galaxy | $M_{\rm BH}[M_\odot]$ $(M_\odot)$ | $M/L_{\rm dyn}/M/L_*$ | IMF |
|---|---|---|---|
| (1) | (2) | (3) | (4) |
| NGC 4570 | $4.04^{+0.9}_{-1.2} \times 10^7$ | $0.98^{+0.02}_{-0.02}$ | Salpeter |
| | $4.2^{+0.6}_{-0.4} \times 10^7$ | $1.14^{+0.03}_{-0.03}$ | Kroupa rev |

**Notes.** Column 1: Galaxy name. Column 2: Derived black hole mass. Column 3: Derived ratio between stellar and dynamical $M/L$ and 5: Assumed IMF for deriving the stellar $M/L$.

### Dark matter

Our dynamical models only work under the assumption of self-consistence (mass follows light). Breaking this assumption by having significant amounts of dark matter in the center can lead to systematic changes in the black hole mass. (Gebhardt & Thomas 2009; Schulze & Gebhardt 2011; Rusli et al. 2013b). We tested the significance of the dark matter in the central regions of our galaxies using the radial acceleration relation (McGaugh et al. 2016; Lelli et al. 2017). As long as the galaxies stay in the linear regime of the radial acceleration relation ($g_{\rm dyn} > g_{\rm crit} = 1.2 \times 10^{-10}$ m s$^{-2}$) it is expected that the dark matter does not contribute extensively to the galactic potential. The total acceleration can be derived from the gravitational potential by $g_{\rm dyn}(R) = -\nabla\Phi_{\rm tot}(R) = V_c^2/R$, where $V_c$ is the circular velocity. We used the mass density (derived in Section 5.1) assuming the dynamical $M/L$ of the best-fitting Schwarzschild model (Table 4.5) to calculate a model circular velocity at a radius equal to the edge of our large-scale kinematical data for each of our target galaxies. Our analysis yielded total accelerations between $8.8 \times 10^{-9}$ and $9 \times 10^{-10}$ m s$^{-2}$ with the smallest acceleration found in NGC 3640. All values lie well above the critical acceleration, and we conclude that our galaxies have likely a negligible contribution of dark matter in the central region that does not affect the dynamical modeling significantly. This is consistent with more direct estimates of the dark matter content of our galaxies from Cappellari et al. (2013a) and Poci et al. (2016). Furthermore, the total accelerations determined in our galaxies are consistent with the accelerations of other ATLAS$^{3D}$ early-type galaxies analyzed by Lelli et al. (2017).

## 6.2 $M_{\rm BH} - \sigma_{\rm e}$ scaling relation

We populated the $M_{\rm BH} - \sigma_{\rm e}$ diagram with the compilation of dynamical black hole masses from Saglia et al. (2016) and Krajnović et al. (2018b). We then added our derived Schwarzschild $M_{\rm BH}$ measurements in combination with the bulge effective velocity dispersions from Cappellari et al. (2013a)(see Table 4.1). The diagram is shown in Figure 3.10. Our measurements are located in the intermediate-mass regime for early-type galaxies where the scatter is very tight. In Figure 3.10, we furthermore show the scaling relations derived in McConnell & Ma (2013), Saglia et al. (2016), and Savorgnan & Graham (2015). All of our black hole mass measurements follow the black hole scaling relation closely. Except for NGC 4281, our measurements are slightly below the scaling relation but within the $1\sigma$ scatter of the relation; NGC 7049 deviates slightly more from the scaling relation.

The massive black holes in NGC 584 and NGC 3640 have already been measured indirectly in the literature. In their study Dullo & Graham (2014) recognized that NGC 584 and NGC 3640 show signatures for a partially depleted core, which can be translated into a black hole

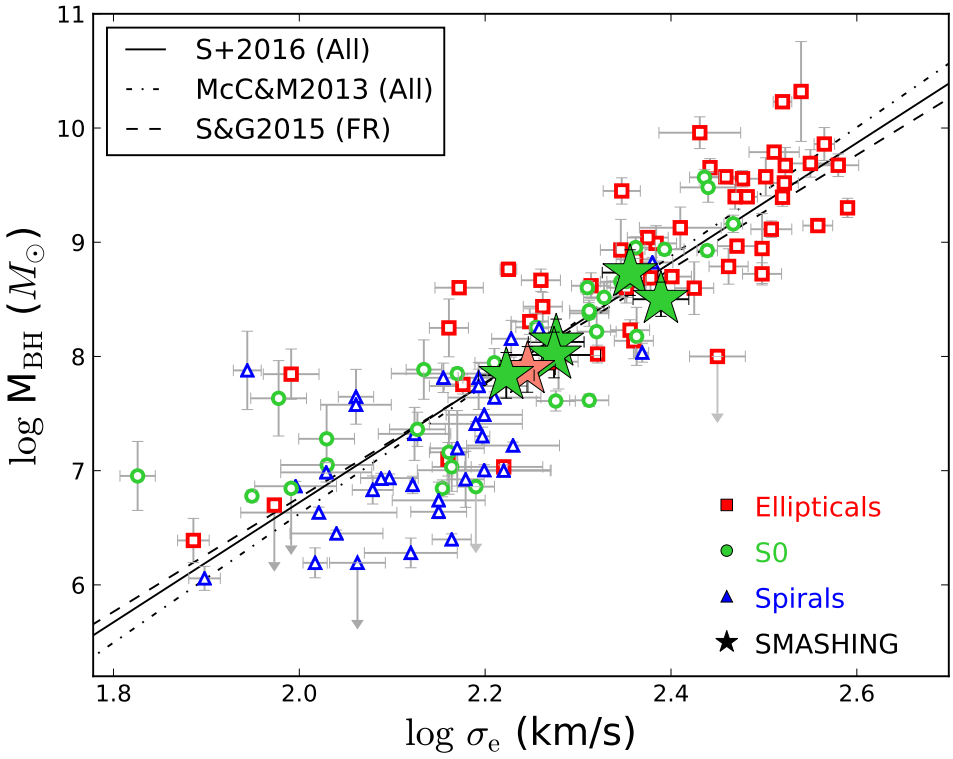


**Figure 3.10 —** Supermassive black hole mass – effective velocity dispersion relation based on the compilation of Saglia et al. (2016). The color scheme indicates the morphological type of the galaxies: elliptical (red), lenticular (green), and spiral (blue). To visualize the general trend we added the global scaling relations by Saglia et al. (2016) and McConnell & Ma (2013) for all galaxy types (solid and dash-dotted line) as well as Savorgnan & Graham (2015) for fast-rotator galaxies (dash-dashed line). Our measurements (highlighted as stars) lie very well on the two scaling relations.

mass of $M_{\rm BH,dep} = (1.95 \pm 1.1) \times 10^8 M_\odot$ for NGC 584 and $M_{\rm BH,dep} = (9.77 \pm 1.1) \times 10^7 M_\odot$ for NGC 3640. These values are consistent with our dynamical mass measurements of $M_{\rm BH,dyn} = (1.34 \pm 0.49) \times 10^8 M_\odot$ for NGC 584 and of $M_{\rm BH,dyn} = (7.73 \pm 0.51) \times 10^M_\odot$ for NGC 3640. We also note that our dynamical mass measurements derived from the Jeans modeling match perfectly with the SMBH masses derived from the depleted cores.

While our measurements follow the general trend of previous mass measurements, a systematic offset seems to emerge between SMBHs in early-type and late-type host galaxies, the latter being significantly lower. Graham & Scott (2013) noted that this offset is also seen for barred versus non-barred galaxies (barred galaxies having larger velocity dispersion). The authors note that most of the late-type galaxies on the $M_{\rm BH} - \sigma_{\rm e}$ relation are actually barred, and it is not clear at this moment if the departure of the late-type galaxies from the scaling relation for the early-type galaxies is driven by bars or is typical for all late-type galaxies. Furthermore, black hole masses measured via $H_2O$ megamasers (e.g., Greene et al. 2010) in possibly barred galaxies also seem to be systematically lower than dynamical black hole mass measurements (which is nicely visualized in Figure 1 of van den Bosch 2016, see also Davis et al. 2019, 2018a). In Section 6.1 we recognized that by taking into account a variable $M/L$ the dynamical mass measurements could shift down by a factor of about 1.5. The radial $M/L$ variation might even be more important for late-type galaxies, except for cases where the $M_{\rm BH}$ is estimated by directly

observing tracers within the SMBH SoI, such as $H_2O$ megamasers. We will investigate this implication in a future paper of this series. Independent from the $M/L$ variation, together with the recently published dynamical mass measurements by Krajnović et al. (2018b) our measurements strengthen the idea of early-type galaxies having more massive black holes than (barred) late-type galaxies and thus following different $M_{BH} - \sigma_e$ relations (e.g., Terrazas et al. 2017; Davis et al. 2019; Martín-Navarro et al. 2018).

## 7 Summary and conclusions

In this work, we have presented the black hole mass measurement of six nearby early-type galaxies (NGC 584, NGC 2784, NGC 3640, NGC 4281, NGC 4570, and NGC 7049). Our measurements are based on AO-assisted K-band SINFONI IFU observations complemented by ground-based IFU data from MUSE, VIMOS, and SAURON from the ATLAS$^{3D}$ survey. All of our target galaxies show regular rotation, and except for NGC 3640 and NGC 7049, a velocity dispersion that increases toward their center. NGC 3640 contains a velocity dispersion dip of about 30 km s$^{-1}$, while NGC 7049 seems to have a flat velocity dispersion profile. This finding is consistent with the kinematic features of the large-scale SAURON data from the ATLAS$^{3D}$ survey and our VIMOS and MUSE data. We combined our kinematic results with photometric mass-models based on the composition of HST, SDSS, and CGS survey data to build dynamical models to measure the mass of the central black holes. We constrained the parameter space of possible masses and $M/L$s using Jeans Anisotropic Modeling on our SINFONI data and then created axisymmetric orbit-superposition Schwarzschild modeling based on both central and large-scale IFU data to derive robust results. We derive black hole masses of $(1.3 \pm 0.5) \times 10^8 M_\odot$ for NGC 584, $(1.0 \pm 0.6) \times 10^8 M_\odot$ for NGC 2784, $(7.7 \pm 5) \times 10^7 M_\odot$ for NGC 3640, $(5.4 \pm 0.8) \times 10^8 M_\odot$ for NGC 4281, $(6.8 \pm 2.0) \times 10^7 M_\odot$ for NGC 4570, and $(3.2 \pm 0.8) \times 10^8 M_\odot$ for NGC 7049, which fit well with the recent black hole – $\sigma_e$ scaling relations.

For three galaxies we find a slight discrepancy in the derived dynamical $M/L$ of the two different methods, as the central values are larger than the $M/L$ derived from the combination of small-scale and large-scale data. Dynamical models typically assume a constant $M/L$ for the sake of simplicity, which is usually not the case in observed galaxies. To test this assumption, we derive the stellar $M/L$ profile from stellar population modeling for the test case of NGC 4570, which does not suffer from dust contamination and has the best quality data. The stellar population modeling shows a negative gradient of about 20% within the effective radius of the galaxy, which is based on variations in stellar age and metallicity. This negative gradient is then included in the dynamical Schwarzschild models, and we derive a black hole mass that is lower by almost 30%, irrespective of further possible stellar $M/L$ re-scaling due to radially constant IMF variations. We conclude that the inclusion of $M/L$ variations has an effect on the order of the general uncertainty of the measurement, but it should be included in dynamical models to lower the systematic uncertainties, which are still very large in dynamical modeling. As was already suspected in different works, this has an interesting implication on the black hole scaling relations as different dynamical methods still suffer from partially inconsistent results. We caution that careful additional analysis of the effect of $M/L$ variations on dynamical models is urgently needed in future studies.

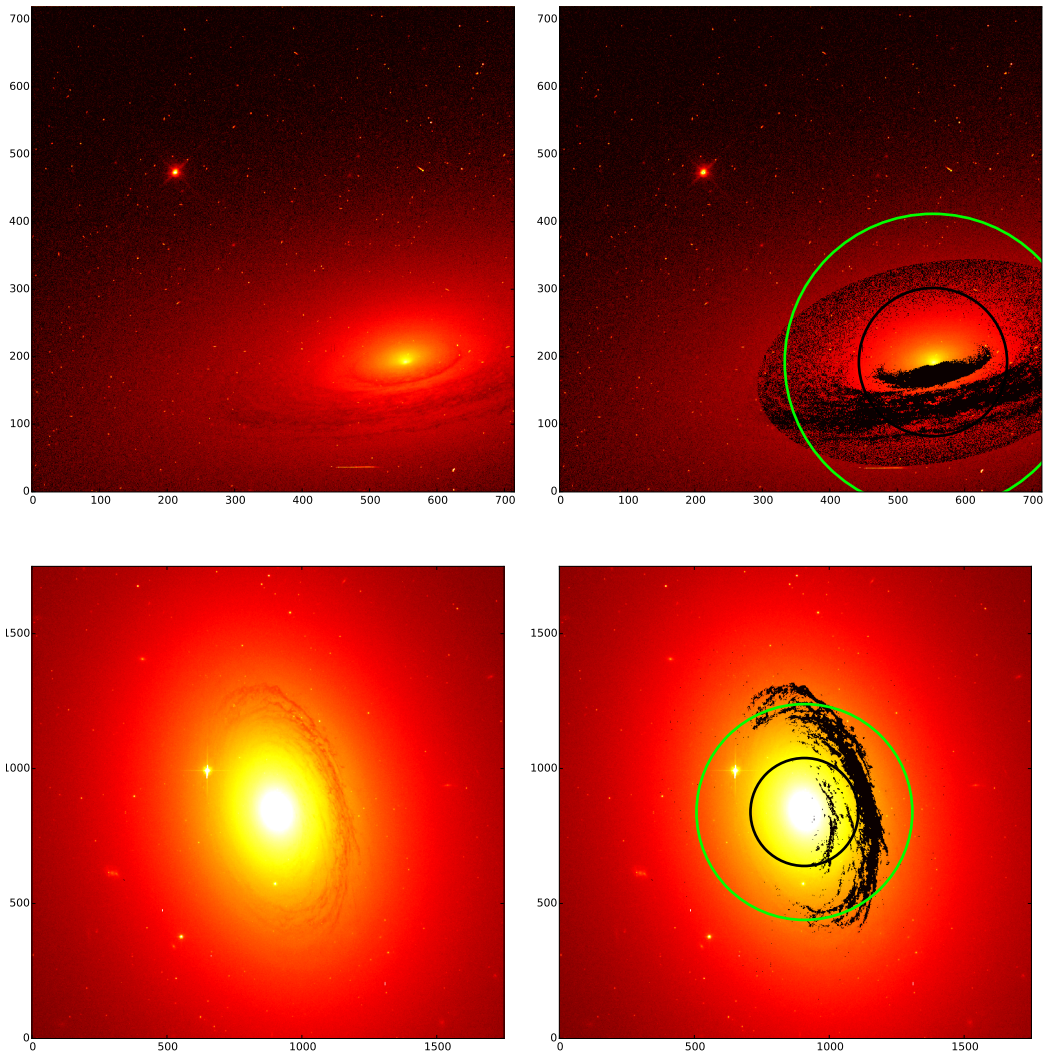

**Figure 3.11 —** Dust-masked region of the HST WFPC2 and ACS images of NGC 4281 (upper panels) and NGC 7049 (lower panels), respectively. The left panels show the original HST images; the right panels show the same image overplotted with the dust mask (black) and circular regions with $r < 5''$ (black) and $r < 10''$ (green), which encompass the region being used for the MGE modeling.

## 8 Dust-corrected images

## 9 Large-scale kinematics

## 10 Comparison of the Schwarzschild dynamical models with the symmetrized data

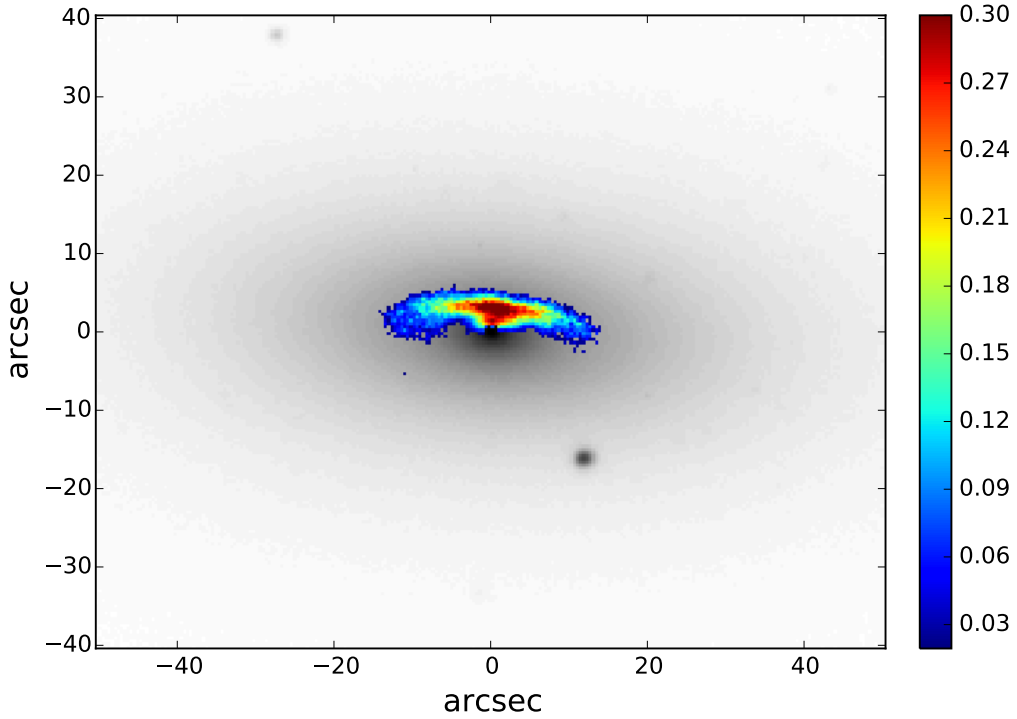


**Figure 3.12 —** Dust-corrected central region of the SDSS r band image of NGC 4281. The correction was only applied within a major axis distance of 16″ (see caption of Fig.A.2). The overplotted color coding indicates the degree of the dust correction, where 0.1 means that the observed flux increased by 10 %.

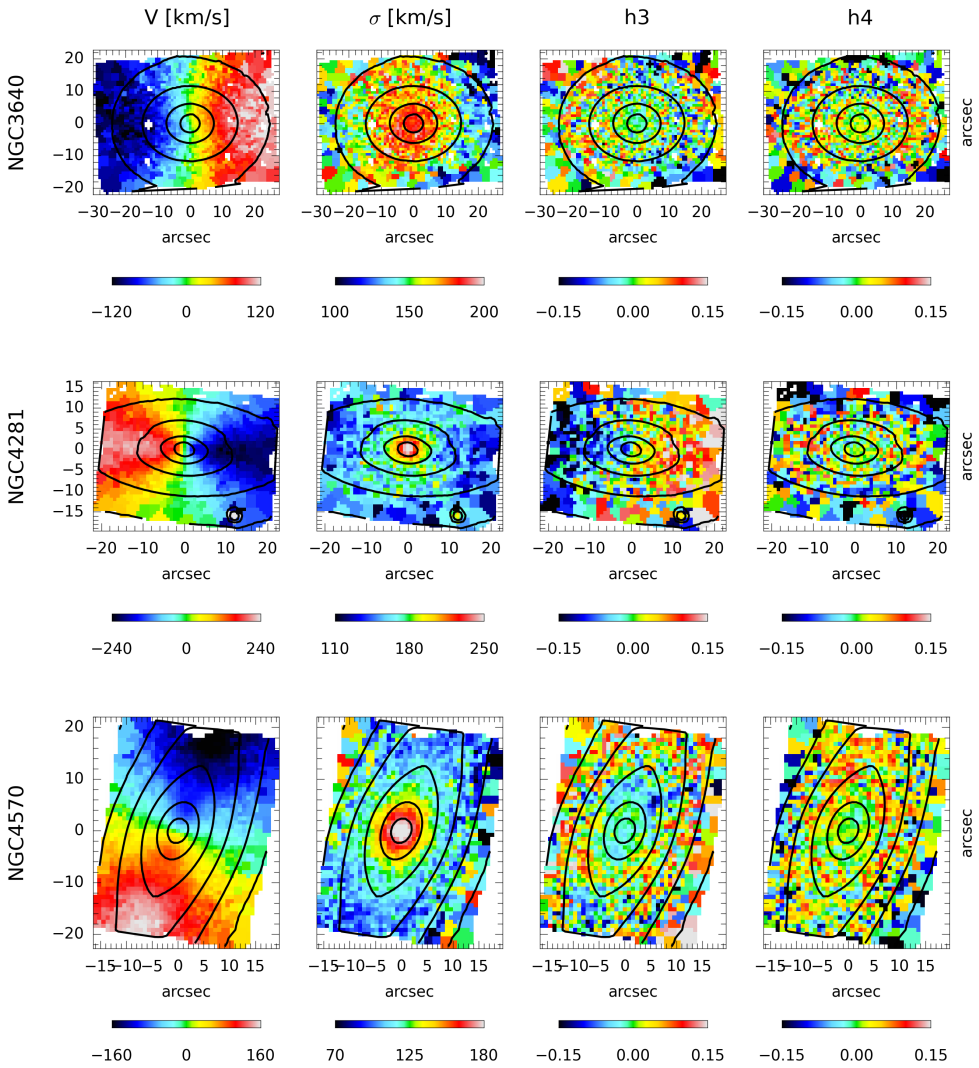


**Figure 3.13 —** Large-scale SAURON stellar kinematics of NGC 3640, NGC 4281, and NGC 4570. Shown are the mean velocity V, velocity dispersion $\sigma$, and the $h_3$ and $h_4$ Hermite polynomials extracted by using pPXF. The galaxies are part of the ATLAS$^{3D}$ project and detailed described in Cappellari et al. (2011). The image orientation is such that north is up and east is left.

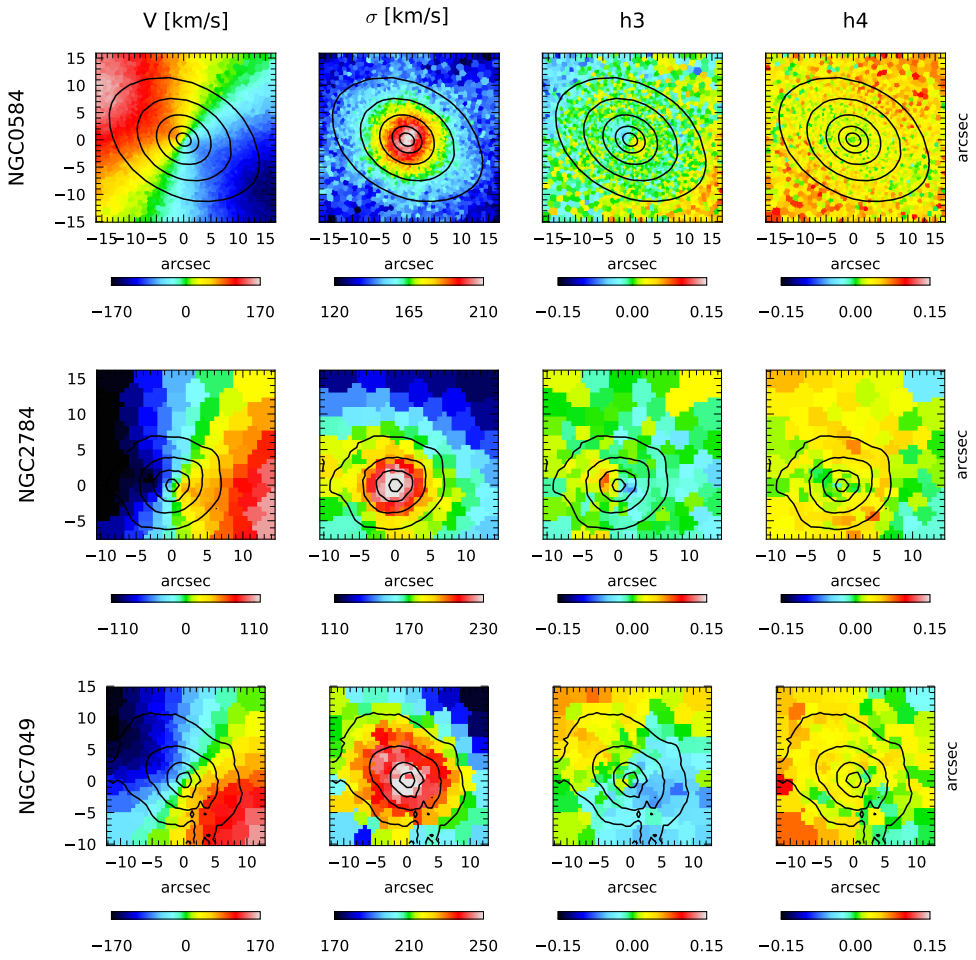


**Figure 3.14 —** Large-scale stellar kinematics of NGC 584 (MUSE), NGC 2784 (VIMOS), and NGC 7049 (VIMOS). Shown are the mean velocity V, velocity dispersion $\sigma$, and the $h_3$ and $h_4$ Hermite polynomials extracted by using pPXF. The data reduction and extraction of the kinematics are detailed described in Section 4.3. The image orientation is such that north is up and east is left.

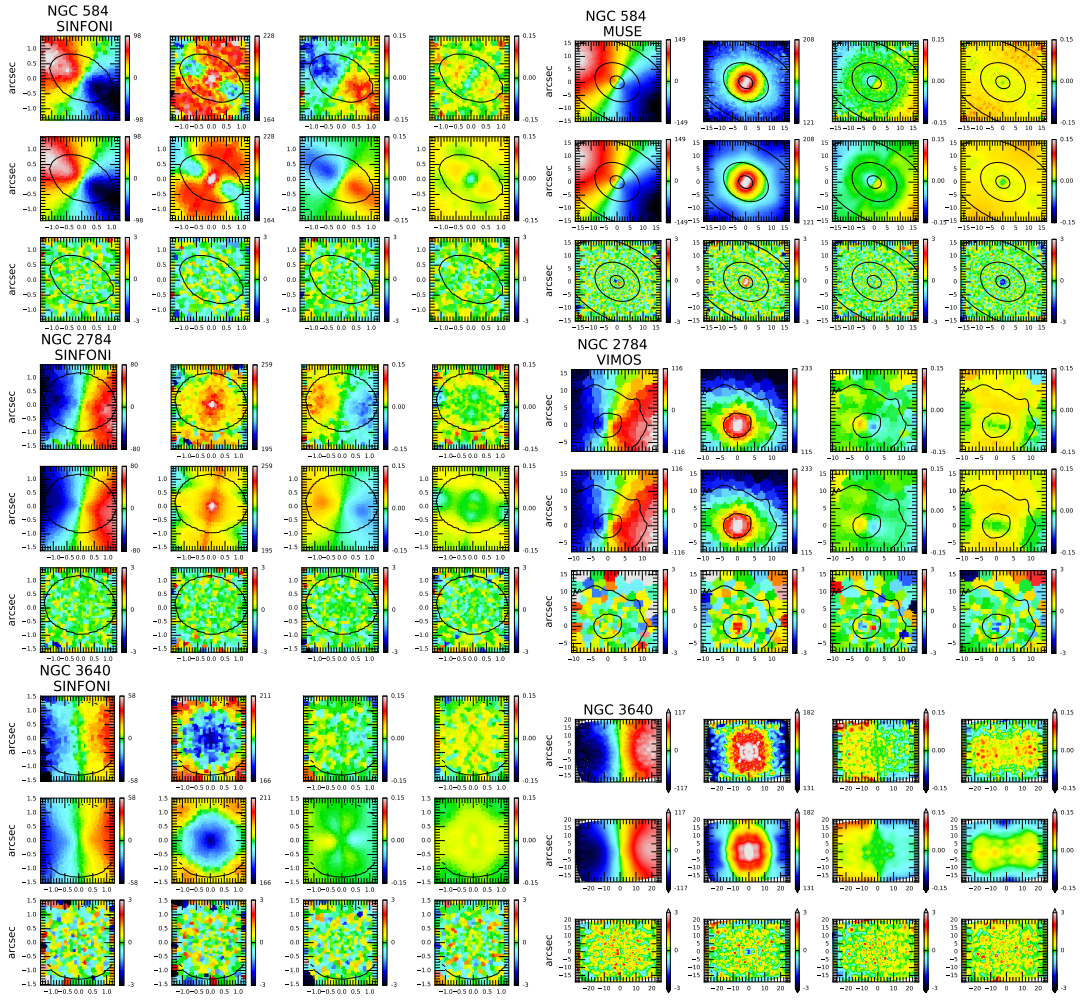


**Figure 3.15 —** Comparison between symmetrized kinematic data and best-fitting Schwarzschild models for the galaxies NGC 584, NGC 2784, and NGC 3640. For each galaxy we show the SINFONI data on the left side and the large-scale data on the right side. The panels are ordered as follows: From left to right: mean velocity, velocity dispersion, and h3 and h4 Gauss-Hermite moments. From top to bottom: symmetrized data, model for the best-fitting parameters from Table 4.5, and residual map defined as difference between the Schwarzschild model and observed kinematics divided by the observational errors.

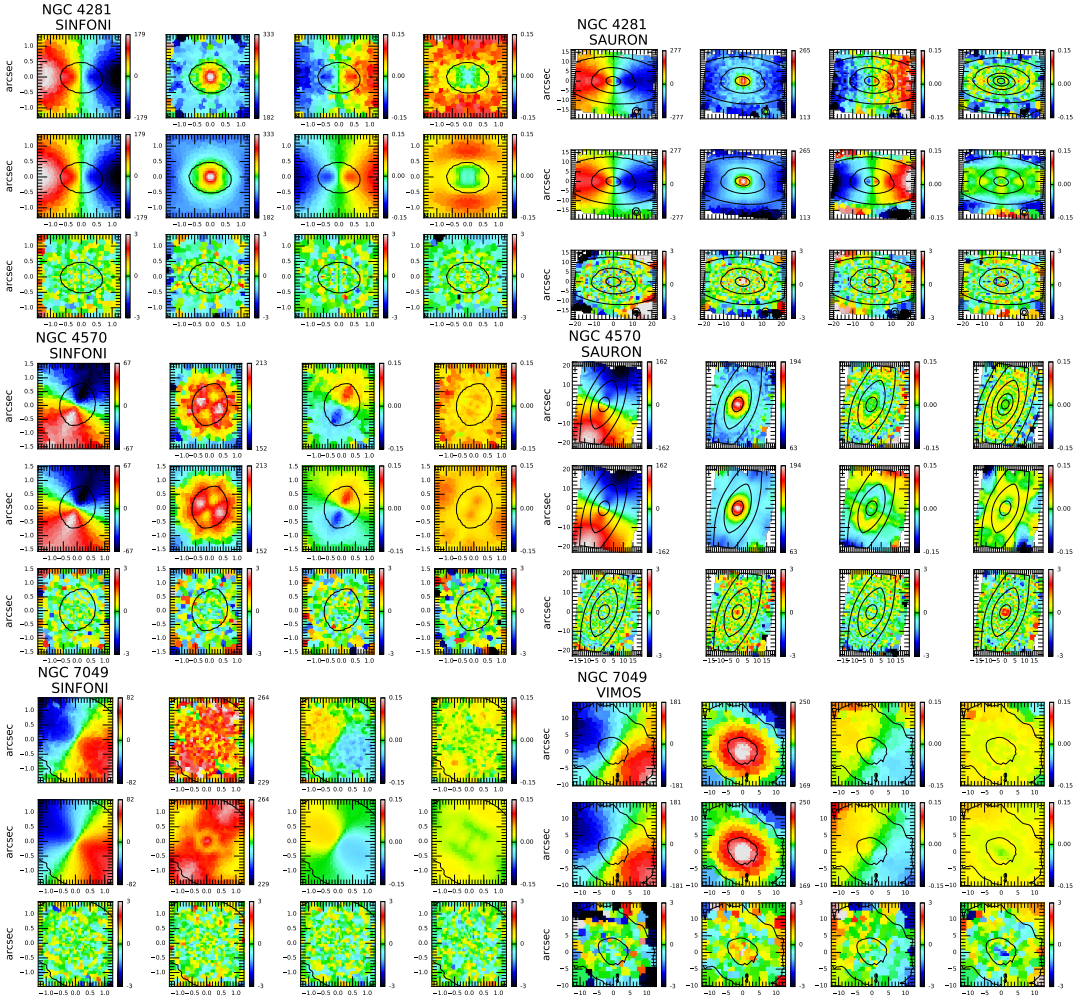


**Figure 3.16 —** Comparison between symmetrized kinematic data and best-fitting Schwarzschild models for the galaxies NGC 4281, NGC 4570, and NGC 7049. For each galaxy we show the SINFONI data on the left side and the large-scale data on the right side. The panels are ordered as follows: From left to right: mean velocity, velocity dispersion, and h3 and h4 Gauss-Hermite moments. From top to bottom: symmetrized data, model for the best-fitting parameters from Table 4.5, and residual map defined as difference between the Schwarzschild model and observed kinematics divided by the observational errors.

# 4 Probing the high-mass end of supermassive black holes with adaptive-optics assisted SINFONI observations

**Sabine Thater, Davor Krajnović et al.**

— A version of this chapter will be submitted to *Astronomy & Astrophysics*. The chapter contains preliminary results which might still change until publication. —

Abstract

Supermassive black holes are believed to play a major role in the evolution of galaxies. In this work, we report six new supermassive stellar-kinematics-based black hole mass measurements of massive early-type galaxies. Most of our galaxies show evidence for triaxiality making them the ideal sample to compare axisymmetric and triaxial Schwarzschild models. We have extracted the stellar kinematics from SINFONI+AO, MUSE, VIMOS and SAURON observations. The stellar kinematic information was then combined with photometric information to build spherical Jeans models and axisymmetric Schwarzschild models independently. From the JAM models, we obtained black hole masses of $(5.26\pm0.79)\times10^8$ $M_\odot$ for NGC 3706, $(2.51\pm2.08)\times10^8$ $M_\odot$ for NGC 4636 and $(1.78 \pm 1.63) \times 10^9$ $M_\odot$ for IC 4329 at $3\sigma$ confidence level. For the other galaxies we cannot constrain the masses robustly and only estimate upper limits of $4.21 \times 10^8$ $M_\odot$ for NGC 3923, $1.04 \times 10^9$ $M_\odot$ for NGC 4261 and $1.73 \times 10^9$ $M_\odot$ for IC 4296. Our axisymmetric models have difficulty to reproduce the observed stellar kinematics. It is not clear yet what could have caused these problems: bad data quality, insufficient spatial resolution or need for triaxiality. In the future, we will work on improving our axisymmetric models and compare them with triaxial Schwarzschild models.

# 1 Introduction

Supermassive black holes are known to be hosted by almost all massive galaxies in the local universe and up to large redshifts. Their role in the evolution of galaxies is not yet understood, but the existence of tight scaling relations between black hole mass and different galaxy properties imply some kind of co-evolution between massive black holes and their host galaxies (e.g., reviews by Kormendy & Ho 2013; Graham 2016; Saglia et al. 2016; Mezcua 2017). Having estimated almost 200 black hole masses dynamically by now (see compilation by van den Bosch 2016), an increased scatter for low-mass and high-mass galaxies became noticeable, which might indicate a non-universal origin of the scaling relations (see Chapter 1). While the low-mass scatter is probably generated by secular versus non-secular evolution in late-type galaxies (as indicated by bar and pseudobulge components), the high-mass end tells a different story. Early photometric observations have shown that massive early-type galaxies can be distinguished in core and power-law galaxies depending on the shape of their nuclear profiles (Ferrarese et al. 1994; Lauer 1985; Lauer et al. 1995; Faber et al. 1997; Rest et al. 2001). Instead of a continuously steep power-law surface brightness cusp, core galaxies show a shallow central light profile, depleted of stars with respect to the extrapolation of outer surface brightness distribution (Graham et al. 2003). The cores have typical sizes between 50 and 500 pc and scale with the mass of the central black holes (Rusli et al. 2013a; Dullo & Graham 2014; Thomas et al. 2016). While core scouring by merging black holes (Milosavljević et al. 2002) after dissipationless mergers is a popular scenario to explain this relation, the formation of depleted cores is still strongly debated. In addition to the depleted core features, massive ellipticals often show boxy instead of disky isophotes and are kinematically classified as slow-rotators (Cappellari et al. 2007; Emsellem et al. 2007), although in rare cases core galaxies can also be found in fast rotators (Krajnović et al. 2013). The different phenotypes of early-type galaxies are indeed also imprinted in the scaling relations. While the kinematical classification into fast and slow rotation might not have a big effect on the $M_{\rm BH} - \sigma$ relation (Savorgnan & Graham 2015), Graham (2012), Scott et al. (2013b) and Graham & Scott (2013) showed that galaxies with and without cores follow different $M_{\rm BH} - M_*$ relations, which might be responsible for the increased scatter in the high-mass end. On the other hand, it was shown that the evolution of black holes might also differ for low and high-mass galaxies (e.g., Krajnović et al. 2018a). While accretion of gas is the main process to grow black holes, high-mass black holes can also acquire a significant amount of mass due to black hole merging after dry mergers (Volonteri 2010) This effect can be up to a factor of two for most massive galaxies (Yoo et al. 2007; Kulier et al. 2015). As it is not clear if the different evolutionary paths of the central black holes or the host galaxies are the main driver for the large scatter in the high-mass end, it is important to obtain more black hole mass measurements in massive galaxies and examine their evolution in great detail.

We present new black hole measurements of six massive galaxies from integral field unit (IFU) data obtained with the SINFONI instrument with adaptive optics. Our sample galaxies were selected to address the origin of the increased scatter in the high-mass end of the scaling relations. Massive galaxies often show triaxial features which cannot be described by axisymmetric models. In this work, we want to learn how black hole mass measurements with axisymmetric and triaxial dynamical models compare for galaxies which are evidently triaxial. This comparison is usually done in an axisymmetric limit and it is not clear if the discrepancies (e.g., van den Bosch & de Zeeuw 2010; Ahn et al. 2018) come from the different assumptions (triaxial versus axisymmetric) or from numerical effects of the implementations.

**Table 4.1 —** The sample

| Galaxy | Type | Distance (Mpc) | Linear scale (pc arcsec$^{-1}$) | $M_K$ (mag) | $R_b$ (arcsec) | $R_e$ (arcsec) | $\sigma_e$ (km s$^{-1}$) | $i$ (°) | profile | $\lambda_{Re}$ | Large Scale |
|---|---|---|---|---|---|---|---|---|---|---|---|
| (1) | (2) | (3) | (4) | (5) | (6) | (7) | (8) | (9) | (10) | (11) | (12) |
| NGC 3706 | E | 43.1 | 209 | −25.10 | 0.11 | 30.6 | 270 | 79 | core | FR | −− |
| NGC 3923 | E4-5 | 21.0 | 102 | −25.09 | −− | 86.4 | 240 | 48 | power-law | SR | VIMOS |
| NGC 4261 | E2-3 | 30.8 | 149 | −25.18 | 1.18 | 38.0 | 265 | 89 | core | SR | ATLAS$^{3D}$ |
| NGC 4636 | E0-1 | 14.3 | 69 | −24.36 | 2.30 | 89.1 | 181 | 89 | core | SR | ATLAS$^{3D}$ |
| IC 4296 | E | 48.9 | 237 | −25.99 | 1.44 | 68.4 | 330 | 57 | core | SR | MUSE |
| IC 4329 | S0 | 56.2 | 272 | −25.74 | 0.79 | 120.0 | 296 | 67 | core | SR | MUSE |

**Notes.** Column 1: Galaxy name. Column 2: Morphological type (de Vaucouleurs et al. 1991). NGC 3706 was likely misclassified in the earlier work, and we adopt the classification by Dullo & Graham (2013). Column 3: Distance to the galaxy (taken from Cappellari et al. (2011) for SAURON/ATLAS$^{3D}$ galaxies or NED for VIMOS and MUSE galaxies), the uncertainties were calculated by dividing the NED standard deviations by $\sqrt{N}$ where N is the number of measurements. Column 4: Linear scale derived from the distance. Column 5: 2MASS total K-band magnitude (Jarrett et al. 2000). Column 6: Break radius from a core-Sérsic fit to the surface brightness profiles. Values are taken from Dullo & Graham (2014), Rusli et al. (2013a),Graham et al. (2003), Capetti et al. (2005) and Lauer et al. (2005). Column 7: Effective radius derived from B-band (CGS) or r-band (ATLAS$^{3D}$) imaging data. The values were taken from Ho et al. (2011) or Cappellari et al. (2013a) for ATLAS$^{3D}$ galaxies. Column 8: Effective velocity dispersion derived by co-adding the spectra of the large-scale optical IFU data in elliptical annuli of the size of the effective radius. For ATLAS$^{3D}$ galaxies taken from Cappellari et al. (2013a). Column 9: Inclination from Cappellari et al. (2013a) for ATLAS$^{3D}$ galaxies and Ho et al. (2011) for remaining galaxies. Column 10: the shape of the surface-brightness profile (core or power-law). Column 11: Angular momentum classification into fast and slow rotators taken from Emsellem et al. (2011). Column 12: Large scale kinematics data which is used for the Schwarzschild dynamical models. The SAURON data comes from the ATLAS$^{3D}$ galaxy survey.

NGC 3379 is the only "triaxial" galaxy for which different Schwarzschild models were tested, but it only has a minor twist in the photometry and shows only weak signs of triaxiality. Nevertheless, a change in black hole mass was noticed for this galaxy. This is the first study, in which three geometrically different codes will be compared. We present the first part of this work in this chapter. The structure of this chapter is as follows. We describe the details of the sample selection and our sample galaxies in Section 2. The different IFU observations and their data reduction are described in Section 3. In Section 4, we explain our kinematics extraction and present the kinematic maps. The kinematic information is combined with luminous mass models to construct spherical Jeans and axisymmetric Schwarzschild dynamical models in Section 5. We discuss our results and give an outlook on future work in Section 6.

## 2 Sample

We present in this chapter the six final galaxies of the SMASHING sample. The six galaxies have early-type morphology and belong to the most massive galaxies in the local universe. They have a core-profile (except for NGC 3923) and can kinematically be classified as slow-rotators (except for NGC 3706). An overview of the galaxy properties is found in Table 4.1. The target selection of our galaxies was described in detail in Chapter 1. To summarize the sample selection, we picked our target galaxies based on the following criteria:

- *resolvable sphere of influence (SoI)*: We calculated the SoI using black hole masses based on the scaling relation by Tremaine et al. (2002) and the velocity dispersions from the ATLAS$^{3D}$ survey reported in Cappellari et al. (2013b). If velocity dispersions were not available, we used the central velocity dispersions from Hyperleda and extrapolated them to the effective radius. This criterium set a limit in distance of about 60 Mpc for our massive galaxies with expected black hole masses of about $10^8\ M_\odot$.
- *availability of high-resolution imaging (HST):* A robust black hole mass measurement requires detailed knowledge of the light distribution in the galaxy center. The best possible spatial resolution can be obtained with HST imaging. As HST is a very competitive telescope, we decided to build our sample based on archival data. When selecting the sample galaxies, we made sure not to include galaxies with obvious bars or merger features.
- *observability with SINFONI:* SINFONI in combination with adaptive optics is next to NIFS the perfect instrument to measure supermassive black hole masses. It combines high spatial resolution close to that of HST with the capability to take spectra in dust-obscured galaxies. Due to its southern position in Paranal (24°40′ S), SINFONI can only observe objects of declination between $-70°$ and $20°$.
- *availablity of an NGS or TTS for LGS:* In order to achieve optimal spatial resolution, we made use of the adaptive optics system which supports the SINFONI instrument. In that case, we required the presence of a natural guide star close to the galaxy (d<60″) unless we used the laser guide star mode. When using the laser guide star AO, a tip-tilt star, a bright star (< 18mag) close to the galaxy, is usually needed to apply zero-order tip-tilt corrections. We often did not have a suitable tip-tilt star close to the galaxy and tip-tilt on the nucleus was not always possible, such that we applied the SINFONI Seeing Enhancer mode, which provided a slight improvement to the natural seeing.

**Table 4.2 —** Details of the SINFONI observing runs

| Galaxy | Date | PID | Pixel scale (mas) | N of exp. | N comb. exp. | $T_{exp}$ (min) | AO mode |
|---|---|---|---|---|---|---|---|
| (1) | (2) | (3) | (4) | (5) | (6) | (7) | (8) |
| NGC 3706 | 2013 May 9,10 | 091.B-0129(A) | 100 | 8 | 5 | 25 | LGS |
| | 2013 May 9,10 | 091.B-0129(A) | 250 | 8 | 7 | 35 | LGS |
| NGC 3923 | 2009 May 18,19 | 083.B-0126(B) | 250 | 8 | 4 | 40 | NGS |
| NGC 4261 | 2010 Apr 13 | 084.B-0086(A) | 250 | 2 | 2 | 30 | LGS |
| | 2013 Feb 21 | 088.B-0206(A) | 250 | 2 | 1 | 30 | LGS |
| NGC 4636 | 2013 May 12,13, Jun 5 | 088.B-0206(A) | 250 | 6 | 5 | 40 | LGS |
| IC 4296 | 2013 May 9,10 | 091.B-0129(A) | 250 | 13 | 9 | 45 | LGS |
| IC 4329 | 2013 May 8,10 | 091.B-0129(A) | 250 | 24 | 22 | 110 | LGS |

**Notes.** Column 1: Galaxy name. Column 2: Dates of the observations. Column 3: Identification number of the Proposal. Column 4: Spatial pixel scaling of the observation. Column 5: Number of available single exposure frames. Column 6: Number of single exposure frames in the combined data cube. Column 7: Combined exposure time in minutes. Column 8: Adaptive optics mode applied for the data, either using a natural guide star (NGS) or a laser guide star (LGS).

**Table 4.3 —** SINFONI spatial resolution

| Galaxy | $FWHM_N$ (arcsec) | $FWHM_B$ (arcsec) | $f_N$ | Strehl |
|---|---|---|---|---|
| (1) | (2) | (3) | (4) | (5) |
| NGC 3706 | 0.28 ± 0.05 | 1.02 | 0.94 | 12 % |
| NGC 3923 | 0.20 ± 0.04 | 0.78 | 0.20 | 14 % |
| NGC 4261 | 0.19 ± 0.02 | 0.56 | 0.41 | 12 % |
| NGC 4636 | 0.24 ± 0.04 | 0.62 | 0.10 | 15 % |
| IC 4296 | 0.18 ± 0.02 | 0.58 | 0.47 | 9 % |
| IC 4329 | 0.23 ± 0.03 | 0.68 | 0.02 | 10 % |

**Notes.** The SINFONI PSF of the data was parametrized by a double Gaussian with a narrow and broad component. We have derived the SINFONI PSFs and Strehl ratios in a similar manner as in chapters 2 and 3. The derived parameters are given in the following columns: Column 1: Galaxy name. Column 2: FWHM of the narrow Gaussian component. Column 3: FWHM of the broad Gaussian component. Column 4: Relative intensity of the narrow component. Column 5: Strehl ratio of the data.

# 3 Observations

Measuring robust supermassive black hole masses is very data-expensive and usually requires both, high-resolution and large-scale spectroscopic and imaging data at high S/N. The high-resolution data is necessary to trace the stellar motion in the vicinity of the black hole, and large-scale information is needed to constrain global galaxy characteristics, such as the mass-to-light ratio and the dark matter content. In the following section, we present the different observations used in this study.

## 3.1 Integralfield-spectroscopic data

### SINFONI

The high-resolution integral-field spectroscopic observations of our six sample galaxies were performed with the Spectrograph for INtegral Field Observations in the Near Infrared (SINFONI; Eisenhauer et al. 2003; Bonnet et al. 2004) instrument mounted on UT4 (Yepun) of the Very Large Telescope (VLT). Between May 2009 and May 2013, we observed each galaxy at K-band grating (1.94 - 2.45 $\mu$m) providing a spectral resolution of $R \sim 4000$ and a pixel scaling of 100 mas (250 mas) leading to a total field-of-view (FOV) on the sky of about $3.2'' \times 3.2''$ ($8'' \times 8''$) per pointing. The observations were performed using an object-sky-object nodding scheme. At the beginning and end of each observing block, a standard star was observed at a similar airmass and with the same instrumental setup to perform the telluric correction with similar atmospheric and instrumental conditions. In addition, we made use of the adaptive optics mode, either using an NGS or an artificial sodium LGS to correct for ground-layer turbulence and optimize the spatial resolution. Details of the observing runs for each galaxy are provided in Table 4.2. Our observations yield a typical spatial resolutions of around $0.2''$ and Strehl ratios of 10% (see Table 4.3). We used the SINFONI data reduction pipeline (version 2.4.8; Modigliani et al. 2007) provided by ESO to reduce the SINFONI data. It handles the steps of bias-correction, dark-subtraction, flat-fielding, non-linearity correction, distortion correction, and wavelength calibration and finally creates data cubes of the single exposures. In addition to the steps of the pipeline, we applied our external routine to correct telluric features within the same night observed standard stars. We refer the readers to Chapter 3 for details of the individual steps of

the data reduction. Finally, we merged the individual data frames by recentering the isophotes of the reconstructed images and Voronoi-binned (Python version 3.1.0; Cappellari & Copin 2003) the generated data cube. The target S/N of the Voronoi-binning was chosen to be between 50 and 70, balancing the desire to keep the central spaxels unbinned and ensure a sufficiently high-resolution in the outer region. We thus obtained, bin diameter sizes of $< 0.2''$ in the center and $0.7 - 1.0''$ at radii larger than $2''$ for the observations at 250mas and bin diameter sizes of $< 0.1''$ in the center and $0.3 - 0.4''$ at radii larger than $1''$ for the observation of NGC 3706 at 100mas.

**MUSE**

The large-field Multi Unit Spectroscopic Explorer (MUSE; Bacon et al. 2010) observations of IC 4296 and IC 4329 were conducted under the science programs 097.B-0776(A) (PI: Emsellem) and 060.A-9100(A) (PI: MUSE Team), respectively. IC 4296 was observed as part of the MUSE Most Massive Galaxies (M3G; Krajnović et al. 2018c) project and has a total exposure time of 1800s divided into ten 180s on-source integrations. IC 4329 was observed during the MUSE commissioning in two different setups separated into a February and May 2015 observation. We used only the February exposures which have a total time of 3600s divided into three 1200s on-source integrations yielding better S/N. We reduced the data using the MUSE data reduction pipeline (Weilbacher et al. 2015), version 1.6. It includes bias and sky subtraction, flatfield correction, wavelength calibration for each on-source observation. In addition to the on-source exposures, a separate sky field and standard star were reduced to extract a sky spectrum, the flux response curve and telluric correction curve which were then used to correct the on-source exposures. After the data reduction, we merged the individual exposures with the MUSE pipeline merging procedure taking the respective offsets into account. In the final data cube, each spaxel has a size of $0.2'' \times 0.2''$ and a spectral sampling of 1.25Å. We only used the central $30'' \times 30''$ of the MUSE FoVs and Voroni-binned these regions to a target S/N of 60, resulting in bin diameter sizes of $0.5''$ in the center and $3''$ at radii larger than $10''$.

**VIMOS**

We obtained large-field data for NGC 3923 using the VIsible Multi Object Spectrograph (VIMOS; Le Fèvre et al. 2003) mounted on UT3 Melipal under the science program 079.B-0402 (B) (PI: Cappellari). Lagerholm et al. (2012) performed the data reduction by using the ESO pipeline[1] (version 2.3.3) and a number of Image Reduction and Analysis Facility (IRAF) tasks. It includes bias and sky subtraction, flatfield calibration, interpolation over bad pixels, cosmic-ray removal, spatial rectification, wavelength calibration with HeArNe lamp exposures, flux calibration with standard stars, and fringe-like pattern removal. After the data reduction, they merged the individual science frames into a final data cube, which we Voronoi-binned to a target S/N of 60 with resulting bin sizes of $0.5''$in the galaxy center and 2-$3''$at radii larger than $7.5''$.

**SAURON**

Large-field observations of NGC 4261 and NGC 4636 were obtained with the Spectrographic Areal Unit for Research on optical Nebulae IFU (SAURON; Bacon et al. 2001) at the 4.2-m William Herschel Telescope of the Observatorio del Roque de los Muchachos on La Palma by the ATLAS$^{3D}$ galaxy survey[2] (Cappellari et al. 2011) team. The data reduction was applied

[1] http://www.eso.org/sci/software/pipelines/
[2] http://purl.org/atlas3d

**Table 4.4 —** HST archival data

| Galaxy (1) | PID (2) | Instrument (3) | Filter (4) |
|---|---|---|---|
| NGC 3706 | 6587 | WFPC2 | W555W |
| NGC 3923 | 9399 | ACS | F814W |
| NGC 4261 | 5124 | WFPC2 | F791W |
| NGC 4636 | 8686 | WFPC2 | F814W |
| IC 4296 | 5910 | WFPC2 | F814W |
| IC 4329 | 8683 | WFPC2 | F814W |

**Notes.** Details of the Hubble Space Telescope observations. Column 1: galaxy name. Column 2: programme identification number. Column 3 and 4: Camera on HST and the filters in which the data were taken.

with the XSAURON software (Bacon et al. 2001) and includes bias and dark subtraction, low-frequency flat-fielding, cosmic-ray removal, wavelength calibration, homogenization of the spectral resolution over the field, sky subtraction and flux calibration. The final IFUs have a FoV of $33'' \times 41''$ with a sampling of $0.94'' \times 0.94''$ square pixels. The kinematics extraction performed by the ATLAS$^{3D}$ team and extensively described in Cappellari et al. (2011), and the kinematic maps were introduced by Krajnović et al. (2011). In this paper, we use the homogeneously reduced publicly available ATLAS$^{3D}$ data[3], which was binned to a target S/N of 40.

### 3.2 Imaging data

A detailed galaxy mass model requires both high-resolution imaging of the center of the galaxy and large FoV, ideally covering r>100″, deep imaging of the galaxy outskirts. For the high-resolution imaging of the center, we downloaded reduced and calibrated HST archival data from the ESA Hubble Science Archive. Depending on the availability, we used Wide-Field Planetary Camera (WFPC2; Holtzman et al. 1995) or Advanced Camera for Survey (ACS; Ford et al. 1998) images. Cosmic rays were removed by taking the median of different aligned individual CR-Split images. For the large FoV imaging of our ATLAS3D targets (NGC 4261 and NGC 4636), we used SDSS images (Abazajian et al. 2009), which we obtained from the ATLAS3D collaboration (Scott et al. 2013a). For the remaining galaxies, we used images of the Carnegie-Irvine Galaxy Survey (Ho et al. 2011; Li et al. 2011; Huang et al. 2013).

## 4 Stellar Kinematics

We measured the line-of-sight velocity distribution for each Voronoi bin of the IFU observations, by using the Python implementation of the penalized Pixel Fitting method [4] (pPXF, Cappellari & Emsellem 2004; Cappellari 2017). The LOSVD is recovered by fitting an optimal template to the observed galaxy spectrum. The optimal template is a non-negative linear combination of a set of stellar templates which were taken from the Gemini Spectral Library of Near-IR Late-Type (Winge et al. 2009) stellar template library for our near-infrared SINFONI data and from the MILES (Sánchez-Blázquez et al. 2006) stellar template library for the optical VIMOS and MUSE data. For each dataset and each galaxy, we performed two sets of stellar kinematics extractions, parametrizing the LOSVD as simple Gaussian (V, $\sigma$) or as Gauss-Hermite polynomials (V, $\sigma$, $h_3$,

[3] http://purl.org/atlas3d
[4] http://purl.org/cappellari/software

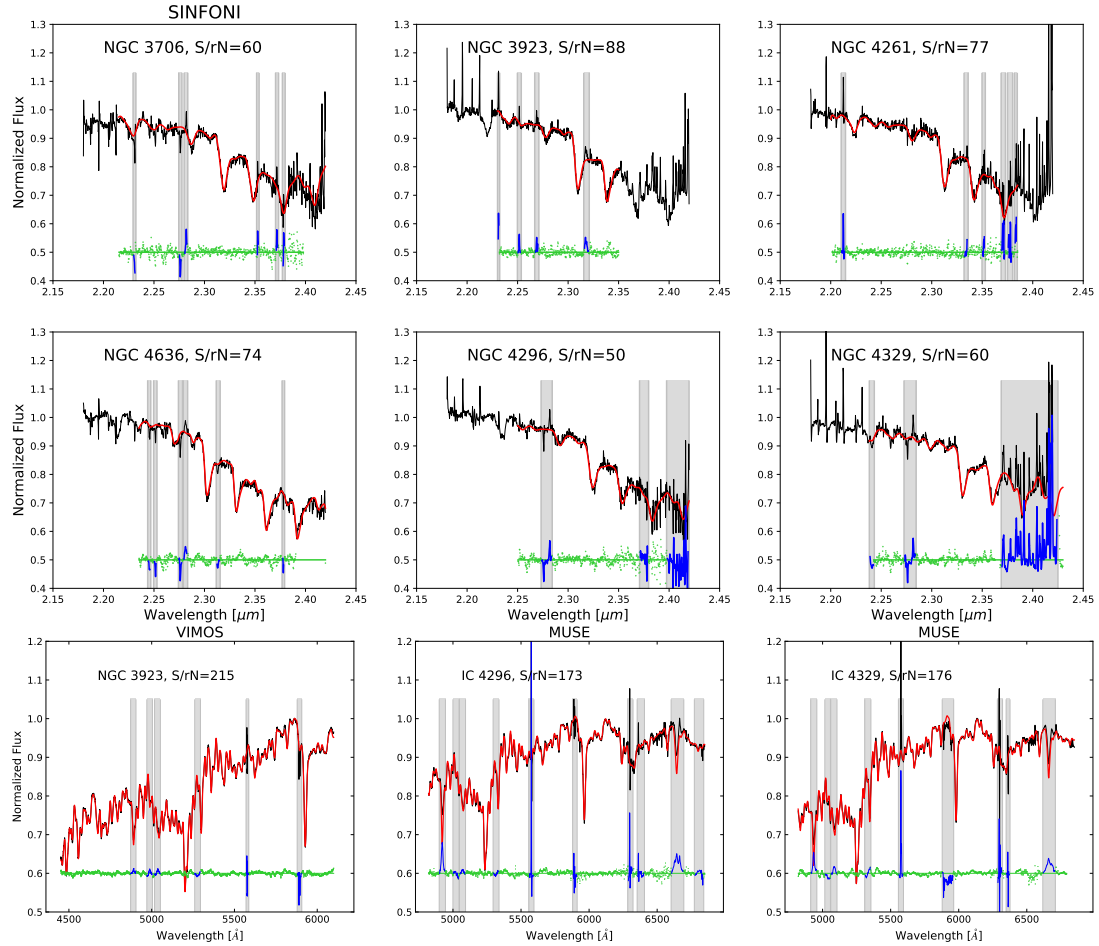


**Figure 4.1 —** Integrated SINFONI, VIMOS and MUSE spectra and pPXF fits of our target galaxies. The integrated spectra (black solid lines) were obtained by summing up all spectra of the IFU data cubes and fitted using the pPXF routine (red lines) in order to derive an optimal template. The fitting residual between spectrum and best fitting model are shown as green dots and are shifted up by 0.5 (0.6 for the bottom panels). Regions which were masked in the fit (often due to emission lines or insufficient sky subtraction) are indicated as grey shaded regions and their residuals are indicated in blue.

$h_4$)(Gerhard 1993; van der Marel & Franx 1993). The first set was later used in the dynamical Jeans models, while the information of all four moments is needed for constructing robust dynamical Schwarzschild models (see Gebhardt et al. 2003 for a different implementation of the Schwarzschild code that fits directly to the LOSVDs). As in previous chapters we carefully tested the effects of using different wavelength ranges, masking and unmasking insufficiently reduced sky- and telluric lines and varying the additive polynomial to mitigate template mismatch effects in our stellar kinematics extraction and obtain a qualitative sense of the kinematical error range. The quantitative errors of the recovered kinematics were derived using Monte Carlo simulations (with 500 realizations) as extensively described in Chapters 2 and 3. In Figure 5.5, we show the best-fitting optimal templates to the integrated SINFONI and MUSE spectra. The key feature in the K-band is the CO absorption band head at about 2.3 $\mu$m. Due to a poor telluric correction, it was not always possible to recover the third and fourth band sufficiently, and we restrained from fitting these lines for half of our sample. The fits to the remaining features are satisfactory, albeit less constraint due to the loss of information. The derived errors of our SINFONI kinematics are relatively high and span typically ranges of about 15 km s$^{-1}$ for mean velocity and about 20 km s$^{-1}$ for the velocity dispersion. IC 4296 has a particularly bad S/N, which translates to huge

errors in the kinematic measurements. On the other hand, the kinematics extraction from the optical VIMOS and MUSE data was much more reliable and passed typical errors of about 7 km $s^{-1}$ for mean velocity and about 10 km $s^{-1}$ for the velocity dispersion (see Figures 5.5). It is planned, to re-examine the telluric correction in the future and hopefully improve the kinematics extraction significantly.

In Figure 4.2, we show the extracted SINFONI stellar kinematics maps of our sample galaxies. Compared to the maps discussed in Chapter 3, some of the massive galaxies in this study show very peculiar kinematic features. NGC 3706 and IC 4296 contain kinematically decoupled components in their center as can be seen in the velocity and velocity dispersion ("2$\sigma$-peak") maps. The velocity maps of NGC 4261 and NGC 4636 show essentially no rotation. Interestingly, in NGC 4261 the velocity is picked up again for radii larger than 2" and suggests prolate rotation. Prolate rotation is found for galaxies which are shaped like a spindle and rotate around their major axis. This sense of rotation seems to be a very common feature in massive galaxies (Ebrová & Łokas 2015; Li et al. 2016; Ebrová & Łokas 2017; Krajnović et al. 2018b) and might originate from dissipation-less equal-mass mergers (Tsatsi et al. 2017). The prolate rotation in NGC 4261 is much clearer visible in the large-scale SAURON data and was already reported in (Krajnović et al. 2011). NGC 3923 is the second galaxy of our sample, which also shows clear signs of prolate rotation. While the rotational velocities of our sample galaxies are very low, reaching only up to around 60 km $s^{-1}$ for most of the cases, the measured velocity dispersion reach up to 350 km $s^{-1}$ for some instances. The low-rotation features of the rotational velocities are also imprinted in the $h_3$-maps. An interesting and very irregular $h_3$ Gauss-Hermite moment map is found for IC 4329, but we expect this feature to result from the bad telluric correction of this galaxy which significantly contaminated the CO-bands. A planned revision of the telluric correction will shed more light on the nature of this feature. The $h_4$ Gauss-Hermite moment maps (kurtosis) of most of our galaxies are strongly biased towards negative values in the nuclear regions. This $h_4$ moment depends on the level of the anisotropy of the stellar system (van der Marel & Franx 1993; Gerhard 1993). Tangentially anisotropic distribution functions produce LOSVDs which are more flat-topped (negative $h_4$) compared to the isotropic case. The tangentially biased $h_4$ moments could thus give a hint of previous core scouring, which leads to the formation of the core in these galaxies (see Chapter 6). It is striking that the only coreless galaxy of our sample has a positive kurtosis. We nevertheless want to caution that the quality of the Hermite moment extraction strongly depends on the quality of the data and are less accurate for the fits of only two out of the four CO-bands (NGC 3923, NGC 4261 and IC 4329).

For the galaxies with available large-scale IFU observations, we also show the large-scale kinematics in the Appendix (Figures 4.10). A visual comparison between the two spatial scales shows mostly consistent results, but the $h_4$-Gauss-Hermite moments are much less biased to extreme positive or negative values in the large-scale maps. Interestingly, a sign change towards negative values is visible in the nuclear regions of all large-scale kinematic maps. Furthermore, the lower spatial resolution of the large-scale MUSE data does not permit the identification of the kinematically decoupled component in IC 4296. A quantitative comparison between the velocity dispersion and the $h_4$-moment of the small and large scale data is shown in Figure 4.3. For the comparison, we averaged the kinematic bins within circular annuli around the kinematic center. In some cases, the small and large scale-data did not match within the errors (indicated by shaded regions), and we had to add or subtract a constant shift to the SINFONI data to match them with the large-scale data. This was done for NGC 3706, NGC 4261, IC 4296 and IC4329. The respective shifting values for the galaxies are shown in Figure 4.3. After the shift, the even moments of the different datasets matched very well and showed the same trends. We have

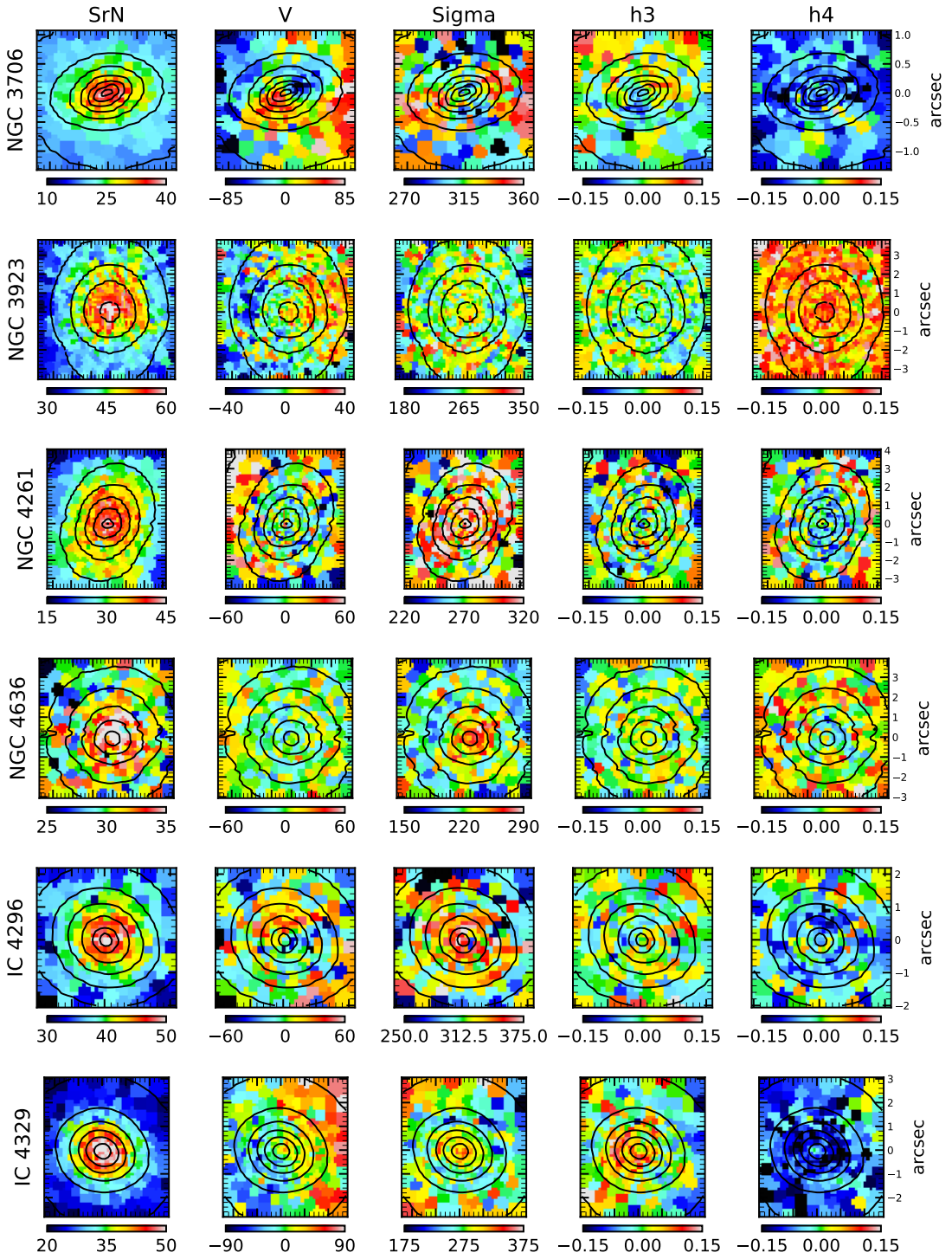


**Figure 4.2 —** SINFONI stellar kinematics (derived from CO bandhead spectroscopy) of our target galaxies (from top to bottom) NGC 3706, NGC 3923, NGC 4261, NGC 4636, IC 4296 and IC 4329. From left to right the panels show maps of signal-to-residual noise (S/N), mean velocity (V), velocity dispersion ($\sigma$) and the Gauss-Hermite moments $h_3$ and $h_4$. The black contours indicate the galaxy surface brightness from the collapsed data cube.

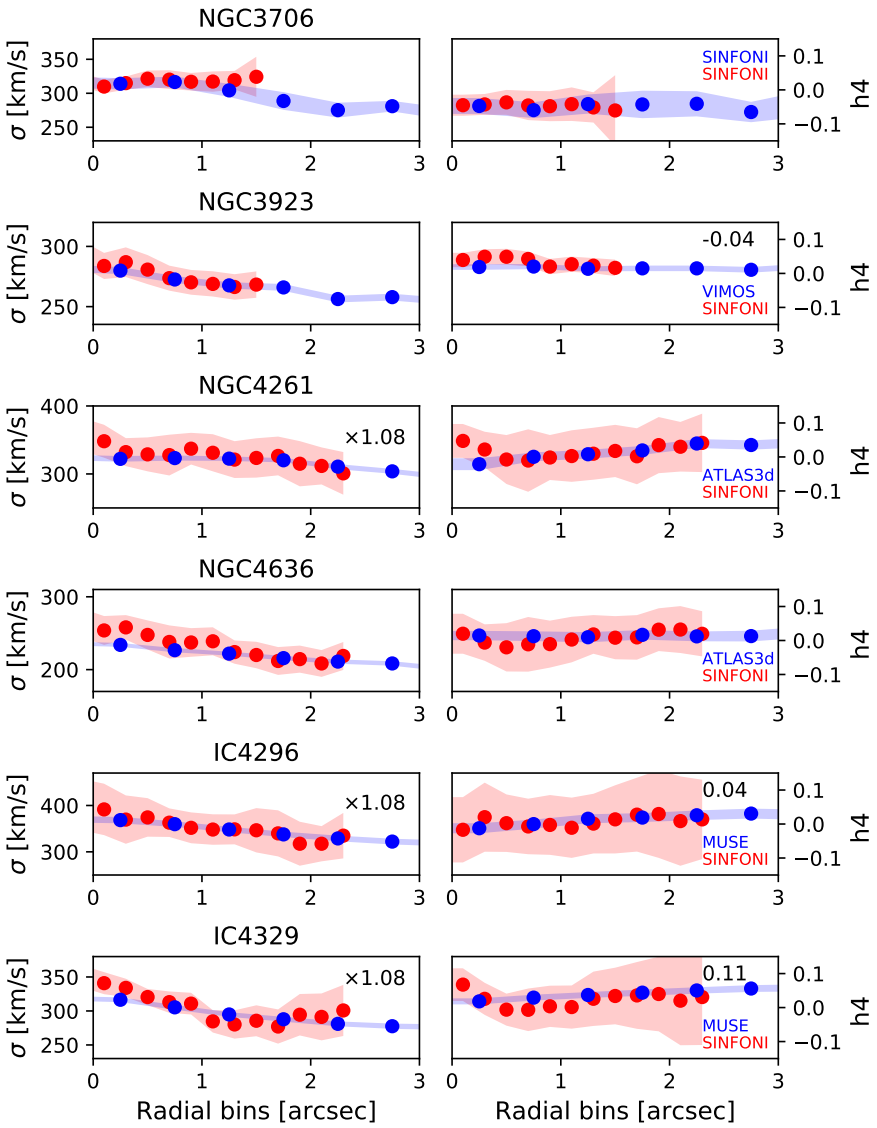


**Figure 4.3 —** Comparison of velocity dispersion and $h_4$ profiles for the SINFONI (red) and the respective large-scale data (blue). The values were averaged within circular annuli around the kinematic center. The error range of the averaged values in the radial bins are calculated via error propagation and are shown as shaded regions. Applied shifts in the SINFONI maps are denoted by the values in the upper right corner of each panel.

discussed the influence of this shift on the black hole mass measurements in Chapter 3 and in Krajnović et al. (2018a) and concluded that we likely impose an uncertainty of less than a factor of two[5].

[5]Krajnović et al. (2018a) show that an upwards shift in velocity dispersion by 8% increases the mass of the black hole by 80%. In order to test the effect for our galaxies, we will also run Schwarzschild models with un-shifted SINFONI kinematics in the future.

# 5 Dynamical Modelling

## 5.1 Mass model

A good knowledge about the distribution of mass and light within the galaxy is indispensable for the dynamical modeling. We used the Multi-Gaussian Expansion (MGE; Emsellem et al. 1994; Cappellari 2002) to describe the surface brightness of our target galaxies analytically. In this method, the surface brightness is measured along equally-spaced wedges and then parametrized by a sum of two-dimensional concentric Gaussians. The parametrized surface brightness is then deprojected to produce the luminosity density, and, assuming a constant mass-to-light ratio, this is then converted to a stellar mass distribution. We fitted both high-resolution HST and deep large-scale imaging data simultaneously, using the MgeFit Python package[6] Version 5.0 of Cappellari (2002). We aligned the surface brightness profiles by re-scaling the large-scale data to the central HST profiles and used the HST imaging for the photometric calibration. During the fit, we carefully masked foreground stars, nearby galaxies and dust lanes. The dust-masking is particularly important in the center of our galaxies in order to assign the right amounts of mass to the luminous and dark (i.e., the supermassive black holes) components. Therefore, we created detailed dust-masks as described in the Appendix of Chapter 3. After careful inspection, we noted that the dust-features were only present in the very center of our galaxies. We, therefore, decided to not perform a dust-correction on the SDSS images as in some galaxies of the previous work.
Figure 4.4 shows the contours of our best-fitting MGE models, which are overlaid on the isophotal maps of the HST images. Most of the model contours reproduce the observed light contours very well. NGC 3706 has a central change of the position angle due to a central ring component which cannot be reproduced by our axisymmetric MGE models. Correct handling of the position angle twist would require triaxial modeling, which will be performed at a later stage of this project.
The final MGE models are described by a sum of 9-16 concentric Gaussians which are listed in Table 3. We calibrated our models by using the photometric zero points from Dolphin (2009), paying particular attention at the gain and filter of our observation, and the magnitudes of the sun from Willmer (2018). One can obtain the density profile of the luminous mass by deprojecting the light model and multiplying it with the $M/L$ of the galaxy in the respective band.

## 5.2 Jeans Anisotropic model

In our first dynamical modeling approach, we used the Jeans Anisotropic Modeling method (JAM; Cappellari 2008, 2015) to fit the derived SINFONI kinematics only and derive the supermassive black hole masses for our sample galaxies. JAM solves the Jeans equations and calculates the second velocity moment projected along the line-of-sight, which compares well with the observable root mean square velocity of the observations $V_{\rm rms} = \sqrt{V^2 + \sigma^2}$. We used two different implementations of the JAM code: For NGC 3706, which is the only fast-rotator, we assumed an axisymmetric potential, while for the other galaxies, all slow-rotators, we assumed a spherical potential. As the axisymmetric code and its usage were detailed described in Chapters 2 and 3, we focus on the spherical JAM model in this section. While slow-rotators are often triaxial and have twists in their kinematics (as seen in Section 4), a triaxial approach with three independent axes of the velocity ellipsoid would be a more appropriate modeling method (van den Bosch et al. 2008). However, on a first-order approximation, a spherical JAM solution is a simple approach to fit the often roundish shaped slow-rotating galaxies. In contrast to our earlier

[6]http://purl.org/cappellari/software/

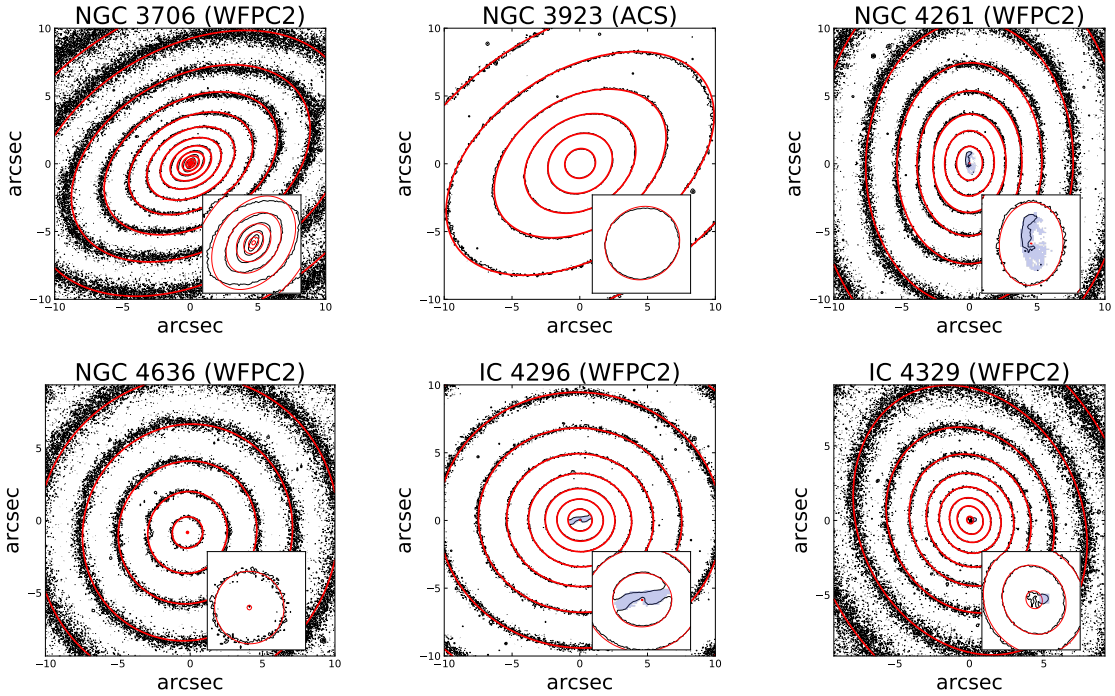


**Figure 4.4 —** Isophotal maps of the WFPC2 and ACS images of our target galaxies within a FoV of $20'' \times 20''$from the photometric center. In the bottom right of each panel we show a cutout of the central $3'' \times 3''$. The contours of our best-fitting MGE model (red) are superimposed on the HST images (black). The MGE models were build from the combined photometric information of HST ($r < 10''$) and wide-field data ($r > 10''$) from the ATLAS$^{3D}$ and the CGS survey. We masked the central dust tori for NGC 4261 and IC 4296, and the foreground star for NGC 4329, before MGE modelling their surface brightness (blue shaded area).

work, we allow for a varying spherical anisotropy $\beta = 1 - \sigma_\theta^2/\sigma_r^2$ when constructing spherical JAM models. In order to distinguish between the core and the outer profile (see also (Cappellari et al. 2015; Drehmer et al. 2015; Ene et al. 2019; Chae et al. 2019), we assume different $\beta$ values for the inner ($< 1''$) and the outer kinematics. The cut is chosen to be applied where the slope of the surface brightness profiles change between the central flat and outer steep profile. A more advanced approach would be to use a smooth radially varying anisotropy which is just fixed by the extreme values of $\beta$ (e.g., Osipkov 1979; Binney & Tremaine 2008) and will be applied at a later stage. Consequently, our JAM models are specified by three parameters: the black hole mass $M_{\rm BH}$, the inner $\beta_{\rm in}$ and outer anisotropy $\beta_{\rm out}$, typically at radii greater than $1.5''$. In order to find the best-fitting model, we used the Bayesian inference method as defined in Section 5.2 of Chapter 3. The best-fit values were calculated as the median of the posterior probability of each parameter. We show a comparison between our observed $V_{\rm rms}$ and the best-fitting JAM models in Figure 4.5. For each of our galaxies, the JAM models reproduce the central $V_{\rm rms}$ peak of the observations, while the outer kinematics suffer from large scatter and large uncertainties and fail to constrain the JAM model. The respective best-fit parameters are summarized in Table 4.5. Our derived anisotropies have a clear trend for all of our galaxies, being negative in the center and growing to robust values around 0.4 towards the outskirts. The negative values imply tangentially biased orbits, which would dominate in a core scouring scenario for core galaxies. However, it is notable that also our prolate coreless galaxy NGC 3923 has a very negative anisotropy. A more detailed analysis of the anisotropy variation and the corresponding orbits will be achieved with Schwarzschild modeling.

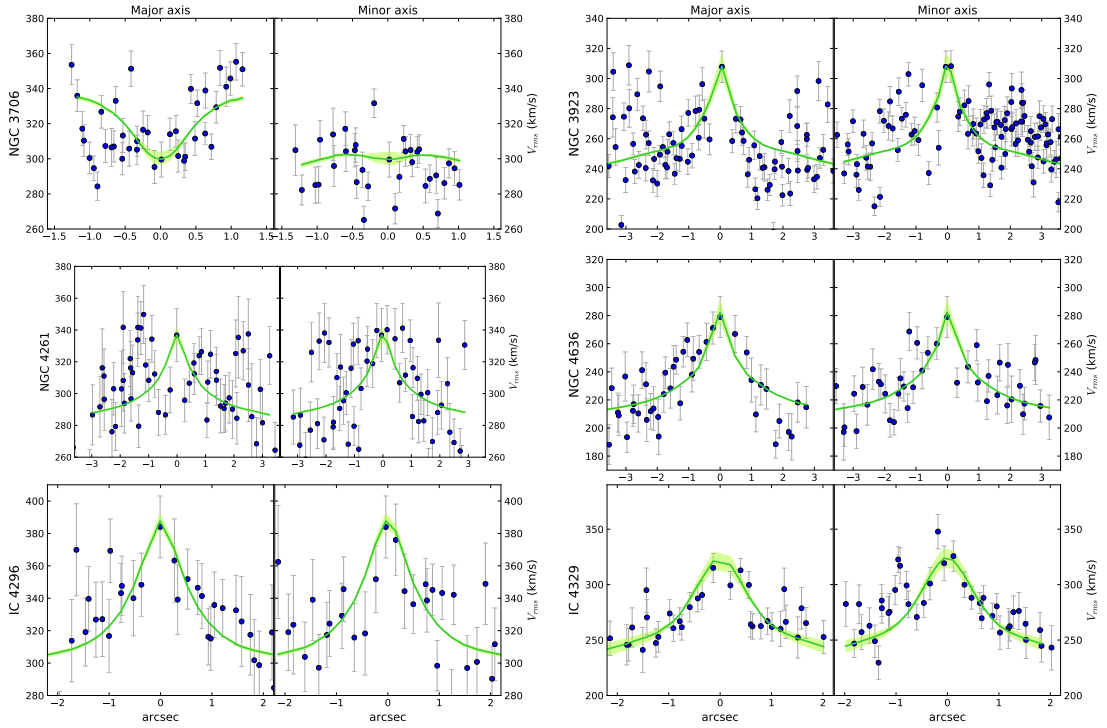


**Figure 4.5 —** Comparison of the $V_{rms}$ profiles between the SINFONI data (blue) and best-fitting JAM models (green) along the major (left) and minor (right) axis. The green shaded region shows JAM models with varying black hole mass by a factor of 1.3 either larger or smaller than the best-fitting mass.

## 5.3 Schwarzschild model

In our second dynamical modeling approach, we used axisymmetric Schwarzschild models to fit the full line-of-sight velocity distribution (V, $\sigma$, $h_3$, $h_4$) derived from both the high-resolution SINFONI and the large-scale data. This method is based on the numerical orbit superposition method by Schwarzschild (1979) and was described and applied in Cappellari et al. (2006). As was mentioned in the previous chapter, the slow rotation and isophotal profile of our galaxies indicate a triaxial shape, meaning an axisymmetric approach might impose significant uncertainties on our results as only orbits allowed in the axisymmetric potential are used to fit the data. Nevertheless, similar galaxies have often been studied based on axisymmetric models only in the past (e.g., Shen & Gebhardt 2010; Rusli et al. 2013b; Mazzalay et al. 2016; Saglia et al. 2016). Therefore, we will use the axisymmetric Schwarzschild models as an approximation and test the applicability of this method to our galaxies, before applying more general triaxial Schwarzschild models later. We will focus on the dynamical modeling in this section but will continue the discussion on triaxiality and its implication in the discussion. The application of Schwarzschild models has extensively been described in previous chapters, and we will only give a summary of the method here.

In the Schwarzschild modeling method, assuming a stationary gravitational potential from the derived galaxy mass density (including a trial mass for the black hole), a library of orbits is created which covers the phase space of the three integrals of motion ($E$,$L_z$,$I_3$). This orbit library is then fitted to the observed kinematics to find the best-fitting superposition of orbits for the respective gravitational potential. Schwarzschild models for a grid of different black hole masses are computed and the best-fitting model is determined based on a $\chi^2$ comparison. The best-fitting model then indicates the best-fitting gravitational potential and thus black hole mass. We created

our orbit library on 21 equipotential shells with logarithmically spaced radii covering the limits of the MGE model, and at each energy, we sampled eight angular and seven radial values. The initial set of orbits is doubled by taking prograde and retrograde orbital motion into account and additionally dithered by $6^3$ individual orbits. The resulting 508 032 orbits were then integrated in the galaxy's potential. The non-negative least squares method is used to assign weights to the orbits and fit the stellar kinematics on both small and large scale while accounting for PSF effects and aperture binning. We first ran coarse grids of M/L and black hole mass centered on the best-fit results of JAM to find the global minimum of the $\chi^2$ distribution. In a second run, we refined the grids around the minimum of the coarse grid to find the best-fitting values of $M_{\rm BH}$ and $M/L$. We present our grids of Schwarzschild models in Figure 4.6 and provide a visual comparison between the best-fit model and the SINFONI kinematics in Figure 4.7. For half of our galaxies (NGC 4261, IC 4296, IC 4329), the models are not able to constrain the black hole mass. It is not clear yet if this is caused by the axisymmetric assumption, the quality of our data or actually undermassive black holes. A visual comparison at NGC 4261 shows that the velocity dispersion is not well reproduced. However, the observed velocity dispersion suffers from large errors which could cause the problems for this galaxy. IC 4296 and IC 4329 have $\chi^2$ minima at slightly too low black hole masses, which is well visible in the velocity dispersion profiles in Figure 4.7. While IC 4296 has also huge errors which hardly constrain the data, it is not clear what causes the problem for IC 4329. The velocity dispersion profiles of NGC 3923 reveals a slight $M_{\rm BH}$ overestimation and an $M_{\rm BH}$ and for NGC 3706. Altogether, the axisymmetric Schwarzschild models did not reproduce the derived stellar kinematics very well, for reasons which are only partially understood yet. In the future, we will continue analyzing what could have caused the problems in the axisymmetric Schwarzschild modeling method. In addition, we will test triaxial Schwarzschild models on our triaxial galaxies and compare them with the axisymmetric models. While we included our best-fitting Schwarzschild models results in Table 4.5, in the subsequent comparisons, we used the more reliable JAM models which are based on spherical geometry. We also give a summary of notes on each galaxy in the following section.

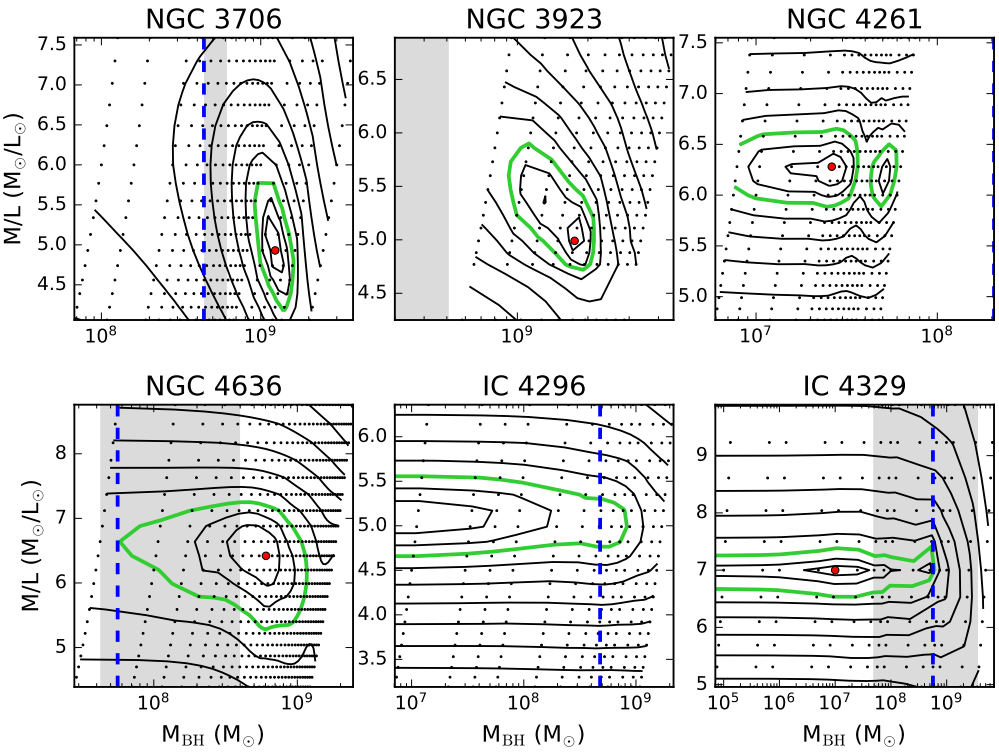


**Figure 4.6 —** Grids of Schwarzschild models between M/Ls and black hole masses $M_{\rm BH}$. The best-fitting model, derived from the minimal $\chi^2$ is marked as red circle. The overlaid contours indicate the $\Delta\chi^2 = \chi^2 - \chi^2_{\rm min}$ levels; the thick green contours show the $3\sigma$ level of the two-dimensional distribution. We have also added the $3\sigma$ limits on the best-fitting $M_{\rm BH}$ from the JAM models (gray shaded regions). The dashed blue line indicates the mass of the black hole which has a radius of the SoI of half the resolution of our SINFONI data (inferred from the narrow component of the AO PSF); this is approximately the lowest black hole mass that we expect to be detectable based on our data.

**Table 4.5 —** Summary of dynamical modelling results

| Galaxy | JAM $M_{BH}$ ($\times 10^8$ $M_\odot$) | M/L ($M_\odot/L_\odot$) | $\beta_{in}$ | $\beta_{out}$ | $\chi^2/d.o.f.$ | Schwarzschild $M_{BH}$ ($\times 10^8$ $M_\odot$) | M/L ($M_\odot/L_\odot$) | $\chi^2/d.o.f.$ |
|---|---|---|---|---|---|---|---|---|
| (1) | (2) | (3) | (4) | (5) | (6) | (7) | (8) | (9) |
| NGC 3706 | $5.26^{+0.79}_{-0.79}$ | $6.64^{+0.11}_{-0.13}$ | $-0.06^{+0.04}_{-0.03}$ | – | 5.43 | $12.30^{+3.50}_{-3.05}$ | $4.93^{+0.84}_{-0.71}$ | 3.57 |
| NGC 3923 | $0.00^{+4.21}_{-0.00}$ | 3.69 | $-0.89^{+0.55}_{-0.11}$ | $0.41^{+0.02}_{-0.06}$ | 5.95 | $17.50^{+3.20}_{-7.40}$ | $4.99^{+0.87}_{-0.22}$ | 2.54 |
| NGC 4261 | $1.31^{+9.12}_{-1.31}$ | 7.49 | $-0.43^{+0.35}_{-0.51}$ | $0.31^{+0.05}_{-0.09}$ | 1.96 | $0.26^{+0.33}_{-0.18}$ | $6.28^{+0.30}_{-0.28}$ | 2.28 |
| NGC 4636 | $2.51^{+1.42}_{-2.08}$ | 4.16 | $-0.23^{+1.23}_{-0.76}$ | $0.33^{+0.17}_{-0.16}$ | 1.89 | $6.06^{+5.45}_{-5.95}$ | $6.42^{+0.70}_{-1.02}$ | 1.53 |
| IC 4296 | $00.00^{+17.30}_{-00.00}$ | 3.30 | $-0.05^{+0.57}_{-0.49}$ | $0.41^{+0.06}_{-0.10}$ | 1.37 | $00.00^{+10.50}_{-00.00}$ | $5.17^{+0.37}_{-0.51}$ | 0.72 |
| IC 4329 | $17.80^{+15.30}_{-17.30}$ | 5.16 | $0.18^{+0.26}_{-0.51}$ | $-0.85^{+1.15}_{-0.15}$ | 1.65 | $0.10^{+4.99}_{-0.10}$ | $6.53^{+0.32}_{-0.53}$ | 0.99 |

Note. - Column 1: galaxy name. Column 2-6: parameters of the JAM models (black hole mass, inner and outer anisotropy parameter and $\chi^2$ of the best-fitting model). Column 7-9: parameters of the Schwarzschild models (black hole mass, mass-to-light ratio and $\chi^2$ of the best-fitting model).

# 6 Discussion

## 6.1 Notes on the individual objects

### NGC 3706

NGC 3706 is a core galaxy with a central ring component, which is tilted with respect to the outer disk and clearly visible in the HST images. In our kinematic maps, we report the counter-rotation ($V_{\rm max} \approx 70$ km s$^{-1}$) of this disk, which is kinematically decoupled from the rotation of the galaxy and produces two $\sigma$ peaks in the velocity dispersion which reach up to 340 km/s. Our derived stellar kinematics are in concordance with the measurements from Gültekin et al. (2014). The formation of the about 20 pc sized stellar ring is likely the consequence of large amounts of gas being delivered to the galaxy center by a recent satellite-galaxy merger (see Bonfini et al. 2018), and thus triggering star formation. Gültekin et al. (2014) also derive a black hole mass[7] $M_{\rm BH} = (5.62 \pm 0.90) \times 10^8 M_\odot$ and a $M/L_{\rm V} \approx 6\, M_\odot/L_\odot$ from axisymmetric Schwarzschild models using HST STIS long-slit kinematics. Our estimated JAM black hole mass $M_{\rm BH} = (5.26 \pm 0.70) \times 10^8 M_\odot$ based on the central 1″ of the SINFONI data is consistent with the previous measurement at $3\sigma$ significance, but both our mass model and dynamical models lack to reproduce both components independently. It is therefore planned to use the triaxial modeling to properly take a changing position angle into account.

### NGC 3923

NGC 3923 is likely in a late phase of a merger between an elliptical galaxy and one or more dwarf galaxies. It is a famous example of a shell galaxy having 42 stellar shells, which extend to large radii and are likely remnants of the tidal interaction between NGC 3923 and its accreted galaxies (Prieur 1988; Bílek et al. 2016). The galaxy also shows evidence for slow prolate rotation with a $V_{\rm max} \approx 30$ km s$^{-1}$ (Carter et al. 1998) which has recently also been observed in several other massive galaxies in IFU galaxy surveys (e.g., Tsatsi et al. 2017; Ene et al. 2018; Krajnović et al. 2018c). Our derived velocity dispersion does not show a pronounced peak, but a slight decrease along the minor axis. Comparing our kinematic data with long-slit data from Carter et al. (1998), all moments match the previously derived kinematics except for the $h_4$ moment. Our values are unusually high, and we expect a template mismatch due to the insufficient telluric correction. As the $h_4$ moment is coupled to the velocity dispersion, we might measure a slightly too low velocity dispersion in our data which would underestimate the black hole mass. This effect will be further analyzed and improved in the future. Saglia et al. (2016) have used SINFONI data to dynamically derive the black hole mass with axisymmetric Schwarzschild models without taking dark matter into account and obtained $M_{\rm BH} = (2.81 \pm 0.85) \times 10^9 M_\odot$ and a $M/L \approx 4.22\, M_\odot/L_\odot$ in the z-band. Their derived black hole mass is significantly above the black hole scaling relations (their Figure 13) and our derived black hole upper limit of $M_{\rm BH} = 4.21 \times 10^8 M_\odot$. For the future, we plan to improve the stellar kinematics extraction and to construct the more appropriate triaxial Schwarzschild models for this prolate-rotating galaxy.

### NGC 4261

NGC 4261 is an elliptical galaxy with prominent radio jets emanating from the nucleus, which can be classified as type 2 LINER (Ho et al. 1997). Perpendicular to the radio jet, a 2″ long, thick nuclear dust disk is clearly visible (Jaffe et al. 1996). The galaxy was classified as core galaxy, but Bonfini et al. (2018) show that nuclear dust can masquerade the galaxy to look like

[7] They assume a distance of 46 Mpc. The value we report here is down-scaled to an assumed distance of 43.1.

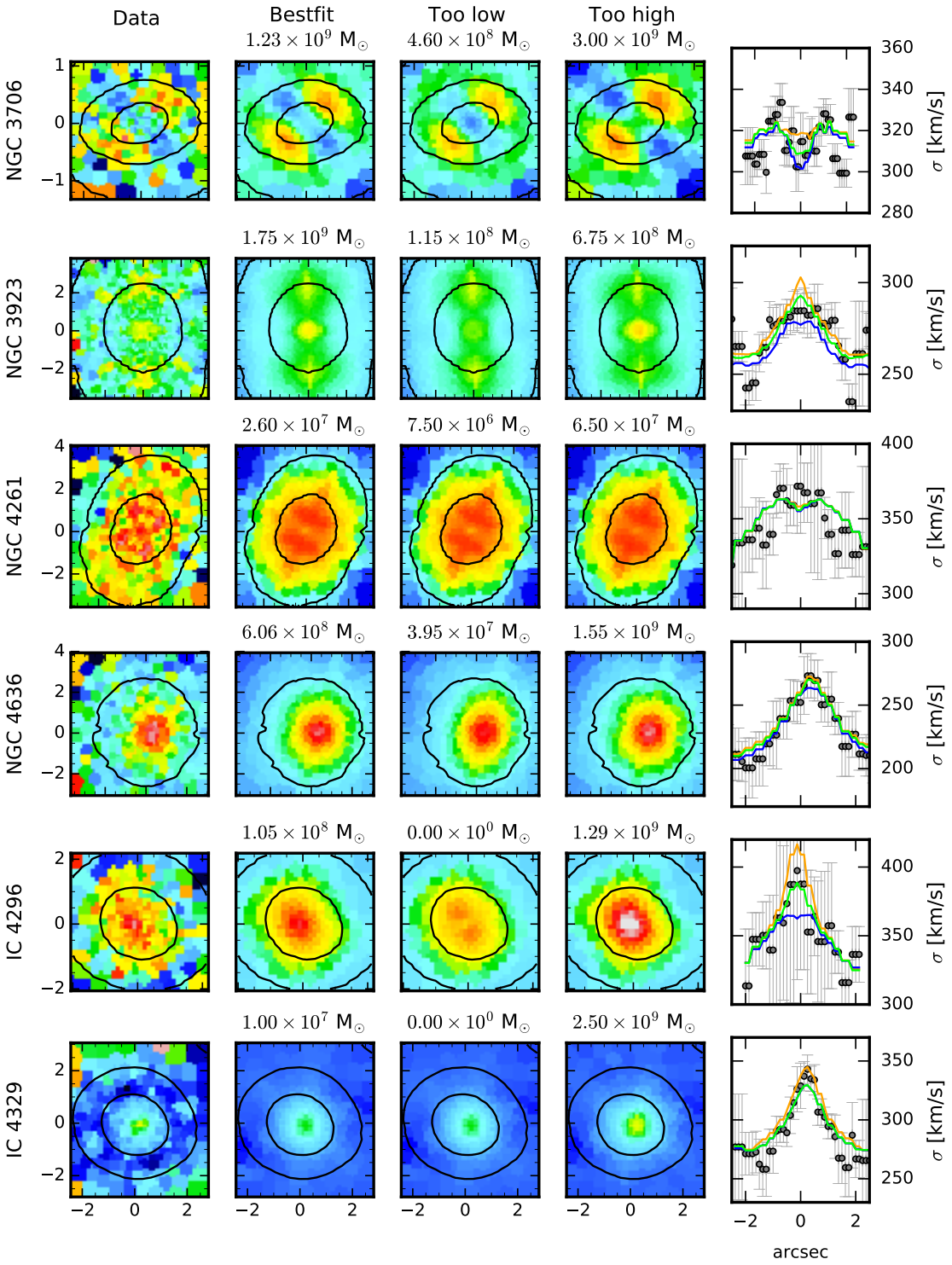


**Figure 4.7 —** Comparison of the velocity dispersion maps from the observed SINFONI data and the Schwarzschild models. Each row shows the maps of one galaxy, respectively. From left to right we present the observed symmetrized velocity dispersion maps from the SINFONI data, and the velocity dispersion maps of the Schwarzschild models from the best fitting, a too low and a too high $M_{\rm BH}$ as well as the profiles along the x = 0 axis. The too low (blue) and too high (orange) black hole masses are chosen to be just outside of the $3\sigma$ $\chi 2$ contours. All models are shown at the respective best-fitting M/L. The high- and low-mass models are clearly ruled out for all galaxies.

a core galaxy. Therefore, a re-evaluation of the core by properly taking the dust into account will be of great advantage for a proper core classification in this galaxy as well as for IC 4296. In our photometric analysis, we have carefully masked the dust disk based on its obscuring characteristics (see also chapter 2 and 3) to obtain a detailed model of the luminous mass in the vicinity of the black hole. Our stellar kinematics reveal almost no rotation in the center, while prolate rotation dominates the larger scales which was already noted in very early studies (Davies & Birkinshaw 1986; Wagner et al. 1988; Krajnović et al. 2011). NGC 4261 was also one of the first galaxies which had their central massive black hole measured. The estimated black hole mass from ionized gas as tracer is $M_{\rm BH} = (4.9 \pm 1.00) \times 10^8 M_\odot$ (Ferrarese et al. 1996), which is again significantly above our derived black hole mass upper limit of $M_{\rm BH} = 1.31 \times 10^8 M_\odot$. It is possible that this strong discrepancy originates from both our models not being able to reproduce the prolate rotation of the galaxy well. NGC 4261 also has a noticeable high $M/L$ as derived by our models, but such large values have also been found in other studies (e.g., Saglia et al. 2016). For the future, we will apply the triaxial Schwarzschild models to NGC 4261 and take the dark matter into account which was shown to be non-negligible (Poci et al. 2016).

### NGC 4636

NGC 4636 has a weak radio jet originating from the galaxy's active nucleus, which was classified as LINER (Ho et al. 1997). The galaxy is a very circular-shaped core-elliptical which is embedded in a fainter envelope containing a large number of globular clusters (Dirsch et al. 2005; Lee et al. 2010). The kinematics of these globular clusters have been analyzed by Schuberth et al. (2006) and they revised earlier claims based on X-Ray data that this galaxy contains exceptionally large amounts of dark matter (Loewenstein & Mushotzky 2003). In fact, dynamical models suggest a similar dark matter fraction as in other elliptical galaxies (Poci et al. 2016). In the isophotal map of NGC 4636, a small dust-lane is visible close to the center of the galaxy. Temi et al. (2003) suspect that this dust-lane was accreted in a recent merger with a gas-rich galaxy. As the lane is very small, we correct for the dust due to the symmetry of our light model. Our stellar kinematic maps show that NGC 4636 is a typical prototype for slow-rotating galaxies revealing no rotation patterns and only very low velocities ($V_{\rm max} \approx 40$ km s$^{-1}$). On the other hand, the velocity dispersion peak is clearly visible, enabling a robust measurement of the black hole mass. NGC 4636 also belongs to the Beifiori et al. (2012) sample, and they measured a mass of $M_{\rm BH} = (3.80 \pm 2.50) \times 10^8 M_\odot$ which is consistent with our measurement assuming a spherical JAM model, but only about half of our best-fit black hole mass from the axisymmetric Schwarzschild models. As thus, NGC 4636 is a useful addition to the galaxies with mass measurements from different kinematical tracers. Although the spherical potential is probably a good assumption for this circular shaped galaxy, we will also include a test with triaxial models in the future.

### IC 4296

IC 4296 shows elliptical morphology and is the giant brightest cluster galaxy of the cluster Abell 3565. Similar to NGC 4261, HST observations have unveiled a distinctive nuclear dust disk in this galaxy (Lauer et al. 2005). The disk component is enveloping a strong radio source from which a double-sided jet extends out to 5′ from the nucleus. IC 4296 has furthermore been classified as core elliptical galaxy in earlier work (e.g., Kormendy & Ho 2013), even though, for similar arguments as for NGC 4261 it needs to be tested how robust the core classification is. Our derived kinematics of this galaxy shows again a very peculiar feature, which is a counterrotating component in the center. This feature was noticed already in very early work by Franx et al. (1989) and Saglia et al. (1993). Unfortunately, the observations of this fascinating

galaxy have the lowest S/N in our sample, and the large error bars make it difficult to identify the counterrotation in the other moments. All the mentioned features made the dynamical modeling very complicated. IC 4296 is the second galaxy of our sample, which was also analyzed by Saglia et al. (2016). They report $M_{\rm BH} = (1.30 \pm 0.23) \times 10^9 M_\odot$ and $M/L_{\rm B} = 5.6\, M_\odot/L_\odot$ from axisymmetric Schwarzschild models. Almost the same mass was also reported from Dalla Bontà et al. (2009) from the kinematics of ionized gas. We predict an upper limit BH mass from the spherical JAM models, which is slightly above their measurement. However, when visually inspecting the models (see Figure 4.7), it is clear that the best-fit model would be produced at a similar mass to the one found by Saglia et al. (2016). However, the derived kinematic errors are so large that it is impossible to constrain the best-fitting model. While we have already put a lot of effort in masking the dust-disk, it extends so far into the center that it is challenging to model the stellar light distribution in the vicinity of the massive black hole. A possible improvement could be achieved by taking the information from all available HST bands into account to correct for the dust contamination (like in chapter 2). Furthermore, using the triaxial assumption could improve the modeling of the two counterrotating components.

#### IC 4329

IC 4329 is a giant lenticular and the giant brightest cluster galaxy of the cluster Abell 3574. Laine et al. (2003) noticed a core in the surface brightness of this galaxy. While the central kinematics do not look very disturbed, due to their proximity, IC 4329 is likely interacting with its neighbor IC 4329A[8]. Two asymmetric features are seen in the kinematics derived from the MUSE data. That is a shift of the rotational velocity along the major axis in opposite directions, respectively. It will be an interesting test to see, whether triaxial Schwarzschild models can reproduce this rotational feature.

### 6.2 Caveats and outlook

In this chapter, we present our ongoing analysis of the six massive early-type galaxies of the SMASHING sample. We report the derived estimates and upper limits of the black hole mass based on dynamical Jeans and axisymmetric Schwarzschild models but still miss an extensive error analysis. Furthermore and crucially, the currently constructed Schwarzschild models do not represent our massive galaxy observations very well. We shortly discuss the main steps that we plan to improve our measurements in the further course of the project.
*Triaxial structure:* While we have applied the spherical assumption for our JAM models, which is an acceptable first-order approximation for our galaxies, the Schwarzschild models certainly require triaxiality. Direct comparisons between triaxial and axisymmetric models have not been reported for many times. van den Bosch & de Zeeuw (2010) constructed triaxial models to derive black hole masses in M32 and NGC 3379. They report the mass measurement in M32 to be consistent for both methods, while the black hole in the more massive NGC 3379 is twice as high as for axisymmetric Schwarzschild models. NGC 3379 is most similar to our galaxies, and the result by van den Bosch & de Zeeuw (2010) implies the possibility of more massive black holes in our galaxies as well. Constructing triaxial dynamical models of our galaxies with the modeling code by van den Bosch et al. (2008) will be the scope of our future analysis.

*Dark matter:* Several studies have reported a dependence between dark matter fractions within $r_{\rm eff}$ and galaxy luminosity, stellar mass, size and velocity dispersion (e.g., Napolitano et al. 2010; Tortora et al. 2012). Ma et al. (2014) show expected large dark matter halo masses for the

[8] https://heasarc.gsfc.nasa.gov/docs/objects/galaxies/ic4329.html

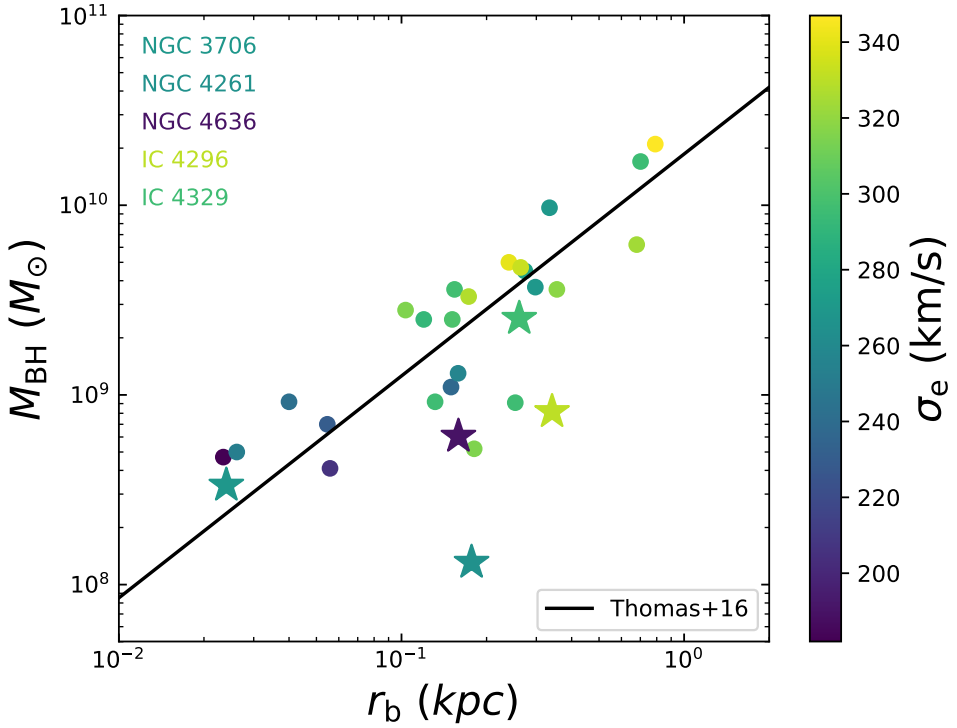


**Figure 4.8 —** Relation between core-Sérsic break radius $r_b$ and black hole mass. We used the compilation of core galaxies from Rusli et al. (2013b) and added our core galaxies. The colours indicate the effective velocity dispersion of the shown galaxies. The turquoise star at $\sim 10^8\ M_\odot$ is NGC 4261. The solid line is the fit to the same sample (except for our measurements) by Thomas et al. (2016).

MASSIVE galaxies, which show similar characteristics to our sample galaxies. We, therefore, expect a possibly non-negligible amount of dark matter in our sample galaxies, which should be accounted for in the dynamical modeling. As was discussed in earlier chapters, the ignorance of dark matter in dynamical modeling can lead to underestimating the derived black hole mass by up to a factor of 2, owing to the degeneracy between the dark matter halo mass, the stellar mass-to-light ratio and the black hole mass (Gebhardt & Thomas 2009; Schulze & Gebhardt 2011; Rusli et al. 2013b). It is furthermore our future goal to investigate the orbital distribution in our sample galaxies to learn about their evolution and the formation of their central cores. Thomas et al. (2014) show that ignoring dark matter in dynamical models can alter the derived orbital structure, orbits being significantly more tangential-biased (see also Binney & Mamon 1982; Gerhard 1993). We will therefore also include dark matter to our dynamical models in the future (in a similar way as described in Chapter 2).

*Scaling relations:* Our sample of high-mass and mostly cored galaxies will be a valuable and significant addition to the current sample of high-mass galaxies. The high-mass region suffers from a large intrinsic scatter which might be caused by different galaxy evolutionary tracks and current problems in the black hole mass measurements. In particular, our five newly measured galaxies with cores will increase the sample of cored galaxies with measured black holes by 30% (see Figure 1.4). We show our preliminary results (using the JAM results) in Figure 4.8 and Figure 6.1 of Chapter 7 and compare them with our compiled literature values. Figure 4.8 shows the relation between black hole mass and the size of the depleted core expressed as core radius ($r_b$) which has received a lot of attention recently (Rusli et al. 2013a; Dullo & Graham 2014;

Thomas et al. 2016; Rantala et al. 2018). Three of our galaxies currently deviate significantly from this relation which could be caused by the ignorance of triaxiality in our models or possibly incorrect break radii which might require a revision (see, e.g. Graham et al. 2003, for discussion on NGC 4636). Furthermore, two of these three galaxies are the galaxies with strong dust disks which might mimic a core. In the future, we will re-create this plot with our final mass measurements and investigate its implications.

# 7 Large-scale kinematics

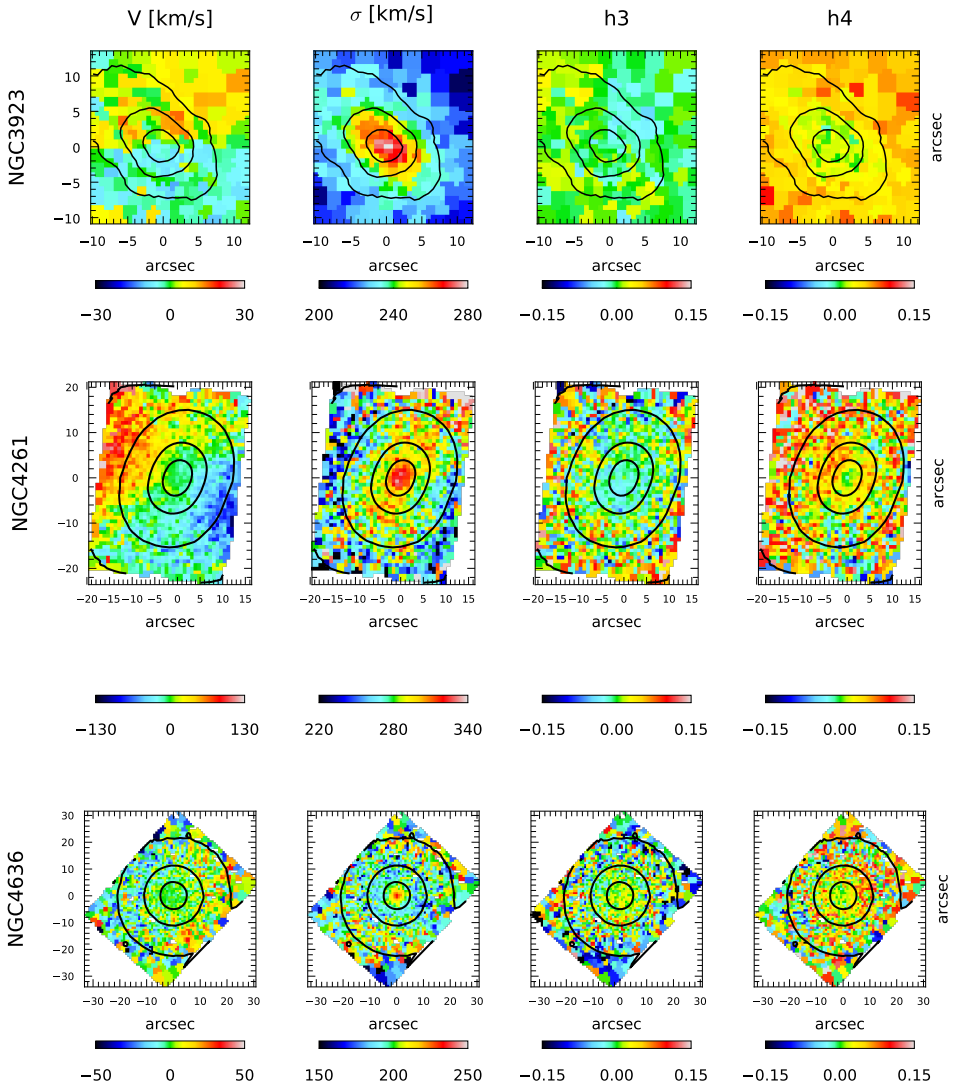


**Figure 4.9 —** Large-scale stellar kinematics of NGC 3923 (VIMOS), NGC 4261 (SAURON) and NGC 4636 (SAURON). Shown are the mean velocity V, velocity dispersion $\sigma$ and the $h_3$ and $h_4$ Hermite polynomials extracted by using pPXF. NGC 4261 and NGC 4636 are part of the ATLAS$^{3D}$ project and detailed described in Cappellari et al. (2011). The image orientation is such that north is up and east is left.

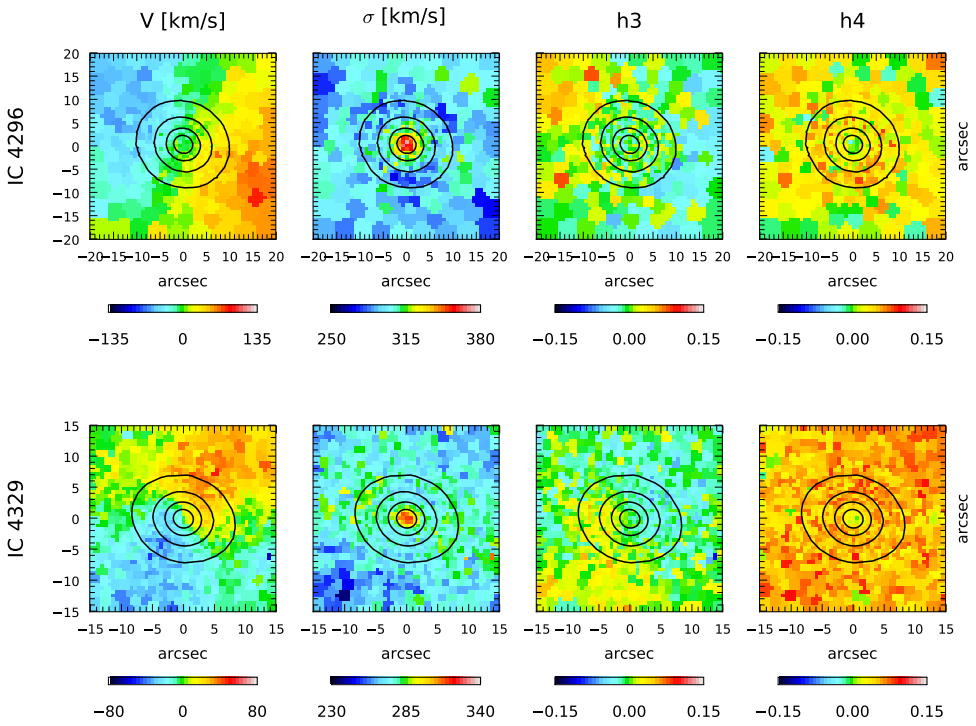


**Figure 4.10 —** Large-scale stellar kinematics of IC 4296 and IC 4329 extracted from the MUSE observations. Shown are the mean velocity V, velocity dispersion $\sigma$ and the $h_3$ and $h_4$ Hermite polynomials extracted by using pPXF.

# 8 Comparison of the Schwarzschild dynamical models with the symmetrized data

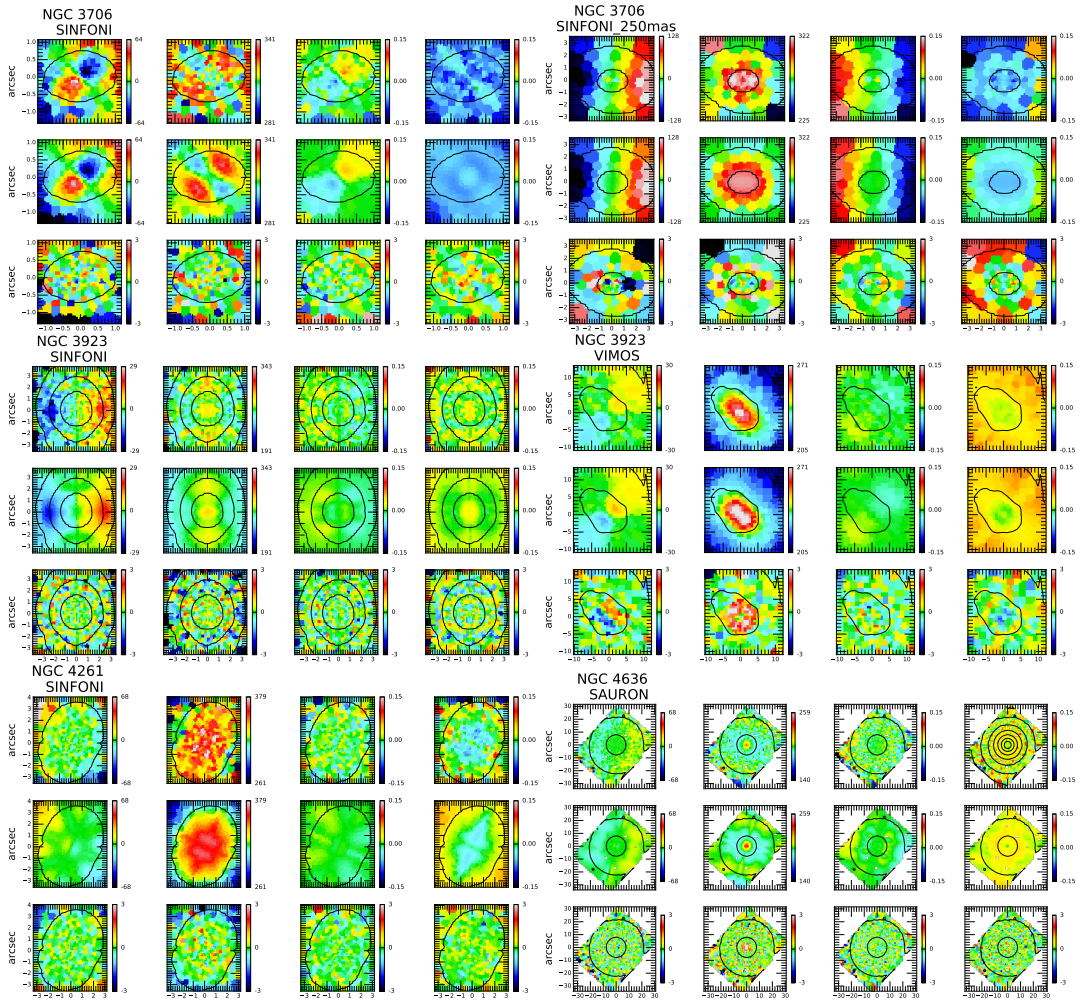


**Figure 4.11 —** Comparison between symmetrized kinematic data and best-fitting Schwarzschild models for the galaxies NGC 3706, NGC 3923, and NGC 4261. For each galaxy we show the SINFONI data on the left side and the large-scale data on the right side. The panels are ordered as follows: From left to right: mean velocity, velocity dispersion, and $h_3$ and $h_4$ Gauss-Hermite moments. From top to bottom: symmetrized data, model for the best-fitting parameters from Table 4.5, and residual map defined as difference between the Schwarzschild model and observed kinematics divided by the observational errors.

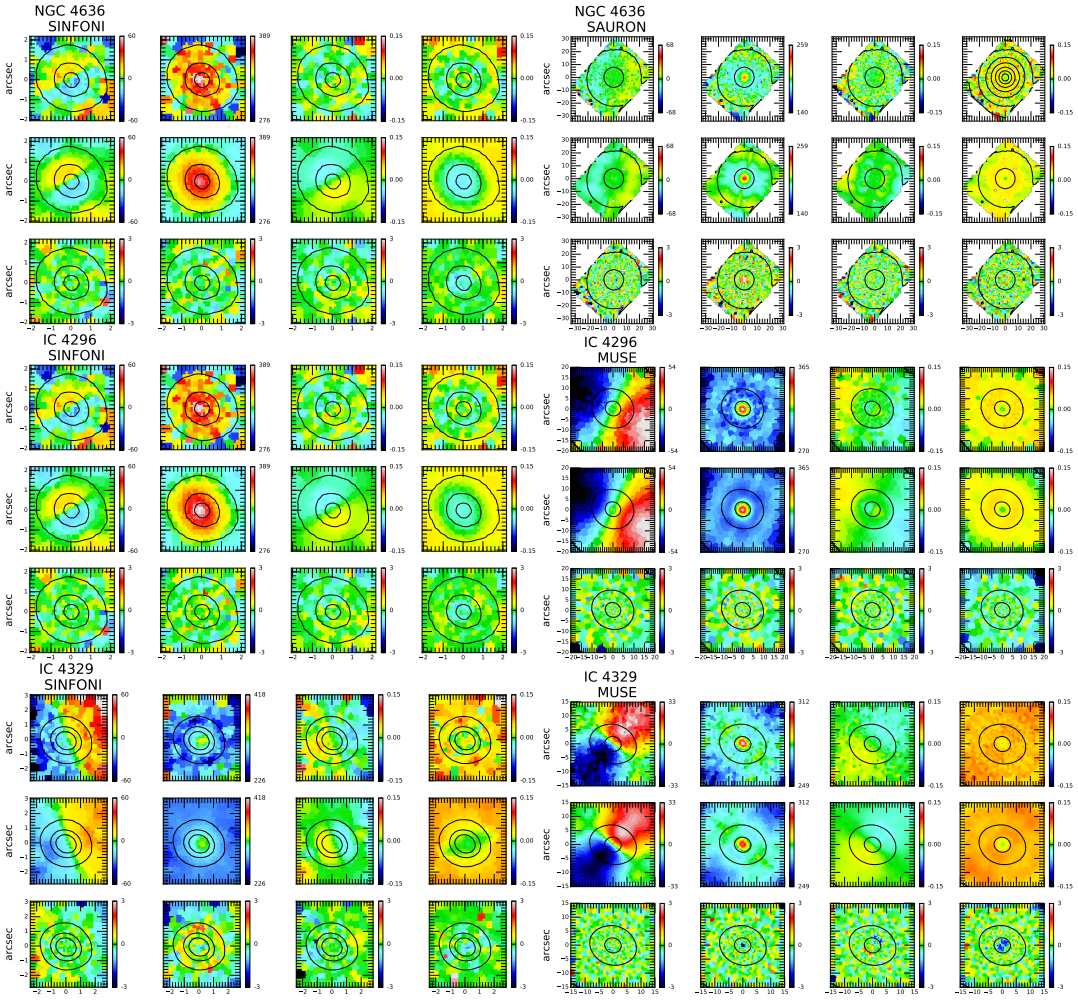


**Figure 4.12 —** Comparison between symmetrized kinematic data and best-fitting Schwarzschild models for the galaxies NGC 4636, IC 4296, and IC 4329. For each galaxy we show the SINFONI data on the left side and the large-scale data on the right side. The panels are ordered as follows: From left to right: mean velocity, velocity dispersion, and $h_3$ and $h_4$ Gauss-Hermite moments. From top to bottom: symmetrized data, model for the best-fitting parameters from Table 4.5, and residual map defined as difference between the Schwarzschild model and observed kinematics divided by the observational errors.

# 5 Testing the robustness of black hole mass determinations with ALMA and MUSE

**Sabine Thater, Davor Krajnović, Satoru Iguchi, Timothy A. Davis, Dieu Nguyen, Peter M. Weilbacher et al.**

— A version of this chapter will be submitted to *Astronomy & Astrophysics*. The chapter contains preliminary results which might still change until publication. —

Abstract

We present two estimates of the mass of the supermassive black hole (SMBH) in the nearby regular early-type LINER galaxy NGC 6958, which are based on two different dynamical tracers (i.e., molecular gas versus stars). The measurement are based on Atacama Large Millimeter/submillimeter Array (ALMA) cycle 3 observations of $^{12}$CO(2-1) emission and adaptive optics-assisted Multi-Unit Spectroscopic Explorer (MUSE) science verification data. The different methods provide black hole masses of $(2.89 \pm 2.05) \times 10^8 M_\odot$ from stellar kinematics and $(1.35 \pm 2.05) \times 10^8 M_\odot$ from the molecular gas kinematics and are consistent within their $3\sigma$ uncertainties. Our results also confirm previous findings, that gas-based methods often provide lower black hole masses than stellar-based methods. In fact, we measure a factor two between both tracers, which is also often found in the literature. We will extensively analyze our datasets in the further course of the project to understand the systematics of the different methods. We will also add a third mass measurement based on ionized gas kinematics of NGC 6958 making this the first study to compare molecular and ionized gas as well as stellar kinematics methods with each other.

# 1 Introduction

The ongoing developments in astronomical instrumentation over the last two decades have substantially improved the observational capabilities allowing us to robustly measure the mass of supermassive black holes in the local universe using a variety of different methods (e.g., review by Kormendy & Ho 2013). Measuring black hole masses is a challenging task that requires the highest possible resolution for both photometric and spectroscopic observations and state-of-the-art data analysis methods. As black holes are per se not visible, we need to trace material in the vicinity of the back hole in order to derive the gravitational potential of black holes. Popular tracers are individual stars (in the Milky Way; Ghez et al. 2008; Gillessen et al. 2009, 2017), masers (e.g., Greene et al. 2016; van den Bosch et al. 2016; Gao & Ho 2017), ionized (Beifiori et al. 2012; Walsh et al. 2013) or molecular gas clouds (Davis 2014; Onishi et al. 2015; Onishi et al. 2017; Davis et al. 2018b; Nguyen et al. 2019) or unresolved stellar systems (Rusli et al. 2013b; Saglia et al. 2016). While a variety of different tracers and methods are available, it is not possible to use a single modeling method to measure the black hole mass for all types of galaxies. Stellar-based methods, as used in this thesis, can be best used for early-type galaxies which usually do not have strongly varying stellar populations nor sub-components like bars or spiral arms. On the other hand, gas is typically found in late-type galaxies and can be used as a tracer if the gas is not strongly disturbed and follows circular orbits. Other methods require the presence of nuclear maser emission or an AGN in the galaxy nucleus. Checks for inconsistencies between the different mass determination methods are important for identifying systematic uncertainties associated with the techniques and deriving robust masses.

Hitherto, cross-checks between different dynamical modeling methods have only been performed for a handful of objects. While the checks give consistent results in a number of cases (Davies et al. 2006; Pastorini et al. 2007; Neumayer et al. 2007; Cappellari et al. 2009), most cross-checks reveal clear discrepancies between different methods (e.g., Verdoes Kleijn et al. 2002; de Francesco et al. 2006; Gebhardt et al. 2011; Walsh et al. 2012, 2013; Onken et al. 2014; Barth et al. 2016, but see also Figure 1.8 of Chapter 1). Even measuring the same galaxy with different stellar dynamical methods does not always provide agreeable black hole masses; see, for instance, NGC3379 (Shapiro et al.2006; van den Bosch & de Zeeuw 2010), NGC1399 (Houghton et al. 2006; Gebhardt et al. 2007) and NGC4258 (Siopis et al.2009; Drehmer et al. 2015), but see also the discussion of our galaxies from Chapter 4. The origin of these discrepancies cannot be pinned down easily, because different methods, different assumptions, and different wavelength regions are used for different tracers probing the potential in different ways. The inhomogeneity of the mass measurements and the low number statistics make it impossible to quantify the systematic uncertainties. However, providing a measure of the systematics from the different methods is mandatory for an in-depth understanding of the origin of the black hole correlations and thus of the formation and growths of supermassive black holes. Particularly, we need to answer the questions: How do systematics change the slope of the scaling relations? How much of the scatter in the black hole scaling relations can be attributed to inconsistencies between the various dynamical measurements?

As we slowly start to reach a statistically relevant galaxy sample with measured black holes, now is the best time to revisit known black hole mass measurements with different methods for two reasons. Firstly, black hole mass measurement has started to become reliable with the advent of the Hubble Space Telescope (HST), but the usage of long-slit compared to modern integral-field spectroscopy flawed early measurements. Secondly, even recent measurements suffer from strong systematic biases associated with the modeling assumptions. It is thus important to

**Table 5.1 —** Basic properties of NGC 6958 taken from the literature.

| Property | | Reference |
|---|---|---|
| Morphological type | S0 | 1 |
| Distance [Mpc] | 35 ± 2 | 2 |
| Linear scale [pc arcsec$^{-1}$] | 170 | 3 |
| Inclination [ $^{\circ}$] | 35.7 | 4 |
| Sersic index | 3.3 | 4 |
| Bulge effective radius [arcsec] | 24.0 | 4 |
| $\sigma_e$ [km s$^{-1}$] | 180 ± 5 | 5 |

**References.** 1: The galaxy had been misclassified in de Vaucouleurs et al. (1991) and we adopt the classification by Sandage & Bedke (1994) and Laurikainen et al. (2010). 2: NED. 3: Calculated from the distance. 4: Based on B-band decomposition from Ho et al. (2011). 5: This work. Derived by co-adding the spectra of the MUSE data in elliptical annuli of the size of the effective radius.

understand and quantify the systematics as detailed as possible, to evaluate the robustness of the mass measurements and shrink the associated uncertainties.

For that purpose, cold molecular gas, detected at low temperatures ($\sim$ 10K), offers a promising probe of the gravitational potential in the vicinity of the black hole (Davis et al. 2013). While cold molecular gas can in principle be affected by non-gravitational forces and turbulences just like ionized gas (e.g., Smajić et al. 2015), molecular clouds tend to follow circular orbits and are unaffected by the dust. Due to its high angular resolution and great sensitivity owing to the large collective area, the Atacama Large Millimeter/submillimeter Array (ALMA) can be used to effectively derive black hole masses in thousands of galaxies with molecular gas disks (Davis 2014). The number of measured black hole masses from molecular gas increases unceasingly (Davis et al. 2013; Onishi et al. 2015; Onishi et al. 2017; Barth et al. 2016; Scharwächter et al. 2016; Davis et al. 2017b, 2018b; Combes et al. 2018; Nguyen et al. 2019; Smith et al. 2019; Nagai et al. 2019; Boizelle et al. 2019), offering a great alternative to estimate black hole masses using nuclear molecular gas disks. It is the goal of this chapter, to compare the black hole mass measurement from the novel molecular gas-based method with the traditional method of stellar kinematics (which was used in the remaining chapters).

In order to connect the results from stellar and molecular gas dynamical models, it was necessary to identify objects which offer the possibility to apply both types of modelings. Early-type galaxies with molecular gas are prime candidates for both types of modeling methods to estimate robust black hole masses and understand the origin of methodological discrepancies. We found such a target in the WISDOM sample (Onishi et al. 2015) that provides high-quality ALMA observations for a large variety of galaxies[1]. In this work, we have targeted the massive fast-rotating early-type WISDOM galaxy NGC 6958, which shows clear signs of a regularly rotating nuclear molecular gas disk (Davis et al. 2013). In addition, NGC 6958 was classified as LINER galaxy showing large equivalent width of H$\alpha$ and [NII]$\lambda$6584 emission (Saraiva et al. 2001; Annibali et al. 2010), which can also be used to estimate the black hole mass. Given its regularity and the availability of gas features, NGC 6958 is a unique case in which three different dynamical tracers can be compared with each other, namely integrated stellar kinematics, ionized and molecular gas kinematics. NGC 6958 is isolated (Madore et al. 2004) but shows evidence of a recent major merger (Malin & Carter 1983) in its outer properties. As we show in Section 4 and

[1]Private communication with Timothy A. Davis

5, the merger does not inflict with our black hole mass measurements as the nuclear kinematics show clear regular features. Based on its expected effective velocity dispersion of around 180 km $s^{-1}$ the galaxy is expected to harbor a black hole of mass $M_{BH} = 2 \times 10^8 M_\odot$ (Saglia et al. 2016) which is detectable ($r_{SoI} = 0.15''$) with our observational facilities of choice. As shown in Figure 1.8 of Chapter 1, this is the mass region where the $M_{BH}$ determined from the (mostly ionized) gas-based measurements seem to be systematically less massive than black holes in galaxies where the estimates are derived from stellar dynamical models. A direct comparison between the two methods and tracers of the gravitational potential offers a crucial test of the associated systematics.

In this chapter, we show the ongoing work of using two independent tracers to derive the black hole mass in NGC 6958, test whether the different methods give consistent results and analyze the systematics associated with the dynamical techniques. This chapter is composed of four sections. We begin by describing the imaging observations and the determination of the galaxy's stellar mass distribution in Section 2 which is needed for the dynamical modeling of the molecular gas motion (Section 3) and the dynamical modeling of the stellar kinematics (Section 4) in the vicinity of the massive black hole. We conclude by comparing the results of the already constructed methods and providing an outlook of how we will continue this project in the future.

## 2 Mass model

A common requirement for the two different dynamical methods is the determination of the gravitational potential of the galaxy. We inferred the galaxy potential directly from the stellar luminosity of the galaxy multiplied with its (variable) mass-to-light ratio $M/L$, which can account for M/L variation and possible dark matter (see Chapter 2). For a precise model of the stellar luminosity, a combination of high-resolution HST and deep large-scale imaging data is essential.

### 2.1 Imaging data

NGC 6958 has been observed with HST for several times. In the archival data, we found short 400s exposures in the F547W band and 160s exposures in F814W band obtained with the Wide Field and Planetary Camera 2 (WFPC2 Holtzman et al. 1995). Also, one 1152s exposure in the H-band (F160W) of the Near Infrared Camera and Multi-Object Spectrometer (NICMOS) was available in the archive. Each of the images has specific advantages and disadvantages, justifying to test light models of different bands in the dynamical modeling. NGC 6958 contains a thick nuclear dust disk, which is better corrected for by using a near-infrared image (F160W). On the other hand, deeper large-scale images were only available in the optical range and are needed to trace the galactic gravitational potential up to large scales. This information is important for the construction of the orbit library. A proper treatment of the nuclear dust is crucial for measuring the black hole mass in all applied methods discussed in this chapter. We decided to use the NICMOS data, but will also test the other available filter bands for alternative mass models at a later point. For the large-scale information of NGC 6958, we used a Two Micron All-Sky Survey H-band image, which we retrieved from the 2MASS archive[2].

### 2.2 Multi-Gaussian Expansion

As in the previous chapters, we used the Multi-Gaussian Expansion (MGE; Cappellari 2002) code to parametrize the surface brightness of NGC 6958 with a set of two-dimensional Gaussians.

[2]https://irsa.ipac.caltech.edu/applications/2MASS/IM/interactive.html

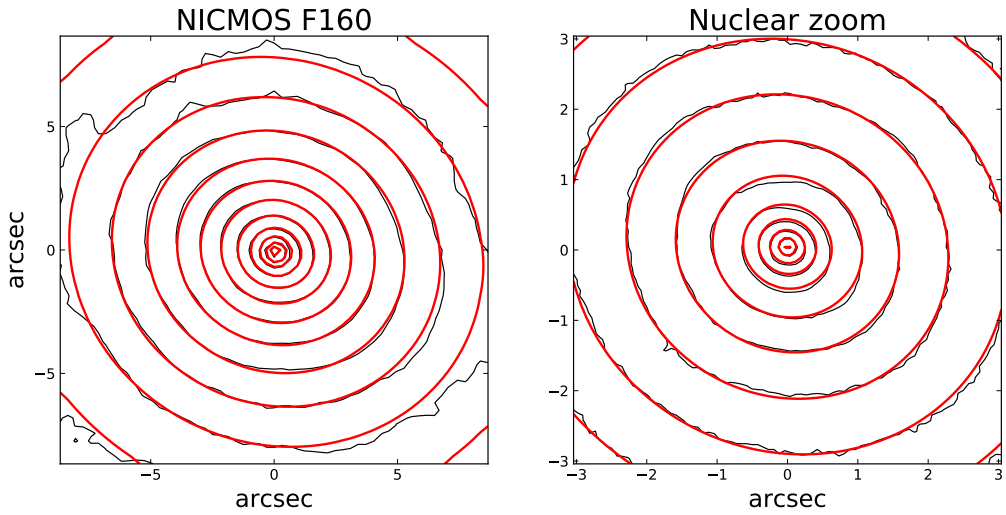


**Figure 5.1 —** Isophotal maps of the NICMOS image of NGC 6958 within a FoV of 20″ × 20″and a cutout of the central 6″ × 6″. The contours of our best-fitting MGE model (red) are superimposed on the HST images (black). The MGE models were build from the combined photometric information of HST (r ≤ 7″) and wide-field 2MASS (r > 7″) data.

We used the HST image for the fit of the central 7″ of the galaxy and the 2MASS image for the outer light distribution. During the fit, we also took the NICMOS PSF (which was also parametrized in a sum of Gaussian) into account in order to obtain a deconvolved MGE model of the galaxy. Figure 5.1 shows our best-fitting MGE model overplotted on the observed surface brightness distribution of NGC 6958. While the central parts of the HST image could be well fitted with the MGE models, we saw a clear isophote twist by almost 30 degrees starting at $r > 15''$. This isophotal twist was also already found by Saraiva et al. (1999) and was possibly generated by a recent merger. Our dynamical models do not account for isophotal twists as they are axisymmetric. However, the center which is probed by our dynamical models shows no significant isophotal twist and relaxed stellar kinematics data (see Figure 5.5). We kept the position angle at a constant. Our final MGE converged for nine concentric Gaussians components. We converted the flux units from pixel-space into physical units of $L_\odot$ $pc^{-2}$ following the guideline and zero points given by Thatte (2009). For the conversion, we adopted a value of $M_{\odot,H} = 4.64$ mag (Willmer 2018) for the absolute AB-magnitude of the sun in the H-band. The converted MGE parameters are shown in Table 3 of the Appendix.

In order to derive a mass model, the two-dimensional light parametrization is then (assuming an axisymmetric potential and the inclination of the galaxy) deprojected into the three-dimensional space. Multiplied with the mass-to-light ratio in the given band, we thus obtained a model of the mass density. For the molecular gas dynamical models, we calculated the circular velocity curve along the galaxy major axis from the mass model using the routine mge_circular_velocity from Cappellari (2008). A similar approach was undergone in Section 5.1 of Chapter 2 to derive a two-dimensional circular velocity model for the observed CO velocity field of NGC 4414.

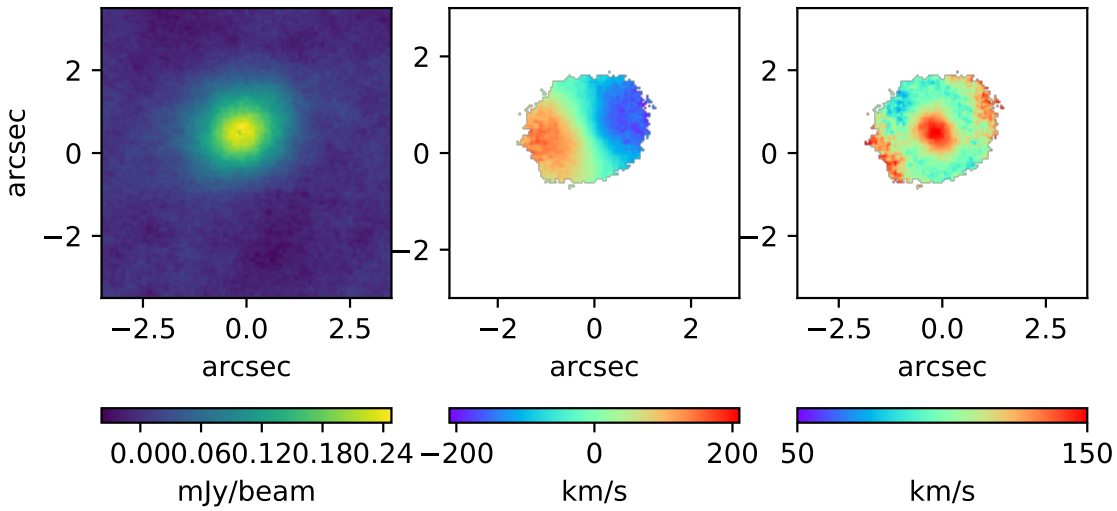


**Figure 5.2 —** Momentum maps of the detected $^{12}$CO(2-1) emission derived from the high-resolution ALMA observation. The panels show the integrated intensity (0th moment), intensity-weighted mean velocity (1st moment) and velocity dispersion (2nd moment).

# 3 ALMA data

## 3.1 Observations and data analysis

NGC 6958 was observed with the Atacama Large Millimeter/submillimeter Array (ALMA) as part of the WISDOM project (Onishi et al. 2017) in cycle 3 (program 2015.1.00466.S, PI: Onishi). Three separate observations were carried out between November 8th, 2015 and April 22th 2016, providing a total integration time of 581s (high angular resolution of 0.03″) and 242s (low angular resolution of 0.5″). Observations were obtained in a frequency band centered at 227.52 GHz (in ALMA Band 6), corresponding to the redshifted $^{12}$CO(2-1) 230.538 GHz line. The raw data were retrieved from the ALMA Science archive and calibrated using the standard ALMA pipeline, as provided by the ALMA regional center staff. Several flags were added to improve the image quality. For the low-resolution the bandpass calibration was applied from J2056-4714, atmospheric phase offsets were determined from J2057-3734 and Titan, and Pallas served as flux calibrator. We then applied the data reduction with Common Astronomy Software Applications (CASA, McMullin et al. 2007) to combine the individual data sets, subtract the continuum emission, a broadband emission that spans all spectral channels, and image the resultant visibility file. While combining the three individual data sets, we carefully examined the effect of different weighting schemes to find the best compromise between resolution and sensitivity. Cleaning was applied down to $1\sigma$ of the dirty maps. The resulting combined emission-line data cube has a spatial scaling of 0.1″ over a field-of-view of 26.6″ × 26.6″ and 75 velocity channels with a velocity width of 10 km/s per channel. The synthesized beam after the combination has major and minor axis FWHM sizes of 0.073″ × 0.057. While we reached a quite high angular resolution by combining the individual high- and low-angular resolution data, working with the resulting cube is computational very expensive owing to its size. We, therefore, performed the initial tests only with the low-angular resolution data cube (beam size 0.70″ × 0.49″), which has a comparable resolution to the MUSE data (see Section 4). As soon as we have finished the initial tests, we will also include the high-resolution data to robustly measure the black hole mass and analyze the effects of resolution on the measurement.

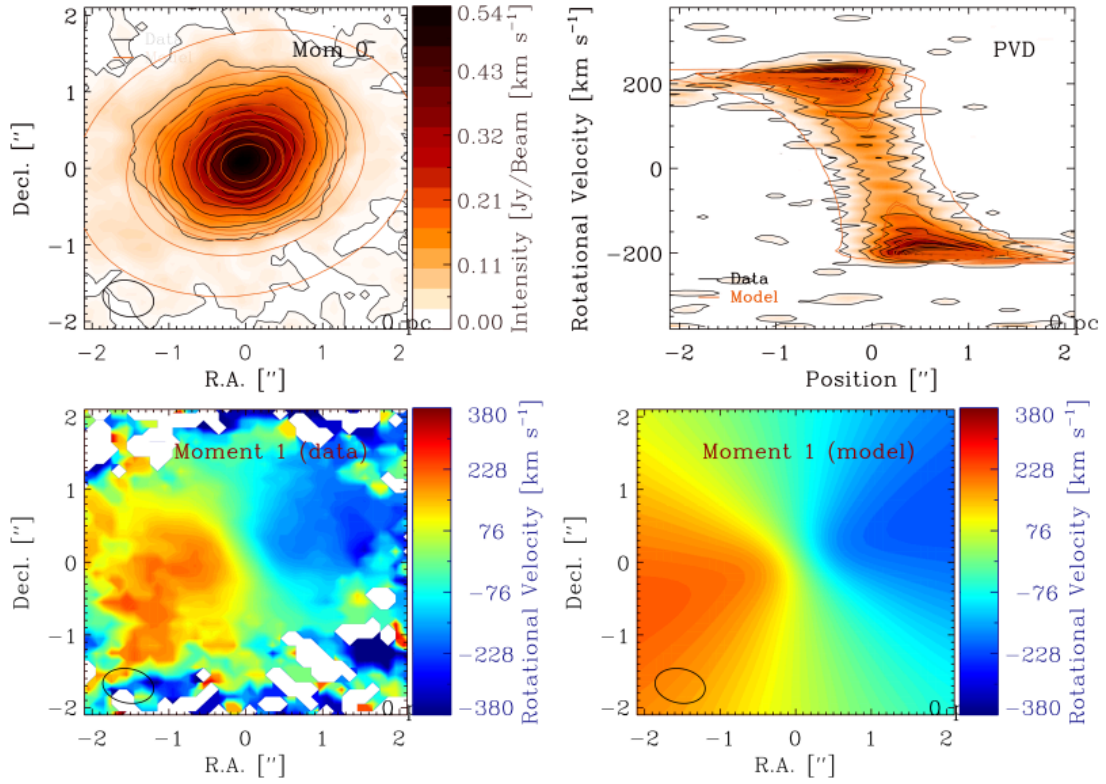


**Figure 5.3 —** Results of the KinMS routine. The upper left and bottom panels show a comparison between the 0th and 1st moment of the ALMA data and the respective moments derived from the simulated KinMS datacube. In the upper right panel, we show the position-velocity diagram (PVD) of the $^{12}$CO(2-1) emission (redscale+black contours) and the simulated model cube (red contours) extracted along the kinematic major axis with a slit of five pixels in width (0.5″).

## 3.2 Molecular gas kinematics modeling

In this method, we estimate the mass of the central black hole by identifying the Keplerian turnover motion of the cold gas disk in the vicinity of the black hole. The position and size of the turnover depend on the black hole mass and can accordingly be used to derive the mass. The main assumption in this method is that the gas moves in circular orbits. We constructed a dynamical model for the molecular gas using the publicly available KINematic Molecular Simulation (KinMS; Davis et al. 2013) routine[3], IDL version 1.7. The routine uses the molecular gas distribution and kinematics, instrumental effects and information of the gravitational potential of the galaxy to simulate a three-dimensional data cube, the two spatial coordinates, and velocity on the third axis as in the observed ALMA cube. We used a Markov chain Monte Carlo (MCMC) method KINMS_MCMC to constrain the morphology of the molecular gas in the center of the galaxy. Therefore, it uses the information on the input gas distribution, the circular velocity curve (derived from the MGE model) and the disk orientation. The gas distribution is usually parametrized as exponential disk described by the surface brightness scaling factor, radial scale radius, and the radius of the massive black hole (Davis et al. 2017b; Onishi et al. 2017). Furthermore, to properly reproduce the observed ALMA data, the beam-smearing and spatial and velocity binning are taken into account by KinMS. In total, our fit consists of 10 parameters (SMBH mass, stellar M/L in the H-band, inclination, position angle, the three parameters of the exponential disks and offsets in the x, y and velocity direction) , which are fitted in the MCMC

[3]https://github.com/TimothyADavis/KinMS

**Table 5.2 —** Double Gaussian Parametrisation of the MUSE PSF

| Data | $\mathrm{fwhm}_1$ (arcsec) | $\mathrm{fwhm}_2$ (arcsec) | f1 |
|---|---|---|---|
| MUSE | 0.715 | 1.997 | 0.64 |

**Notes.** Column 1 & 2: Full width at half maximum of the two Gaussians. Column 3: relative flux of the first Gaussian.

routine, making the fit very computationally expensive. We ran the fitting routine for $3 \times 10^6$ iterations and obtained a preliminary best-fitting black hole mass of $(1.35 \pm 0.09) \times 10^8\ M_\odot$, mass-to-light ratio in the H-band of $0.83 \pm 0.03\ M_\odot/L_\odot$, inclination of $41.0 \pm 0.2°$ (after marginalizing over the remaining best-fitting parameters). We caution that the errors are currently very small and we will re-examine their calculation in the future. A comparison for the 0. and 1.moment and the position-velocity diagram (PVD) between our ALMA data and the best-fitting KinMS model is shown in Figure 5.3. Our model reproduces the observations already very well, but require further improvements in the future. This effect is, in particular, visible in the PVD which indicates a slight underprediction of the rotational velocity in the model (and thus underprediction for the black hole mass). The underprediction is however likely only of the order of 10-20% and will not resolve any estimated black hole mass discrepancies (see next section). In the future, we will improve the KinMS models to estimate robust black hole masses with clear uncertainties. We will then exchange the low-angular resolution ALMA data with the high-resolution data, which shows the turnover motion more clearly. In the last and most crucial step, we will investigate the different assumptions made in these modeling methods and its implication for the measured black hole mass. Assumptions are, for instance, the motion on circular orbits, the morphology of the gas disk as well as its thickness which is currently not included in our models.

# 4 MUSE data

## 4.1 Observations and data reduction

We obtained adaptive optics (AO) assisted Multi-Unit Spectroscopic Explorer (MUSE; Bacon et al. 2010) science verification data under the science program 60.A-9193(A) (PI: Krajnović) in the night of the 18th of September 2017. The GALACSI AO system was developed to optimize the performance of MUSE and consists of four sodium laser guide stars, a deformable secondary mirror on UT4 and an infrared low-order sensor to provide a near-diffraction limited observation at visible wavelength. Due to bad weather conditions, we could not make use of the full AO capabilities and achieved a spatial resolution of $0.7''$ derived from the method described in the previous chapters. Our MUSE observation has a total exposure time of 2040s divided into four 510s on-source integrations. We performed the data reduction using the MUSE data reduction pipeline (Weilbacher et al. 2015), version 2.6. The pipeline includes bias and sky subtraction, flatfield correction, wavelength, and flux calibration and telluric correction of each on-source observation. Furthermore, in the new version 2.6, a correction of wiggles that are visible in the spectral domain of high S/N data in AO modes are properly corrected for. After the data reduction, we merged the individual exposures with the MUSE pipeline merging procedure taking the respective offsets into account. In the final datacube, each spaxel has a size of $0.2'' \times 0.2''$ and spectral sampling of 1.25Å. We only used the central $30'' \times 30''$ of the MUSE FoV as we noted a kinematic twist for radii larger than $15''$ (whereas the kinematics are very regular within this radius). The respectively cut MUSE data was then Voroni-binned (Cappellari & Copin 2003) to

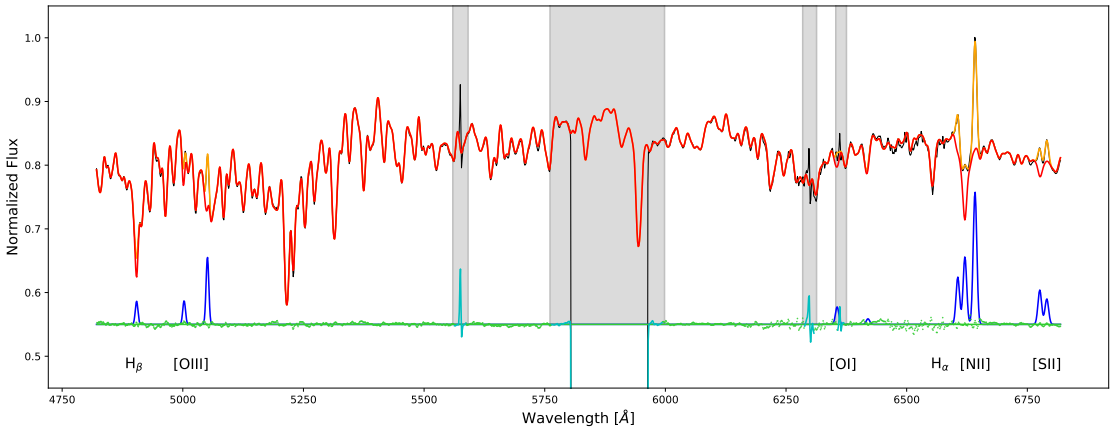


**Figure 5.4 —** Integrated MUSE spectra and pPXF fit of NGC 6958. The integrated spectrum (solid black lines) was obtained by summing up all spectra of the IFU data cubes (within 15″). This integrated spectrum was fitted using the pPXF routine (red lines) to derive an optimal template. The fitting residual between spectrum and best fitting model are shown as green dots and are shifted up by 0.55. Regions which were masked in the fit, owing to either the AO NaD laser or insufficient sky correction, are indicated as grey shaded regions.

a target S/N of 70, resulting in mostly unbinned information in the center and 1″ – 2″ bin sizes at radii larger than 7″.

## 4.2 Stellar and ionized gas kinematics

As in the previous chapters, we used the python implementation of the penalized Pixel Fitting method[4] (pPXF, Cappellari & Emsellem 2004; Cappellari 2017) to measure the line-of-sight velocity distribution (LOSVD) of each Voronoi bin of the MUSE data. The stellar templates were taken from the medium-resolution Isaac Newton Telescope library of empirical spectra (MILES, Sánchez-Blázquez et al. 2006; Falcón-Barroso et al. 2011) stellar library (version 9.1). As the MILES templates have a similar spectral resolution to the MUSE spectra[5], we did not need to degrade any of the two datasets. We used the full sample consisting of 980 stars that span the wavelength range 4760Å to 7400 Å and fitted the wavelength range from 4800 Å to 6500 Å in the galaxy spectrum. The region between 5750 Å and 6000 Å was blocked in the observation to avoid contamination and saturation of the detector by the strong sodium laser light. During the pPXF fit, we masked the blocked region and insufficiently reduced sky lines. The stellar continuum was modeled with a fourth-order additive Legendre polynomial.

The residuals from the stellar fit showed a richness of emission line features, such that we decided to fit for the emission lines and the stellar continuum simultaneously. We were thus able to detect and measure the H$\alpha\lambda$6563 and H$\beta\lambda$4861 Balmer lines and the [OIII]$\lambda\lambda$4959, 5007, [OI]$\lambda\lambda$6364, 6300, [NII]$\lambda\lambda$6548, 6583 and [SII]$\lambda\lambda$6716, 6731 forbidden line doublets over the whole MUSE FoV. The fluxes of the doublets were held at a 3:1 ratio. We show our best-fitting optimal template in Figure 5.4. After having found the optimal template (using both stellar continuum and gas emission information), we re-ran pPXF on the individual spectra of each bin of the MUSE observations and fitted the optimal template to extract the stellar kinematics.

[4]http://purl.org/cappellari/software

[5]Note that the MUSE LSF is not uniform over the complete wavelength range. We have analyzed the effect of the non-uniformity on our extracted kinematics in Chapter 3. By not convolving the MILES spectra adaptively to the spectral resolution of MUSE, we impose a systematic uncertainty of about 5 km s$^{-1}$ in the velocity dispersion.

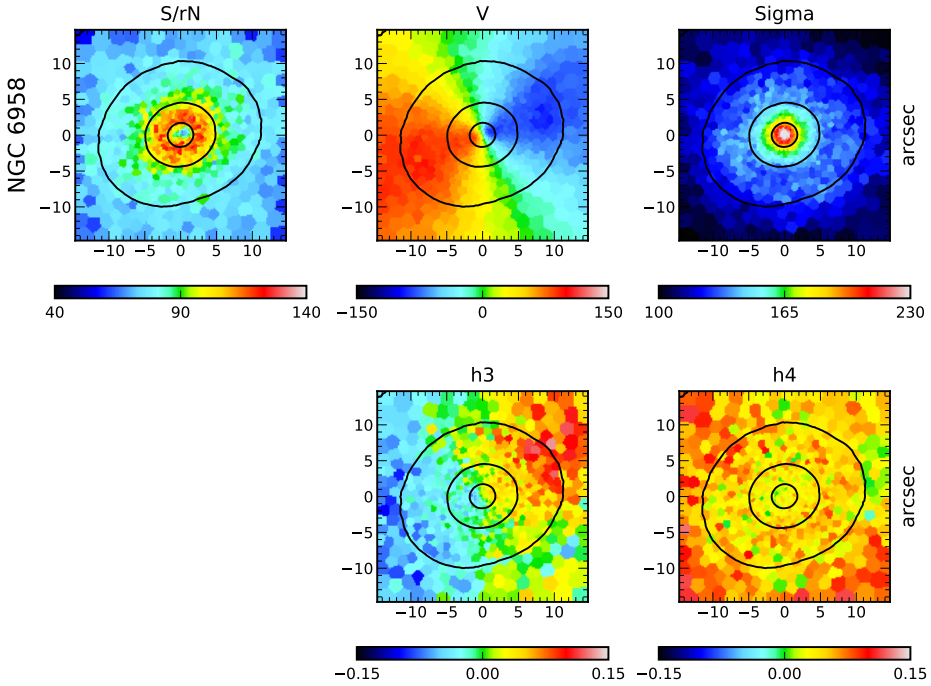


**Figure 5.5 —** MUSE stellar kinematics derive from our full-spectrum fit. From left to right the panels show kinematic maps of signal-to-residual noise (S/N), mean velocity (V), velocity dispersion ($\sigma$) and the Gauss-Hermite moments $h_3$ and $h_4$. The black contours indicate the galaxy surface brightness from the collapsed data cube.

We then estimated the uncertainties using Monte Carlo simulations (with 500 realizations) as described in the previous chapters. Due to the high S/N of the observations (see Figure 5.5), we obtained very low errors of typically about 5 km s$^{-1}$ for the mean velocity, 5 km s$^{-1}$ for the velocity dispersion and 0.02 and 0.04 for the Gauss-Hermite polynomials.

We show our extracted stellar kinematics maps in Figure 5.5 and the kinematic maps of the ionized gas in Figure 5.6. As expected from the selection criteria for this galaxy, the extracted stellar kinematics of NGC 6958 are very smooth and do not show any strong irregularities in the central 15″. The velocities reach up to 130 km s$^{-1}$, and a clear velocity dispersion peak is visible reaching up to 250 km s$^{-1}$. The h3 moment also shows the clear anti-correlation to the mean velocity, and the h4 moment increases slightly asymmetrically with increasing radius. All in all, NGC 6958 has very regular stellar kinematics in is therefore perfectly suited for the tests that we want to perform in this chapter. The extracted emission-line maps show a slightly different picture to the stellar kinematic maps. For each of the four lines, we present the ionized gas distribution based on the amplitude-to-noise ratio A/N (measured with the rms-noise of the stellar spectrum), the mean velocity and the velocity dispersion of the LOSVD. Based on the arguments in Sarzi et al. (2006), we decided our emission line fits to be reliable for A/N < 3 and masked the bins at lower A/N for each emission line independently. The morphology of the ionized gas distribution and kinematics are very similar in the different emission lines but differs strongly from the stellar kinematics maps. The gas rotates at faster velocities and shows

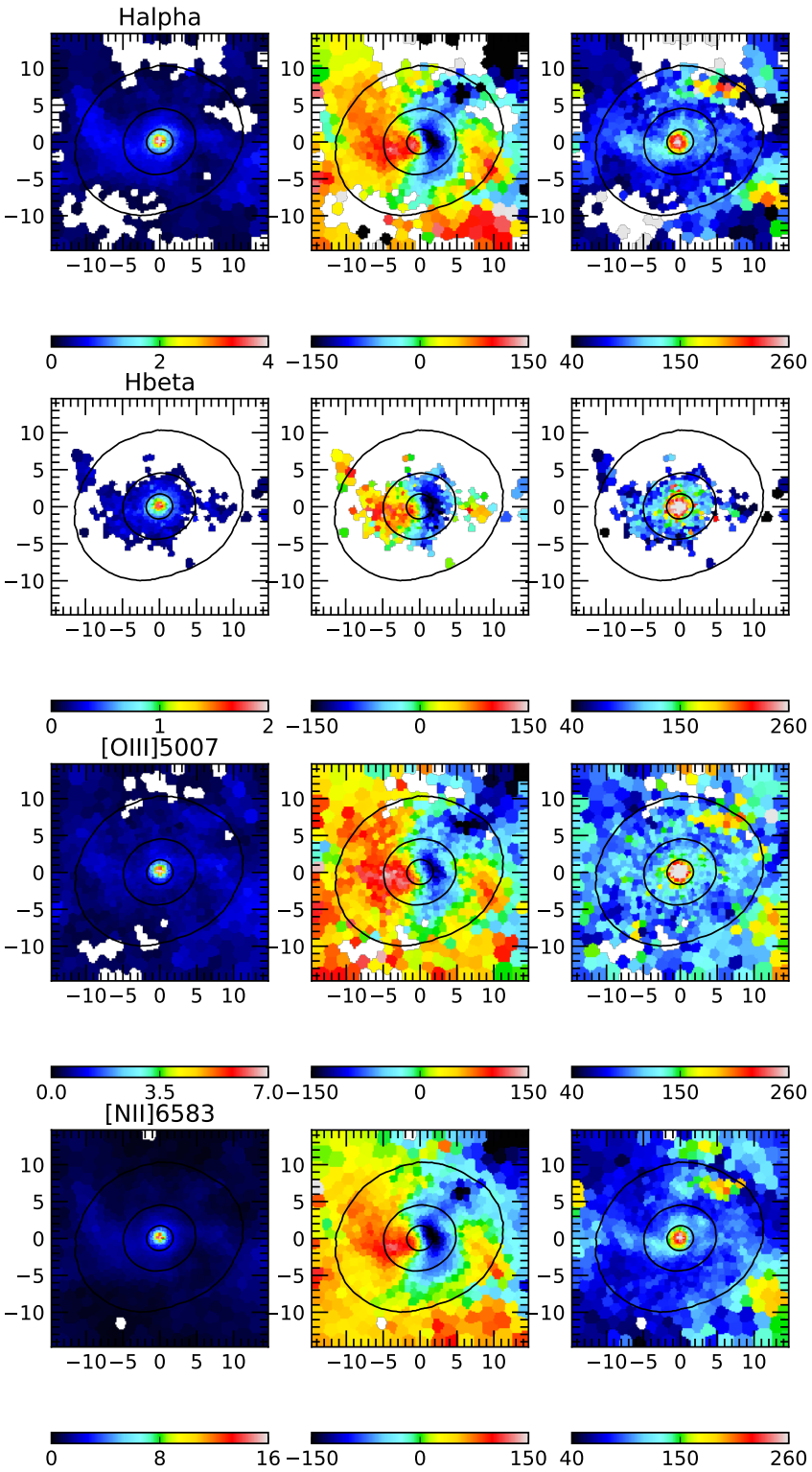


**Figure 5.6 —** MUSE ionized-gas kinematics derived from the full-spectrum fit. The panels show the ionized-gas distribution (based on the amplitude-to-noise ratio), mean velocity and velocity dispersion traced by H$\alpha$, H$\beta$, [OIII], and [NII]. The numbers in the distribution map indicate the amplitude-to-noise ratio of the line in the respective bin. The values below an amplitude-to-noise ratio of 3 were masked.

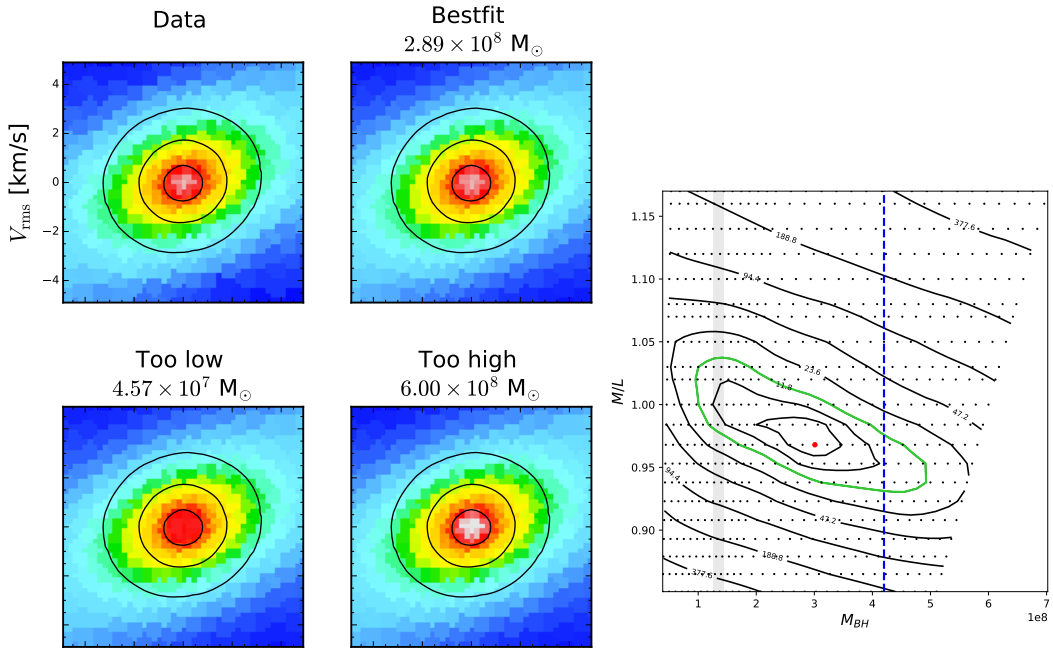


**Figure 5.7 —** Results of the Schwarzschild modeling method for NGC 6958. The right panel shows the grid of our Schwarzschild models (indicated as black dots) over various mass-to-light ratios M/L and black hole masses $M_{\rm BH}$. The best-fitting model was derived as the minimum of the $\chi^2$-distribution and is shown as large red dot. The overplotted contours indicate the $\Delta\chi^2$=$\chi^2$-$\chi^2_{\rm min}$ levels, the green contour denoting the $3\sigma$ level. We also added the $3\sigma$ threshold of the KinMS models from the molecular gas observations (gray shaded region). The dashed blue line indicates the minimal black hole mass that we expect to be robustly detectable based on the SoI argument (based on half the resolution of our MUSE+AO data). We also show a $V_{\rm rms}$ comparison of the central $5'' \times 5''$ between our data, the model with the best-fitting black hole as well as models of clearly too low and too high black hole masses.

a lower velocity dispersion in the center as expected. It is notable that, while the ionized gas shows very regular features in the central 5″, outside of this region, we see very irregular and chaotic structures largely dominated by receding motion. It is not yet clear, what physical effects drive the irregular motion of the gas, but we will investigate this in the future of this project. We note that the central 5″ are perfectly suited to derive the black hole mass based on ionized gas kinematics and thus provide a third independent measurement. We will also perform this measurement in the future to have a comparison of the effects of cold versus warm gas tracers. For now, we will focus on the stellar-based dynamical model, which is described in the next section.

## 4.3 Schwarzschild model

We used the axisymmetric Schwarzschild (1979) modeling method to obtain a second independent black hole mass measurement that is based on the stellar kinematics of NGC 6958. The Schwarzschild models were computed as described in the previous chapters by running a grid of models of the two free parameters ($M_{\rm BH}$, $M/L$). We ran a first coarse grid along $M_{\rm BH} = [10^6, 5 \times 10^9]\, M_\odot$ and $M/L = [0.1, 3.0]\, M_\odot/L_\odot$ to find an indication of the global minimum of the $\chi^2$ distribution.

We, then, centered a refined grid on that global $\chi^2$ minimum and ran a grid of 31 trial $M_{\rm BH}$ and 21 $M/L$ values. Figure 5.7 shows our final grid of Schwarzschild models for NGC 6958. From the overplotted $\chi^2$ contours, we derived the best-fitting parameters to be $M_{\rm BH} = (2.89 \pm 2.05) \times 10^8\, M_\odot$

**Table 5.3 —** Results of the different black hole mass measurement methods

| Method | Scales (arcsec) | $\theta_{inst}$ (arcsec) | $M_{\rm BH}$ ($\times 10^8\,M_\odot$) | $M/L$ ($M_\odot/L_\odot$) | $\chi^2$/d.o.f. |
|---|---|---|---|---|---|
| KinMS | 2 | 0.5 | $1.35^{\pm 0.09}$ | $0.83^{\pm 0.03}$ | – |
| Schwarzschild | 15 | 0.7 | $2.89^{\pm 2.05}$ | $0.98^{0.06}$ | 0.79 |

**Notes.** Column 1: $M_{\rm BH}$ measurement method. Column 2: Size of the probed region. For the molecular gas, this is the radius of the gas disk. For the MUSE measurements, half the size of the FoV used in the specific method. Column 3: Spatial resolution of the data used in the methods. Column 4, 5 and 6: Parameters of the best-fitting models (black hole mass $M_{\rm BH}$, mass-to-light ratio (M/L) and the $\chi^2$ over the degree of freedoms).

and $M/L = 0.98 \pm 0.06\,M_\odot/L_\odot$ within $3\sigma$ significance ($\Delta\chi^2 = 11.8$). The figure also shows the measured black hole mass from the molecular gas dynamics, which is consistent with the Schwarzschild modeling result (but a factor of two lower). In this plot, we have also indicated the lowest black hole mass detectable based on the SoI argument. While resolving the SoI was a necessary condition for the robustness of black hole mass estimates for a long time (see e.g. discussion by Kormendy & Ho 2013), Krajnović et al. (2009) and our work of Chapter 2 has shown that when one uses high-quality IFU data and the sophisticated Schwarzschild modeling method, the hard-limit SoI argument reduces to a guideline of what masses are measurable. In fact, Figure 5.7 implies that we can robustly measure a black hole mass which is a third of the nominal minimal detectable black hole mass of $\sim 8\times10^8 M_\odot$. The robustness of our measurement is also illustrated on the $V_{\rm rms}$ maps in Figure 5.7, given that the model $V_{\rm rms}$ of the too low and too high black hole masses significantly deviate from the observed $V_{\rm rms}$. A comparison of the remaining kinematic moments for the best-fitting Schwarzschild model and the observation is also shown in Figure 5.8.

## 5 Discussion and outlook

The goal of this work is to robustly measure black hole masses with different methods, compare them, and learn about the associated systematic uncertainties to better understand the measurement accuracy. We have estimated the black hole masses using two different methods based on different dynamical tracers (i.e., molecular gas versus stars). The derived results are shown in Table 5, but we caution that we still need to test the methods extensively such that the final masses can still change. According to the current results, the different methods provide black hole masses that are consistent within their $3\sigma$ uncertainties. Our results also confirm previous findings (discussed in Figure 1.8 of Chapter 1), that gas-based methods often provide lower black hole masses than stellar-based methods. In fact, we measure a factor two between both tracers, which is also often found in the literature. For the future, we plan to continue this project by extensively testing the different assumptions in the different modeling schemes and analyzing the effects of the used mass model (in particular in the presence of nuclear dust). Learning about the associated systematics of the modeling methods will help us to understand whether some of the scatter in the black hole scaling relations is generated from the different $M_{\rm BH}$ measurement methods. We will, furthermore, estimate the black hole mass from the ionized gas kinematics derived from the MUSE observations. As such, this work will, for the first time provide a black hole mass comparison between the methods of molecular and ionized gas as well as stellar motion as a tracer.

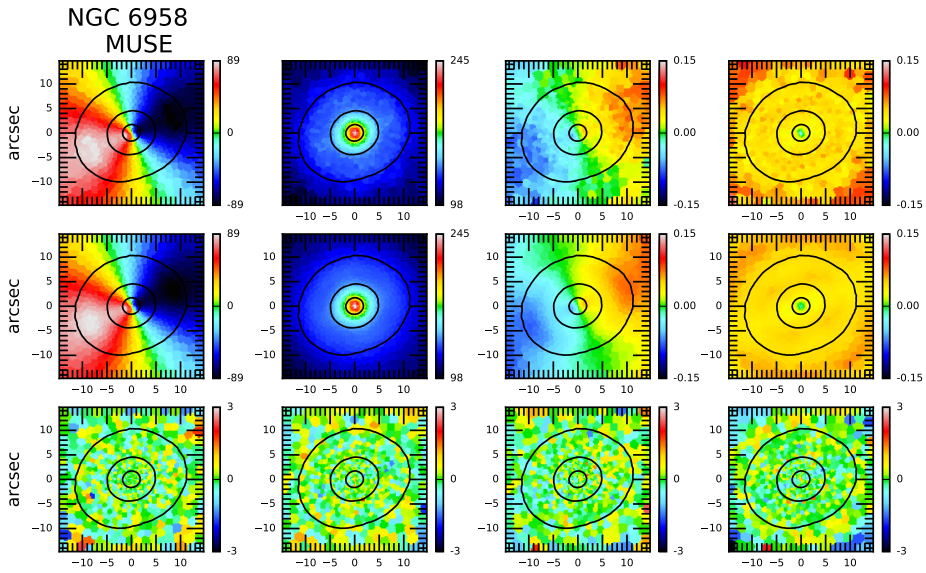


**Figure 5.8 —** Comparison between symmetrized stellar kinematic data and the best-fitting Schwarzschild model. From left to right, we show the mean velocity, velocity dispersion, h3, and h4 Gauss-Hermite moments. From top to bottom: symmetrized data, Schwarzschild model for the best-fitting parameters from Table 5 and residual maps between the Schwarzschild model and the symmetrized data divided by the respective errors.

# 6 Conclusion and Outlook

The goal of this PhD thesis was to refine our understanding of the connection between supermassive black holes and their host galaxies. While several tight empirical relations between massive black hole and their host galaxy imply an evolutionary link between both components, the exact role of the massive black hole in galaxy evolution is not yet understood. I have adressed this problem by estimating robust black hole masses in several early-type galaxies and studying their location in the $M_{\rm BH} - \sigma_{\rm e}$ relation. It was my goal to pin down the measurements as robustly as possible by using integralfield data in combination with adaptive optics, state-of-the art modeling methods and considering a large variety of possible systemtatic uncertainties.

In the chapters 2 to 5, I have reported 13 new black hole mass estimates (three of them could possibly be upper limits) and one upper limit, which combined with the mass measurements of Krajnović et al. (2018b) add a significant contribution to the current black hole data base. In the following chapter, I will reflect on the implication of our new measurements on the $M_{\rm BH} - \sigma_{\rm e}$ relation which was extensively discussed in Chapter 1. I will then give a short overview of how new observing campaigns and instruments will improve solving current selection biases in order to learn about the role of the supermassive black hole in galaxy evolution.

## 1 Revisiting the $M_{\rm BH} - \sigma_{\rm e}$ relation

In Figure 6.1, we show an update of the $M_{\rm BH} - \sigma_{\rm e}$ relation with our mass measurement of the complete SMASHING sample[1] for the first time. We have populated the $M_{\rm BH} - \sigma_{\rm e}$ diagram with the dynamical mass measurements of our black hole catalog that we introduced in Chapter 1 (see Appendix). The catalog is based on the compilations by van den Bosch (2016) and Saglia et al. (2016) and we have added a few recent estimates from the literature. We have excluded the measurements from the reveberation mapping (e.g., Bentz & Katz 2015) and ionized gas dynamics which often only provided upper limits (e.g. Beifiori et al. 2012) and a number of measurements which we found to be unreliable due to poor data or insufficient dynamical modeling. In total, our compilation comprises 128 literature black hole estimates + 20 SMASHING black holes (including our upper limits).
The histograms in Figure 6.1 show how significant our sample increases the total number of robust measurements in different velocity dispersion and black hole bins. Our galaxy sample

[1]The SMASHING sample is composed of all galaxies discussed in this thesis and the additional galaxies measured by Krajnović et al. (2018b)

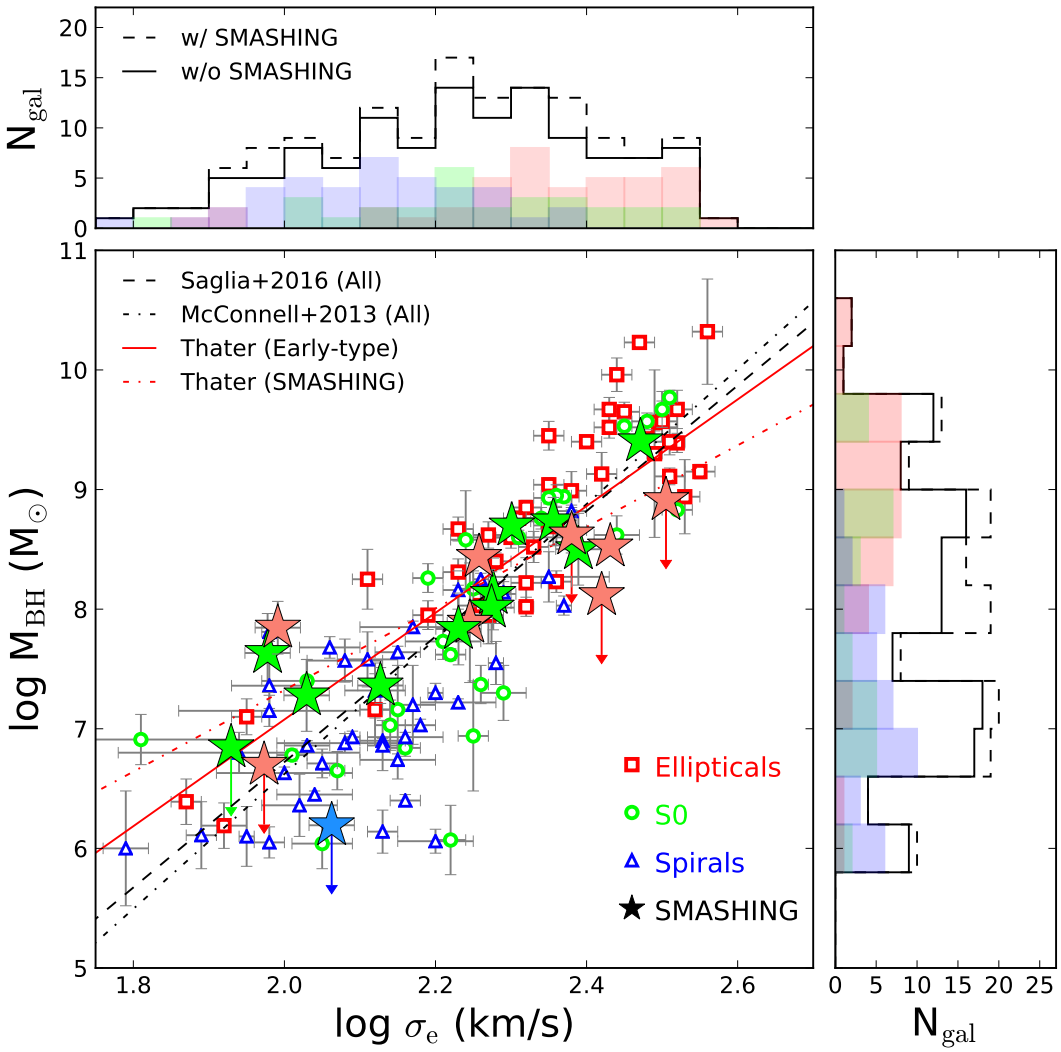


**Figure 6.1 —** Supermassive black hole mass – effective velocity dispersion relation based on the black hole mass measurements of our catalog which is based on the compilations by (van den Bosch 2016) and (Saglia et al. 2016). The color scheme indicates the morphological type of the galaxies: elliptical (red), lenticular (green), and spiral (blue). To visualize the general trend we added the global scaling relations by Saglia et al. (2016) and McConnell & Ma (2013) for all galaxy types (solid and dash-dotted line). Our measurements (highlighted as stars) lie very well on the two scaling relations. We also show our fits to the early-type galaxies of the sample and to the SMASHING sample only.

**Table 6.1 —** Linear regression coefficients for the $M_{BH} - \sigma_e$ relation

| Subset | N | $\alpha$ | $\beta$ |
|---|---|---|---|
| (1) | (2) | (3) | (4) |
| w/o SMASHING | 71 | 8.41 ± 0.06 | 4.80 ± 0.32 |
| w/ SMASHING | 88 | 8.42 ± 0.05 | 4.46 ± 0.29 |
| SMASHING | 17 | 8.35 ± 0.08 | 3.41 ± 0.65 |

**Notes.** Details of the bayesian linear regression. Column 1: Subsets of the black hole sample. We only selected early-type galaxies of the massive black hole catalog and excluded upper limits. Column 2: sample size. Column 3 and 4: slope and intercept of the relation.

was chosen to provide uniform black hole measurements extending from low-$\sigma_e$ toward high-$\sigma_e$ and this is clearly reflected in the histograms. Our sample most significantly adds to the velocity bins below 100 km s$^{-1}$, which was only marginally populated by early-type galaxies before, and at the velocity bin around 230 km s$^{-1}$. Now, we want to compare the exact position of our measurements in the $M_{BH} - \sigma_e$ diagram with the previous measurements. Almost all of our measurements are very well aligned with recently adopted scaling relations. Half of our sample lies slightly above the scaling relation by Saglia et al. (2016) and McConnell et al. (2013), the other half lies below. We do have two galaxies in the low-mass region, which lie significantly above and one galaxy in the high-mass region, which lies significantly below the scaling relation. For a quantitative comparison, we fitted our data points using a linear regression method in the logarithmic cfs space of the two observables

$$\log(M_{BH}/M_\odot) = \alpha + \beta \log(\sigma_e/200\,\mathrm{km\,s^{-1}}) \tag{6.1}$$

which is the typical approach when analysing the scaling relations (e.g., McConnell & Ma 2013; Kormendy & Ho 2013; Davis et al. 2018b). For that purpose, we developed a simple robust Bayesian analysis to determine the slope and intercept of the $M_{BH} - \sigma_e$ relation. The routine is based on the emcee python package (Foreman-Mackey et al. 2013) and also takes the measurement errors of $M_{BH}$ and $\sigma_e$ into account. In a later stage of this project, we will also derive the relation based on the more commonly applied "bisector" line regression method (Akritas & Bershady 1996) which also considers measurement errors of both coordinates and allows intrinsic scatter in the data.

For our analysis, we excluded late-type galaxies from our sample as they follow a different scaling relation (see Chapter 1). We then divided the remaining galaxy sample of our compilation into three different subsamples: previous literature estimates, our new SMASHING results and a combination of both. Table 6.1 summarizes the fitting results to the individual subsets, the respective relations are also shown in Figure 6.1. We have included the fit of our SMASHING results only in order to have a comparison of our new uniformly measured black hole masses with the literature values. This fit clearly deviates strongly from recent scaling relations having a much shallower slope. However, while covering a large $\sigma_e$-range, our sample size is very small and this scaling relation is not representative for all early-type galaxies. Therefore, in the following we will focus on the combined sample of SMASHING and literature galaxies. It is immediately clear, that the addition of our sample significantly alters the previous shape of the scaling relation. The most significant contribution comes from the overmassive low-$\sigma_e$ and undermassive high-$\sigma_e$ galaxies, which produce a much shallower scaling relation than previously discussed. By including our SMASHING sample into the fit, the slope changes from values around $\beta \approx 4.8$ (4.9 in Greene et al. 2016) toward 4.46 which is much closer to the theoretical value of the King (2003) model as discussed in Section 2.3 of Chapter 1. In Figure 6.2, we show

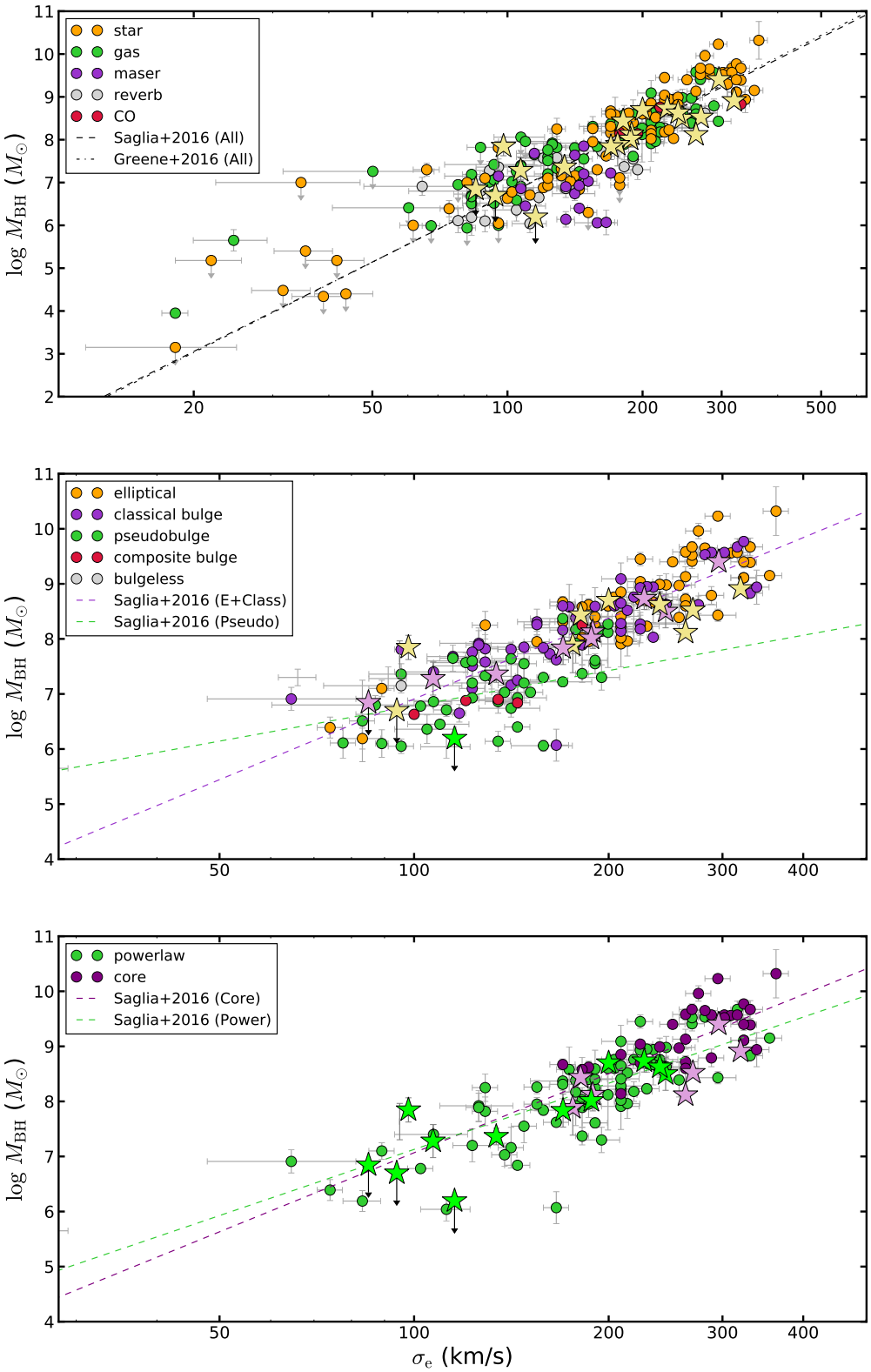


**Figure 6.2 —** $M_{BH} - \sigma_e$ relation for different sub-samples of the appended MBH compendium of van den Bosch (2016). These are the same plots as in the introduction but including the results of our SMASHING sample (a) MBH measured with different methods. (b) Different bulge classifications. (c) Core galaxies versus core-less galaxies.

the $M_{\rm BH} - \sigma_{\rm e}$ diagrams with the different subsamples from Chapter 1 again. This time we have also added our results from the SMASHING sample. It is clear, that all our measurements lie well within the scatter of the previous measurements and do not show any unexpected outliers. We do note, that some of our core galaxies at 300 km s$^{-1}$ have relatively low massive black holes. As we have discussed in Chapter 5, this could be caused by some of these galaxies not being cored, but only significantly attenuated by nuclear dust disks. The galaxies would then actually lie well within the scatter of the other coreless galaxies. Alternatively, they could be offset due to ignoring the triaxiality, which could decrease the mass by up to a factor of two. This is an effect that we will certainly continue pursuing in the future. Furthermore, it will be interesting to gather more elliptical galaxies and investigate, whether we can find more substantial evidence for different scaling relations for massive and low-mass ellipticals as is predicted by Krajnović et al. (2018b). Our black hole catalog provides the ideal starting point to test additional galaxy subsets which point towards different evolutions (such as fast- versus slow rotators).

## 2 Systematic effects on black hole mass measurements

Next to determining massive black hole masses, evaluating the accuracy of black hole masses is crucial for improving the understanding of the interplay between the central black holes and their host galaxies. To what level of robustness the mass can be determined remains an open question. It is therefore important to get a good handle on the systematic effects, which can have a significant effect on the derived supermassive black hole masses. We made sure to devote a substantial time of our analysis to test various aspects of uncertainty on our data.

In Chapter 2, we measured an unusually low undermassive upper limit mass for NGC 4414. We carefully tested the effects of dust contamination and dark matter inclusion. NGC 4414 is the only late-type galaxy of our sample and shows a large amount of dust pollution on the facing side (see Figures 3.11 and 3.11). We masked and corrected the dust with great care, but noticed that owing to the asymmetric character of the dust, the upper mass limit did not change significantly. It needs to be noted that the uncorrected models certainly represented the data less well indicating the importance of a dust-correction. This conclusion would definitely change with a more symmetric dust distribution, higher dust coverage and dust extending to the very center of the data. In these cases, the dust contamination can vastly change the measured black hole mass depending on the obscuration level of the dust. We also derived the dark matter content in NGC 4414 from CO data and dynamical models and only found a small fraction of about 10%. On the other hand, we noticed that the change due to mass-to-light ratio ($M/L$) variation was also about 10% within 0.5″ and 6.5″, which is probed by our data. The gradients due to dark matter and $M/L$ variation run in opposite directions and mainly cancel each other out. We therefore concluded that a constant $M/L$ ratio is an adequate assumption for this galaxy to account for the small amounts of dark matter in the center (see also McConnell et al. 2013).
The quality of $M_{\rm BH}$ measurements has often been assigned based on the fact whether the sphere of influence (SoI) was resolved by the data suggesting that the SoI is a very hard limit. For NGC 4414, we were able to derive an upper limit which is well below the mass deduced from the SoI argument. Crucially, this suggests that when one uses high quality IFU data, the predicted SoI should be taken only as a very rough guide for the possible $M_{\rm BH}$ one could measure (see also Krajnović et al. 2009).

In Chapter 3, we determined the black hole masses of six early-type galaxies of the intermediate $\sigma_e$ range. We then carefully tested the effect of $M/L$ variation on the black hole mass measurement of NGC 4570, which is the most regular galaxy in the intermediate mass-range of

our SMASHING sample. $M/L$ gradients were confirmed for early-type galaxies in a number of recent works (e.g., Boardman et al. 2017; Vaughan et al. 2018; Ferreras et al. 2019). We derived the $M/L$ in NGC 4570 at different radii and noticed a descrease with radius by about 20% owing to radial changes in the stellar metallicity. We concluded our analysis with a test on NGC 4570 taking into account a variable $M/L$ when constructing dynamical JAM models. When considering $M/L$ variations,we find that the dynamically determined black hole mass from NGC 4570 decreases by 30%, which agrees with McConnell et al. (2013) who noticed that the SMBH mass decreases by about 20-30% by taking $M/L$ gradients into account. Further investigations are needed in the future to account for the impact of radial $M/L$ gradients on dynamical modeling.

In Chapter 4, we have estimated black hole masses in six massive galaxies using axisymmetric Jeans and Schwarzschild models. Compared to low-mass galaxies, most massive galaxies have a recent merging history which is often still imprinted in the appearance and shape of the galaxies. In the future, we want to evaluate our current estimates by re-assessing the effects of dark matter on the dynamical modeling of those types of galaxies. Rusli et al. (2013b) noted that the effect of dark matter is negligible if the SoI is well resolved. We will add dark matter to our models and test for possible limitations of this statement. In a second step, we will apply triaxial dynamical modeling to our galaxies and compare the results with our in this chapter presented measurements based on spherical or axisymmetric assumptions. This will be the first study to test three independent dynamical models on triaxial-shaped galaxies.

In Chapter 5, we used two different measurement methods based on different dynamical tracers to derive the black hole mass of NGC 6958. NGC 6958 is the ideal target for such a kind of study as it is an early-type galaxy, has a sufficiently massive expected black hole mass and did not show any signs of disturbance. We used our AO-assisted MUSE Science Verification data and ALMA observations from the WISDOM survey (Onishi et al. 2017) to dynamically measure the black hole mass based on stellar kinematics versus rotating cold molecular gas kinematics. Similar to the comparisons we showed in Figure 1.8 of Chapter 1, in this work we determined slightly discrepant black hole masses (but consistent within their uncertainties), the stellar-based being twice as massive as the gas-based. As the origin of this discrepancy is not clear yet, we will continue this work by performing a detailed analysis of the associated model assumptions and their validity. Understanding these systematic offsets becomes increasingly important as ALMA is a wonderful instrument to study massive black holes with great spatial resolution for a large number of local and more distant galaxies (see Figure 1.6 of Chapter 1). In continuation of this project, it will also be interesting to compare the stellar-based measurements of NGC 4261 and NGC 4636 of Chapter 4 with available gas-based measurements from the literature. Last, but not least our MUSE+AO data does not only provide us with stellar, but also ionized gas kinematics, which can be used to estimate the black hole mass via two different methods, but on the same data. Cross-comparing as many measurement methods as possible will provide a better understanding of the measurement errors, specifically, the systematics associated with the dynamical techniques, and the general accuracy of black hole mass measurements.

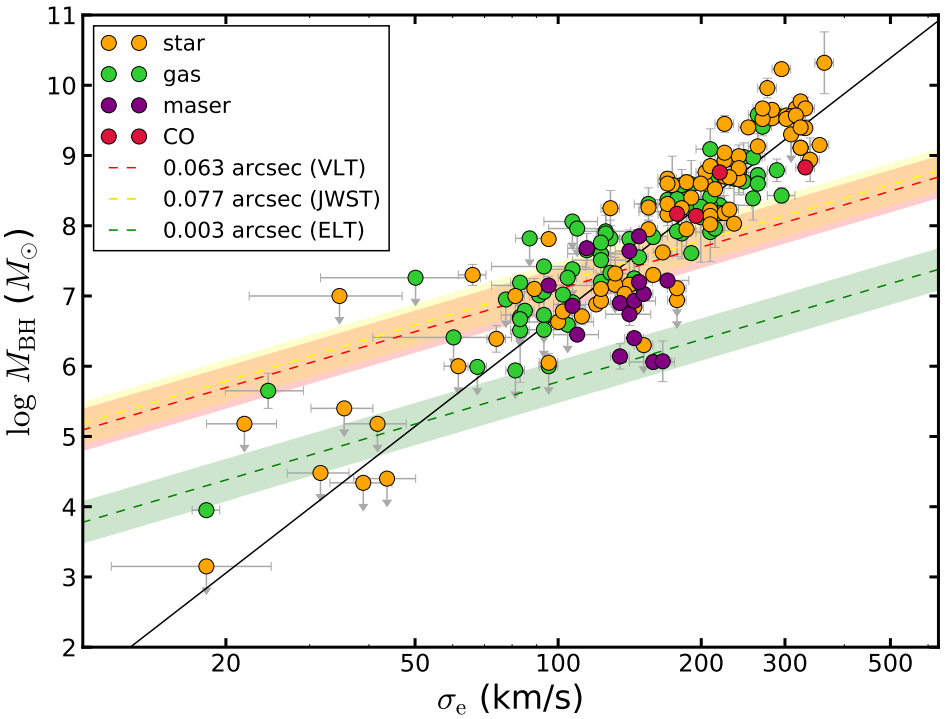


**Figure 6.3 —** Influence of resolution in the $M_{\rm BH} - \sigma_{\rm e}$ diagram. We have filled the diagram with the black hole mass measurements of our catalog. The different colors of the measurements indicate the measurement method (reverberation mapping was excluded). The black solid line is the best-fit from (Saglia et al. 2016) for all galaxies. We have also included lines of the expected minimal detectable black holes based on future facilities. They are calculated based on equation 7.2, a distance of 20 Mpc and using the diffraction limit of VLT, JWST and ELT. The main message is: ELT will be "THE" telescope to go for in the future, to push the current black hole mass limit down by one magnitude.

## 3 Future perspectives

While the first part of this thesis (Chapters 2 and 3) was based on published results, I have presented preliminary results of my work in the following three chapters. An outlook over the planned continuation of the work in the further course of the project was extensively described in the respective chapters. Therefore, I will conclude this thesis with a short outlook based on the question: what advantages are expected from future observational facilities for the study of the black hole scaling relations?

The detection of supermassive black holes and robust mass measurements would be impossible without the large steps in technical developments and the great progress in dynamical modeling which were achieved in the last three decades: Starting with high-spatial resolution imaging and spectroscopy from the Hubble Space Telescope toward a major improvement due to the development of integral-field spectroscopy with adaptive optics on 10-m class telescopes have significantly improved our black hole mass sample from tens of black holes around the year 2000 to almost 200 black holes by now. Last, but not least, using radio interferometry with the ALMA telescope, we can make use of unprecedented spatial resolution reaching almost 0.04″ which enables us to recover new mass detection limits .
The next most important telescopes for massive black hole mass measurements will be the

James Webb Space Telescope (JWST), the Extremely Large Telescope (ELT) and other 30m telescopes which are planned for the next decade. A rough guideline for their achievable spatial resolution can be determined based on the diffraction limit which depends on the observed wavelength and the diameter of the mirror. While JWST will reach a similar spatial resolution as VLT ($\theta_{\mathrm{JWST,df}} \approx 0.077''$), the ground-based ELT will provide significantly improved theoretical spatial resolution ($\theta_{\mathrm{ELT,df}} \approx 0.0032''$)[2]. It needs to be noted that the diffraction limit is usually not reached in reality due to imperfections in the mirrors and instrumental misalignments. Futhermore, ELT will be ground-based such that atmospheric seeing will further worsen the spatial resolution. We have determined a rough estimate of the minimal detectable mass based on the SoI argument, but allowing for a possible detection at a resolution which covers twice the SoI (due to arguments that we have presented in Chapter 1 and 2). The minimal detectable mass is then

$$M_{\mathrm{BH,min}} = \frac{1}{2} \times 10^6 \times \left(\frac{\theta_{\mathrm{inst}}}{0.1''}\right) \times \left(\frac{\sigma_{\mathrm{e}}}{100\,\mathrm{kms}^{-1}}\right)^2 \times \left(\frac{D}{\mathrm{Mpc}}\right) \tag{6.2}$$

based on equation 1.4 of Chapter 1. We want to caution again that this detectable mass should not be treated as hard limit and is just a guideline. The galaxies of our catalagoue have an average distance of 20 Mpc, whereas in single, very massive cases and a great spatial resolution we can measure up to 100 Mpc. We therefore used this average value to derive a possible minimal detectable black hole mass. Figure 6.3 shows the expected mass limits with respect to the effective velocity dispersion. Comparing the current mass limit of VLT (and other near-infrared 8m telescopes) with the observations, we clearly approach our observational limits inflicting crucial biases on the sample. While JWST will not be able to give a substantial improvement over current 8m telescopes (except for being a near-infrared telescope in space), the ELT will be able to lower the detectable mass by more than a magnitude.

One can also reverse this argument and calculate to which redshifts we will be able to estimate robust dynamical black hole masses. Gültekin et al. (2019) has perfomed this test for ELT and show that we will be able to reach redshifts around z=1.5 for stellar-based methods and up to z=2.0 for gas-based methods. In the next decade, ELT will therefore be the key facility to advance the state of the field by pushing down the detectable minimum black hole mass in the local universe and widen the redshift coverage. It will enable us to better constrain current models and learn more about the role of supermassive black holes in galaxy evolution.

[2]The values were calculated based on an averaged wavelength of 2$\mu$m (K-band) for a 6.5m mirror for JWST, on 2$\mu$m (K-band) for a 8.2m mirror for VLT and on 5000Å for a 40m mirror for ELT.

# A Additional material

## 1 Dust correction and masking

As the presence of dust can have a crucial effect on the galaxy mass modeling, we had to correct and mask the dust polluted image pixels before constructing the mass models. NGC 4281 and NGC 7049 contain extended nuclear dust rings that are well visible in the HST images (see Figure 3.11). Furthermore, we found a small dust ring in the HST image of NGC 2784 and large structures of dust in NGC 4414. We applied a dust mask for the HST small-scale images for all four galaxies and a dust correction for the SDSS large-scale image of NGC 4281 and NGC 4414.

### 1.1 SDSS image

Before deriving the MGE model from the SDSS/r-band image, we corrected it for the effects of dust absorption based on the method described in Cappellari et al. (2002); Scott et al. (2013a). The main assumption of this method is that the dust can be summed up to a light absorbing screen between the observer and the galaxy (Carollo et al. 1997; Cappellari et al. 2002). Due to the extinction, this screen changes the intrinsic color of the dust-affected galaxy fragments which are assumed to have the same intrinsic color as the adjacent regions. According to the Galactic extinction law we derived the r-band extinction $A_r$ from the color excess between the g- and i-band images $A_r = 1.15\,\mathrm{E(g-i)}$. The main steps of our dust correction were the following: 1) For each pixel, the color (g-i) was calculated and plotted over the logarithm of the semi-major axis distance; 2) Assuming that the intrinsic galaxy color varies linearly with the logarithm of the radius, we performed a robust linear fit to the radial color profile to determine the underlying color gradient of the galaxy. The color profile of NGC 4414 is presented in Fig. A.1. As typically for spiral galaxies, the profile shows a color gradient with the central regions being redder than the outskirts of the galaxy. The color excess E(g-i) was then computed for each pixel as the difference between measured and intrinsic galaxy color. Thus, we retrieved a E(g-i) color excess map of NGC 4414. All pixels above a threshold, chosen to be E(g-i)> 0.11, were significantly affected by dust extinction and corrected in the SDSS/r-band image by using the Galactic extinction law. The method corrected patchy dust absorption which could be found in the disk regions of the eastern side of NGC 4414 which faces towards us (Fig. 2.13). The Figure also shows quantitatively how much of the measured flux was corrected (where 0.1 means 10% (blue) and 0.25 means 25% (orange)). The largest correction was approximately 25% of the measured flux in the eastern side of NGC 4414. The lines in the center of the image are edge artifacts from assembling the single SDSS images to a large FOV montage and were masked in

the surface brightness modeling. We performed the same dust-correction method for NGC 4281. In this galaxy, the largest correction was approximately 35% of the measured flux. For NGC 7049, we noted that the dust content in this galaxy is mostly concentrated in the center (within the HST PC FoV) and we decided to only apply the dust-masking of the HST images (see next Section).

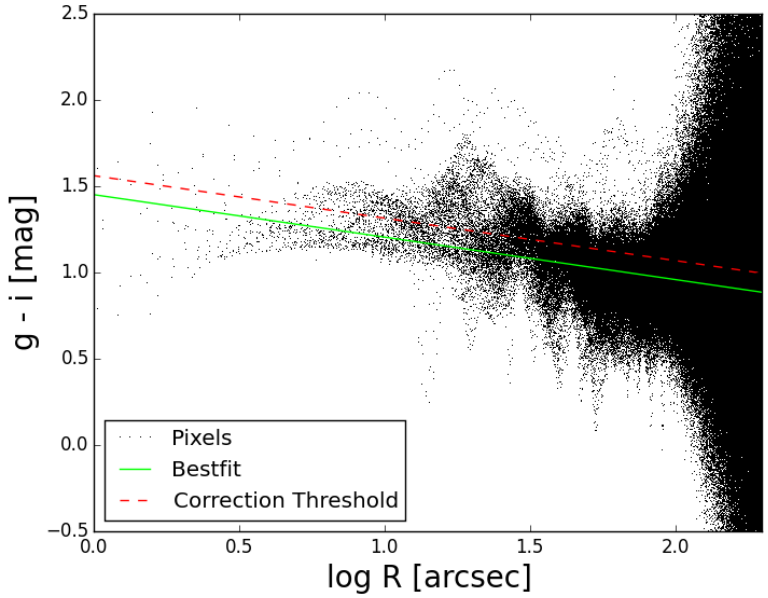


**Figure A.1 —** Color profile of the SDSS g-i map used for the dust correction in NGC 4414. The best-fitting linear line obtained by a robust fit is shown in green. We decided the red line to be the threshold in order to assure the same width of the gradient under the line-fit and above. All pixels above the red line and for $\log(d) < 1.9\,(\approx 80)$ [arcsec] were corrected for extinction.

### 1.2 WFPC2 PC images

As NGC 4414 shows further dust patterns in the central regions, we also attempted to correct the dust in the F606W PC image. This dust correction is very important for the models as the PC image probes the direct vicinity of the black hole. It was not possible to apply the same dust correction as for the SDSS r-band image, as NGC 4414 PC images of other bands were all saturated in the center. Therefore, we decided for creating a dust mask in order to account for dust attenuation in the MGE modeling.
We chose to mask those pixels which deviated significantly from the characteristic galaxy surface brightness profile (Fig. A.3). Both the dust patches and hot pixels are clearly evident in this profile. We distinguished the dust affected from the unaffected pixels by fitting the lower envelope of the main surface brightness profile with an appropriate function (four parameter logistic function) and masked the pixels below this fit. The masked pixels are shown in Fig. 2.14. For NGC 2784, NGC 4281, and NGC7049 the nuclear dust ring reaches into the very central regions of the galaxies. It was therefore necessary to also correct for dust in the HST small-scale images.

## 2 Determination of the point spread functions

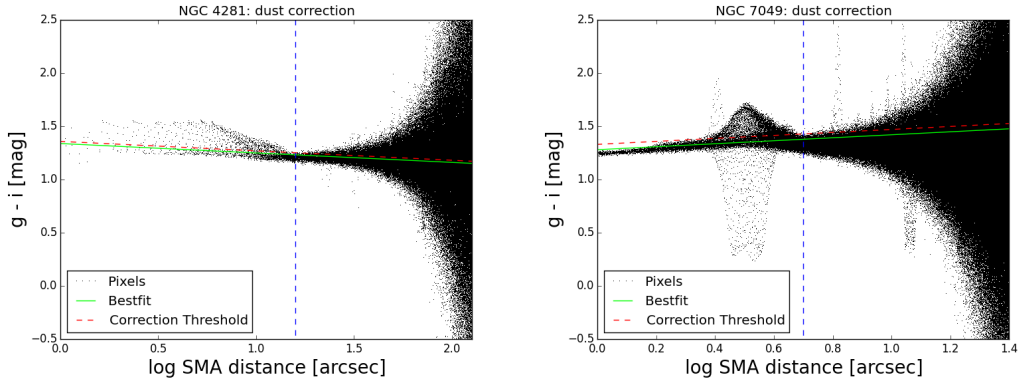


**Figure A.2 —** Color profile of the NGC 4281 and NGC 7049 SDSS (g-i) images used for the dust correction. The central dust rings are clearly identified in the upper left quadrant. The best-fitting linear function obtained from a robust fit is shown in green; the slightly shifted red line is the correction threshold. For NGC 4281, all pixels above the red line and for $\log(r) < 1.2$ ($\approx 16$ [arcsec]) were corrected for dust extinction.

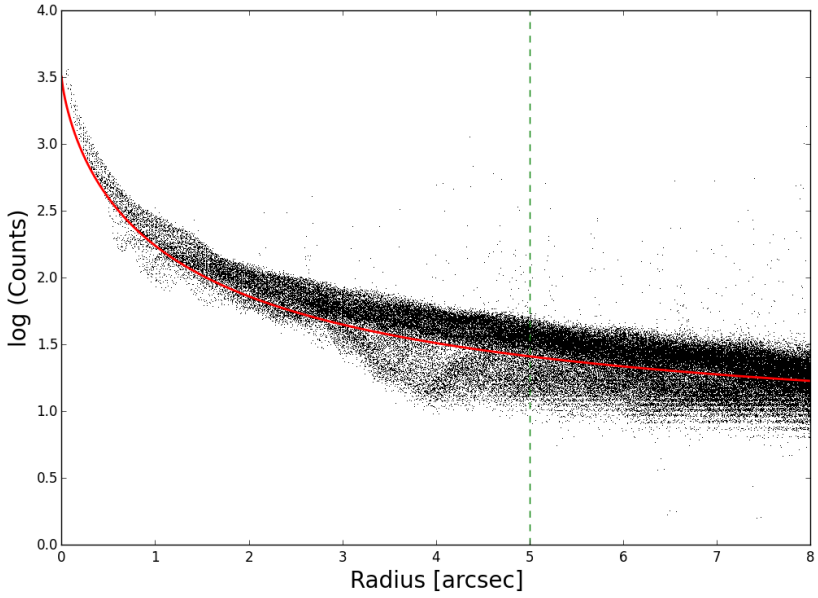


**Figure A.3 —** Logarithmic surface brightness profile (in photon counts) of the HST F606W image used for the dust-masking in NGC 4414. Every dot is a pixel in the image, the lower envelope fit of the surface brightness is given by the red solid line. Each pixel below the line is masked in the photometric measurement of the MGE. The green dashed line marks the edge of the image which is used for the MGE modeling.

## 2.1 HST spatial resolution

In order to compare the MGE model of our galaxies (Section 4.1) with the observed surface brightness, it is necessary to convolve it with the central image PSF. We generated the PSF for the HST images by using Tiny Tim. The PSF was modeled by a sum of concentric circular Gaussians using the MGE method. Each of the Gaussians was assigned a relative weight which is normalized such that the sum of the weights equals one. The MGE parameters of the single Gaussians are given in Table B.1. On the other hand, modeling the Tiny Tim PSF with one circular Gaussian, we obtained FWHM = 0.09″ for WFPC2.

## 2.2 NIFS, SINFONI and GMOS spatial resolution

In order to determine to which scales we can probe the inner dynamics of NGC 4414, a proper estimate of the spatial resolution of our IFU data is indispensable. When no point sources can be found in the observed FOV, the observed images have to be compared with reference images of significantly higher resolution (Davies 2008; Krajnović et al. 2009). The WFPC2 image that we obtained to derive our luminosity mass model provides sufficient resolution. The spatial resolution of the IFU's could then be determined by convolving the HST image with a PSF and then degrading the image until it matched the reconstructed IFU image. A good description for the PSF can be obtained by a sum of two circular and concentric Gaussians, G, one having a broad- and the other a narrow shape

$$G_{PSF} = f_1 \times G(FWHM_1) + (1 - f_1) \times G(FWHM_2), \tag{A.1}$$

where $f_1$ is the relative flux of the narrow Gaussian. We used two Gaussians to determine the PSF of the NIFS observation and a single Gaussian for the GMOS observation. In order to compare the different images with each other, we aligned them by rotating them such that the major and minor axes of the galaxies were coinciding. After the convolution, the HST image was rebinned to the same pixel scale as the respective IFU observation. The best fitting PSF parameters are found by minimizing the residual between the convolved HST image and the reconstructed IFU image. Finally, the PSF of the HST image (Sect. 2.1) had to be added quadratically to the measured PSFs. The best-fitting parameters of our PSFs are given in Table 2.2 and a comparison of the light profiles of the used images along the major axis is shown in Fig. A.4. The convolved HST profiles (blue dashed lines) reproduce the IFU (open circles) profiles very well in the majority of cases.

## 2.3 Strehl ratio

The Strehl ratio measures the effect of wavefront aberrations on the optical quality of the observations. It can be determined by comparing the peak intensity of the measured PSF and the peak intensity of the ideal diffraction limited PSF assuming an ideal working LGS AO. In this work, we obtained the FWHM of the narrow Gaussian component of the NIFS observation to be 0.126″ (see table 2), while the diffraction limited FWHM at 2.2 microns on the Gemini 8 m telescope is approximately 0.07" (McGregor et al. 1999). We created normalized 2D Gaussians from those two FWHM and compared the peak intensities to obtain a Strehl ratio of 30.8%. At 2.3 microns, the diffraction limit of the VLT telescope ($d$= 8.2 m) is approximately 0.07 ″. Dividing the peak intensities for our SINFONI galaxies resulted into Strehl ratios of around 10 % for our SINFONI observations

**Table A.1 —** MGE parametrization of the HST PSF

| N584 WFPC2 F555W | | N2784 WFPC2 F547M | | N3640 WFPC2 F555W | | N3706 WFPC2 F555W | |
|---|---|---|---|---|---|---|---|
| norm | $\sigma$ (arcsec) | norm | $\sigma$ (arcsec) | norm | $\sigma$ (arcsec) | norm | $\sigma$ (arcsec) |
| (1) | (2) | (1) | (2) | (1) | (2) | (1) | (2) |
| 0.1972 | 0.0173 | 0.2430 | 0.0173 | 0.1951 | 0.0173 | 0.2460 | 0.0173 |
| 0.5832 | 0.0484 | 0.5591 | 0.0463 | 0.5847 | 0.0475 | 0.5395 | 0.0466 |
| 0.0923 | 0.1251 | 0.0902 | 0.1186 | 0.0960 | 0.1200 | 0.0990 | 0.1230 |
| 0.0676 | 0.3116 | 0.0685 | 0.3012 | 0.0687 | 0.3075 | 0.0699 | 0.3002 |
| 0.0186 | 0.4724 | 0.0391 | 0.8523 | 0.0144 | 0.5062 | 0.0140 | 0.6389 |
| 0.0409 | 0.8753 | – | – | 0.0411 | 0.8630 | 0.0316 | 1.0002 |

| N3923 ACS F814W | | N4261 WFPC2 F791M | | N4281 WFPC2 F606W | | N4414 WFPC2 F606W | |
|---|---|---|---|---|---|---|---|
| norm | $\sigma$ (arcsec) | norm | $\sigma$ (arcsec) | norm | $\sigma$ (arcsec) | norm | $\sigma$ (arcsec) |
| (1) | (2) | (1) | (2) | (1) | (2) | (1) | (2) |
| 0.5279 | 0.0456 | 0.2244 | 0.0198 | 0.1995 | 0.0173 | 0.2380 | 0.0173 |
| 0.2757 | 0.1346 | 0.6138 | 0.0614 | 0.5631 | 0.0489 | 0.5690 | 0.0511 |
| 0.0839 | 0.3572 | 0.0625 | 0.1804 | 0.0498 | 0.1158 | 0.0842 | 0.1450 |
| 0.0694 | 0.9233 | 0.0661 | 0.4201 | 0.0680 | 0.1477 | 0.0683 | 0.3340 |
| 0.0431 | 2.2842 | 0.0331 | 1.0031 | 0.0782 | 0.3278 | 0.0406 | 0.8470 |
| – | – | – | – | 0.0414 | 0.8395 | – | – |

| N4570 WFPC2 F555W | | N4636 WFPC2 F814M | | N6958 NICMOS F160W | | N7049 ACS F814W | |
|---|---|---|---|---|---|---|---|
| norm | $\sigma$ (arcsec) | norm | $\sigma$ (arcsec) | norm | $\sigma$ (arcsec) | norm | $\sigma$ (arcsec) |
| (1) | (2) | (1) | (2) | (1) | (2) | (1) | (2) |
| 0.1956 | 0.0173 | 0.2409 | 0.0206 | 0.5214 | 0.5883 | 0.1517 | 0.0284 |
| 0.5863 | 0.0479 | 0.5988 | 0.0628 | 0.3336 | 1.7679 | 0.6483 | 0.0649 |
| 0.0927 | 0.1258 | 0.0643 | 0.1805 | 0.0444 | 5.524 | 0.0983 | 0.1513 |
| 0.0668 | 0.3080 | 0.0646 | 0.4196 | 0.1006 | 9.892 | 0.0620 | 0.4047 |
| 0.0172 | 0.4619 | 0.0314 | 0.9955 | – | – | 0.0166 | 0.8361 |
| 0.0414 | 0.8506 | – | – | – | – | 0.8506 | 1.6155 |

| I4296 WFPC2 F814W | | I4329 WFPC2 F814M | |
|---|---|---|---|
| norm | $\sigma$ (arcsec) | norm | $\sigma$ (arcsec) |
| (1) | (2) | (1) | (2) |
| 0.2471 | 0.0211 | 0.2401 | 0.0206 |
| 0.5840 | 0.0635 | 0.5976 | 0.0627 |
| 0.0677 | 0.1805 | 0.0650 | 0.1793 |
| 0.0706 | 0.4221 | 0.0664 | 0.4230 |
| 0.0307 | 0.9956 | 0.0308 | 0.9975 |

**Notes.** Specifics of the single Gaussians from the MGE parametrisation of the HST image PSF for each galaxy. The first columns show the normalised relative weights of each Gaussian and the second columns show the dispersion $\sigma$ of each Gaussian (converted into arcsec), respectively.

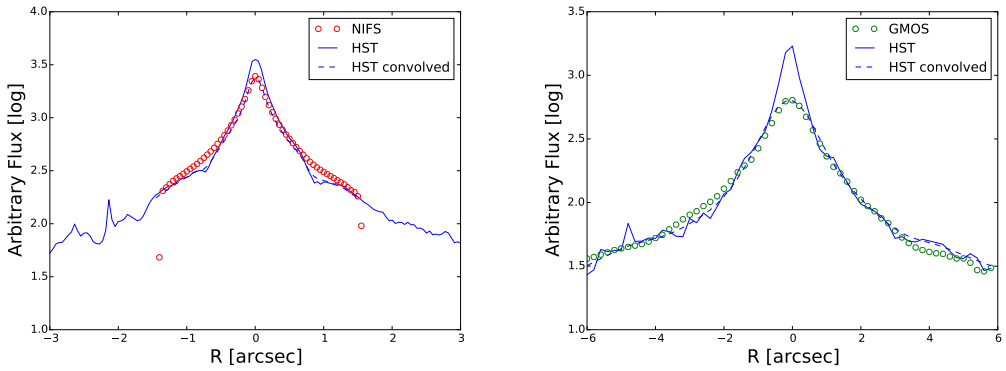


**Figure A.4 —** Determination of the NIFS (top) and GMOS (bottom) PSF by comparing the light profiles of the NIFS/GMOS and HST images along the major axis. In both panels the open circles denote the IFU profiles and blue solid lines the HST profiles. The HST profiles were convolved with the PSFs of Table 2.2 to fit the IFU data and are shown as dashed blue lines.

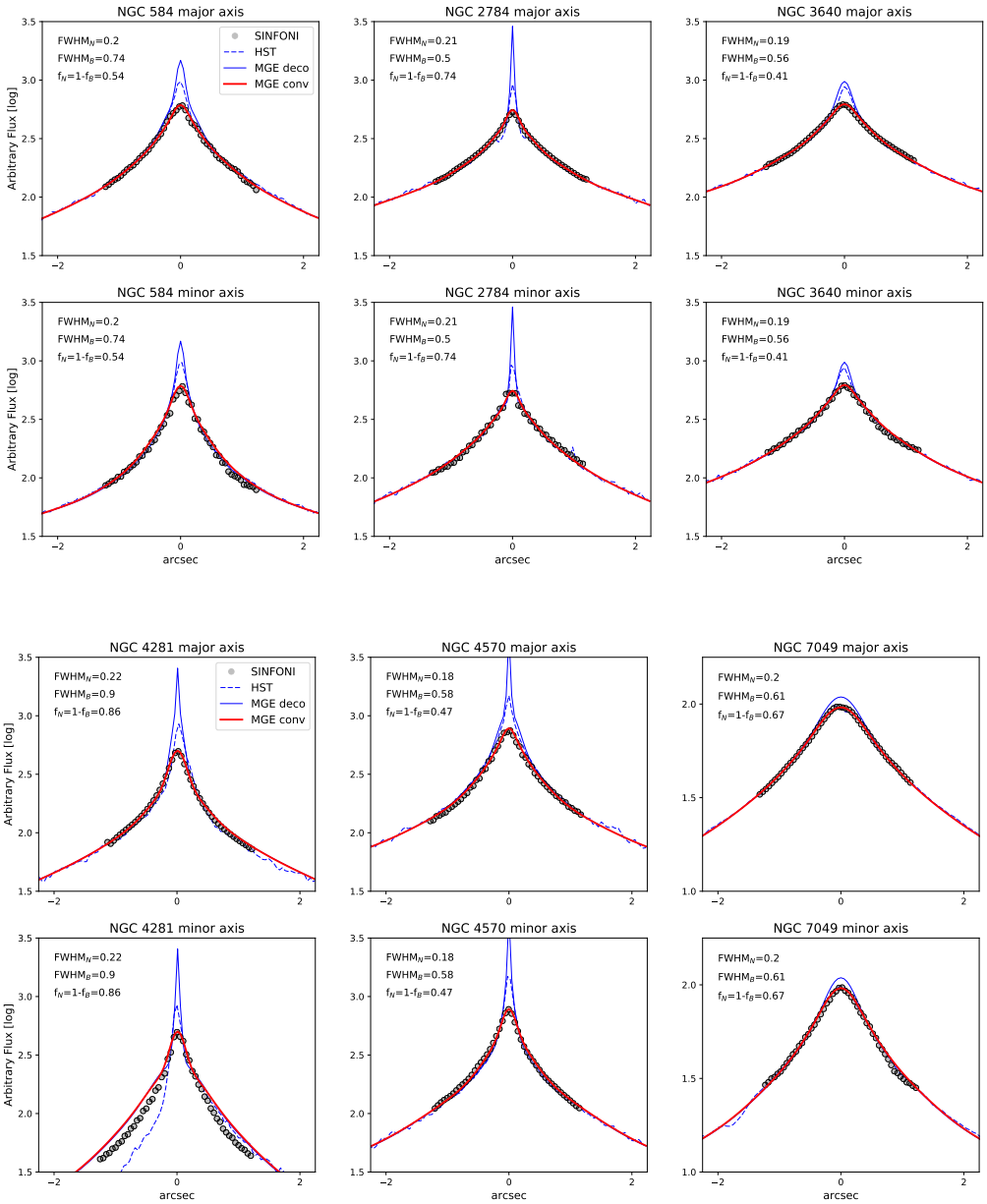


**Figure A.5 —** Determination of the SINFONI AO spatial resolution by comparing the surface brightness from the SINFONI reconstructed images with the respective convolved MGE models. Shown are the surface brightness profiles along the galaxy semimajor (top panel) and minor axis (bottom panel) of the SINFONI IFU image(red circles), deconvolved MGE model (green dashed line), convolved MGE model (black solid line), and HST image (blue dashed line) used to create the MGE model. The light profiles of NGC 2784, NGC 4281, and NGC 7049 show clear signatures of nuclear dust. Before comparing the profiles, all images were rotated such that the major and minor axis would match the vertical and horizontal image axis. The parameters of the double Gaussians used to describe the SINFONI PSFs are given in the upper left corner.

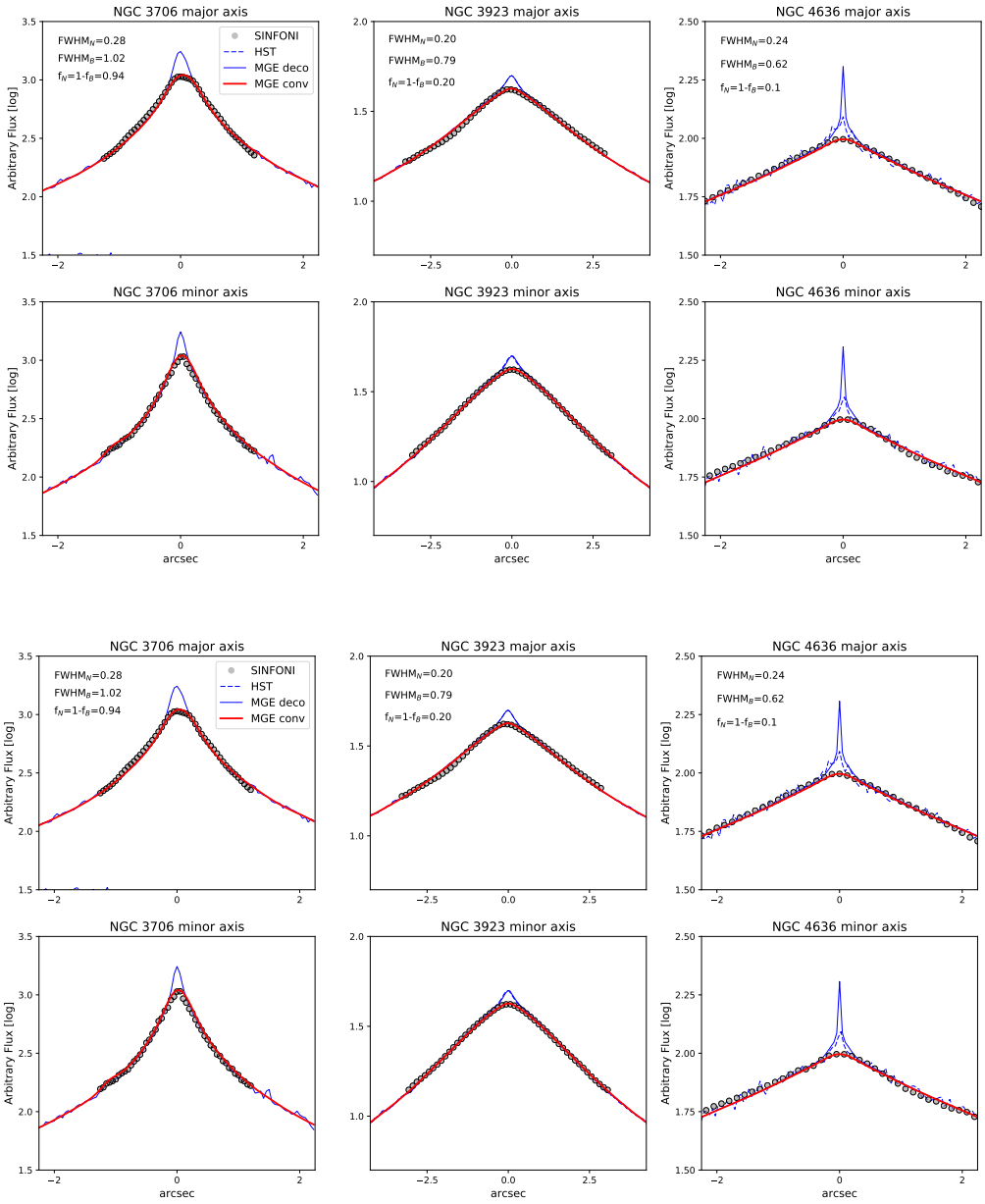


**Figure A.6 —** Determination of the SINFONI AO spatial resolution by comparing the surface brightness from the SINFONI reconstructed images with the respective convolved MGE models. Shown are the surface brightness profiles along the galaxy semimajor (top panel) and minor axis (bottom panel) of the SINFONI IFU image(red circles), deconvolved MGE model (green dashed line), convolved MGE model (black solid line), and HST image (blue dashed line) used to create the MGE model. Before comparing the profiles, all images were rotated such that the major and minor axis would match the vertical and horizontal image axis. The parameters of the double Gaussians used to describe the SINFONI PSFs are given in the upper left corner.

# 3 MGE parametrization of target galaxies

**Table A.2 —** Multi-Gaussian Expansion parameters

| | I4296 | (F814W) | | | I4329 | (F814M) | | |
|---|---|---|---|---|---|---|---|---|
| j | $\log M_j$ ($M_\odot$) | $\log I_j$ ($L_\odot$ pc$^{-2}$) | $\sigma_j$ (arcsec) | $q_j$ | $\log M_j$ ($M_\odot$) | $\log I_j$ ($L_\odot$ pc$^{-2}$) | $\sigma_j$ (arcsec) | $q_j$ |
| (1) | (2) | (3) | (4) | (5) | (2) | (3) | (4) | (5) |
| 1 | 7.144 | 4.645 | 0.017 | 0.9 | 9.807 | 3.828 | 0.68 | 0.86 |
| 2 | 10.019 | 3.983 | 1.012 | 0.91 | 10.214 | 3.592 | 1.393 | 0.9 |
| 3 | 10.187 | 3.601 | 1.916 | 0.9 | 10.428 | 3.218 | 2.741 | 0.9 |
| 4 | 10.521 | 3.433 | 3.405 | 0.91 | 10.531 | 2.758 | 5.578 | 0.79 |
| 5 | 10.606 | 2.996 | 6.235 | 0.9 | 10.562 | 2.216 | 10.807 | 0.79 |
| 6 | 10.721 | 2.616 | 10.978 | 0.91 | 10.919 | 2.208 | 18.895 | 0.6 |
| 7 | 10.925 | 2.37 | 18.494 | 0.9 | 11.408 | 1.941 | 45.099 | 0.6 |
| 8 | 11.0 | 2.059 | 28.87 | 0.9 | 10.895 | 0.906 | 82.258 | 0.6 |
| 9 | 10.715 | 1.459 | 39.351 | 1.0 | 11.56 | 1.183 | 117.966 | 0.71 |
| 10 | 11.32 | 1.59 | 67.86 | 1.0 | – | – | – | – |
| 11 | 11.724 | 1.003 | 212.638 | 1.0 | – | – | – | – |
| | N584 | (F555W) | | | N2784 | (F547M) | | |
| j | $\log M_j$ ($M_\odot$) | $\log I_j$ ($L_\odot$ pc$^{-2}$) | $\sigma_j$ (arcsec) | $q_j$ | $\log M_j$ ($M_\odot$) | $\log I_j$ ($L_\odot$ pc$^{-2}$) | $\sigma_j$ (arcsec) | $q_j$ |
| (1) | (2) | (3) | (4) | (5) | (2) | (3) | (4) | (5) |
| 1 | 7.746 | 4.891 | 0.055 | 0.80 | 7.421 | 4.981 | 0.061 | 0.8 |
| 2 | 8.371 | 4.496 | 0.201 | 0.64 | 8.1 | 4.313 | 0.287 | 0.8 |
| 3 | 8.371 | 4.496 | 0.201 | 0.64 | 8.802 | 4.273 | 0.674 | 0.8 |
| 4 | 9.137 | 3.872 | 1.014 | 0.61 | 9.169 | 3.998 | 1.413 | 0.8 |
| 5 | 9.225 | 3.468 | 1.544 | 0.82 | 8.094 | 2.901 | 1.93 | 0.45 |
| 6 | 9.625 | 3.399 | 2.667 | 0.81 | 9.403 | 3.69 | 2.635 | 0.8 |
| 7 | 9.944 | 3.137 | 5.089 | 0.84 | 9.795 | 3.602 | 4.581 | 0.8 |
| 8 | 9.759 | 2.666 | 8.320 | 0.61 | 9.993 | 3.043 | 10.944 | 0.8 |
| 9 | 10.231 | 2.764 | 12.257 | 0.66 | 9.293 | 1.83 | 19.749 | 0.8 |
| 10 | 10.304 | 2.210 | 26.342 | 0.61 | 10.042 | 2.785 | 20.772 | 0.45 |
| 11 | 10.366 | 1.748 | 48.130 | 0.61 | 10.376 | 2.215 | 58.832 | 0.45 |
| 12 | 10.274 | 1.046 | 77.768 | 0.95 | 9.182 | 0.355 | 94.984 | 0.8 |
| 13 | – | – | – | – | 10.204 | 1.614 | 96.422 | 0.45 |

| | N3640 | (F555W) | | | N3706 | (F555W) | | |
|---|---|---|---|---|---|---|---|---|
| j | $\log M_j$ ($M_\odot$) | $\log I_j$ ($L_\odot\,\mathrm{pc}^{-2}$) | $\sigma_j$ (arcsec) | $q_j$ | $\log M_j$ ($M_\odot$) | $\log I_j$ ($L_\odot\,\mathrm{pc}^{-2}$) | $\sigma_j$ (arcsec) | $q_j$ |
| (1) | (2) | (3) | (4) | (5) | (2) | (3) | (4) | (5) |
| 1 | 7.719 | 4.239 | 0.094 | 0.8 | 8.432 | 4.569 | 0.078 | 0.66 |
| 2 | 8.403 | 3.999 | 0.259 | 0.9 | 9.045 | 4.437 | 0.173 | 0.75 |
| 3 | 9.074 | 3.85 | 0.677 | 0.86 | 9.524 | 4.25 | 0.368 | 0.76 |
| 4 | 9.542 | 3.62 | 1.553 | 0.82 | 9.931 | 4.043 | 0.776 | 0.7 |
| 5 | 9.698 | 3.238 | 2.969 | 0.78 | 10.228 | 3.72 | 1.579 | 0.71 |
| 6 | 10.074 | 3.052 | 5.736 | 0.76 | 10.433 | 3.374 | 3.089 | 0.66 |
| 7 | 10.237 | 2.683 | 10.588 | 0.76 | 10.74 | 3.042 | 6.448 | 0.66 |
| 8 | 10.222 | 2.408 | 13.376 | 0.86 | 10.791 | 2.448 | 13.549 | 0.66 |
| 9 | 10.274 | 2.074 | 22.256 | 0.76 | 10.504 | 1.968 | 14.866 | 0.85 |
| 10 | 10.345 | 1.807 | 29.307 | 0.95 | 10.955 | 1.875 | 31.65 | 0.66 |
| 11 | 10.36 | 1.295 | 60.314 | 0.76 | 11.09 | 1.398 | 64.06 | 0.66 |
| 12 | 10.676 | 1.286 | 78.209 | 0.95 | 11.175 | 0.562 | 162.432 | 0.85 |

| | N3923 | (F814W) | | | N4261 | (F791W) | | |
|---|---|---|---|---|---|---|---|---|
| j | $\log M_j$ ($M_\odot$) | $\log I_j$ ($L_\odot\,\mathrm{pc}^{-2}$) | $\sigma_j$ (arcsec) | $q_j$ | $\log M_j$ ($M_\odot$) | $\log I_j$ ($L_\odot\,\mathrm{pc}^{-2}$) | $\sigma_j$ (arcsec) | $q_j$ |
| (1) | (2) | (3) | (4) | (5) | (2) | (3) | (4) | (5) |
| 1 | 7.511 | 3.462 | 0.218 | 0.98 | 7.079 | 4.712 | 0.017 | 0.75 |
| 2 | 9.105 | 3.685 | 1.056 | 0.98 | 10.231 | 4.002 | 1.45 | 0.77 |
| 3 | 9.76 | 3.629 | 2.649 | 0.8 | 10.678 | 3.745 | 3.373 | 0.72 |
| 4 | 10.057 | 3.274 | 6.485 | 0.6 | 10.704 | 3.059 | 7.873 | 0.68 |
| 5 | 10.483 | 2.995 | 14.072 | 0.64 | 11.029 | 2.894 | 12.493 | 0.84 |
| 6 | 10.605 | 2.401 | 32.142 | 0.64 | 11.01 | 2.41 | 21.475 | 0.83 |
| 7 | 10.871 | 2.012 | 64.846 | 0.71 | 11.248 | 2.042 | 41.355 | 0.9 |
| 8 | 11.206 | 1.365 | 191.974 | 0.78 | 11.21 | 1.551 | 77.251 | 0.73 |
| 9 | – | – | – | – | 11.421 | 0.986 | 200.418 | 0.65 |

| | N4281 | (F606W) | | | N4414 | (F606W) | | |
|---|---|---|---|---|---|---|---|---|
| j | $\log M_j$ ($M_\odot$) | $\log I_j$ ($L_\odot\,\mathrm{pc}^{-2}$) | $\sigma_j$ (arcsec) | $q_j$ | $\log M_j$ ($M_\odot$) | $\log I_j$ ($L_\odot\,\mathrm{pc}^{-2}$) | $\sigma_j$ (arcsec) | $q_j$ |
| (1) | (2) | (3) | (4) | (5) | (2) | (3) | (4) | (5) |
| 1 | 7.583 | 5.364 | 0.017 | 0.67 | 8.609 | 5.18 | 0.056 | 0.81 |
| 2 | 8.472 | 4.907 | 0.086 | 0.6 | 8.585 | 4.563 | 0.116 | 0.75 |
| 3 | 9.043 | 4.159 | 0.353 | 0.75 | 9.254 | 4.677 | 0.245 | 0.6 |
| 4 | 9.513 | 3.904 | 0.812 | 0.75 | 9.164 | 4.121 | 0.325 | 1.0 |
| 5 | 9.762 | 3.616 | 1.663 | 0.62 | 9.581 | 4.034 | 0.75 | 0.6 |
| 6 | 9.815 | 3.127 | 3.56 | 0.47 | 9.764 | 3.719 | 1.081 | 0.91 |
| 7 | 10.098 | 2.947 | 5.139 | 0.65 | 10.411 | 3.507 | 3.066 | 0.82 |
| 8 | 10.338 | 2.552 | 12.854 | 0.45 | 10.858 | 2.818 | 13.226 | 0.6 |
| 9 | 10.565 | 2.187 | 25.399 | 0.45 | 11.26 | 2.455 | 31.926 | 0.6 |
| 10 | 10.238 | 1.371 | 44.588 | 0.45 | 10.814 | 1.506 | 56.887 | 0.6 |
| 11 | 10.432 | 1.219 | 53.51 | 0.69 | 10.809 | 1.103 | 76.561 | 0.83 |

| | N4570 | (F555W) | | | N4636 | (F814M) | | |
|---|---|---|---|---|---|---|---|---|
| j | $\log M_j$ ($M_\odot$) | $\log I_j$ ($L_\odot\,\mathrm{pc}^{-2}$) | $\sigma_j$ (arcsec) | $q_j$ | $\log M_j$ ($M_\odot$) | $\log I_j$ ($L_\odot\,\mathrm{pc}^{-2}$) | $\sigma_j$ (arcsec) | $q_j$ |
| (1) | (2) | (3) | (4) | (5) | (2) | (3) | (4) | (5) |
| 1 | 7.276 | 6.043 | 0.017 | 0.3 | 5.7 | 4.151 | 0.017 | 0.95 |
| 2 | 7.738 | 4.647 | 0.096 | 0.7 | 6.808 | 3.41 | 0.145 | 0.95 |
| 3 | 5.773 | 2.611 | 0.104 | 0.7 | 7.956 | 3.334 | 0.594 | 0.95 |
| 4 | 7.063 | 3.709 | 0.199 | 0.3 | 9.038 | 3.556 | 1.6 | 0.95 |
| 5 | 8.184 | 4.248 | 0.254 | 0.7 | 9.685 | 3.518 | 3.521 | 0.95 |
| 6 | 7.713 | 4.071 | 0.277 | 0.3 | 10.025 | 3.263 | 6.979 | 0.95 |
| 7 | 8.683 | 4.055 | 0.565 | 0.7 | 10.198 | 2.751 | 15.356 | 0.95 |
| 8 | 9.167 | 3.862 | 1.23 | 0.7 | 10.128 | 2.378 | 23.52 | 0.82 |
| 9 | 9.676 | 3.623 | 2.911 | 0.7 | 10.599 | 2.201 | 51.269 | 0.76 |
| 10 | 8.024 | 1.938 | 4.617 | 0.3 | 10.903 | 1.84 | 113.613 | 0.72 |
| 11 | 9.575 | 2.893 | 6.005 | 0.7 | 10.853 | 1.102 | 250.864 | 0.72 |
| 12 | 9.67 | 2.72 | 12.491 | 0.3 | – | – | – | – |
| 13 | 9.618 | 2.436 | 16.321 | 0.3 | – | – | – | – |
| 14 | 10.059 | 2.431 | 27.262 | 0.3 | – | – | – | – |
| 15 | 9.899 | 1.7 | 52.604 | 0.3 | – | – | – | – |
| 16 | 9.573 | 0.865 | 61.819 | 0.7 | – | – | – | – |

| | N6958 | (F160W) | | | N7049 | (F814W) | | |
|---|---|---|---|---|---|---|---|---|
| j | $\log M_j$ ($M_\odot$) | $\log I_j$ ($L_\odot\,\mathrm{pc}^{-2}$) | $\sigma_j$ (arcsec) | $q_j$ | $\log M_j$ ($M_\odot$) | $\log I_j$ ($L_\odot\,\mathrm{pc}^{-2}$) | $\sigma_j$ (arcsec) | $q_j$ |
| (1) | (2) | (3) | (4) | (5) | (2) | (3) | (4) | (5) |
| 1 | 8.457 | 5.786 | 0.057 | 0.82 | 9.189 | 3.665 | 0.461 | 1.0 |
| 2 | 9.142 | 5.209 | 0.229 | 0.92 | 9.782 | 3.578 | 1.121 | 0.81 |
| 3 | 9.49 | 4.603 | 0.704 | 0.88 | 10.248 | 3.271 | 2.812 | 0.76 |
| 4 | 9.876 | 4.27 | 1.599 | 0.89 | 10.662 | 2.88 | 7.217 | 0.74 |
| 5 | 10.112 | 3.864 | 3.327 | 0.9 | 10.962 | 2.343 | 18.627 | 0.76 |
| 6 | 9.995 | 3.078 | 7.525 | 0.82 | 10.859 | 1.573 | 40.635 | 0.74 |
| 7 | 10.276 | 2.752 | 14.798 | 0.86 | 10.752 | 0.774 | 90.431 | 0.74 |
| 8 | 9.922 | 1.85 | 28.438 | 0.82 | 10.688 | 0.463 | 103.299 | 1.0 |
| 9 | 10.484 | 1.84 | 49.758 | 1.0 | – | – | – | – |

**Notes.** Details of the MGE parametrisation for each galaxy. We show the number of the Gaussian component (1), the total mass (2), the surface brightness in the specified band (3), the velocity dispersion (4) and the axial ratio (5) for each Gaussian component. The dynamical $M/L$ from the Schwarzschild models (Table 4.5) was used to determine the mass of each Gaussian component.

# 4 JAM Markov chain Monte Carlo models

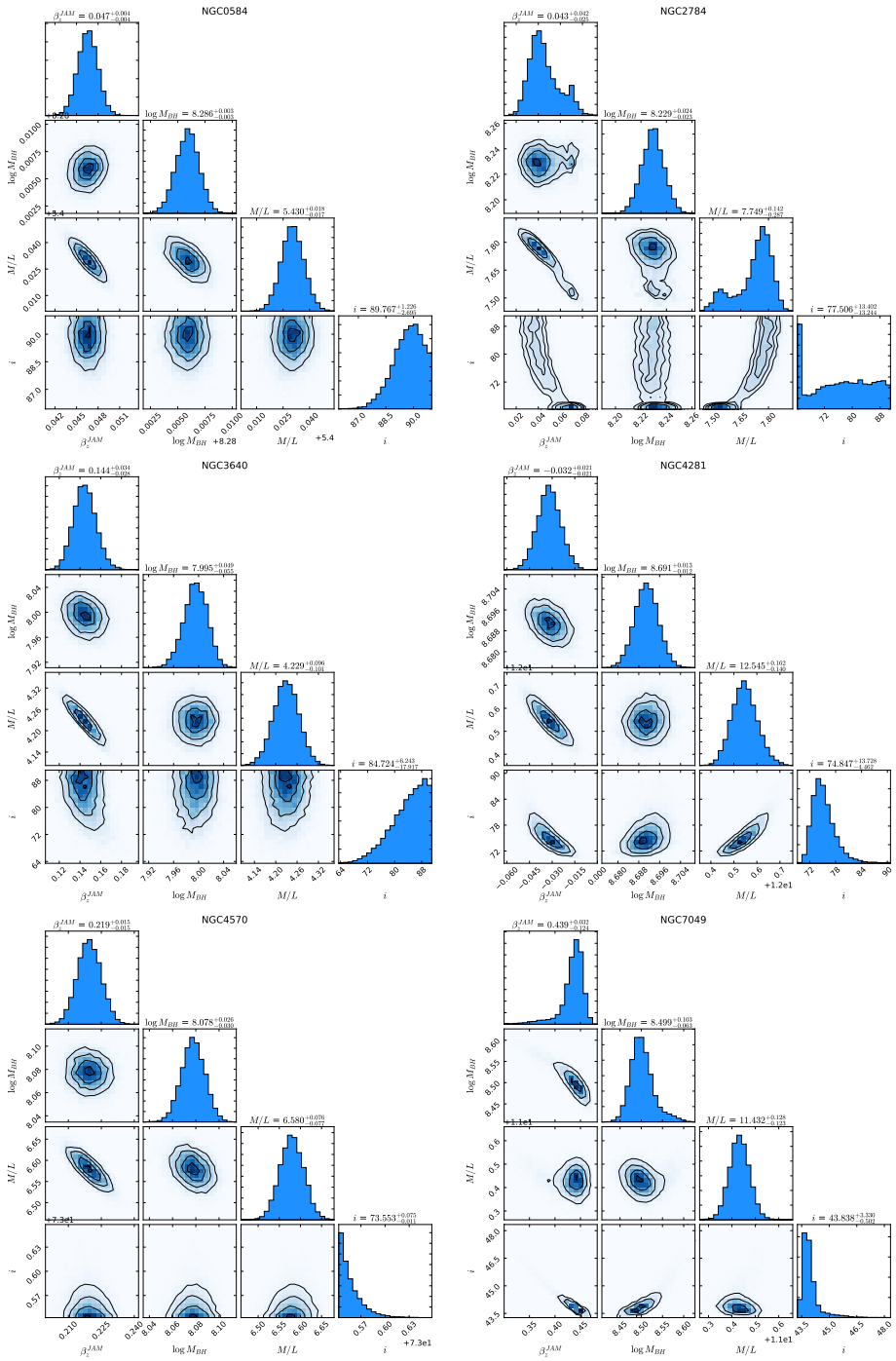


**Figure A.7 —** Markov chain Monte Carlo posterior probability distribution of the JAM model parameters ($M_{BH}$, $\beta$ M/L and inclination) for each galaxy of Chapter 3. The contour plots show the two-dimensional distributions for each parameter combination; the histograms show the projected one-dimensional distributions.

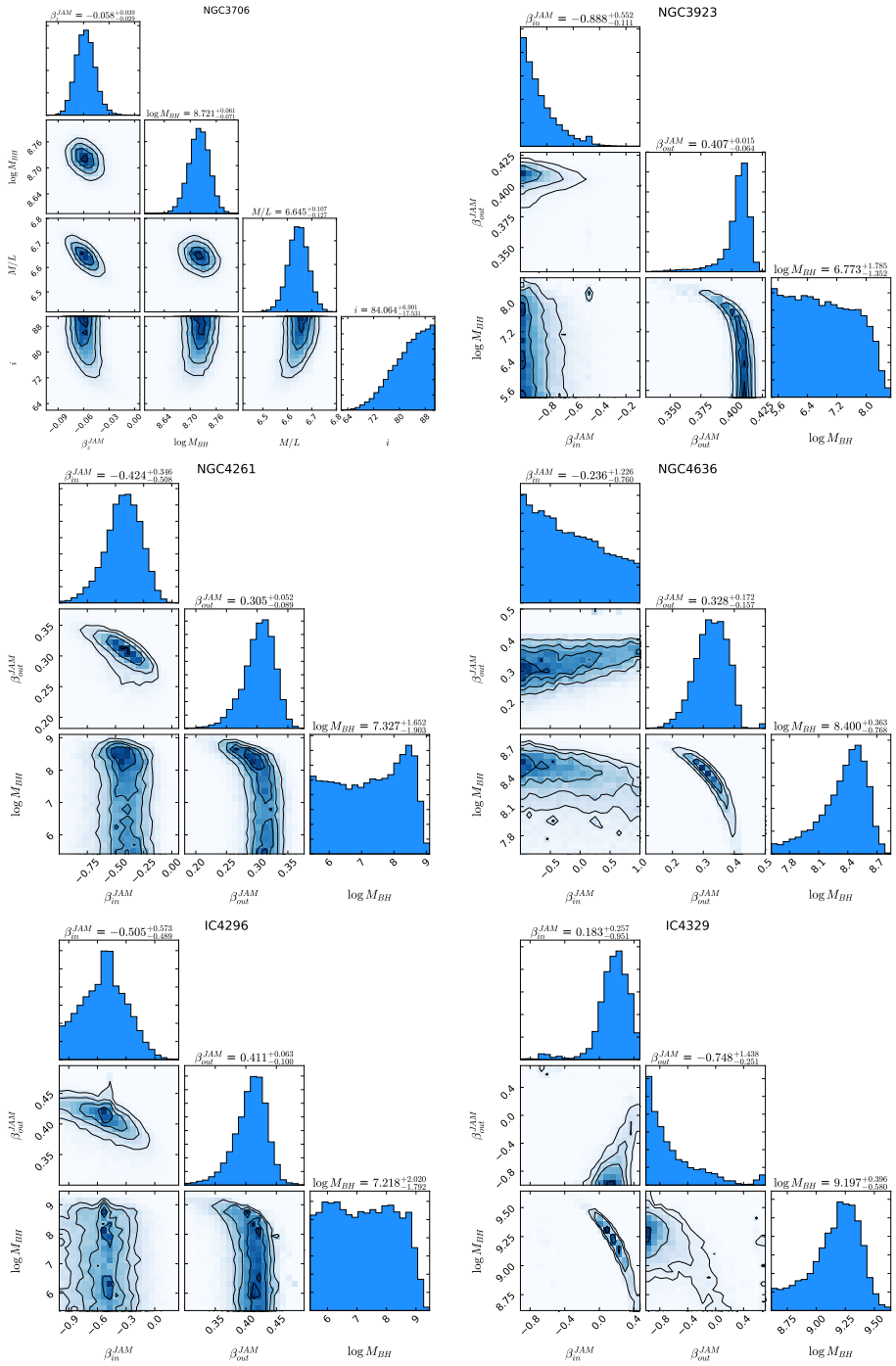


**Figure A.8 —** MCMC posterior probability distribution of the JAM model parameters ($M_{BH}$, inner and outer $\beta$) for each galaxy of Chapter 4. The contour plots show the two-dimensional distributions for each parameter combination; the histograms show the projected one-dimensional distributions. For NGC 4636 and IC 4329, I show a zoom around the maximum of the posterior distributions, but caution that there is a non-zero probability for very low masses ($\sim 10^6\ M_\odot$).

# 5 Accronyms and Abbreviations

AGN: Active Galactic Nucleus

AO: Adaptive Optics

BLR: Broad Line Region

CBE: Collisionless Boltzmann equation

DF: Distribution Function

DM: Dark Matter

IFU: Integral Field Unit

JAM: Jeans Anisotropic MGE

LOSVD: Line-Of-Sight Velocity Distribution

MGE: Multi Gaussian Expansion

NLR: Narrow Line Region

pPXF: penalized Pixel-Fitting

PSF: Point Spread Function

PVD: Position-Velocity Diagram

RM: Reverberation Mapping

SMBH: SuperMassive Black Hole

# Bibliography


Abazajian, K. N., Adelman-McCarthy, J. K., Agüeros, M. A., et al. 2009, ApJS, 182, 543

Abbott, B. P., Abbott, R., Abbott, T. D., et al. 2016, Physical Review Letters, 116, 061102

Abuter, R., Amorim, A., Bauboeck, M., et al. 2019

Agarwal, B., Dalla Vecchia, C., Johnson, J. L., Khochfar, S., & Paardekooper, J.-P. 2014, MNRAS, 443, 648

Agarwal, B., Khochfar, S., Johnson, J. L., et al. 2012, MNRAS, 425, 2854

Aguerri, J. A. L., Balcells, M., & Peletier, R. F. 2001, A&A, 367, 428

Ahn, C. P., Seth, A. C., Cappellari, M., et al. 2018, ApJ, 858, 102

Alatalo, K., Davis, T. A., Bureau, M., et al. 2013, MNRAS, 432, 1796

Alexander, T. & Natarajan, P. 2014, Science, 345, 1330

Allington-Smith, J., Murray, G., Content, R., et al. 2002, in Astronomical Society of the Pacific Conference Series, Vol. 282, Galaxies: the Third Dimension, ed. M. Rosada, L. Binette, & L. Arias, 415

Alonso, M. S., Coldwell, G., & Lambas, D. G. 2013, A&A, 549, A141

Anglés-Alcázar, D., Özel, F., & Davé, R. 2013, ApJ, 770, 5

Annibali, F., Bressan, A., Rampazzo, R., et al. 2010, A&A, 519, A40

Antonucci, R. 1993, ARA&A, 31, 473

Araya Salvo, C., Mathur, S., Ghosh, H., Fiore, F., & Ferrarese, L. 2012, ApJ, 757, 179

Athanassoula, E. 2005, MNRAS, 358, 1477

Athanassoula, E., Lambert, J. C., & Dehnen, W. 2005, MNRAS, 363, 496

Atkinson, J. W., Collett, J. L., Marconi, A., et al. 2005, MNRAS, 359, 504

Bañados, E., Venemans, B. P., Mazzucchelli, C., et al. 2018, Nature, 553, 473

Baade, W. & Minkowski, R. 1954, ApJ, 119, 215

Bacon, R., Accardo, M., Adjali, L., et al. 2010, in Proceedings of the SPIE, Vol. 7735, Ground-based and Airborne Instrumentation for Astronomy III, 773508

Bacon, R., Copin, Y., Monnet, G., et al. 2001, MNRAS, 326, 23

Baldassare, V. F., Reines, A. E., Gallo, E., & Greene, J. E. 2015, The Astrophysical Journal, 809, L14

Balick, B. & Brown, R. L. 1974, ApJ, 194, 265

Barack, L., Cardoso, V., Nissanke, S., et al. 2018

Barausse, E., Shankar, F., Bernardi, M., Dubois, Y., & Sheth, R. K. 2017, MNRAS, 468, 4782

Barnabè, M., Dutton, A. A., Marshall, P. J., et al. 2012, MNRAS, 423, 1073

Barnes, J. E. 1988, ApJ, 331, 699

Barnes, J. E. 1992, ApJ, 393, 484

Baron, D., Netzer, H., Prochaska, J. X., et al. 2018

Barrow, K. S. S., Aykutalp, A., & Wise, J. H. 2018, Nature Astronomy, 2, 987

Barth, A. J., Darling, J., Baker, A. J., et al. 2016, ApJ, 823, 51

Barth, A. J., Ho, L. C., & Sargent, W. L. W. 2002, The Astronomical Journal, 124, 2607âĂŞ2614

Barth, A. J., Pancoast, A., Thorman, S. J., et al. 2011, ApJ, 743, L4

Barth, A. J., Sarzi, M., Rix, H.-W., et al. 2001, ApJ, 555, 685

Batcheldor, D. 2010, ApJ, 711, L108

Batiste, M., Bentz, M. C., Raimundo, S. I., Vestergaard, M., & Onken, C. A. 2017, ApJ, 838, L10

Baugh, C. M., Cole, S., Frenk, C. S., Benson, A. J., & Lacey, C. G. 1999, in Astronomical Society of the Pacific Conference Series, Vol. 163, Star Formation in Early Type Galaxies, ed. P. Carral & J. Cepa, 227

Begelman, M. C. & Volonteri, M. 2017, MNRAS, 464, 1102

Begelman, M. C., Volonteri, M., & Rees, M. J. 2006, MNRAS, 370, 289

Beifiori, A., Courteau, S., Corsini, E. M., & Zhu, Y. 2012, MNRAS, 419, 2497

Beifiori, A., Maraston, C., Thomas, D., & Johansson, J. 2011, A&A, 531, A109
Beifiori, A., Sarzi, M., Corsini, E. M., et al. 2009, ApJ, 692, 856
Bell, E. F. & de Jong, R. S. 2001, ApJ, 550, 212
Bellocchi, E., Ascasibar, Y., Galbany, L., et al. 2019, A&A, 625, A83
Bellovary, J. M., Holley-Bockelmann, K., Gültekin, K., et al. 2014, MNRAS, 445, 2667
Bellstedt, S., Forbes, D. A., Romanowsky, A. J., et al. 2018, MNRAS, 476, 4543
Bender, R., Saglia, R. P., & Gerhard, O. E. 1994, MNRAS, 269, 785
Bennert, V. N., Treu, T., Auger, M. W., et al. 2015, ApJ, 809, 20
Bentz, M. C., Batiste, M., Seals, J., et al. 2016, The Astrophysical Journal, 831, 2
Bentz, M. C., Denney, K. D., Grier, C. J., et al. 2013, ApJ, 767, 149
Bentz, M. C. & Katz, S. 2015, PASP, 127, 67
Bentz, M. C., Walsh, J. L., Barth, A. J., et al. 2009, ApJ, 705, 199
Bernardi, M., Sheth, R. K., Tundo, E., & Hyde, J. B. 2007, ApJ, 660, 267
Berrier, J. C., Davis, B. L., Kennefick, D., et al. 2013, ApJ, 769, 132
Best, P. N., Kauffmann, G., Heckman, T. M., et al. 2005, MNRAS, 362, 25
Bhattacharyya, D. & Mangalam, A. 2018, Journal of Astrophysics and Astronomy, 39, 4
Bílek, M., Cuillandre, J.-C., Gwyn, S., et al. 2016, A&A, 588, A77
Binney, J. & Mamon, G. A. 1982, MNRAS, 200, 361
Binney, J. & Tremaine, S. 1987, Galactic dynamics
Binney, J. & Tremaine, S. 2008, Galactic Dynamics: Second Edition (Princeton University Press)
Blandford, R. D. & McKee, C. F. 1982, ApJ, 255, 419
Blumenthal, G. R., Faber, S. M., Primack, J. R., & Rees, M. J. 1984, Nature, 311, 517
Boardman, N. F., Weijmans, A.-M., van den Bosch, R., et al. 2017, MNRAS, 471, 4005, ionized gas kinematics
Bodenheimer, P. 1995, ARA&A, 33, 199
Boehle, A., Ghez, A. M., Schödel, R., et al. 2016, ApJ, 830, 17
Bois, M., Bournaud, F., Emsellem, E., et al. 2010, MNRAS, 406, 2405
Boizelle, B. D., Barth, A. J., Walsh, J. L., et al. 2019
Bond, J. R., Arnett, W. D., & Carr, B. J. 1984, ApJ, 280, 825
Bonfini, P., Bitsakis, T., Zezas, A., et al. 2018, MNRAS, 473, L94
Bonfini, P. & Graham, A. W. 2016, The Astrophysical Journal, 829, 81
Bonnet, H., Abuter, R., Baker, A., et al. 2004, The Messenger, 117, 17
Braatz, J. A., Wilson, A. S., & Henkel, C. 1996, ApJS, 106, 51
Braatz, J. A., Wilson, A. S., & Henkel, C. 1997, ApJS, 110, 321
Braine, J., Brouillet, N., & Baudry, A. 1997, A&A, 318, 19
Bromm, V., Coppi, P. S., & Larson, R. B. 2002, ApJ, 564, 23
Bromm, V. & Larson, R. B. 2004, ARA&A, 42, 79
Bromm, V. & Loeb, A. 2003, ApJ, 596, 34
Brown, J. S., Valluri, M., Shen, J., & Debattista, V. P. 2013, ApJ, 778, 151
Bu, D.-F. & Yang, X.-H. 2019, MNRAS, 484, 1724
Busch, G. 2016, ArXiv e-prints
Buta, R. J., Sheth, K., Athanassoula, E., et al. 2015, ApJS, 217, 32
Capetti, A., Marconi, A., Macchetto, D., & Axon, D. 2005, A&A, 431, 465
Cappellari, M. 2002, MNRAS, 333, 400
Cappellari, M. 2008, MNRAS, 390, 71
Cappellari, M. 2015
Cappellari, M. 2016, ARA&A, 54, 597
Cappellari, M. 2017, MNRAS, 466, 798
Cappellari, M., Bacon, R., Bureau, M., et al. 2006, MNRAS, 366, 1126
Cappellari, M. & Copin, Y. 2003, MNRAS, 342, 345
Cappellari, M. & Emsellem, E. 2004, PASP, 116, 138
Cappellari, M., Emsellem, E., Bacon, R., et al. 2007, MNRAS, 379, 418

Cappellari, M., Emsellem, E., Krajnović, D., et al. 2011, MNRAS, 413, 813
Cappellari, M., McDermid, R. M., Alatalo, K., et al. 2012, Nature, 484, 485
Cappellari, M., McDermid, R. M., Alatalo, K., et al. 2013a, MNRAS, 432, 1862
Cappellari, M., McDermid, R. M., Bacon, R., et al. 2010, in American Institute of Physics Conference Series, Vol. 1240, American Institute of Physics Conference Series, ed. V. P. Debattista & C. C. Popescu, 211–214
Cappellari, M., Romanowsky, A. J., Brodie, J. P., et al. 2015, ApJ, 804, L21
Cappellari, M., Scott, N., Alatalo, K., et al. 2013b, MNRAS, 432, 1709
Cappellari, M., Verolme, E. K., van der Marel, R. P., et al. 2002, ApJ, 578, 787
Carollo, C. M., Franx, M., Illingworth, G. D., & Forbes, D. A. 1997, ApJ, 481, 710
Carollo, C. M., Stiavelli, M., & Mack, J. 1998, AJ, 116, 68
Carter, D., Thomson, R. C., & Hau, G. K. T. 1998, MNRAS, 294, 182
Chae, K.-H., Bernardi, M., & Sheth, R. K. 2019, ApJ, 874, 41
Chatzopoulos, S., Fritz, T. K., Gerhard, O., et al. 2015, MNRAS, 447, 948
Chen, Y.-C. & Hwang, C.-Y. 2017, Ap&SS, 362, 230
Cid Fernandes, R., Stasińska, G., Mateus, A., & Vale Asari, N. 2011, MNRAS, 413, 1687
Clark, P. C., Glover, S. C. O., Klessen, R. S., & Bromm, V. 2011, ApJ, 727, 110
Clavel, J., Reichert, G. A., Alloin, D., et al. 1991, ApJ, 366, 64
Cleveland, W. S. 1979, Journal of the American Statistical Association, 74, 829
Cleveland, W. S. & Devlin, S. J. 1988, Journal of the American Statistical Association, 83, 596
Coccato, L., Sarzi, M., Pizzella, A., et al. 2006, MNRAS, 366, 1050
Colpi, M. 2018
Combes, F., Garcia-Burillo, S., Audibert, A., et al. 2018, A&A, 623,, A79
Costantin, L., Corsini, E. M., Méndez-Abreu, J., et al. 2018, MNRAS, 481, 3623
Cresci, G. & Maiolino, R. 2018, Nature Astronomy, 2, 179
Cretton, N., de Zeeuw, P. T., van der Marel, R. P., & Rix, H.-W. 1999, ApJS, 124, 383
Cretton, N. & van den Bosch, F. C. 1999, The Astrophysical Journal, 514, 704âĂŞ724
Croton, D. J., Springel, V., White, S. D. M., et al. 2006, MNRAS, 365, 11
Dalla Bontà, E., Ferrarese, L., Corsini, E. M., et al. 2009, ApJ, 690, 537
Darling, J. 2017, ApJ, 837, 100
Davies, R. 2008, in 2007 ESO Instrument Calibration Workshop, ed. A. Kaufer & F. Kerber, 249
Davies, R. I. 2007, Monthly Notices of the Royal Astronomical Society, 375, 1099âĂŞ1105
Davies, R. L. & Birkinshaw, M. 1986, ApJ, 303, L45
Davies, R. L., Burstein, D., Dressler, A., et al. 1987, ApJS, 64, 581
Davis, B. L., Graham, A. W., & Cameron, E. 2018a, ApJ, 869, 113
Davis, B. L., Graham, A. W., & Cameron, E. 2019, ApJ, 873, 85
Davis, B. L., Graham, A. W., & Seigar, M. S. 2017a, MNRAS, 471, 2187
Davis, T. A. 2014, MNRAS, 443, 911
Davis, T. A., Alatalo, K., Bureau, M., et al. 2012, Monthly Notices of the Royal Astronomical Society, 429, 534
Davis, T. A., Bureau, M., Cappellari, M., Sarzi, M., & Blitz, L. 2013, Nature, 494, 328
Davis, T. A., Bureau, M., Onishi, K., et al. 2017b, MNRAS, 468, 4675
Davis, T. A., Bureau, M., Onishi, K., et al. 2018b, MNRAS, 473, 3818
Dayal, P., Rossi, E. M., Shiralilou, B., et al. 2019, MNRAS, 486, 2336
de Blok, W. J. G., Józsa, G. I. G., Patterson, M., et al. 2014, A&A, 566, A80
de Francesco, G., Capetti, A., & Marconi, A. 2006, A&A, 460, 439
de Francesco, G., Capetti, A., & Marconi, A. 2008, A&A, 479, 355
De Lorenzi, F., Hartmann, M., Debattista, V. P., Seth, A. C., & Gerhard, O. 2013, MNRAS, 429, 2974
De Lucia, G., Fontanot, F., Wilman, D., & Monaco, P. 2011, MNRAS, 414, 1439
De Lucia, G., Springel, V., White, S. D. M., Croton, D., & Kauffmann, G. 2006, MNRAS, 366, 499

de Vaucouleurs, G., de Vaucouleurs, A., Corwin, Jr., H. G., et al. 1991, Third Reference Catalogue of Bright Galaxies. Volume I: Explanations and references. Volume II: Data for galaxies between $0^h$ and $12^h$. Volume III: Data for galaxies between $12^h$ and $24^h$.
de Zeeuw, P. T., Bureau, M., Emsellem, E., et al. 2002, MNRAS, 329, 513
Debattista, V. P., Kazantzidis, S., & van den Bosch, F. C. 2013, ApJ, 765, 23
Dékány, I., Minniti, D., Catelan, M., et al. 2013, ApJ, 776, L19
den Brok, M., Seth, A. C., Barth, A. J., et al. 2015, ApJ, 809, 101
Denney, K. D., Peterson, B. M., Pogge, R. W., et al. 2010, ApJ, 721, 715
Devecchi, B. & Volonteri, M. 2009, ApJ, 694, 302
Devecchi, B., Volonteri, M., Colpi, M., & Haardt, F. 2010, MNRAS, 409, 1057
Devecchi, B., Volonteri, M., Rossi, E. M., Colpi, M., & Portegies Zwart, S. 2012, MNRAS, 421, 1465
Devereux, N., Ford, H., Tsvetanov, Z., & Jacoby, G. 2003, AJ, 125, 1226
Di Matteo, T., Colberg, J., Springel, V., Hernquist, L., & Sijacki, D. 2008, ApJ, 676, 33
Di Matteo, T., Springel, V., & Hernquist, L. 2005, Nature, 433, 604
Dijkstra, M., Ferrara, A., & Mesinger, A. 2014, MNRAS, 442, 2036
Dijkstra, M., Haiman, Z., Mesinger, A., & Wyithe, J. S. B. 2008, MNRAS, 391, 1961
Dirsch, B., Schuberth, Y., & Richtler, T. 2005, A&A, 433, 43
Dittenber, B. & Valluri, M. 2017, in American Astronomical Society Meeting Abstracts, Vol. 229, American Astronomical Society Meeting Abstracts #229, 144.04
Doeleman, S. S., Weintroub, J., Rogers, A. E. E., et al. 2008, Nature, 455, 78
Dolphin, A. E. 2009, PASP, 121, 655
Doré, O., Werner, M. W., Ashby, M., et al. 2016
Drehmer, D. A., Storchi-Bergmann, T., Ferrari, F., Cappellari, M., & Riffel, R. A. 2015, MNRAS, 450, 128
Du, M., Debattista, V. P., Shen, J., Ho, L. C., & Erwin, P. 2017, ApJ, 844, L15
Du, P., Zhang, Z.-X., Wang, K., et al. 2018, ApJ, 856, 6
Duc, P.-A., Cuillandre, J.-C., Alatalo, K., et al. 2011, in IAU Symposium, Vol. 277, Tracing the Ancestry of Galaxies, ed. C. Carignan, F. Combes, & K. C. Freeman, 238–241
Duc, P.-A., Cuillandre, J.-C., Karabal, E., et al. 2015, MNRAS, 446, 120
Dullo, B. T. & Graham, A. W. 2013, ApJ, 768, 36
Dullo, B. T. & Graham, A. W. 2014, MNRAS, 444, 2700
Dullo, B. T., Graham, A. W., & Knapen, J. H. 2017, MNRAS, 471, 2321
Ebisuzaki, T., Makino, J., Tsuru, T. G., et al. 2001, ApJ, 562, L19
Ebrová, I. & Łokas, E. L. 2015, ApJ, 813, 10
Ebrová, I. & Łokas, E. L. 2017, ApJ, 850, 144
Eckart, A. & Genzel, R. 1996, Nature, 383, 415
Eckart, A., Zajacek, M., Parsa, M., et al. 2018
Eggen, O. J., Lynden-Bell, D., & Sandage, A. R. 1962, ApJ, 136, 748
Eisenhauer, F., Abuter, R., Bickert, K., et al. 2003, in Proceedings of the SPIE, Vol. 4841, Instrument Design and Performance for Optical/Infrared Ground-based Telescopes, ed. M. Iye & A. F. M. Moorwood, 1548–1561
Eisenstein, D. J. & Loeb, A. 1995, ApJ, 443, 11
Emsellem, E. 2013, MNRAS, 433, 1862
Emsellem, E., Cappellari, M., Krajnović, D., et al. 2011, MNRAS, 414, 888
Emsellem, E., Cappellari, M., Krajnović, D., et al. 2007, MNRAS, 379, 401
Emsellem, E., Cappellari, M., Peletier, R. F., et al. 2004, MNRAS, 352, 721
Emsellem, E., Monnet, G., & Bacon, R. 1994, A&A, 285
Ene, I., Ma, C.-P., McConnell, N. J., et al. 2019
Ene, I., Ma, C.-P., Veale, M., et al. 2018
Erwin, P. 2008, in IAU Symposium, Vol. 245, Formation and Evolution of Galaxy Bulges, ed. M. Bureau, E. Athanassoula, & B. Barbuy, 113–116
Erwin, P., Beltrán, J. C. V., Graham, A. W., & Beckman, J. E. 2003, ApJ, 597, 929

Erwin, P., Saglia, R. P., Fabricius, M., et al. 2015, MNRAS, 446, 4039
Event Horizon Telescope Collaboration, Akiyama, K., Alberdi, A., et al. 2019a, ApJ, 875, L1
Event Horizon Telescope Collaboration, Akiyama, K., Alberdi, A., et al. 2019b, ApJ, 875, L4
Event Horizon Telescope Collaboration, Akiyama, K., Alberdi, A., et al. 2019c, ApJ, 875, L6
Faber, S. M., Tremaine, S., Ajhar, E. A., et al. 1997, AJ, 114, 1771
Fabian, A. C. 1999, MNRAS, 308, L39
Fabian, A. C. 2012, ARA&A, 50, 455
Fabricius, M. H., Saglia, R. P., Fisher, D. B., et al. 2012, ApJ, 754, 67
Falcón-Barroso, J. 2016, in Astrophysics and Space Science Library, Vol. 418, Galactic Bulges, ed. E. Laurikainen, R. Peletier, & D. Gadotti, 161
Falcón-Barroso, J., Lyubenova, M., van de Ven, G., et al. 2017, A&A, 597, A48
Falcón-Barroso, J., Sánchez-Blázquez, P., Vazdekis, A., et al. 2011, A&A, 532, A95
Fall, S. M. & Efstathiou, G. 1980, MNRAS, 193, 189
Feldmeier-Krause, A., Zhu, L., Neumayer, N., et al. 2016, Monthly Notices of the Royal Astronomical Society, stw3377
Ferrara, A., Salvadori, S., Yue, B., & Schleicher, D. 2014, MNRAS, 443, 2410
Ferrarese, L., Côté, P., Dalla Bontà, E., et al. 2006, ApJ, 644, L21
Ferrarese, L. & Ford, H. 2005, Space Sci. Rev., 116, 523
Ferrarese, L., Ford, H. C., & Jaffe, W. 1996, ApJ, 470, 444
Ferrarese, L. & Merritt, D. 2000, ApJ, 539, L9
Ferrarese, L., van den Bosch, F. C., Ford, H. C., Jaffe, W., & O'Connell, R. W. 1994, AJ, 108, 1598
Ferreras, I., Scott, N., Barbera, F. L., et al. 2019
Filippenko, A. V. & Ho, L. C. 2003, ApJ, 588, L13
Fisher, D. B. & Drory, N. 2010, ApJ, 716, 942
Fisher, D. B. & Drory, N. 2016, in Astrophysics and Space Science Library, Vol. 418, Galactic Bulges, ed. E. Laurikainen, R. Peletier, & D. Gadotti, 41
Fisher, D. B., Drory, N., & Fabricius, M. H. 2009, ApJ, 697, 630
Forbes, J. C., Krumholz, M. R., Burkert, A., & Dekel, A. 2014, MNRAS, 438, 1552
Ford, H. C., Bartko, F., Bely, P. Y., et al. 1998, in Proceedings of the SPIE, Vol. 3356, Space Telescopes and Instruments V, ed. P. Y. Bely & J. B. Breckinridge, 234–248
Foreman-Mackey, D., Hogg, D. W., Lang, D., & Goodman, J. 2013, PASP, 125, 306
Franx, M., Illingworth, G., & Heckman, T. 1989, ApJ, 344, 613
Freedman, W. L., Madore, B. F., Gibson, B. K., et al. 2001, ApJ, 553, 47
Frenk, C. S. & White, S. D. M. 2012, Annalen der Physik, 524, 507
Fryer, C. L., Woosley, S. E., & Heger, A. 2001, ApJ, 550, 372
Gadotti, D. A. 2009, MNRAS, 393, 1531
Gadotti, D. A. & Kauffmann, G. 2009, MNRAS, 399, 621
Gao, F., Braatz, J. A., Reid, M. J., et al. 2017, ApJ, 834, 52
Gao, F., Braatz, J. A., Reid, M. J., et al. 2016, ApJ, 817, 128
Gao, H. & Ho, L. C. 2017, ApJ, 845, 114
Gao, H., Ho, L. C., Barth, A. J., & Li, Z.-Y. 2018, ApJ, 862, 100
Gaskell, M. 2014, Nature Physics, 10, 414
Gaspari, M., Ruszkowski, M., & Oh, S. P. 2013, MNRAS, 432, 3401
Gebhardt, K., Adams, J., Richstone, D., et al. 2011, ApJ, 729, 119
Gebhardt, K., Bender, R., Bower, G., et al. 2000, ApJ, 539, L13
Gebhardt, K., Lauer, T. R., Kormendy, J., et al. 2001, AJ, 122, 2469
Gebhardt, K., Richstone, D., Tremaine, S., et al. 2003, ApJ, 583, 92
Gebhardt, K. & Thomas, J. 2009, ApJ, 700, 1690
Gerhard, O. E. 1993, MNRAS, 265, 213
Gerhard, O. E. & Binney, J. J. 1996, MNRAS, 279, 993
Ghez, A. M., Salim, S., Hornstein, S. D., et al. 2005, ApJ, 620, 744
Ghez, A. M., Salim, S., Weinberg, N. N., et al. 2008, ApJ, 689, 1044

Ghosh, H., Mathur, S., Fiore, F., & Ferrarese, L. 2008, ApJ, 687, 216
Gillessen, S., Eisenhauer, F., Fritz, T. K., et al. 2013, in IAU Symposium, Vol. 289, Advancing the Physics of Cosmic Distances, ed. R. de Grijs, 29–35
Gillessen, S., Eisenhauer, F., Trippe, S., et al. 2009, ApJ, 692, 1075
Gillessen, S., Plewa, P. M., Eisenhauer, F., et al. 2017, ApJ, 837, 30
Ginat, Y. B., Meiron, Y., & Soker, N. 2016, MNRAS, 461, 3533
Goerdt, T., Moore, B., Read, J. I., & Stadel, J. 2010, ApJ, 725, 1707
Goldbaum, N. J., Krumholz, M. R., & Forbes, J. C. 2015, ApJ, 814, 131
Goldbaum, N. J., Krumholz, M. R., & Forbes, J. C. 2016, ApJ, 827, 28
Goodman, J. & Weare, J. 2010, Communications in Applied Mathematics and Computational Science, Vol. 5, No. 1, p. 65-80, 2010, 5, 65
Graham, A. 2015, Highlights of Astronomy, 16, 360
Graham, A. W. 2004, ApJ, 613, L33
Graham, A. W. 2008, ApJ, 680, 143
Graham, A. W. 2012, ApJ, 746, 113
Graham, A. W. 2016, Galactic Bulges, 418, 263
Graham, A. W. & Driver, S. P. 2007, ApJ, 655, 77
Graham, A. W., Erwin, P., Caon, N., & Trujillo, I. 2001, ApJ, 563, L11
Graham, A. W., Erwin, P., Trujillo, I., & Asensio Ramos, A. 2003, AJ, 125, 2951
Graham, A. W. & Li, I.-h. 2009, ApJ, 698, 812
Graham, A. W., Onken, C. A., Athanassoula, E., & Combes, F. 2011, MNRAS, 412, 2211
Graham, A. W. & Scott, N. 2013, ApJ, 764, 151
Graham, A. W. & Spitler, L. R. 2009, MNRAS, 397, 2148
Gravity Collaboration, Abuter, R., Amorim, A., et al. 2018, A&A, 615, L15
Gravity Collaboration, Amorim, A., Bauböck, M., et al. 2019
Greene, J. E. & Ho, L. C. 2005, ApJ, 630, 122
Greene, J. E. & Ho, L. C. 2006, ApJ, 641, L21
Greene, J. E., Ho, L. C., & Barth, A. J. 2008, ApJ, 688, 159
Greene, J. E., Peng, C. Y., Kim, M., et al. 2010, ApJ, 721, 26
Greene, J. E., Seth, A., den Brok, M., et al. 2013, ApJ, 771, 121
Greene, J. E., Seth, A., Kim, M., et al. 2016, ApJ, 826, L32
Greenhill, L. J., Jiang, D. R., Moran, J. M., et al. 1995, ApJ, 440, 619
Greif, T. H., Bromm, V., Clark, P. C., et al. 2012, MNRAS, 424, 399
Grier, C. J., Martini, P., Watson, L. C., et al. 2013, ApJ, 773, 90
Grier, C. J., Trump, J. R., Shen, Y., et al. 2017
Griv, E., Gedalin, M., & Jiang, I.-G. 2019, MNRAS, 484, 218
Guérou, A., Krajnović, D., Epinat, B., et al. 2017, A&A, 608, A5
Gültekin, K., Barth, A., Gebhardt, K., et al. 2019
Gültekin, K., Gebhardt, K., Kormendy, J., et al. 2014, ApJ, 781, 112
Gültekin, K., Richstone, D. O., Gebhardt, K., et al. 2009, ApJ, 698, 198
Gultekin, K., Tremaine, S., Loeb, A., & Richstone, D. O. 2011
Habouzit, M., Volonteri, M., Latif, M., Dubois, Y., & Peirani, S. 2016
Hagiwara, Y., Doi, A., Hachisuka, K., & Horiuchi, S. 2018, , 70, 54
Haiman, Z., Brandt, W. N., Vikhlinin, A., et al. 2019
Häring, N. & Rix, H.-W. 2004, ApJ, 604, L89
Hartmann, M., Debattista, V. P., Cole, D. R., et al. 2014, MNRAS, 441, 1243
Hastings, W. K. 1970, Biometrika, 57, 97
Heger, A. & Woosley, S. E. 2002, ApJ, 567, 532
Hekatelyne, C., Riffel, R. A., Sales, D., et al. 2018, MNRAS, 474, 5319
Henkel, C., Greene, J.-E., & Kamali, F. 2018, in IAU Symposium, Vol. 336, Astrophysical Masers: Unlocking the Mysteries of the Universe, ed. A. Tarchi, M. J. Reid, & P. Castangia, 69–79
Hirano, S., Hosokawa, T., Yoshida, N., Omukai, K., & Yorke, H. W. 2015, MNRAS, 448, 568

Hirano, S., Hosokawa, T., Yoshida, N., et al. 2014, ApJ, 781, 60
Hirschmann, M., Dolag, K., Saro, A., et al. 2014, MNRAS, 442, 2304
Ho, L. C., Filippenko, A. V., & Sargent, W. L. W. 1997, ApJS, 112, 315
Ho, L. C., Greene, J. E., Filippenko, A. V., & Sargent, W. L. W. 2009, The Astrophysical Journal Supplement Series, 183, 1
Ho, L. C. & Kim, M. 2014, ApJ, 789, 17
Ho, L. C. & Kim, M. 2015, ApJ, 809, 123
Ho, L. C., Li, Z.-Y., Barth, A. J., Seigar, M. S., & Peng, C. Y. 2011, The Astrophysical Journal Supplement Series, 197, 21
Holtzman, J. A., Burrows, C. J., Casertano, S., et al. 1995, PASP, 107, 1065
Hoormann, J. K., Martini, P., Davis, T. M., et al. 2019
Hopkins, P. F., Bundy, K., Croton, D., et al. 2010, ApJ, 715, 202
Hosokawa, T., Omukai, K., Yoshida, N., & Yorke, H. W. 2011, Science, 334, 1250
Hu, J. 2008, MNRAS, 386, 2242
Huang, K.-W., Feng, Y., & Matteo, T. D. 2019
Huang, S., Ho, L. C., Peng, C. Y., Li, Z.-Y., & Barth, A. J. 2013, The Astrophysical Journal, 766, 47
Hyde, J. B., Bernardi, M., Sheth, R. K., & Nichol, R. C. 2008, MNRAS, 391, 1559
Inayoshi, K. & Haiman, Z. 2014, MNRAS, 445, 1549
Ishibashi, W. & Fabian, A. C. 2012, MNRAS, 427, 2998
Ishibashi, W. & Fabian, A. C. 2014, MNRAS, 441, 1474
Izquierdo-Villalba, D., Bonoli, S., Spinoso, D., et al. 2019
Jaffe, W., Ford, H., Ferrarese, L., van den Bosch, F., & O'Connell, R. W. 1996, ApJ, 460, 214
Jahnke, K. & Macciò, A. V. 2011, ApJ, 734, 92
Jansky, K. G. 1933, Popular Astronomy, 41, 548
Jarrett, T. H., Chester, T., Cutri, R., et al. 2000, AJ, 119, 2498
Jeans, J. H. 1922, MNRAS, 82, 122
Jeter, B., Broderick, A. E., & McNamara, B. R. 2018
Jia, S., Lu, J. R., Sakai, S. ., et al. 2019
Jin, Y., Zhu, L., Long, R. J., et al. 2019, MNRAS
Johnson, J. L., Greif, T. H., & Bromm, V. 2008, MNRAS, 388, 26
Johnson, J. L., Whalen, D. J., Fryer, C. L., & Li, H. 2012, ApJ, 750, 66
Johnston, E. J., Aragón-Salamanca, A., & Merrifield, M. R. 2014, MNRAS, 441, 333
Kalinova, V., van de Ven, G., Lyubenova, M., et al. 2017, MNRAS, 464, 1903
Kanbur, S. M., Ngeow, C., Nikolaev, S., Tanvir, N. R., & Hendry, M. A. 2003, A&A, 411, 361
Kaspi, S., Smith, P. S., Netzer, H., et al. 2000, ApJ, 533, 631
Kauffmann, G. & Charlot, S. 1998, MNRAS, 294, 705
Kauffmann, G. & White, S. D. M. 1993, MNRAS, 261
Khochfar, S., Emsellem, E., Serra, P., et al. 2011, MNRAS, 417, 845
King, A. 2003, ApJ, 596, L27
Kollatschny, W. 2003, A&A, 407, 461
Kormendy, J. 1993, in IAU Symposium, Vol. 153, Galactic Bulges, ed. H. Dejonghe & H. J. Habing, 209
Kormendy, J. & Bender, R. 1996, ApJ, 464, L119
Kormendy, J. & Bender, R. 2009, ApJ, 691, L142
Kormendy, J., Bender, R., & Cornell, M. E. 2011, Nature, 469, 374
Kormendy, J., Drory, N., Bender, R., & Cornell, M. E. 2010
Kormendy, J., Drory, N., Cornell, M. E., & Bender, R. 2007, in Bulletin of the American Astronomical Society, Vol. 39, American Astronomical Society Meeting Abstracts, 860
Kormendy, J. & Fisher, D. B. 2008, Kormendy, J., & Fisher, D. B. Galaxy Disks, ed. J. G. Funes, S. J. & E. M. Corsini (San Francisco: ASP), 297, Kormendy, Galaxy Disks, ed. J. G. Funes, S. J. & E. M. Corsini (San Francisco: ASP), 297, Kormendy,J.,&Fisher,D.B.2008,inFormationandEvolutionof GalaxyDisks,ed.J.G.Funes,S.J.&E.M.Corsini(SanFrancisco:ASP), 297
Kormendy, J., Fisher, D. B., Cornell, M. E., & Bender, R. 2009, ApJS, 182, 216

Kormendy, J. & Gebhardt, K. 2001, in American Institute of Physics Conference Series, Vol. 586, 20th Texas Symposium on relativistic astrophysics, ed. J. C. Wheeler & H. Martel, 363–381
Kormendy, J. & Ho, L. C. 2013, Annu. Rev. Astro. Astrophys., 51, 511
Kormendy, J. & Illingworth, G. 1982, ApJ, 256, 460
Kormendy, J. & Kennicutt, Jr., R. C. 2004, ARA&A, 42, 603
Kormendy, J. & Richstone, D. 1995, Annual Review of Astronomy and Astrophysics, 33, 581
Kotilainen, J. K., León-Tavares, J., Olguín-Iglesias, A., et al. 2016, ApJ, 832, 157
Krajnović, D., Alatalo, K., Blitz, L., et al. 2013, MNRAS, 432, 1768
Krajnović, D., Cappellari, M., de Zeeuw, P. T., & Copin, Y. 2006, MNRAS, 366, 787
Krajnović, D., Cappellari, M., Emsellem, E., McDermid, R. M., & de Zeeuw, P. T. 2005, MNRAS, 357, 1113
Krajnović, D., Cappellari, M., & McDermid, R. M. 2018a, MNRAS, 473, 5237
Krajnović, D., Cappellari, M., McDermid, R. M., et al. 2018b, MNRAS, 477, 3030
Krajnović, D., Emsellem, E., Cappellari, M., et al. 2011, MNRAS, 414, 2923
Krajnović, D., Emsellem, E., den Brok, M., et al. 2018c, MNRAS, 477, 5327
Krajnović, D., McDermid, R. M., Cappellari, M., & Davies, R. L. 2009, MNRAS, 399, 1839
Krist, J. & Hook, R. 2001, The Tiny Tim User's Manual, version 6.3
Kroupa, P. 2001, MNRAS, 322, 231
Kulier, A., Ostriker, J. P., Natarajan, P., Lackner, C. N., & Cen, R. 2015, ApJ, 799, 178
Kuntschner, H., Emsellem, E., Bacon, R., et al. 2010, MNRAS, 408, 97
Kuo, C. Y., Braatz, J. A., Condon, J. J., et al. 2011, ApJ, 727, 20
Lablanche, P.-Y., Cappellari, M., Emsellem, E., et al. 2012, MNRAS, 424, 1495
Lacey, C. & Cole, S. 1994, MNRAS, 271, 676
Lagerholm, C., Kuntschner, H., Cappellari, M., et al. 2012, Astronomy & Astrophysics, 541, A82
Lagos, C. D. P., Cora, S. A., & Padilla, N. D. 2008, MNRAS, 388, 587
Laine, S., van der Marel, R. P., Lauer, T. R., et al. 2003, AJ, 125, 478
Läsker, R., Ferrarese, L., van de Ven, G., & Shankar, F. 2014, ApJ, 780, 70
Latif, M. A. & Ferrara, A. 2016, Publications of the Astronomical Society of Australia, 33
Latif, M. A., Schleicher, D. R. G., Schmidt, W., & Niemeyer, J. 2013, ApJ, 772, L3
Lauer, T. R. 1985, ApJ, 292, 104
Lauer, T. R., Ajhar, E. A., Byun, Y.-I., et al. 1995, AJ, 110, 2622
Lauer, T. R., Faber, S. M., Gebhardt, K., et al. 2005, AJ, 129, 2138
Lauer, T. R., Faber, S. M., Richstone, D., et al. 2007, ApJ, 662, 808
Laurikainen, E., Salo, H., Buta, R., Knapen, J. H., & Comerón, S. 2010, MNRAS, 405, 1089
Lawson, C. L. & Hanson, R. J. 1974, Solving least squares problems
Le Fèvre, O., Saisse, M., Mancini, D., et al. 2003, in Proceedings of the SPIE, Vol. 4841, Instrument Design and Performance for Optical/Infrared Ground-based Telescopes, ed. M. Iye & A. F. M. Moorwood, 1670–1681
Lee, M. G., Park, H. S., Hwang, H. S., et al. 2010, ApJ, 709, 1083
Lelli, F., McGaugh, S. S., Schombert, J. M., & Pawlowski, M. S. 2017, ApJ, 836, 152
Leung, G. Y. C., Leaman, R., van de Ven, G., et al. 2018, MNRAS, 477, 254
Li, H., Li, R., Mao, S., et al. 2016, MNRAS, 455, 3680
Li, L.-X. 2012, MNRAS, 424, 1461
Li, Z., Sellwood, J. A., & Shen, J. 2017a, ApJ, 850, 67
Li, Z.-Y., Ho, L. C., & Barth, A. J. 2017b, ApJ, 845, 87
Li, Z.-Y., Ho, L. C., Barth, A. J., & Peng, C. Y. 2011, The Astrophysical Journal Supplement Series, 197, 22
LIGO Scientific Collaboration, null the Virgo Collaboration, Abbott, B. P., et al. 2018
Livingston, W. & Wallace, L. 1991, An atlas of the solar spectrum in the infrared from 1850 to 9000 cm-1 (1.1 to 5.4 micrometer)
Lodato, G. & Natarajan, P. 2006, MNRAS, 371, 1813
Loeb, A. & Rasio, F. A. 1994, ApJ, 432, 52

Loewenstein, M. & Mushotzky, R. 2003, Nuclear Physics B Proceedings Supplements, 124, 91
López-Cruz, O., Añorve, C., Birkinshaw, M., et al. 2014, ApJ, 795, L31
Lynden-Bell, D. 1969, Nature, 223, 690
Lynden-Bell, D. & Rees, M. J. 1971, MNRAS, 152, 461
Ma, C.-P., Greene, J. E., McConnell, N., et al. 2014, ApJ, 795, 158
Madau, P., Haardt, F., & Dotti, M. 2014, ApJ, 784, L38
Madore, B. F., Freedman, W. L., & Bothun, G. D. 2004, ApJ, 607, 810
Magorrian, J. 2019, MNRAS, 484, 1166
Magorrian, J., Tremaine, S., Richstone, D., et al. 1998, AJ, 115, 2285
Malin, D. F. & Carter, D. 1983, ApJ, 274, 534
Maoz, D. 2007, MNRAS, 377, 1696
Marconi, A. & Hunt, L. K. 2003, ApJ, 589, L21
Marian, V., Jahnke, K., Mechtley, M., et al. 2019
Martin, G., Kaviraj, S., Volonteri, M., et al. 2018, MNRAS, 476, 2801
Martín-Navarro, I., Brodie, J. P., Romanowsky, A. J., Ruiz-Lara, T., & van de Ven, G. 2018, Nature, 553, 307
Martín-Navarro, I., Vazdekis, A., La Barbera, F., et al. 2015, ApJ, 806, L31
Martínez, A. F. O. & Andernach, H. 2016
Martizzi, D., Teyssier, R., & Moore, B. 2012, MNRAS, 420, 2859
Matsuoka, Y., Onoue, M., Kashikawa, N., et al. 2019, ApJ, 872, L2
Mazzalay, X., Maciejewski, W., Erwin, P., et al. 2014, MNRAS, 438, 2036
Mazzalay, X., Thomas, J., Saglia, R. P., et al. 2016, MNRAS, 462, 2847
McConnell, N. J., Chen, S.-F. S., Ma, C.-P., et al. 2013, ApJ, 768, L21
McConnell, N. J. & Ma, C.-P. 2013, ApJ, 764, 184
McDermid, R. M., Alatalo, K., Blitz, L., et al. 2015, MNRAS, 448, 3484
McDermid, R. M., Emsellem, E., Shapiro, K. L., et al. 2006, MNRAS, 373, 906
McGaugh, S. S., Lelli, F., & Schombert, J. M. 2016, Physical Review Letters, 117, 201101
McGregor, P. J., Conroy, P., Bloxham, G., & van Harmelen, J. 1999, Publ. Astron. Soc. Aust, 16, 273âĂŞ287
McGregor, P. J., Hart, J., Conroy, P. G., et al. 2003, in Proceedings of the SPIE, Vol. 4841, Instrument Design and Performance for Optical/Infrared Ground-based Telescopes, ed. M. Iye & A. F. M. Moorwood, 1581–1591
McLure, R. J., Willott, C. J., Jarvis, M. J., et al. 2004, MNRAS, 351, 347
McMullin, J. P., Waters, B., Schiebel, D., Young, W., & Golap, K. 2007, in Astronomical Society of the Pacific Conference Series, Vol. 376, Astronomical Data Analysis Software and Systems XVI, ed. R. A. Shaw, F. Hill, & D. J. Bell, 127
McNamara, B. R. & Nulsen, P. E. J. 2012, New Journal of Physics, 14, 055023
Mechtley, M., Jahnke, K., Windhorst, R. A., et al. 2016, ApJ, 830, 156
Mejía-Restrepo, J. E., Trakhtenbrot, B., Lira, P., Netzer, H., & Capellupo, D. M. 2016, MNRAS, 460, 187
Melia, F. & McClintock, T. M. 2015, Proceedings of the Royal Society of London Series A, 471, 20150449
Merritt, D., Ferrarese, L., & Joseph, C. L. 2001, Science, 293, 1116
Merritt, D., Mikkola, S., & Szell, A. 2007, ApJ, 671, 53
Metzroth, K. G., Onken, C. A., & Peterson, B. M. 2006, ApJ, 647, 901
Mezcua, M. 2017, International Journal of Modern Physics D, 26, 1730021
Mezcua, M., Hlavacek-Larrondo, J., Lucey, J. R., et al. 2018, MNRAS, 474, 1342
Milosavljević, M., Merritt, D., Rest, A., & van den Bosch, F. C. 2002, MNRAS, 331, L51
Mitzkus, M., Cappellari, M., & Walcher, C. J. 2016, Monthly Notices of the Royal Astronomical Society, 464, 4789
Miyoshi, M., Moran, J., Herrnstein, J., et al. 1995, Nature, 373, 127
Modigliani, A., Hummel, W., Abuter, R., et al. 2007, arXiv e-prints, astro

Momjian, E., Carilli, C. L., Walter, F., & Venemans, B. 2014, AJ, 147, 6
Monnet, G., Bacon, R., & Emsellem, E. 1992, A&A, 253, 366
Morabito, L. K. & Dai, X. 2012, ApJ, 757, 172
Morsony, B. J., Gracey, B. T., Workman, J. C., & Yoon, D. 2017, ApJ, 843, 29
Mortlock, D. J., Warren, S. J., Venemans, B. P., et al. 2011, Nature, 474, 616
Naab, T., Oser, L., Emsellem, E., et al. 2014, MNRAS, 444, 3357
Naab, T. & Ostriker, J. P. 2017, ARA&A, 55, 59
Naab, T. & Trujillo, I. 2006, MNRAS, 369, 625
Nagai, H., Onishi, K., Kawakatu, N., et al. 2019
Napolitano, N. R., Romanowsky, A. J., & Tortora, C. 2010, MNRAS, 405, 2351
Natarajan, P. 2014, General Relativity and Gravitation, 46, 1702
Natarajan, P., Ricarte, A., Baldassare, V., et al. 2019
Navarro, J. F., Frenk, C. S., & White, S. D. M. 1996, ApJ, 462, 563
Navarro, J. F., Frenk, C. S., & White, S. D. M. 1997, ApJ, 490, 493
Netzer, H. 2015, ARA&A, 53, 365
Netzer, H., Lira, P., Trakhtenbrot, B., Shemmer, O., & Cury, I. 2007, ApJ, 671, 1256
Netzer, H. & Peterson, B. M. 1997, in Astrophysics and Space Science Library, Vol. 218, Astronomical Time Series, ed. D. Maoz, A. Sternberg, & E. M. Leibowitz, 85
Neumann, J., Wisotzki, L., Choudhury, O. S., et al. 2017, A&A, 604, A30
Neumayer, N., Cappellari, M., Reunanen, J., et al. 2007, The Astrophysical Journal, 671, 1329âĂŞ1344
Nguyen, D. D., den Brok, M., Seth, A. C., et al. 2019
Nguyen, D. D., Seth, A. C., Neumayer, N., et al. 2018, ApJ, 858, 118
Noel-Storr, J., Baum, S. A., & O'Dea, C. P. 2007, ApJ, 663, 71
Noel-Storr, J., Baum, S. A., Verdoes Kleijn, G., et al. 2003, ApJS, 148, 419
Nowak, N., Saglia, R. P., Thomas, J., et al. 2008, MNRAS, 391, 1629
Ollongren, A. 1962, , 16, 241
Omukai, K., Schneider, R., & Haiman, Z. 2008, ApJ, 686, 801
Onishi, K., Iguchi, S., Davis, T. A., et al. 2017, MNRAS, 468, 4663
Onishi, K., Iguchi, S., Sheth, K., & Kohno, K. 2015, ApJ, 806, 39
Onken, C. A., Ferrarese, L., Merritt, D., et al. 2004, ApJ, 615, 645
Onken, C. A. & Kollmeier, J. A. 2008, ApJ, 689, L13
Onken, C. A. & Peterson, B. M. 2002, ApJ, 572, 746
Onken, C. A., Valluri, M., Brown, J. S., et al. 2014, ApJ, 791, 37
Osipkov, L. P. 1979, Soviet Astronomy Letters, 5, 42
Pacucci, F., Baldassare, V., Cappelluti, N., et al. 2019
Pacucci, F., Natarajan, P., Volonteri, M., Cappelluti, N., & Urry, C. M. 2017, ApJ, 850, L42
Pacucci, F., Volonteri, M., & Ferrara, A. 2015, MNRAS, 452, 1922
Padovani, P., Alexander, D. M., Assef, R. J., et al. 2017, A&ARv, 25, 2
Park, D., Kelly, B. C., Woo, J.-H., & Treu, T. 2012, ApJS, 203, 6
Park, D., Woo, J.-H., Denney, K. D., & Shin, J. 2013, ApJ, 770, 87
Pastorini, G., Marconi, A., Capetti, A., et al. 2007, A&A, 469, 405
Paturel, G., Theureau, G., Fouqué, P., et al. 2002, A&A, 383, 398
Peebles, P. J. E. 1972, ApJ, 178, 371
Peletier, R. F., Valentijn, E. A., & Jameson, R. F. 1990, A&A, 233, 62
Peng, C. Y. 2007, ApJ, 671, 1098
Penoyre, Z., Moster, B. P., Sijacki, D., & Genel, S. 2017, MNRAS, 468, 3883
Pesce, D. W., Braatz, J. A., Condon, J. J., & Greene, J. E. 2018, ApJ, 863, 149
Peterson, B. M. & Wandel, A. 1999, ApJ, 521, L95
Peterson, B. M. & Wandel, A. 2000, ApJ, 540, L13
Petts, J. A., Gualandris, A., & Read, J. I. 2015, MNRAS, 454, 3778
Pezzulli, E., Valiante, R., & Schneider, R. 2016, MNRAS, 458, 3047
Pillepich, A., Springel, V., Nelson, D., et al. 2018, MNRAS, 473, 4077

Planck Collaboration, Aghanim, N., Akrami, Y., et al. 2018
Poci, A., Cappellari, M., & McDermid, R. M. 2016, MNRAS, 467:, 1397,2017
Portegies Zwart, S. F., Baumgardt, H., Hut, P., Makino, J., & McMillan, S. L. W. 2004, Nature, 428, 724
Portegies Zwart, S. F., Makino, J., McMillan, S. L. W., & Hut, P. 1999, A&A, 348, 117
Portinari, L. & Salucci, P. 2010, A&A, 521, A82
Posacki, S., Cappellari, M., Treu, T., Pellegrini, S., & Ciotti, L. 2015, MNRAS, 446, 493
Postman, M., Lauer, T. R., Donahue, M., et al. 2012, ApJ, 756, 159
Press, W. H. 2007, Numerical recipes : the art of scientific computing, 3rd edn. (Cambridge University Press)
Prieur, J.-L. 1988, ApJ, 326, 596
Prugniel, P., Nieto, J. L., Bender, R., & Davoust, E. 1988, A&A, 204, 61
Qian, E. E., de Zeeuw, P. T., van der Marel, R. P., & Hunter, C. 1995, MNRAS, 274, 602
Rantala, A., Johansson, P. H., Naab, T., Thomas, J., & Frigo, M. 2018, ApJ, 864, 113
Rantala, A., Johansson, P. H., Naab, T., Thomas, J., & Frigo, M. 2019, ApJ, 872, L17
Ravindranath, S., Ho, L. C., & Filippenko, A. V. 2002, ApJ, 566, 801
Rawle, T. D., Smith, R. J., Lucey, J. R., & Swinbank, A. M. 2008, MNRAS, 389, 1891
Rees, M. J. 1978, The Observatory, 98, 210
Reid, M. J., Braatz, J. A., Condon, J. J., et al. 2009a, ApJ, 695, 287
Reid, M. J., Menten, K. M., Zheng, X. W., Brunthaler, A., & Xu, Y. 2009b, ApJ, 705, 1548
Reines, A. E. & Comastri, A. 2016, , 33, e054
Reines, A. E., Greene, J. E., & Geha, M. 2013, The Astrophysical Journal, 775, 116
Reines, A. E., Sivakoff, G. R., Johnson, K. E., & Brogan, C. L. 2011, Nature, 470, 66âĂŞ68
Reines, A. E. & Volonteri, M. 2015, ApJ, 813, 82
Rest, A., van den Bosch, F. C., Jaffe, W., et al. 2001, AJ, 121, 2431
Ricci, F., La Franca, F., Marconi, A., et al. 2017, MNRAS, 471, L41
Richstone, D. O. 1982, ApJ, 252, 496
Richstone, D. O. & Tremaine, S. 1988, ApJ, 327, 82
Rix, H.-W., de Zeeuw, P. T., Cretton, N., van der Marel, R. P., & Carollo, C. M. 1997, ApJ, 488, 702
Roberts, C. A., Bentz, M., Valluri, M., et al. 2019, in American Astronomical Society Meeting Abstracts, Vol. 233, American Astronomical Society Meeting Abstracts #233, 330.02
Rusli, S. P., Erwin, P., Saglia, R. P., et al. 2013a, AJ, 146, 160
Rusli, S. P., Thomas, J., Saglia, R. P., et al. 2013b, AJ, 146, 45
Rybicki, G. B. 1987, in IAU Symposium, Vol. 127, Structure and Dynamics of Elliptical Galaxies, ed. P. T. de Zeeuw, 397
Saglia, R. P., Bertin, G., Bertola, F., et al. 1993, ApJ, 403, 567
Saglia, R. P., Opitsch, M., Erwin, P., et al. 2016, ApJ, 818, 47
Sahu, N., Graham, A. W., & Davis, B. L. 2019
Sakurai, Y., Yoshida, N., & Fujii, M. S. 2019, MNRAS, 484, 4665
Sakurai, Y., Yoshida, N., Fujii, M. S., & Hirano, S. 2017, MNRAS, 472, 1677
Salpeter, E. E. 1955, ApJ, 121, 161
Sánchez, S. F., Kennicutt, R. C., Gil de Paz, A., et al. 2012, A&A, 538, A8
Sánchez-Blázquez, P., Peletier, R. F., Jiménez-Vicente, J., et al. 2006, MNRAS, 371, 703
Sandage, A. & Bedke, J. 1994, The Carnegie Atlas of Galaxies. Volumes I, II.
Sani, E., Marconi, A., Hunt, L. K., & Risaliti, G. 2011, MNRAS, 413, 1479
Saraiva, M. F., Bica, E., Pastoriza, M. G., & Bonatto, C. 2001, A&A, 376, 43
Saraiva, M. F., Ferrari, F., & Pastoriza, M. G. 1999, A&A, 350, 399
Sargent, W. L. W., Young, P. J., Boksenberg, A., et al. 1978, ApJ, 221, 731
Sarzi, M., Falcón-Barroso, J., Davies, R. L., et al. 2006, MNRAS, 366, 1151
Sarzi, M., Rix, H.-W., Shields, J. C., et al. 2001, ApJ, 550, 65
Sarzi, M., Spiniello, C., La Barbera, F., Krajnović, D., & van den Bosch, R. 2018, MNRAS, 478, 4084
Savorgnan, G., Graham, A. W., Marconi, A., et al. 2013, MNRAS, 434, 387
Savorgnan, G. A. D. & Graham, A. W. 2015, MNRAS, 446, 2330

Savorgnan, G. A. D., Graham, A. W., Marconi, A., & Sani, E. 2016, ApJ, 817, 21
Scharwächter, J., Combes, F., Salomé, P., Sun, M., & Krips, M. 2016, MNRAS, 457, 4272
Schaye, J., Crain, R. A., Bower, R. G., et al. 2015, MNRAS, 446, 521
Schlafly, E. F. & Finkbeiner, D. P. 2011, ApJ, 737, 103
Schleicher, D. R. G., Fellhauer, M. A., Boekholt, T., et al. 2018
Schuberth, Y., Richtler, T., Dirsch, B., et al. 2006, A&A, 459, 391
Schulze, A. & Gebhardt, K. 2011, ApJ, 729, 21
Schulze, A. & Wisotzki, L. 2011, A&A, 535, A87
Schulze, F., Remus, R.-S., Dolag, K., et al. 2018, MNRAS, 480, 4636
Schwarzschild, M. 1979, ApJ, 232, 236
Scott, N., Cappellari, M., Davies, R. L., et al. 2013a, MNRAS, 432, 1894
Scott, N., Graham, A. W., & Schombert, J. 2013b, ApJ, 768, 76
Seigar, M. S., Kennefick, D., Kennefick, J., & Lacy, C. H. S. 2008, ApJ, 678, L93
Seth, A., Agüeros, M., Lee, D., & Basu-Zych, A. 2008, ApJ, 678, 116
Seth, A. C., van den Bosch, R., Mieske, S., et al. 2014, Nature, 513, 398
Sexton, R. O., Canalizo, G., Hiner, K. D., et al. 2019
Shankar, F., Bernardi, M., Richardson, K., et al. 2019, MNRAS, 485, 1278
Shankar, F., Bernardi, M., & Sheth, R. K. 2017, MNRAS, 466, 4029
Shankar, F., Bernardi, M., Sheth, R. K., et al. 2016, MNRAS
Shapiro, K. L., Cappellari, M., de Zeeuw, T., et al. 2006, MNRAS, 370, 559
Sheinis, A. I. & López-Sánchez, Á. R. 2017, AJ, 153, 55
Shen, J. & Gebhardt, K. 2010, ApJ, 711, 484
Shen, J. & Sellwood, J. A. 2004, ApJ, 604, 614
Shen, Y. 2013
Shen, Y., Horne, K., Grier, C. J., et al. 2016, ApJ, 818, 30
Shetty, S. & Cappellari, M. 2015, MNRAS, 454, 1332
Shlosman, I., Frank, J., & Begelman, M. C. 1989, Nature, 338, 45
Sijacki, D., Springel, V., Di Matteo, T., & Hernquist, L. 2007, MNRAS, 380, 877
Silk, J. 2013, ApJ, 772, 112
Silk, J. & Rees, M. J. 1998, A&A, 331, L1
Silva, D. R., Kuntschner, H., & Lyubenova, M. 2008, ApJ, 674, 194
Simmons, B. D., Lintott, C., Schawinski, K., et al. 2012
Simmons, B. D., Smethurst, R. J., & Lintott, C. 2017
Singh, V., Ishwara-Chandra, C. H., Sievers, J., et al. 2015, MNRAS, 454, 1556
Skrutskie, M. F., Cutri, R. M., Stiening, R., et al. 2006, AJ, 131, 1163
Slater, R., Nagar, N. M., Schnorr-Müller, A., et al. 2019, A&A, 621, A83
Slavcheva-Mihova, L. & Mihov, B. 2011, A&A, 526, A43
Smajić, S., Moser, L., Eckart, A., et al. 2015, A&A, 583, A104
Smethurst, R. J., Masters, K. L., Lintott, C. J., et al. 2018, MNRAS, 473, 2679
Smith, M. D., Bureau, M., Davis, T. A., et al. 2019, MNRAS
Smole, M., Micic, M., & Martinović, N. 2015, MNRAS, 451, 1964
Somerville, R. S. & Davé, R. 2015, ARA&A, 53, 51
Springel, V., Di Matteo, T., & Hernquist, L. 2005, MNRAS, 361, 776
Stacy, A., Bromm, V., & Lee, A. T. 2016, MNRAS, 462, 1307
Stone, N. C., Küpper, A. H. W., & Ostriker, J. P. 2017, MNRAS, 467, 4180
Susa, H., Hasegawa, K., & Tominaga, N. 2014, ApJ, 792, 32
Tacchella, S., Diemer, B., Hernquist, L., et al. 2019
Takeo, E., Inayoshi, K., Ohsuga, K., Takahashi, H. R., & Mineshige, S. 2019
Temi, P., Mathews, W. G., Brighenti, F., & Bregman, J. D. 2003, ApJ, 585, L121
Tenneti, A., Wilkins, S. M., Di Matteo, T., Croft, R. A. C., & Feng, Y. 2019, MNRAS, 483, 1388
Terrazas, B. A., Bell, E. F., Woo, J., & Henriques, B. M. B. 2017, ApJ, 844, 170

Thater, S., Krajnović, D., Bourne, M. A., et al. 2017, A&A, 597, A18
Thatte, D. 2009, NICMOS Data Handbook v. 8.0
Thomas, J., Ma, C.-P., McConnell, N. J., et al. 2016, Nature, 532, 340
Thomas, J., Saglia, R. P., Bender, R., Erwin, P., & Fabricius, M. 2014, ApJ, 782, 39
Thomas, J., Saglia, R. P., Bender, R., et al. 2011, MNRAS, 415, 545
Thomas, N., Davé, R., Anglés-Alcázar, D., & Jarvis, M. 2019
Tonini, C., Mutch, S. J., Croton, D. J., & Wyithe, J. S. B. 2016, MNRAS, 459, 4109
Toomre, A. 1977, in Evolution of Galaxies and Stellar Populations, ed. B. M. Tinsley & R. B. G. Larson, D. Campbell, 401
Toomre, A. & Toomre, J. 1972, ApJ, 178, 623
Tortora, C., La Barbera, F., Napolitano, N. R., de Carvalho, R. R., & Romanowsky, A. J. 2012, MNRAS, 425, 577
Tremaine, S., Gebhardt, K., Bender, R., et al. 2002, ApJ, 574, 740
Tsatsi, A., Lyubenova, M., van de Ven, G., et al. 2017, A&A, 606, A62
Tundo, E., Bernardi, M., Hyde, J. B., Sheth, R. K., & Pizzella, A. 2007, ApJ, 663, 53
Turk, M. J., Abel, T., & O'Shea, B. 2009, Science, 325, 601
Urry, C. M. & Padovani, P. 1995, PASP, 107, 803
Valdes, F., Gupta, R., Rose, J. A., Singh, H. P., & Bell, D. J. 2004, ApJS, 152, 251
Valiante, R., Schneider, R., Volonteri, M., & Omukai, K. 2016, MNRAS, 457, 3356
Vallejo, O., Braine, J., & Baudry, A. 2002, A&A, 387, 429
Vallejo, O., Braine, J., & Baudry, A. 2003, Ap&SS, 284, 715
Valluri, M., Ferrarese, L., Merritt, D., & Joseph, C. L. 2005, ApJ, 628, 137
Valluri, M., Shen, J., Abbott, C., & Debattista, V. P. 2016, ApJ, 818, 141
Valluri, M., Vasiliev, E., Bentz, M., & Shen, J. 2018, in AAS/Division of Dynamical Astronomy Meeting, Vol. 49, AAS/Division of Dynamical Astronomy Meeting, 303.01
van den Bosch, F. C., Jaffe, W., & van der Marel, R. P. 1998, MNRAS, 293, 343
van den Bosch, R. C. E. 2016, The Astrophysical Journal, 831, 134
van den Bosch, R. C. E. & de Zeeuw, P. T. 2010, MNRAS, 401, 1770
van den Bosch, R. C. E., Gebhardt, K., Gültekin, K., et al. 2012, Nature, 491, 729
van den Bosch, R. C. E., Gebhardt, K., Gültekin, K., Yıldırım, A., & Walsh, J. L. 2015, ApJS, 218, 10
van den Bosch, R. C. E., Greene, J. E., Braatz, J. A., Constantin, A., & Kuo, C.-Y. 2016
van den Bosch, R. C. E., van de Ven, G., Verolme, E. K., Cappellari, M., & de Zeeuw, P. T. 2008, MNRAS, 385, 647
van der Marel, R. P., Cretton, N., de Zeeuw, P. T., & Rix, H.-W. 1998, ApJ, 493, 613
van der Marel, R. P. & Franx, M. 1993, ApJ, 407, 525
Vaughan, S. P., Davies, R. L., Zieleniewski, S., & Houghton, R. C. W. 2018, MNRAS, 479, 2443
Vazdekis, A., Sánchez-Blázquez, P., Falcón-Barroso, J., et al. 2010, MNRAS, 404, 1639
Veale, M., Ma, C.-P., Greene, J. E., et al. 2017, MNRAS, 471, 1428
Venemans, B. P., Walter, F., Decarli, R., et al. 2017, ApJ, 851, L8
Verdoes Kleijn, G. A., van der Marel, R. P., de Zeeuw, P. T., Noel-Storr, J., & Baum, S. A. 2002, AJ, 124, 2524
Verdoes Kleijn, G. A., van der Marel, R. P., & Noel-Storr, J. 2006, AJ, 131, 1961
Vestergaard, M. 2002, ApJ, 571, 733
Vestergaard, M. & Peterson, B. M. 2006, ApJ, 641, 689
Villarroel, B., Nyholm, A., Karlsson, T., et al. 2017, ApJ, 837, 110
Villforth, C., Herbst, H., Hamann, F., et al. 2019, MNRAS, 483, 2441
Vittorini, V., Shankar, F., & Cavaliere, A. 2005, MNRAS, 363, 1376
Vogelsberger, M., Genel, S., Springel, V., et al. 2014, MNRAS, 444, 1518
Voggel, K. T., Seth, A. C., Neumayer, N., et al. 2018, ApJ, 858, 20
Volonteri, M. 2010, The Astronomy and Astrophysics Review, 18, 279âĂŞ315
Volonteri, M. 2012, Science, 337, 544
Volonteri, M., Dubois, Y., Pichon, C., & Devriendt, J. 2016, MNRAS, 460, 2979

Volonteri, M. & Rees, M. J. 2005, ApJ, 633, 624
Volonteri, M., Silk, J., & Dubus, G. 2015, ApJ, 804, 148
Wagner, S. J., Bender, R., & Moellenhoff, C. 1988, A&A, 195, L5
Walsh, J. L., Barth, A. J., Ho, L. C., & Sarzi, M. 2013, ApJ, 770, 86
Walsh, J. L., Barth, A. J., & Sarzi, M. 2010, ApJ, 721, 762
Walsh, J. L., van den Bosch, R. C. E., Barth, A. J., & Sarzi, M. 2012, ApJ, 753, 79
Walsh, J. L., van den Bosch, R. C. E., Gebhardt, K., et al. 2015, ApJ, 808, 183
Walsh, J. L., van den Bosch, R. C. E., Gebhardt, K., et al. 2016, ApJ, 817, 2
Wandel, A., Peterson, B. M., & Malkan, M. A. 1999, ApJ, 526, 579
Watkins, L. L., van de Ven, G., den Brok, M., & van den Bosch, R. C. E. 2013, MNRAS, 436, 2598
Wehner, E. H. & Harris, W. E. 2006, ApJ, 644, L17
Weilbacher, P. M., Streicher, O., Urrutia, T., et al. 2015, 485, p. 451, 2014, ADASSXXIII.MansetandForshay(eds.),ASPconf.ser.,vol.
Weinberger, R., Springel, V., Pakmor, R., et al. 2018, MNRAS, 479, 4056
White, S. D. M. 1979, ApJ, 229, L9
White, S. D. M. & Rees, M. J. 1978, MNRAS, 183, 341
Wild, V., Heckman, T., & Charlot, S. 2010, MNRAS, 405, 933
Willmer, C. N. A. 2018, ApJS, 236, 47
Willott, C. J., Albert, L., Arzoumanian, D., et al. 2010, AJ, 140, 546
Willott, C. J., Delorme, P., Omont, A., et al. 2007, AJ, 134, 2435
Winge, C., Riffel, R. A., & Storchi-Bergmann, T. 2009, ApJS, 185, 186
Wong, T., Blitz, L., & Bosma, A. 2004, ApJ, 605, 183
Woo, J.-H., Schulze, A., Park, D., et al. 2013, ApJ, 772, 49
Woo, J.-H., Treu, T., Barth, A. J., et al. 2010, ApJ, 716, 269
Woo, J.-H., Yoon, Y., Park, S., Park, D., & Kim, S. C. 2015, ApJ, 801, 38
Woods, T. E., Agarwal, B., Bromm, V., et al. 2018
Wu, H., Shao, Z., Mo, H. J., Xia, X., & Deng, Z. 2005, ApJ, 622, 244
Yajima, H. & Khochfar, S. 2016, MNRAS, 457, 2423
Yang, X.-H. & Bu, D.-F. 2018, MNRAS, 476, 954
Yong, S. Y., Webster, R. L., & King, A. L. 2016, , 33, e009
Yoo, J., Miralda-Escudé, J., Weinberg, D. H., Zheng, Z., & Morgan, C. W. 2007, ApJ, 667, 813
Yoon, I. 2017, MNRAS, 466, 1987
York, D. G., Adelman, J., Anderson, Jr., J. E., et al. 2000, AJ, 120, 1579
Young, J. S., Xie, S., Tacconi, L., et al. 1995, ApJS, 98, 219
Young, L. M., Bureau, M., Davis, T. A., et al. 2011, MNRAS, 414, 940
Young, P. J., Westphal, J. A., Kristian, J., Wilson, C. P., & Landauer, F. P. 1978, ApJ, 221, 721
Zhang, W., Woosley, S. E., & Heger, A. 2008, ApJ, 679, 639
Zhao, W., Braatz, J. A., Condon, J. J., et al. 2018, ApJ, 854, 124
Zoghbi, A., Wilkins, D. R., Brenneman, L., et al. 2019
Zubovas, K. 2017
Zubovas, K. & King, A. R. 2012, MNRAS, 426, 2751
Zubovas, K. & King, A. R. 2019, General Relativity and Gravitation, 51, 65

# Publications

## Refereed publications

1. *A low upper mass limit for the central black hole in the late-type galaxy NGC 4414*
   **Thater, S.**, Krajnović, D., Bourne, M.A., Cappellari, M., de Zeeuw, T., Emsellem, E., Magorrian, J., McDermid, R.M., Sarzi, M., van de Ven, G.
   Astronomy & Astrophysics (2017), 597, A18

2. *A quartet of black holes and a missing duo: probing the low-end of the $M_{BH}$ - $\sigma$ relation with the adaptive optics assisted integral field spectroscopy*
   Krajnović, D., Cappellari, M., McDermid, R.M., **Thater, S.**, Nyland, K., de Zeeuw, T., Falcón-Barroso, J., Khochfar, S., Kuntschner, H., Sarzi, M., Young, L.M.
   Monthly Notices of the Astronomical Royal Society (2018), 477, 2670

3. *Six new supermassive black hole mass determinations from adaptive-optics assisted SINFONI observations*
   **Thater, S.**, Krajnović, D., Cappellari, M., Davis, T.A., de Zeeuw, P.T., McDermid, R.M., Sarzi, M.
   Astronomy & Astrophysics (2019), 625, A62

## Submitted articles and articles in preparation

4. *The MSSM4 Project - I: Dynamical measurement of the central black hole mass in NGC 3504 using molecular gas kinematics*
   Nguyen, D.D., den Brok, M., Seth, A.C., Iguchi, S., Greene, J., Davis, T., Imanishi, M., Izumi, T., Cappellari, M., Neumayer, N., Nyland, Tsukui, T., Nakanishi, K., Ngyuen, P.M., Nguyen Q.L., **Thater, S.,** Bureau, M., Onishi, K., Voggel, K.T., Dinh, T.V.
   Astrophysical Journal (2019), arXiv:1707.04554, submitted

5. *Testing the robustness of black hole mass measurements with ALMA and MUSE*
   **Thater, S.** et al.
   (2019), in preparation

6. *Probing the high-mass end of super- massive black holes with adaptive-optics assisted SINFONI observations*
   **Thater, S.** et al.
   (2020), in preparation

## Additional publications

7. *Doctoral Researchers in the Leibniz Association: Final Report of the 2017 Leibniz PhD Survey*
   Arcudi, A., Cumurovic, A., Gotter, C., Graeber, D., Philippe, J., Ott, V., Schanze, J.-L., **Thater, S.**, Weltin, M., Yenikent, S.
   Online: https://www.ssoar.info/ssoar/handle/document/61363

# Aknowledgement

There could not be a more exciting time to study supermassive black holes than now. During the time of my PhD, the first gravitational waves were detected and the first image of a supermassive black hole could be taken. Both confirming general relativity and the presumable existence of supermassive black holes. The two discoverys had a large impact on social media and many public channels, such that even in my leisure time, I was drawn ('gravitationally pulled') towards black holes. Indeed, they are simply fascinating.

Writing a PhD thesis is a not a simple walk and would not be successful without the support of many people.

First and foremost, I would like to thank my supervisor and mentor Davor Krajnović for your guidance, support, patience and encouragement over the last four years, and also before starting my PhD already. I can just repeat again and again: Thank you for being available whenever I needed your help, reading my written output at 11 pm but also at 6 am, such that I could just meet my deadlines. Thank you for everything!

I also want to thank Lutz Wisotzki for introducing me into the field of Extragalactic Astrophysics from early on and making me be a member of your wonderful working group. I also want to thank the other members of my thesis commitee: Philipp Richter and Karl Gebhardt.

A special thanks goes to the ALMA people who made my dream to visit and research in Japan come true. Most of all Satoru Iguchi for hosting and advising me on ALMA, interferometry and Japanese. It was a great pleasure to work with you. I want to thank Andreas Schulze and Timothy A. Davis (and of course Davor) for the preparatory work, finding a suitable advisor, finding a good project and so on. The stay would have been impossible without you. Kyoko Onishi deserves a special thanks for hosting me in Matsuyama for half a week and inviting me for the best Japanese food, while discussing black holes! Could there be anything better?

I also want to thank Jonelle Walsh for giving me the exciting opportunity to visit Texas and observe NIFSLP galaxies with the Harlan J. Smith Telescope. These were probably some of the best and most exciting nights in my life. In that respect, I also want to thank Aaron Barth for hosting me at the University of California for half a week.

During the last four years, I have met many wonderful and inspiring people. Probably the most important (and I bet you knew already that I would put you first ;D) Rikke Lund Saust. The best traveling, swimming (even in the cold Danish water), singing, cycling and everything mate. Thank you for just always being there and doing crazy stuff together! I also want to thank Engin, Thomas and Iris for always having our obligatory "Kakao" together and preventing me from getting too stressed.

I also want to thank all my friends and colleagues from AIP. Thank you Man I, Justus, Josie, Kris, Ilaria, Khadiga, Sanja, Anika, Yohana and just everyone! From NAOJ, thank you Andrea, Dieu, Takafumi, Tako, Sai-san, Otaku-san and everyone else.

The dynamical mass measurement of supermassive black holes requires a large amount of various different data sets (both ground- and space-based), large amounts of computational power to derive sufficient dynamical models and last but not least time. Between the first plans of this project, proposal writing an data acquisition, more than 10 years have passed by. I want to thank all the members of the ATLAS$^{3D}$ team and especially Michele Cappellari, Tim de Zeeuw, Richard Dermid, Marc Sarzi and Glenn van de Ven. It was a pleasure to work with you!

I also want to thank the members of the IT team of AIP and NAOJ, in particular Karl Heinz. Research would be impossible without you!

From time to time, one indeed needs to escape from the exciting scientific life. I want to thank my dear friends for always being there when I need you: Jens, Benni, Torben, Svenja, Fabian, Philipp, Berna, Ursula, Sascha, Anna, Annie, Elena and everyone else whom I forgot to mention ("sorry"). Thank you so much!

I am especially grateful for the unlimited support of my family. Thank you for believing in me and making my dream to study Astronomy come true!

Last but not least, I want to thank Enrico for being the best and most caring boyfriend one can have! Thank you for your patience, withstanding my stressy times and just being there! You are the best!